

# **Non-Evaporable Getter Thin Film Coatings for Vacuum Applications**

**Thèse No. 2652 (2002)**

Présentée à la Faculté Sciences de Base  
Section de Physique

**ECOLE POLYTECHNIQUE FÉDÉRALE DE LAUSANNE**

POUR L'OBTENTION DU GRADE DE DOCTEUR ÈS SCIENCES

**PAR**

**Alexandra Prodromides**

Ingénieur diplômée de l'ENSI de Caen,  
DEA en sciences des matériaux, Université de Caen, France  
et de nationalité française

*Acceptée sur proposition du jury :*

Prof. Francis Lévy, directeur de thèse  
Dr. Cristoforo Benvenuti, rapporteur  
Prof. Harald Brune, rapporteur  
Prof. Louis Schlapbach, rapporteur

Lausanne EPFL  
2002

# Abstract

Getters are solid materials capable of chemisorbing gas molecules on their surface: getters are chemical pumps. They are widely used for a variety of applications such as in particle accelerators, vacuum tubes, field-emission display (FED), inert gas purification systems, H<sub>2</sub> plasma purification, hydrogen species recycling as in the Tokamak Fusion Test Reactor. Among the different Non-Evaporable Getter (NEG) materials tested, the TiZrV alloys have the lowest activation temperature. For this reason, the TiZrV coatings were the object of this work. In particular, the aim of this investigation was to understand how to optimise three important properties of TiZrV coatings: to achieve the lowest possible activation temperature ( $T_a$ ), and to obtain the highest pumping speed and surface pumping capacity. This objective is important in the context of the Large Hadron Collider (LHC) accelerator, since, before this work, the understanding and the knowledge of the TiZrV coating properties were insufficient to adopt it for this machine.

In the present investigation, TiZrV coatings (250 samples) of various compositions have been deposited by DC (Direct-Current) diode magnetron sputtering. The influence of the substrate material, substrate roughness, substrate temperature ( $T_s$ ), film composition, on the activation temperature and pumping properties have been investigated in order to optimise the deposition parameters for vacuum applications. The characterisation of the films has been carried out by Auger Electron Spectroscopy (AES), X-ray Photoelectron Spectroscopy (XPS) and Energy Dispersive X-ray spectroscopy (EDX) for the surface and bulk chemical composition, respectively, and by X-Ray Diffraction (XRD), Scanning Electron Microscopy (SEM), Transmission Electron Microscopy (TEM) and Scanning Tunnelling Microscopy (STM) for the morphology and crystallinity. The performances of the best coatings selected through the above mentioned methods have been investigated by pumping speed measurements of H<sub>2</sub>, CO and N<sub>2</sub>.

The main results of this investigation are the following. XRD measurements prove that depending on their composition, the TiZrV coatings can be grouped into two families which are sharply separated with respect to their grain size: polycrystalline films, with grain size above 100 nm and nanocrystalline films with grain size below 5 nm. TEM images clearly reveal grains with sizes in the nanometer range for the tested samples of the second family.

The surface of the NEG TiZrV coatings was analysed by AES, in order to monitor their activation behaviour. It resulted that TiZrV coatings of different compositions can be divided into two groups: one group of high activation temperature ( $T_a > 200$  °C for 1 hour heating) and one of low activation temperature ( $T_a < 200$  °C for 1 hour heating). For the first time, a clear relation between morphology and activation has been found: without exception, the TiZrV NEG films with low activation temperature are among the coatings crystallising with small grain size (below 5 nm).

For TiZrV coatings sputtered in identical conditions, different substrate materials were found to induce different morphologies, but identical crystallinity (nanocrystallinity) and activation temperature.

The increased surface roughness, obtained by deposition on rough copper, does not accelerate the activation process, but clearly increases pumping speed and surface pumping capacity.

The substrate temperature during sputter deposition ( $T_s$ ) also increases the roughness of a coating on copper without changing its crystallinity up to 250 °C. The ideal copper-substrate temperature is  $T_s = 250$  °C both in terms of sticking probabilities and surface pumping capacity. By combining this coating temperature with a rough substrate, the surface pumping capacity results in the same level of pumping capacity for a 2  $\mu\text{m}$  thick coating as for the available commercial NEG films more than 100  $\mu\text{m}$  thick.

The maximum pumping speed is obtained by heating the coating at 250 °C for activation. For higher heating temperatures, the pumping speed decreases. This feature had already been observed, although in a different temperature range, for other NEG films (namely the St707). Thermal instability of the crystalline structure, pollution of the NEG coating due to the substrate, pollution by a gas, do not appear to be relevant for the deterioration of the NEG properties. The possibility of other types of surface modifications (formation of unsuitable surface phases by segregation, removal of lattice defects and/or nanoprotusions) which could not be detected by means of the available investigation methods, remains open.

In conclusion, the present study has improved the knowledge of the properties of TiZrV getter films. Coatings of optimised characteristics may be reliably produced on vacuum chambers made of different materials. The acquired knowledge is sufficient to adopt this solution for the LHC accelerator at CERN, where about 5 km of this machine will be coated as well as the intersection vacuum chambers for the physic experiments. Meanwhile, coated chambers have already been successfully used on other accelerators, namely at ESRF (Grenoble, France) and Elettra (Trieste, Italy).

# Version abrégée

Les getters sont de matériaux solides capables de chimisorber des molécules gazeuses sur leur surface: ce sont des pompes chimiques. Ils sont utilisés pour des applications aussi variées que dans les accélérateurs de particules, les tubes à vide, les systèmes à effet de champ, les systèmes de purification de gaz inertes, la purification des plasmas de  $H_2$ , le recyclage d'hydrogène dans les Tokamaks. Parmi les différents matériaux Getter Non-Evaporables (NEG) testés, les alliages de TiZrV ont la plus basse température d'activation. Pour cette raison, les films TiZrV ont été choisis comme sujet de ce travail. Le but de cette recherche était plus particulièrement de comprendre comment optimiser les trois propriétés fondamentales suivantes des films NEG de TiZrV: atteindre la plus basse température d'activation ( $T_a$ ), obtenir les plus hautes vitesses de pompages et capacités surfaciques possibles. Cet objectif est important dans le cadre de l'accélérateur de particules LHC (Large Hadron Collider), puisqu'au démarrage de ce travail, la compréhension et les connaissances des films NEG de TiZrV étaient insuffisantes pour qu'ils soient utilisés dans la machine.

Dans le cadre de ce travail, des films TiZrV (250 échantillons) de différentes compositions ont été déposés par pulvérisation cathodique en configuration diode, magnétron, en courant continu. L'influence du matériau utilisé pour le substrat, de la rugosité du substrat, de la température du substrat pendant le dépôt ( $T_s$ ), et de la composition du film sur la température d'activation et les propriétés de pompage a été étudiée dans le but d'optimiser les paramètres de déposition. La caractérisation des films a été faite par spectroscopie Auger, spectroscopie X de photoélectrons et spectroscopie à dispersion d'énergie, en ce qui concerne la composition chimique de la surface et du matériau massif. La diffraction de rayons X, la microscopie électronique à balayage, la microscopie électronique à transmission et la microscopie à effet tunnel ont permis d'étudier la morphologie et la cristallinité. Les meilleurs films qui ont été sélectionnés grâce à ces méthodes ont été étudiés par des mesures de vitesse de pompage de  $H_2$ , CO et  $N_2$ .

Les principaux résultats de cette recherche sont les suivants. D'après les mesures de diffraction X, les films TiZrV de différentes compositions peuvent être regroupés en 2 familles distinctes, en fonction de leur taille de grains: les films polycristallins ont une taille de grains supérieure à 100 nm et les nanocristallins ont une taille de grains inférieure à 5 nm. Les



images de microscopie électronique à transmission révèlent des grains de l'ordre de quelques nanomètres dans le cas des échantillons de la seconde famille qui ont été testés. La surface des films NEG TiZrV a été analysée par spectroscopie Auger dans le but de suivre son activation. Il a résulté que les films TiZrV de différentes compositions peuvent être séparés en deux groupes: l'un de haute température d'activation ( $T_a > 200$  °C pour un chauffage de 1 heure) et l'autre de basse température d'activation ( $T_a < 200$  °C pour un chauffage de 1 heure). Pour la première fois, une relation claire entre la morphologie et l'activation a été trouvée: sans aucune exception, les films NEG TiZrV avec une basse température d'activation cristallisent avec une taille moyenne de grains inférieure à 5 nm.

Des films TiZrV pulvérisés dans des conditions identiques sur des substrats de nature différente ont des morphologies différentes, mais la même cristallinité (nanocristallinité) et la même température d'activation. L'augmentation de la rugosité de la surface, obtenue par déposition sur cuivre rugueux, n'accélère pas le procédé d'activation, mais augmente la vitesse de pompage et la capacité surfacique de pompage. La température du substrat pendant la déposition par pulvérisation cathodique ( $T_s$ ) augmente également la rugosité du film déposé sur cuivre, sans modifier sa cristallinité, jusqu'à 250 °C. La température idéale du substrat de cuivre pendant le dépôt est  $T_s = 250$  °C aussi bien en ce qui concerne la probabilité de collage que la capacité surfacique de pompage. En combinant cette température de dépôt avec la rugosité du substrat, la capacité surfacique de pompage est la même pour le film de 2  $\mu\text{m}$  d'épaisseur et les NEG commerciaux de 100  $\mu\text{m}$ .

Le maximum de vitesse de pompage est obtenu en chauffant le film à 250 °C pendant l'activation. Si on le chauffe à plus haute température, la vitesse de pompage diminue. Ce phénomène a déjà été observé, même si c'était à plus haute température, pour d'autres NEG (comme le St707). On a établi que l'effet de l'instabilité thermique de la structure cristalline, de la pollution du film NEG par le substrat, de la pollution par un gaz, ne sont pas à l'origine de la détérioration des propriétés des NEG TiZrV.

En conclusion, cette étude a permis d'améliorer les connaissances des propriétés des films getters de TiZrV. Les films ainsi optimisés peuvent être utilisés de façon fiable pour recouvrir des chambres à vide faites de différents matériaux. Les connaissances acquises sont suffisantes pour adopter cette solution pour l'accélérateur LHC au CERN, où environ 5 km de la machine seront recouverts d'un tel film ainsi que les intersections des chambres à vide pour les expériences de physique. Des chambres ainsi recouvertes de NEG ont déjà été utilisées avec succès dans d'autres accélérateurs tels que l'ESRF (Grenoble, France) et Elettra (Trieste, Italie).

## Acronyms

AES	Auger Electron Spectroscopy
bcc	body-centred cubic
DC	Direct-Current
EDX	Energy Dispersive X-ray spectroscopy
ESD	Electron Stimulated Desorption
ESRF	European Synchrotron Radiation Facility
FED	Field-Emission Display
fcc	face centered-cubic
GDMS	Glow Discharge Mass Spectroscopy
hcp	hexagonal close-packed
LEED	Low-Energy Electron Diffraction
LEP	Large Electron Positron collider
LHC	Large Hadron Collider accelerator
NEG	Non-Evaporable Getter
OFE	Oxygen-Free Electronic copper
SEM	Scanning Electron Microscopy
SEY	Secondary Electron emission Yield
STM	Scanning Tunnelling Microscopy
TEM	Transmission Electron Microscopy
UHV	Ultra High Vacuum
XPS	X-ray Photoelectron Spectroscopy
XRD	X-Ray Diffraction

## Constants

h	Planck constant = $6.6257 \times 10^{-34}$ J s
k	Boltzman constant = $1.38065 \times 10^{-23}$ J K <sup>-1</sup>
N <sub>A</sub>	Avogadro constant = $6.0221367 \times 10^{23}$ mol <sup>-1</sup>
R	molar gas constant = $8.314$ J K <sup>-1</sup> mol <sup>-1</sup> = $1.98 \times 10^{-3}$ kcal mol <sup>-1</sup> K <sup>-1</sup>

# Notations

$A$	NEG coated surface = $A_f + A_v$
$A_f$	area of the flat surface of the NEG coating
$A_v$	total area of the entrance orifices of the voids on the surface of the NEG coating
$c$	concentration
$C_i$	conductance of gas $i$
$d$	diameter of the voids
$D(T)$	diffusion coefficient (or diffusivity) of $i$ at temperature $T$ : $D(T) = D_i \cdot e^{\frac{-E_i}{R \cdot T}}$
$D_i$	constant in the diffusivity equation of $i$
$E_i$	activation energy for diffusion of $i$
$F_i$	flux of gas $i$
$K$	equilibrium constant of a reaction
$L$	diffusion length
$\ell_m$	distance over which is made the measurement of average roughness
$M$	molecular weight
$M_{Me}$	molar mass of metal Me
$n^2$	density of the voids per cm <sup>2</sup> of NEG coated surface
$p$	multiplicity of adsorption sites
$P$	pressure
$P_{H_2}$	dissociation pressure, or equilibrium pressure of H <sub>2</sub>
$P_v$	vapour pressure
$Q$	= $Q_f + Q_v$ = gas quantity pumped for the pumping speed $S = S_v + S_f$
$Q_f$	gas quantity pumped on $A_f$
$Q_i$	quantity of gas $i$ pumped
$Q_o$	gas quantity needed to saturate the surface of the NEG which would not present any orifice on its surface
$Q_v$	gas quantity pumped on $A_v$
$R_a$	average roughness
$R_t$	maximum roughness depth
$S_f$	pumping speed of the flat outer surface of the NEG per unit area
$S_i$	pumping speed per unit area of $i$
$S_o$	initial pumping speed of the NEG per unit area
$S_v$	pumping speed of the voids of the NEG per unit area

$t$	time
$T$	absolute temperature in K
$T_a$	activation temperature
$T_m$	melting temperature
$T_s$	temperature of the substrate during the sputtering process
$x_i$	solubility limit of $i$
$\alpha_i$	sticking probability of $i$
$\alpha_f$	sticking probability on flat clean surface
$\alpha_v$	sticking probability at the entrance of the voids
$\Delta G_{ox}$	free energy of formation of an oxide
$\Delta G_{ss}$	free energy of formation of a solid solution, per oxygen atom
$\Delta H_{ox}$	enthalpy of formation of an oxide
$\Delta H_{ss}$	enthalpy of formation of a solid solution, per oxygen atom
$\delta_i$	deposition rate of $i$
$\Delta S_{ox}$	entropy of an oxide
$\Delta S_{ss}$	entropy of a solid solution, per oxygen atom
$\rho_{Me}$	density of metal Me
$\tau$	mean sojourn time
$\tau_0$	period of vibration of an adsorbed molecule
$\omega$	average grain size

# Contents

<b>Abstract</b>	<b>iii</b>
<b>Version Abrégée</b>	<b>v</b>
<b>Acronyms</b>	<b>vii</b>
<b>Constants</b>	<b>vii</b>
<b>Notations</b>	<b>viii</b>
<b>1 Introduction</b>	<b>1</b>
1.1 Definition of getter materials . . . . .	1
1.2 Quantities defining getter vacuum performance . . . . .	2
1.3 Evolution of getter technology for particle accelerators . . . . .	3
1.4 Getter technology for applications other than particle accelerators . . . . .	5
1.5 Selection of getter material . . . . .	6
1.6 Benefits of thin-film getter coatings . . . . .	8
1.6.1 Low outgassing and ultimate pressure . . . . .	8
1.6.2 Simplified chamber construction . . . . .	8
1.6.3 Low secondary-electron yield . . . . .	9
1.7 The purpose of this study and intermediate conclusions . . . . .	10
<b>2 Gas gettering: general considerations</b>	<b>11</b>
2.1 Activation mechanism . . . . .	11
2.1.1 Metal, oxide and oxygen in solid solution . . . . .	11
2.1.2 Diffusivity and solubility limit . . . . .	16
2.1.3 The role of temperature and time for the activation for pure metals . . . . .	26
2.1.4 Bulk or grain boundary limiting diffusion . . . . .	30
2.1.5 Conclusions . . . . .	32
2.2 Pumping speed and capacity . . . . .	33
2.2.1 Effect of surface roughness . . . . .	33
2.2.2 H <sub>2</sub> absorption . . . . .	33

2.2.3	CO and N <sub>2</sub> adsorption . . . . .	33
2.2.4	Pumping of gas mixtures . . . . .	37
<b>3</b>	<b>NEG coatings preparation</b>	<b>39</b>
3.1	Sputtering methods . . . . .	39
3.1.1	Sputtering technique and deposition rate . . . . .	39
3.1.2	Plasma . . . . .	43
3.1.3	Sputtering configurations . . . . .	45
3.1.4	Influence of pressure and temperature . . . . .	48
3.1.5	Common cathodes for alloy deposition . . . . .	49
3.2	Sputtering systems and parameters . . . . .	50
3.2.1	Substrate preparation . . . . .	50
3.2.2	Geometries used for the sputtering systems . . . . .	53
3.2.3	Purity of the cathodes . . . . .	62
<b>4</b>	<b>Methods for the characterisation of thin getter coatings</b>	<b>65</b>
4.1	Elemental composition of thin getter films . . . . .	65
4.1.1	Energy Dispersive X-ray spectroscopy (EDX) . . . . .	65
4.1.2	Glow Discharge Mass Spectroscopy (GDMS) . . . . .	66
4.2	Morphology and crystallographic structure of thin getter films . . . . .	66
4.2.1	X-Ray Diffraction (XRD) . . . . .	66
4.2.2	Transmission Electron Microscopy (TEM) . . . . .	68
4.2.3	Scanning Electron Microscopy (SEM) . . . . .	68
4.2.4	Laser dynamic focusing . . . . .	69
4.3	Thermal activation of thin getter films . . . . .	70
4.3.1	Physical phenomena implied in the thermal activation . . . . .	70
4.3.2	Operational definition of activation temperature ( $T_a$ ) . . . . .	70
4.3.3	Activation temperature evaluation by surface analytical methods . . .	70
4.3.4	Evaluation of gettering properties by pumping speed measurements .	75
<b>5</b>	<b>Results</b>	<b>79</b>
5.1	Influence of the TiZrV film composition . . . . .	79
5.1.1	Film crystallinity . . . . .	79
5.1.2	Activation temperature . . . . .	84
5.2	Influence of the substrate . . . . .	92
5.2.1	Material of the substrate . . . . .	92
5.2.2	Substrate roughness . . . . .	95
5.3	Influence of the substrate temperature $T_s$ . . . . .	98
5.3.1	Film morphology . . . . .	99
5.3.2	Film crystallinity . . . . .	101

5.3.3	Pumping speed for CO and H <sub>2</sub> and surface pumping capacity . . . . .	102
5.4	Influence of the surface load of a gas on the pumping speed for other gases . .	108
5.4.1	Influence of N <sub>2</sub> surface load on the pumping speed of H <sub>2</sub> and CO . . .	108
5.4.2	Influence of the CO surface load on the pumping speed of H <sub>2</sub> , CO and N <sub>2</sub> . . . . .	110
5.5	Effects of intermediate air venting on the pumping speed of H <sub>2</sub> and CO (ageing)	112
5.6	Intermediate conclusions . . . . .	116
5.7	Summary of the results . . . . .	117
<b>6</b>	<b>Discussion</b>	<b>119</b>
6.1	Influence of the crystalline state on the activation temperature . . . . .	119
6.1.1	The nanocrystalline structure of TiZrV . . . . .	119
6.1.2	Activation of TiZrV compared to TiZrCr, TiZrNb . . . . .	122
6.1.3	Conclusions . . . . .	126
6.2	Decrease of pumping speed at $T \geq 250$ °C . . . . .	127
6.2.1	Crystallisation . . . . .	127
6.2.2	Poisoning from the substrate . . . . .	129
6.2.3	Poisoning by gas . . . . .	133
6.2.4	Conclusions . . . . .	134
<b>7</b>	<b>Conclusions</b>	<b>135</b>
<b>8</b>	<b>Glossary</b>	<b>139</b>
<b>9</b>	<b>Appendix</b>	<b>143</b>
9.1	Sample description and labelling . . . . .	143
9.2	SEM micrographs of NEG coatings deposited at different substrate tempera- tures ( $T_s$ ) . . . . .	145
	<b>Curriculum Vitae</b>	<b>169</b>

# Chapter 1

## Introduction

The present study is being undertaken in the frame of the LHC (Large Hadron Collider accelerator) project at CERN. While in the earlier case of LEP (Large Electron Positron collider), a channel parallel to the beam channel was available for pumping [1], in the LHC, this solution cannot be used because of space constraints. This restriction has stimulated the search for a new distributed pumping concept based on getter thin film coatings. The use of aluminium alloy chambers and the fact that some parts of the machine cannot be heated to a temperature higher than 200 °C have motivated the search for new materials that can be activated by heating at unusually low temperatures.

### 1.1 Definition of getter materials

When a gas molecule is adsorbed on a surface, its mean sojourn time  $\tau$ , proportional to the reciprocal of the desorption probability [2], is given by Frenkel's law, established in 1924:

$$\tau = \tau_0 \cdot e^{\frac{E}{RT}} \quad (1.1)$$

where  $T$  is the surface temperature,  $E$  is the binding energy, and  $R$  is the molar gas constant (8.314 J K<sup>-1</sup> mol<sup>-1</sup>).  $\tau_0$ , the period of vibration of the adsorbed molecule, is assumed to be of the order of 10<sup>-13</sup> s independently of the specific gas–solid combination. A surface provides a good pumping action when  $\tau$  is much larger than the duration of the experiment, which can vary from some minutes (for instance in a characterisation system such as an Auger electron spectrometer) to some weeks (e.g. in accelerator facilities).

Physisorption implies van der Waals forces of electrostatic nature. They are characterised by binding energies typically lower than 50 kJ mol<sup>-1</sup> or 0.4 eV molecule<sup>-1</sup>. For instance, for physisorbed Ar, CO, N<sub>2</sub>, CO<sub>2</sub> with a binding energy of about 25 kJ mol<sup>-1</sup>, a typical  $\tau$  value at 300 K is 10<sup>-11</sup> s [3]. Consequently, in the case of physisorption, pumping can only be achieved by surface cooling (cryopumping) because the mean sojourn time at room temperature is too short.



Chemisorption implies chemical forces which involve interactions between valence electrons and are characterised by binding energies typically larger than  $50 \text{ kJ mol}^{-1}$ , such as in covalent, ionic or metallic bondings [4]. The corresponding  $\tau$  values at 300 K are for instance  $3 \times 10^{-6} \text{ s}$  for a weak chemical energy of  $50 \text{ kJ mol}^{-1}$ , 100 s for  $\text{H}_2$  chemisorbed with a binding energy of  $100 \text{ kJ mol}^{-1}$  and  $4 \times 10^9 \text{ s}$  (more than 100 years) for CO chemisorbed on Ni with  $150 \text{ kJ mol}^{-1}$  [3]. Then, chemisorption allows Ultra High Vacuum (UHV), i.e. pressures in the range from  $10^{-9} \text{ Torr}$  to  $10^{-12} \text{ Torr}$ , to be maintained even at room temperature.

Materials able to react chemically with gas molecules and to form stable chemical compounds are called getters. As a consequence, getters cannot pump chemically inert gases like noble gases. It is also hard to pump methane at room temperature. At room temperature, all adsorbed gases (except  $\text{H}_2$  which can diffuse into the bulk) remain on the getter surface, resulting in a progressive reduction of the pumping speed as active surface sites become blocked. When intolerably low values are reached, the initial reactivity of the pumping surface has to be restored. Getter materials are classified in two families depending on the method used for the production of the active surface: evaporable and non-evaporable getters [3].

For evaporable getters, the active surface is obtained by *in situ* sublimation under vacuum of a fresh metallic film [3].

For Non-Evaporable Getters (NEG), the active surface is produced by thermal diffusion of the surface contaminants into the bulk of the NEG material itself. After air exposure, the main contaminant is oxygen present in the passivating oxide layer.

## 1.2 Quantities defining getter vacuum performance

The vacuum performances of a given getter, after activation, are mainly denoted by pumping speed or sticking probability, surface pumping capacity, ultimate pressure, and  $\text{H}_2$  dissociation pressure.

The pumping speed of a pump is defined as the ratio of the throughput (see Glossary in Chapter 8) of a given gas to the partial pressure of that gas near the pump intake [5]; it is expressed in  $[\ell \text{ s}^{-1}]$ . The pumping speed per unit area is defined as:

$$S = \alpha C [\ell \text{ s}^{-1} \text{ cm}^{-2}] \quad (1.2)$$

where  $\alpha$  is the sticking probability ( $0 \leq \alpha \leq 1$ ), and  $C$  is the conductance, expressed in  $[\ell \text{ s}^{-1} \text{ cm}^{-2}]$  [3]. In the molecular flow regime (see Glossary in Chapter 8),  $C$  does not depend on the pressure. It may be expressed as:

$$C = 3.64 \sqrt{\frac{T}{M}} [\ell \text{ s}^{-1} \text{ cm}^{-2}] \quad (1.3)$$

with  $T$  the absolute temperature in K and  $M$  the molecular weight. If every molecule impinging on a surface is captured, i.e. for  $\alpha = 1$ ,  $C$  represents the pumping speed of the surface;

in that case, for example  $S = 12 [\ell \text{s}^{-1} \text{cm}^{-2}]$  for  $\text{N}_2$  at room temperature [3].

The surface pumping capacity represents the number of atoms or molecules which are captured by the getter before its pumping speed vanishes, i.e. before it stops sorbing gas [6]. It is expressed in number of molecules or in pressure-volume units (for instance  $[\text{Torr } \ell]$ ). It is in general obtained during the pumping speed measurement.

The ultimate pressure or base pressure [5], [7], [8] of a system designates the lowest total pressure that can be produced and measured reproducibly after baking in a vacuum system at room temperature. It is evaluated as being the ratio of the rate of gas entering into the system, the so-called gas load, to the effective pumping speed. In a vacuum system, there are mainly three sources of gas, i.e. the gas produced or introduced by (i) leaks, (ii) outgassing (thermal and stimulated), and (iii) permeation [5], [9]. For all-metal baked vacuum systems, the main residual gas is  $\text{H}_2$ .

As for other gases, the mechanism associated with  $\text{H}_2$  solution in a getter material is described as a three step process: (i) dissociation of the gas molecules at the gas-surface interface; (ii) sorption at the superficial sites; (iii) dissolution in the bulk of getter material, through diffusion mechanisms. However,  $\text{H}_2$  is the only gas of which sorption is thermally reversible. The dissociation pressure, or equilibrium pressure  $P_{\text{H}_2}$ , describes the equilibrium between the flux of thermal desorption and the flux of pumping of  $\text{H}_2$ .  $P_{\text{H}_2}$  depends on  $c$ , the concentration of the solid solution of mono-atomic hydrogen, and on  $T$ , the temperature of the getter, according to Sievert's law (see Glossary in Chapter 8) [10], [11]:

$$P_{\text{H}_2} = A \cdot c^2 \cdot e^{\frac{\Delta H}{kT}} \quad (1.4)$$

were  $A$  and  $\Delta H$  are constant parameters depending on the getter material, which can be determined experimentally. The parameter  $A$  includes the entropic contribution towards the dissociation reaction of  $\text{H}_2$  and  $\Delta H$  is the reaction enthalpy. The  $P_{\text{H}_2}$  of a given NEG material has to be very low to be compatible with operation in UHV. The solid solution is thermodynamically stable up to a value called the solubility limit (see Glossary in Chapter 8). Approaching this concentration, the interactions between the solute atoms tend to increase, and hydride phases nucleate. This has to be avoided because it can cause getter damage.

### 1.3 Evolution of getter technology for particle accelerators

The evolution of getter technology for particle accelerators is described in Ref. [12].

A standard UHV vacuum system consists of an all-metal chamber to which one or many pumps are connected by means of flanges. As far as particle accelerators and storage rings are concerned, the rise in beam energy has led to the progressive reduction of the vacuum chamber diameter thus reducing the conductance [13]. Integrated linear pumping appeared to be an appropriate solution to the new geometric constraints. This was first achieved by using 'integrated' sputter-ion pumps, making use of the magnetic-field generated by the machine

bending-magnets [1]. However, during initial pumpdown, the magnets are not powered so that additional appendage sputter-ion pumps are required to obtain and maintain the vacuum. Furthermore, the magnetic field is lower during particle injection. This feature not only implies a reduced pumping speed but, in the specific case of LEP, was particularly dramatic because the low field value was dangerously close to the pump Penning-discharge extinction threshold [1].

A linear Non-Evaporable Getter (NEG) pump, not needing a magnetic field for operation, was consequently preferred. The NEG's potentially higher pumping speed as well as their intrinsic mechanical simplicity are further advantages. In practice, the St101 NEG commercially available from SAES-Getters (Milan, Italy) was used on 23 of the 27 km of the LEP machine. It consists of a 100-micron-thick layer of  $\text{Zr}_{84}\text{Al}_{16}$  (weight composition) powder coating on both sides of a 30-mm-wide constantan ( $\text{Cu}_{55}\text{Ni}_{45}$  weight composition) strip. After air exposure, the St101 activation requires heating to 750 °C for about half an hour. This temperature was reached by passing a current through the strip. In this way a distributed, continuous pumping was achieved. As for the integrated sputter-ion pumps, the non-evaporable getter strips were located in a channel parallel to the beam channel (Fig. 1.1).

Further progress was made feasible by the St707 NEG from SAES-Getters ( $\text{Zr}_{70}\text{V}_{24.6}\text{Fe}_{5.4}$  weight composition), which only requires heating to about 400 °C for activation. If the vacuum system is stainless steel, the activation can be induced during the bakeout. It is called passive activation. This feature is particularly attractive because, on the one hand, it removes the need for specific electric powering, control, insulation and feedthroughs [1] and on the other hand, it allows an increase of the NEG area and consequently of its pumping speed. Complete covering of the inner surface of a vacuum chamber with St707 strips ('total' NEG pump) results in a pumping speed larger than  $10^4 \ell \text{ s}^{-1}$  per linear metre and pressures in the  $10^{-14}$  Torr range [14].

The evolution from the standard vacuum system configuration to the 'total' NEG pump solution took about 20 years. This evolution was characterised by improving the vacuum characteristics of the getters and by moving the pumps progressively closer to the vacuum chamber walls.

This approach results in more effective pumping, but does not reduce the gas load due to outgassing of the chamber walls, which is the main obstacle to achieving UHV conditions in an all-metal system [3]. The gas load reduction can be obtained by coating the vacuum system walls with NEG thin film (see paragraph 1.6), which are passively activated during *in situ* bakeout to recover their chemical reactivity.

## 1.4 Getter technology for applications other than particle accelerators

In the context of CERN, the main application of getters is a ultra high vacuum application, in the LHC. Getters are also used in a variety of other applications.

- Vacuum tubes.

Electron tubes are used for example as picture tubes, receiving tubes or transmitting tubes. The residual gases in vacuum tubes are directly or indirectly responsible for tube defects and, in the long run, they are the principal cause of tube failure. The most noticeable effects are: (i) the fall in cathode emission due to the alteration of the surface resistance and changes in the chemical composition of the base metal; (ii) damage to cathode due to positive ion bombardment; (iii) screen spots due to negative ion bombardment; (iv) variation of applied potentials due to contaminated surfaces; (v) arcing in high voltage tubes. The tubes have a seal-off pressure of for instance  $10^{-4}$  to  $10^{-5}$  Torr for picture tubes. The getter has to cope with reducing and maintaining the pressure in the  $10^{-6}$  to  $10^{-8}$  Torr region [15]. Evaporated barium film is employed for such applications.

- Field-emission display (FED).

FED is one of the approaches for display companies to produce flat and lightweight screens that also offer outstanding picture quality. FED is essentially a cathode-ray tube squashed into a thickness of a few millimetres. In this type of display, electrons emitted from a specially designated cathode are directed towards a screen coated with phosphors. The electron current activates the phosphors which emit light. The applications of flat panel displays include medical instruments, entertainment and multimedia systems, desktop and portable computers. Several companies like Pixtech in France, Motorola and Candescent in the US, Futuba in Japan, are working towards manufacturing field-emission displays on an industrial scale. A crucial element of the display operation is the vacuum level inside the device. Any residual gas molecules inside the display can prevent emitted electrons from reaching the phosphor-coated screen, so degrading the image. For this reason, the vacuum level inside the device must typically be better than  $10^{-5}$  to  $10^{-6}$  Torr during operation. Even if this vacuum level is achieved when the display is fabricated, outgassing processes from different components in the display cause the vacuum to degrade during its operation. Getters are presented as the most effective way to continually remove the outgassed molecules from the display [16]. Non-evaporable TiZrV films like those studied in this work could be used for such an application [17].

- Inert gas purification systems.

Some applications require pure rare gases, as for chromatographic carrier gases or for atmospheres used for semiconductor production. In order to purify those gases, cryogenic

fractional distillation is commonly used. However, it is not sufficient to reach the ppm impurity levels. The St101 getter from SAES-Getters allows this impurity level to be reached and maintained for long periods [18].

- H<sub>2</sub> plasma purification.

The presence of plasma impurities impacts the fusion power gain in two major respects in apparatus such as the Tokamak Fusion Test Reactor. First, the radiative losses, which attend impurities and which increase strongly with atomic number, reduce plasma temperature and subsequently the fusion power gain. Besides adding to the radiation losses, impurities also cause a reduction in the deuterium and tritium densities for fixed electron densities which reduce the fusion power gain [19]. One technique which has been used successfully in a number of tokamaks to control impurities is gettering [20], [21]. This purification can be obtained by using Ti sublimation pumps. Deuterium can be desorbed from Ti films in reasonable times at 250 °C even in the presence of impurities such as C and O. Another relevant getter is the St101 bulk getter which reversibly absorbs hydrogenic species while chemisorbing impurities such as C, N and O.

- Hydrogen species recycling as in the Tokamak Fusion Test Reactor [19].

The hydrogen which is introduced into the vessel at the start of a plasma experiment is ionised and magnetically confined during the discharge. Nevertheless, it escapes slowly to the walls. Particles are confined during tens of milliseconds but the plasma pulses last several seconds in the ASDEX and TEXTOR tokamaks. A hydrogen ion may go to the wall and return a hundred times during the discharge. This recycling has been defined as the repeated interchange of hydrogen fuel between plasma and the wall. The walls of the fusion reactor are exposed to considerable flux densities ( $> 10^{17} \text{ cm}^{-2} \text{ s}^{-1}$ ) of hydrogen particles. Hydrogen recycling is thus important and unavoidable in fusion research and technology [22]. This can be obtained with Ti sublimation pumps which was also quoted as a way to control impurities [23].

## 1.5 Selection of getter material

The activation temperature ( $T_a$ ) of commercially available NEG strips is compatible with the baking temperature of stainless steel chambers. By lowering the activation temperature to 200 °C, the actual NEG coatings open a wider choice of substrate materials (aluminium, copper) suitable for the construction of the chamber in which passive activation of the getter is possible. Before the present study was started, several getter compositions had been investigated aiming at reducing the temperature of activation.

During the activation, the oxygen contained in the surface passivation oxide layer is dissolved into the material bulk by heating. To that end, the selected material should provide

a reasonable solubility limit for oxygen. Furthermore, a high solubility limit is essential to accommodate oxygen accumulation due to many activation air-exposure (so-called venting) cycles [12]. The thickness of the oxide layer formed during air exposure is 2–3 nm. A 1-micron-thick film would present an oxygen concentration of 2–3% after 10 such cycles. The oxygen concentration could be lowered by increasing the film thickness. Nevertheless, a solubility limit of at least 10% is desirable to guarantee a reasonable NEG life time [24].

Another essential parameter property is a high diffusivity for oxygen.

In addition to the high solubility and diffusivity of oxygen mentioned above, the NEG material should also have a high reactivity, i.e. large enthalpies of adsorption, for the main gas to be pumped in UHV vacuum system, namely CO, CO<sub>2</sub>, H<sub>2</sub> and a low dissociation pressure for hydrogen to provide low H<sub>2</sub> partial pressure in the system [1], [24], [25]. In contrast to oxygen, it is not crucial for the solubility limit for hydrogen to be high because H<sub>2</sub> can be released by heating.

The selected getter material should also provide other essential features, namely good adhesion to the substrate, high mechanical resistance and high melting point (to withstand cathode heating during the coating process). Furthermore, in some cases (e.g. for use in particle accelerators) it should be non-magnetic and present a low photoelectric and secondary electron yield to reduce electron emission and avoid multipacting [24], [25]. Finally, it should be non-toxic, non-pyrophoric and, if possible, inexpensive.

Among the many elements that provide good gettering properties, the transition metals of the 4<sup>th</sup> group of the periodic table (Ti, Zr, Hf) fulfil the most restrictive condition of the high solubility limit for oxygen, which exceeds 10% only for these elements. Another family of elements, the transition metals of 5<sup>th</sup> group (V, Nb, Ta) provide much higher oxygen diffusivity but a lower oxygen solubility limit. Therefore, elements of the 4<sup>th</sup> and 5<sup>th</sup> groups and some of their binary and ternary combinations have been taken as a starting point for a first experimental study [24].

Table 1.1: Summary of the activation temperature ( $T_a$ ) evolution of the main NEG<sub>s</sub>.

Getter	$T_a$ for 24 h heating [°C]	Refs.	Equivalent for 100% activation
St101 Zr <sub>84</sub> Al <sub>16</sub> (content in weight)	600	[1]	740 °C for 45 min
St707 Zr <sub>70</sub> V <sub>24.6</sub> Fe <sub>5.4</sub> (content in weight)	350	[26]	400 °C for 60 min
TiZr (atomic content)	250	[24]	300 °C for 2 h
Ti <sub>30</sub> Zr <sub>30</sub> V <sub>40</sub> (atomic content)	180	[27]	200 °C for 2 h

The progress achieved by NEG coatings with respect to bulk NEG is illustrated in Table 1.1.

## 1.6 Benefits of thin-film getter coatings

Compared to traditional NEG strips, the thin film getter used as coatings provide the following advantages.

### 1.6.1 *Low outgassing and ultimate pressure*

Thin film getter coatings lower the pressure in a vacuum system by transforming the vacuum chamber from a gas source to a pump.

The thermal outgassing of the vacuum chamber is reduced by trapping the gas coming from the underlying surface, which is generally the limiting factor of the ultimate vacuum in an all-metal system.

Furthermore, the NEG coating reduces also the degassing induced by ions, electrons [13] or photons (in particular synchrotron light [13], [28], [29]). This feature is crucial for accelerators where it results in a longer beam lifetime, in a lower risk of pressure bumps, and in a lower level of bremsstrahlung radiation. Such benefits have been illustrated with a Ti-Zr-V coated stainless steel chamber on a dedicated beamline at the European Synchrotron Radiation Facility, ESRF. After NEG activation, a reduction of the total degassing produced by synchrotron-radiation-induced desorption by at least a factor 380 has been measured [29].

### 1.6.2 *Simplified chamber construction*

The NEG coating is only a few microns thick so that it can be used in a vacuum chamber of limited conductance without needing a dedicated pumping channel, which results in a complicated mechanical design. As an illustration, a LEP chamber (Fig. 1.1) in which a NEG strip is used is compared to what could be done when using a NEG coating (Fig. 1.2).

In spite of being thinner than the powder coatings of traditional NEG strips by almost two orders of magnitude, thin getter coatings provide pumping speeds and total surface capacities very similar to those of the St707 NEG from SAES-Getters. They also withstand several activation/air venting cycles without excessive performance deterioration [27].

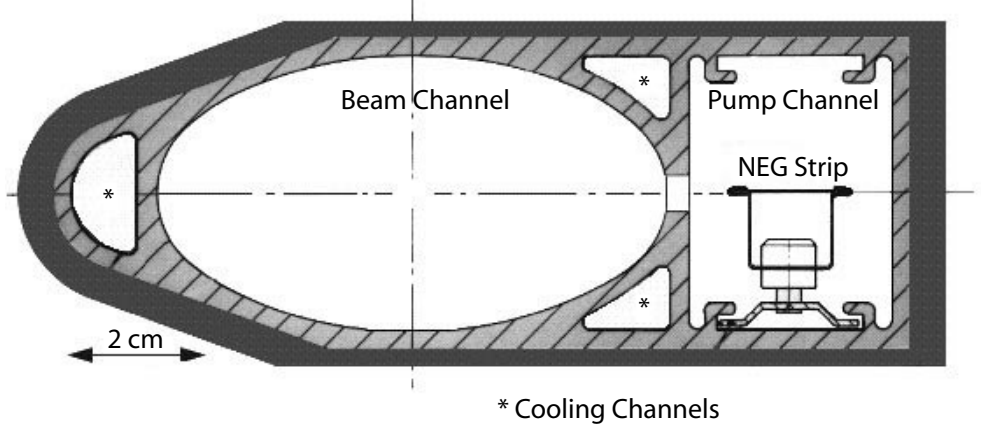


Fig. 1.1: Design of the cross-section of a LEP vacuum chamber (from Ref. [28]).

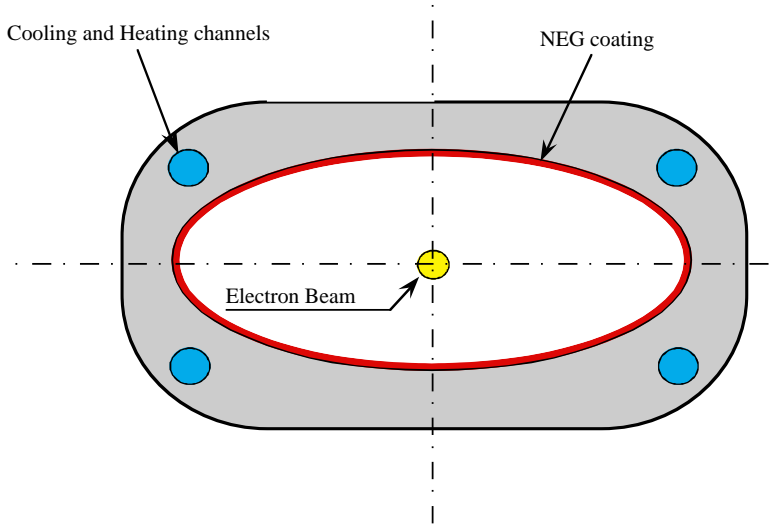


Fig. 1.2: Simplified chamber making use of a NEG coating.

### 1.6.3 Low secondary-electron yield

Secondary electrons are emitted upon primary electron irradiation. Secondary Electron emission Yield (SEY), is defined as the number of secondary electrons emitted per incident primary electron. A low secondary-electron yield reduces the risk of resonant electron multiplication, so-called multipacting [30], [31], [32]. Consequently, devices subjected to particle bombardment whose performances are hampered by multipacting, as is the case for particle accelerator vacuum systems [33], require a low SEY [34], [35]. For instance, for the internal surfaces of the LHC vacuum system, a critical maximum SEY of 1.35 is predicted, above which beam instabilities can occur [36]. The maximum SEY of air-exposed  $\text{Ti}_{50}\text{Zr}_{50}$  and  $\text{Ti}_{30}\text{Zr}_{20}\text{V}_{50}$  (atomic) coating decreases from above 2.0 to below 1.1 after a 2-hour heating at 250 °C and 200 °C, respectively [37]. For a similar decrease, typical metals for the construction of particle accelerator vacuum systems (stainless steel, copper, aluminium) require much higher heating



temperatures than the NEG coatings investigated. As an example, the SEY of a technical copper surface decreases from 2.5 to only 1.9 during a 24-hour bake-out at 200 °C [38]. It is also important that the SEY of CO-saturated NEG coatings be low.

## **1.7 The purpose of this study and intermediate conclusions**

In 1998, when this work was started, some TiZrV thin-film coatings with suitable properties were available. The aim of this study was to improve further these material properties and provide a better understanding of the basic mechanisms leading to the activation. This understanding will allow us to establish rules for the selection of new materials with even lower activation temperatures and improved gettering properties.

# Chapter 2

## Gas gettering: general considerations

### 2.1 Activation mechanism

#### 2.1.1 Metal, oxide and oxygen in solid solution

During the activation of a NEG material, the oxygen atoms are moved from the surface oxide to the solid solution. A thermodynamic description of this process can be obtained considering the free energy of formation of the oxide  $\Delta G_{ox}$  (Eq. (2.1)) and that of the solid solution  $\Delta G_{ss}$  (Eq. (2.2)) per oxygen atom, for infinite dilution:

$$\Delta G_{ox} = \Delta H_{ox} - T \cdot \Delta S_{ox} \quad (2.1)$$

$$\Delta G_{ss} = \Delta H_{ss} - T \cdot \Delta S_{ss} \quad (2.2)$$

where  $\Delta H$  and  $\Delta S$  are changes of the enthalpy and of the entropy of the two states respectively. The enthalpy data are summarised in Table 2.1 ( $\Delta H_{ss}$ ) and Table 2.2 ( $\Delta H_{ox}$ ) and are compared in Fig 2.1. The values of  $\Delta H_{ss}$  significantly depend on the concentration of oxygen in the solid solution. The order of magnitude of  $\Delta H$  and  $\Delta S$ , for the metals of interest, are about  $500 \text{ kJ mol}^{-1}$  and  $10 \text{ J mol}^{-1} \text{ K}^{-1}$ , respectively. A closed system containing oxide and oxygen solid solution will evolve in the direction that allows the minimum value of the free energy to be attained.

When  $\Delta G_{ox} < \Delta G_{ss}$ , oxygen dissolution is inhibited. In the reverse case the solid solution phase is favoured. For the case  $\Delta G_{ox} = \Delta G_{ss}$  the two phases are in equilibrium and the concentration in the solid solution is called solubility limit ( $x_o$ ).

For the particular case of  $\Delta G_{ox} > \Delta G_{ss}$  (dissolution allowed):

$$\Delta H_{ox} - \Delta H_{ss} > -T(\Delta S_{ss} - \Delta S_{ox}) \quad (2.3)$$

The entropic term  $-T(\Delta S_{ss} - \Delta S_{ox})$  is always negative. Therefore, in the case of  $|\Delta H_{ss}| > |\Delta H_{ox}|$  (see Table 2.3), the inequality (2.3) is always true. As a consequence, dissolution is always thermodynamically allowed independently of the value of the temperature until reaching the solubility limit. The limiting factor of the reaction of reduction of the oxide is in this case kinetic. This is the case for Ti, Zr and Hf.

When  $|\Delta H_{ss}| < |\Delta H_{ox}|$  both terms of the inequality (2.3) are negative and hence the entropic part could play an important role. Actually, it can happen that only for values of temperature larger than a given threshold is the inequality still valid. This is true for V, Nb and Ta. For a larger difference of the two enthalpies, the entropic term cannot compensate even at high temperature and therefore dissolution is hindered. This is the case for Cr and most of the other elements.

The three different cases are well illustrated in the phase diagrams of Fig. 2.2 to Fig. 2.8.

For Ti, Zr and Hf, the solubility limit does not depend much on the temperature. This reflects the fact that  $\Delta G_{ss}$  at infinite dilution does not depend on  $T$  and so the difference of free energy ( $\Delta G_{ss} - \Delta G_{ox}$ ) between the infinite dilution and the solubility limit is constant (Fig. 2.2, Fig. 2.3, Fig. 2.4).

For V, Nb and Ta the difference of free energy depends on temperature and the same is valid for the solid solution (Fig. 2.5, Fig. 2.6, Fig. 2.7).

Finally, for Cr, the solubility is so low that its range cannot be resolved in the phase diagram (Fig. 2.8).

A part from these important thermodynamic considerations, for the applications, kinetic aspects should also be studied.

Table 2.1: Thermochemical data:  $\Delta H_{ss}$  is the heat of dissolution of oxygen in pure metal at 298 K in kilo-Joule per mole of  $O_2$  for infinite dilution.

Groups	Metal	$-\Delta H_{ss}$ [kJ mol <sup>-1</sup> ]	Refs.
4 <sup>th</sup>	Ti $\alpha$	560.67	[41]
	Zr $\alpha$	619.23	[41]
	Hf	552.29	[41]
5 <sup>th</sup>	V	422.15	[42]
		422.15	[41]
	Nb	383.85	[41]
	Ta	386.00	[43]
		385.96	[41]
6 <sup>th</sup>	Cr	221.97	[41]

Table 2.2: Thermochemical data:  $\Delta H_{ox}$  is the heat of formation of the oxide at 298 K in kilo-Joule per mole of oxide [39], [40].

Groups	Metal-oxide	$-\Delta H_{ox}$ [kJ mol <sup>-1</sup> ]
3 <sup>rd</sup>	Sc – Sc <sub>2</sub> O <sub>3</sub>	1906.7
	Y – Y <sub>2</sub> O <sub>3</sub>	1906.7
	La – La <sub>2</sub> O <sub>3</sub>	1794.1
4 <sup>th</sup>	Ti – TiO	542.9
	Ti – Ti <sub>2</sub> O <sub>3</sub>	1521.6
	Ti – Ti <sub>3</sub> O <sub>5</sub>	2457.2
	Ti – TiO <sub>2</sub>	944.1
	Zr – ZrO <sub>2</sub>	1101.3
	Hf – HfO <sub>2</sub>	1113.7
5 <sup>th</sup>	V – VO	432.0
	V – V <sub>2</sub> O <sub>3</sub>	1219.4
	V – VO <sub>2</sub>	713.7
	V – V <sub>2</sub> O <sub>5</sub>	1551.3
	Nb – NbO	419.8
	Nb – NbO <sub>2</sub>	799.3
	Nb – Nb <sub>2</sub> O <sub>5</sub>	1900.8
	Ta – Ta <sub>2</sub> O <sub>5</sub>	2047.3
6 <sup>th</sup>	Cr – Cr <sub>2</sub> O <sub>3</sub>	1130.4
	Cr – CrO <sub>2</sub>	582.8
	Cr – CrO <sub>3</sub>	579.9

Table 2.3: Energy of dissolution of oxygen in pure metals compared to the heat of formation of the stable oxide containing the lowest number of oxygen atoms per atom of metal.

Groups	Metal-oxide	$\Delta H_{ox}$ [kJ mol <sup>-1</sup> ] per O atom	$\Delta H_{ss}$ [kJ mol <sup>-1</sup> ]
4 <sup>th</sup>	Ti - TiO	-542.9	-560.67
	Zr - ZrO <sub>2</sub>	-550.65	-619.23
	Hf - HfO <sub>2</sub>	-556.9	-552.29
5 <sup>th</sup>	V - VO	-432.0	-422.15
	Nb - NbO	-419.8	-383.85
	Ta - Ta <sub>2</sub> O <sub>5</sub>	-409.5	-385.96
6 <sup>th</sup>	Cr - Cr <sub>2</sub> O <sub>3</sub>	-376.8	-221.97



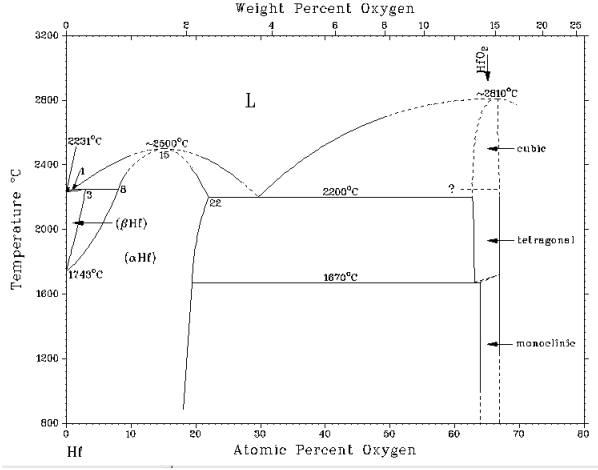


Fig. 2.4: Hf-O phase diagram [44].

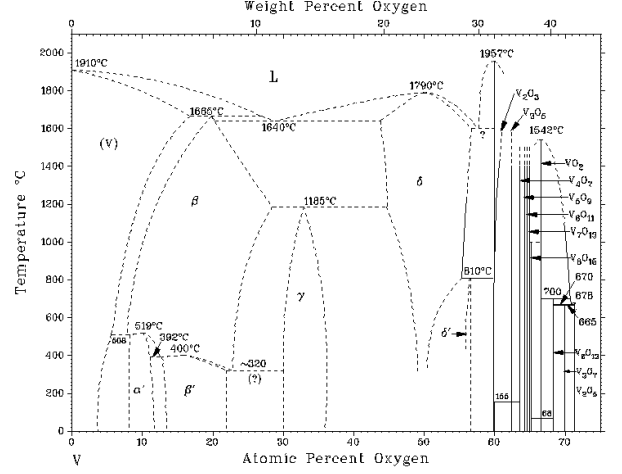


Fig. 2.5: V-O phase diagram [44].

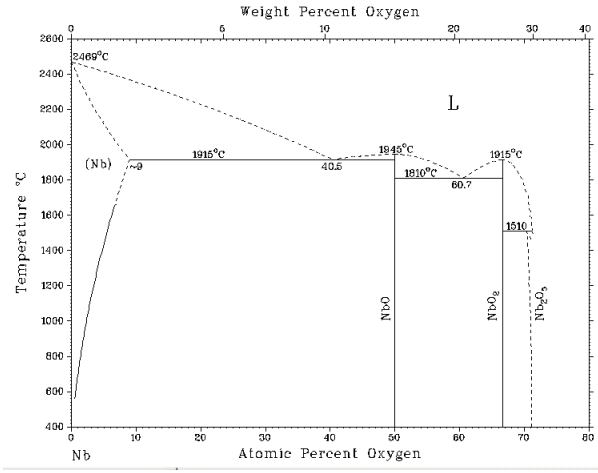


Fig. 2.6: Nb-O phase diagram [44].

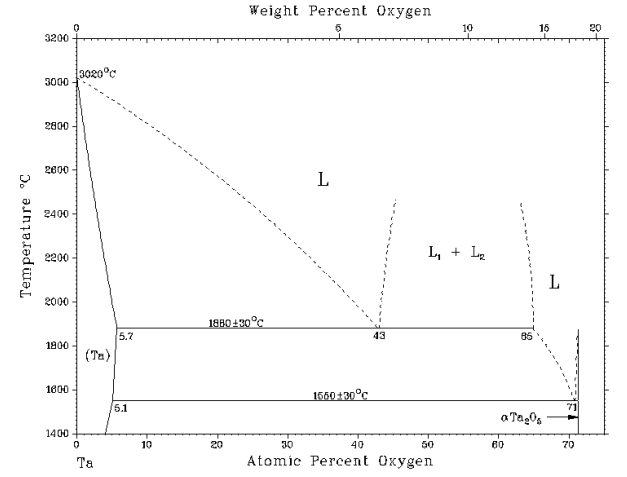


Fig. 2.7: Ta-O phase diagram [44].

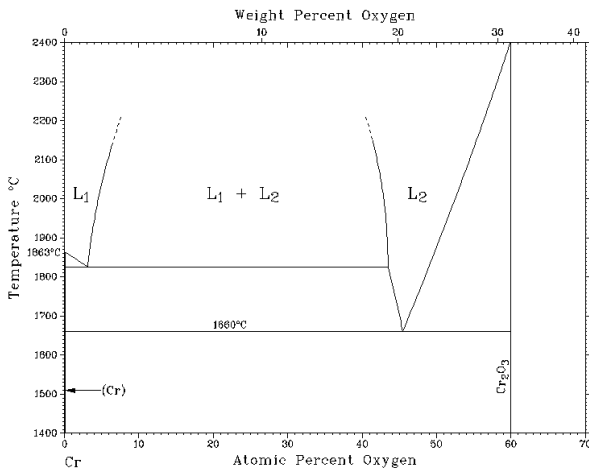


Fig. 2.8: Cr-O phase diagram [44].

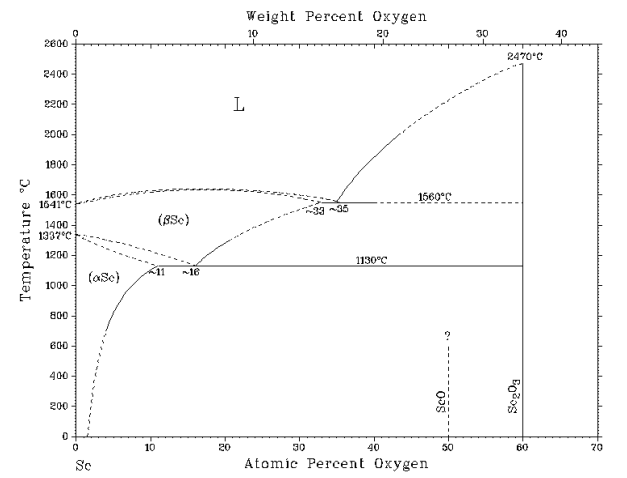


Fig. 2.9: Sc-O phase diagram [44].

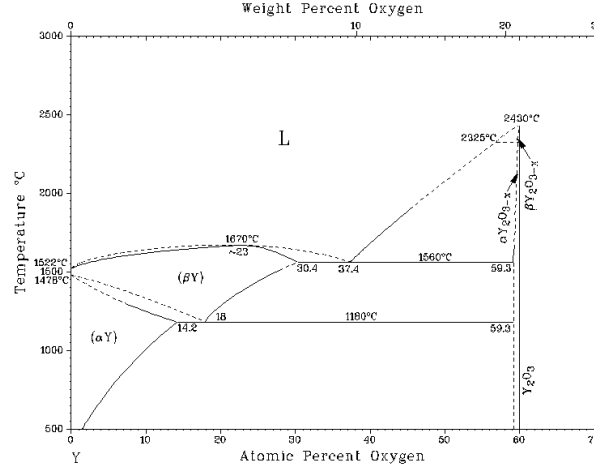


Fig. 2.10: Y-O phase diagram [44].

### 2.1.2 Diffusivity and solubility limit

Two important parameters for the description of the activation mechanism are the diffusivity and the solubility limit of oxygen. Some values of diffusivity and solubility limit of N, H and C are also quoted because they are the main impurities in non-evaporable getters after oxygen.

The data quoted in this paragraph are valid in the case of single crystals. Data are not available in the case of polycrystalline structures. It is important to note that the diffusivity is increased by grain boundaries with respect to a single crystal [45]. The solubility limit value also increases in the presence of polycrystals. Indeed, if the diffusivity is supposed not to be a limiting factor, the surface of each grain is available for oxygen uptake instead of just the surface of the film. Consider the case of a film with a flat surface and of thickness  $h$ . The grains are modelled by a cube of length  $a$ . The surface of the cube is  $6a^2$ . The surface available for oxygen uptake is about  $(h/a) \cdot 6$  times higher than in the case of the flat surface alone. If  $h = 2 \mu\text{m}$  and  $a = 5 \text{ nm}$ ,  $(h/a) \cdot 6 = 2400$ .

- Diffusivity and solubility limit of oxygen

The numerical values of diffusivity and solubility limit of oxygen are reported in Table 2.4 and Table 2.5 for the elements of the 3<sup>rd</sup>, 4<sup>th</sup> and 5<sup>th</sup> groups.

$D(T)$  is the diffusion coefficient (or diffusivity) of the element  $i$  in metal at temperature  $T$ :

$$D(T) = D_i \cdot e^{\frac{-E_i}{R \cdot T}} \quad (2.4)$$

$D_i$  is a constant [ $\text{cm}^2 \text{ s}^{-1}$ ],  $E_i$  is the activation energy for diffusion of the element  $i$  [ $\text{J mol}^{-1}$ ], and  $R$  is the molar gas constant =  $8.314 \text{ [J K}^{-1} \text{ mol}^{-1}]$ .

In the case of oxygen, the diffusion coefficient (or diffusivity) in metal at temperature  $T$  is:

$$D(T) = D_o \cdot e^{\frac{-E_o}{R \cdot T}} \quad (2.5)$$

$D_o$  is a constant [ $\text{cm}^2 \text{s}^{-1}$ ],  $E_o$  is the activation energy for diffusion of oxygen [ $\text{J K}^{-1} \text{mol}^{-1}$ ].

The metal-oxygen phase diagrams are given in Fig. 2.2 to Fig. 2.10 as the main source of information for the solubility limit of oxygen.

Table 2.4: Numerical values of diffusivity of oxygen for the elements of the 3<sup>rd</sup>, 4<sup>th</sup> and 5<sup>th</sup> groups.

Group	Metal	$D_o$ [cm <sup>2</sup> s <sup>-1</sup> ]	$E_o$ [J mol <sup>-1</sup> ]	$T$ [K]	Refs.	
3 <sup>rd</sup>	Sc ( $\alpha$ )	$D = 2.8 \times 10^{-6}$		1498	[45]	
		$1.16 \times 10^{10}$	448 530	1470–1700	[46]	
	Y ( $\alpha$ )	$9.4 \times 10^{-3}$	86 700	1173–1733	[45]	
	La	$D = 6.6 \times 10^{-7}$		1083	[45]	
4 <sup>th</sup>	Ti ( $\alpha$ )	0.45	201 000	573–1223	[45]	
		0.8	200 830	673–1123	[47]	
		$2.03 \times 10^{+5}$	315 168	1199–1423	[48]	
	Zr ( $\alpha$ )	$6.61 \times 10^{-2}$	184 200	563–923	[45]	
		$6.61 \times 10^{-2}$	184 100	563–923	[49]	
		$9.13 \times 10^{-5}$	124 770	< 973	[50]	
		Along [0001]	0.115	186 046	523–773	[51]
		Along [10 $\bar{1}$ 0]	1.07	193 286	523–773	[51]
	Hf ( $\alpha$ )	0.66	212 800	773–1323	[45]	
		$D = 3.8 \times 10^{-11}$		1073	[45]	
		0.66	212 550	773–2073	[49]	
5 <sup>th</sup>	V	$2.46 \times 10^{-2}$	123 490	333–2098	[45]	
		$1.90 \times 10^{-2}$	122 850	333–2098	[42]	
		$1.3 \times 10^{-2}$	121 600	489–774	[51]	
	Nb	$5.86 \times 10^{-3}$	109 650	296–1823	[45]	
		$6.95 \times 10^{-3}$	110 000	296–1823	[45]	
		$4.2 \times 10^{-3}$	107 200	303–1773	[45]	
		$1.38 \times 10^{-2}$	111 530	296–1873	[52]	
		$8.0 \times 10^{-2}$	116 320	403–1073	[52]	
	Ta	$1.05 \times 10^{-2}$	110 430	298–1673	[45]	
		$1.14 \times 10^{-2}$	110 940	298–1873	[43]	
		$1.9 \times 10^{-2}$	114 819	700–900	[53]	



Table 2.5: Numerical values of solubility limit of oxygen ( $x_o$ ) for the elements of the 3<sup>rd</sup>, 4<sup>th</sup> and 5<sup>th</sup> groups.

Group	Metal	$x_o$ atomic %	$T$ [K]	Refs.
3 <sup>rd</sup>	Sc	2	400	[54]
		0.33	673	[55]
		4.2	773	[55]
		18	1453	[55]
4 <sup>th</sup>	Ti	33	600–900	[54]
		30	–	[56]
		32	0–1800	[55]
	Zr	29	473–773	[55] [57]
		35	2338	[55]
	Hf	17	1000–2200	[54]
5 <sup>th</sup>	V	4	200–600	[54]
		3.5	473–573	[55]
		$\log x_o = -3.918 + 7.383 \times 10^{-3}T - 6.711 \times 10^{-6}T^2 + 2.083 \times 10^{-9}T^3$	935–1415	[42]
		$\log x_o = -0.77 - (387/T)$	973–1473	[42]
		7	973	[58]
		$\log x_o \text{ weight} = 0.705 - (515/T)$	473–1023	[59]
	Nb	$\log x_0 = -0.33 - (1680/T)$	1073–1773	[52]
		0.013	1123	[52]
		$-\log_e x_o = (8600 \text{ cal g}^{-1}/RT) + 0.516$	973–1823	[60]
		0.20	973	[61] [62]
		0.45	1173	[61] [62]
		0.33	418	[63]
		$\log x_o \text{ weight} = -32 + 3.33 \times (1000/T)$	1050–1373	[64]
		1.15	973	[64]
		6	2048	[65]
		1	973	[58]
	Ta	$\log x_o = -0.78 - (980/T)$	873–2153	[43]
		4	1600	[54]
		0.4	823	[66]
		0.10	1000	[61] [62]
		0.30	1373	[61] [62]
		5	1323	[67]
		$\log x_o \text{ (ppm)} = 4.130 - (1279/T)$	873–1173	[68]
		2	973	[58]

The diffusion length  $L$  during the time  $t$  at temperature  $T$  is given by [69]:

$$L = \sqrt{D(T) \cdot t} \quad . \quad (2.6)$$

For the transition metals of the 4<sup>th</sup> and 5<sup>th</sup> groups, a summary of the diffusion length ( $L$ ) and solubility limit ( $x_o$ ) of oxygen at 300 °C are given in Table 2.6 and Table 2.7, respectively.

Table 2.6: Numerical values of diffusion length of oxygen ( $L$ ), in nanometres, for the elements of the 4<sup>th</sup> and 5<sup>th</sup> groups for 2 hours heating at 300 °C. The values are calculated according to Eq. (2.6), on the basis of diffusion data from Ref. [45].

4 <sup>th</sup> group	5 <sup>th</sup> group
Ti	V
0.4	300
Zr	Nb
0.9	650
Hf	Ta
0.1	800

Table 2.7: Numerical values of solubility limit of oxygen ( $x_o$ ) for the elements of the 4<sup>th</sup> and 5<sup>th</sup> groups at 300 °C.

4 <sup>th</sup> group	5 <sup>th</sup> group
Ti	V
33 [54]	4 [54]
Zr	Nb
29 [55]	0.01 [52]
Hf	Ta
17 [54]	0.4 [66]

These diffusion length data indicate that metals of the 5<sup>th</sup> group have higher diffusivity of oxygen than those of the 4<sup>th</sup> group, or, put another way, that body-centred cubic (bcc) crystalline structures have higher diffusivity than the hexagonal close-packed (hcp) ones.

These solubility limit values (Table 2.7, Table 2.9) indicate that metals of the 4<sup>th</sup> group have higher storage capacities of oxygen and nitrogen than those of the 5<sup>th</sup> group, or, put another way, that hcp crystalline structures have higher storage capacities than the bcc ones. This was also experimentally observed for Ti and implemented in the model of Ref. [56]. It is said in the latter reference that both stable titanium modifications, the bcc and hcp phases, are considered to dissolve oxygen interstitially into their octahedral voids.

- Diffusivity and solubility limit of nitrogen

Data about diffusivity (Table 2.8) and solubility limit (Table 2.9) of nitrogen for the elements of the 3<sup>rd</sup>, 4<sup>th</sup> and 5<sup>th</sup> groups are reported from literature.

Table 2.8: Diffusivity of nitrogen for the elements of the 3<sup>rd</sup>, 4<sup>th</sup> and 5<sup>th</sup> groups.

Group	Metal	$D_N$ [cm <sup>2</sup> s <sup>-1</sup> ]	$E_N$ [J mol <sup>-1</sup> ]	$T$ [K]	Refs.
3 <sup>rd</sup>	Sc ( $\alpha$ )	$D = 6.2 \times 10^{-7}$		1488	[45]
	Sc ( $\alpha, \beta$ )	$8.66 \times 10^5$	344 870	1470–1700	[46]
	Y ( $\alpha$ )	$D = 3.1 \times 10^{-6}$		1508	[45]
4 <sup>th</sup>	Ti ( $\alpha$ )	0.21	224 000	723–973	[45]
		$8.0 \times 10^{-5}$	134 310	1073–1773	[47]
		$7.56 \times 10^{-4}$	159 400	1070–1940	[47]
		6.75	284 696	1573–1783	[53]
		$1.2 \times 10^{-2}$	189 450	1173–1673	[50]
	Zr ( $\alpha$ )	0.56	241 400	773–973	[45]
		$6.7 \times 10^{-2}$	218 340	1173–1973	[49]
	Hf ( $\alpha$ )	$2.4 \times 10^{-2}$	242 300	823–1173	[45]
		$1.2 \times 10^4$	404 010	1923–1983	[49]
	5 <sup>th</sup>	V	$4.17 \times 10^{-2}$	148 460	333–2098
$5.02 \times 10^{-2}$			151 050	440–1923	[45]
$4.17 \times 10^{-2}$			148 360	333–2098	[42]
Nb		$2.56 \times 10^{-2}$	152 100	543–1873	[45]
		$5.1 \times 10^{-2}$	156 900	470–2075	[52]
		$9.8 \times 10^{-2}$	161 600	633–933	[50]
Ta		$3.7 \times 10^{-3}$	156 800	483–630	[45]
		$5.21 \times 10^{-3}$	158 480	483–1673	[45]
		$4.25 \times 10^{-3}$	159 790	373–1573	[43]
		0.24	171 240	1073–1573	[50]

Table 2.9: Numerical values of solubility limit of nitrogen ( $x_N$ ) for the elements of the 3<sup>rd</sup>, 4<sup>th</sup> and 5<sup>th</sup> groups.

Group	Metal	$x_N$ [atomic %]	$T$ [K]	Refs.
3 <sup>rd</sup>	Y ( $\alpha$ )	< 0.1	1000	[54]
4 <sup>th</sup>	Zr	22	973	[44]
5 <sup>th</sup>	V	1.5	400	[54]
	Nb	< 0.1	up to 800	[54]
		0.5	573	[61]
		0.5	1773	[62]
		< 0.1	573	[62]
	Ta	4	1200	[54]
		0.5	573	[62] [61]
		2	873	[62]
		4	1273	[62]
		5.5	293	[62]

- Diffusivity and solubility limit of hydrogen

Data have been collected about diffusivity (Table 2.10) and solubility limit (Table 2.11) of hydrogen for the elements of the 3<sup>rd</sup>, 4<sup>th</sup> and 5<sup>th</sup> groups.

Table 2.10: Diffusivity of hydrogen for the elements of the 3<sup>rd</sup>, 4<sup>th</sup> and 5<sup>th</sup> groups.

Group	Metal	$D_H[\text{cm}^2 \text{ s}^{-1}]$	$E_H[\text{J mol}^{-1}]$	$T [\text{K}]$	Refs.
3 <sup>rd</sup>	Y ( $\alpha$ )	$1.03 \times 10^{-1}$	64 350	673–773	[45]
		0.103	64 310	673–773	[46]
4 <sup>th</sup>	Ti ( $\alpha$ )	$2.8 \times 10^{-5}$	23 850	293–500	[45] [47]
	Zr ( $\alpha$ )	$1.09 \times 10^{-3}$	47 730	333–548	[45]
		$4 \times 10^{-2}$	56 930	330–970	[49]
		$D = 1.98 \times 10^{-10}$		423	[51]
		$4.15 \times 10^{-3}$	39 650	723–973	[50]
	Hf ( $\alpha$ )	$6.0 \times 10^{-4}$	41 800	473–633	[45]
5 <sup>th</sup>	V	$4.4 \times 10^{-4}$	5 690	110–930	[45]
		$3.1 \times 10^{-4}$	4 340	148–666 K for $x_H < 0.043$	[42]
	Nb	$5.4 \times 10^{-4}$	10 520	235–830	[45]
		$1.2 \times 10^{-3}$	11 290	235–830	[45]
		$1.2 \times 10^{-4}$	6 670	165–250	[45]
		$9.0 \times 10^{-5}$	6 560	120–260 K for $x_H < 0.043$	[52]
		$5.0 \times 10^{-4}$	10 230	260–560 K for $x_H < 0.043$	[52]
		$2.15 \times 10^{-2}$	99 230	333–873	[50]
		$5.4 \times 10^{-4}$	10 613	270–560	[53]
	Ta ( $\alpha$ )	$3.39 \times 10^{-4}$	58 620	–	[45]
		$6.1 \times 10^{-4}$	14 650	273–433	[45]
		$4.4 \times 10^{-4}$	13 510	250–670 for $x_H < 0.053$	[43]

Table 2.11: Solubility limit of hydrogen ( $x_H$ ) for the elements of the 3<sup>rd</sup>, 4<sup>th</sup> and 5<sup>th</sup> groups.

Group	Metal	$x_H$ atomic %	$T$ [K]	Refs.
3 <sup>rd</sup>	Sc ( $\alpha$ )	36	900	[54]
		$\log x_H = -0.389 - (50.8/T)$	273–1273	[46]
	Y ( $\alpha$ )	$\log x_H = -0.32 - (127/T)$	300–1125	[46]
	La	0	0–550	[54] [55]
		1.4	560	[55]
4 <sup>th</sup>	Ti ( $\alpha$ )	3	300	[54]
		6.8	573	[54]
	Zr ( $\alpha$ )	$\log x_H = -1.28 - (850/T)$	385–523	[49]
		$5.4 \times 10^{-4}$	370	[49]
		6	823	[55]
		0	0–520	[55]
		0	0–400	[54]
		1	500	[54]
	Hf ( $\alpha$ )	0	200–700	[54]
5 <sup>th</sup>	V	0	0–200	[54]
		3	300	[54]
		$\log x_H = 0.5 - (646/T)$	120–335	[42]
	Nb ( $\alpha$ )	$< 0.1$	0–180	[54]
		5.7	300	[54]
		$\log x_H = 0.62 - (587/T)$	105–445	[52]
	Ta	$< 0.1$	0–100	[54]
		20	300	[54]
		$\log x_H = 1.65 - (743/T)$	130–290	[43]

A comparison of diffusivity of C, H, O and N in different metals is illustrated in Fig. 2.11, Fig. 2.12, Fig. 2.13, by comparing their diffusion lengths after 2 hours. I calculated those diffusion lengths in Ti, Zr and V using the diffusivity data of C, H, O and N that are given in Table 2.12, Table 2.10, Table 2.4, and Table 2.8, respectively and that are all quoted from Ref. [45]. The diffusion is faster for H than for C, O and is the slowest for N.

Table 2.12: Diffusivity of C in Ti, Zr and V.

Metal	$D_C$ [cm <sup>2</sup> s <sup>-1</sup> ]	$E_C$ [J mol <sup>-1</sup> ]	$T$ [K]	Refs.
Ti ( $\alpha$ )	$7.9 \times 10^{-4}$	127 700	873–1073	[45]
V	$8.8 \times 10^{-3}$	116 364	333–2098	[45]
Zr ( $\alpha$ )	$2 \times 10^{-3}$	151 590	873–1123	[45]

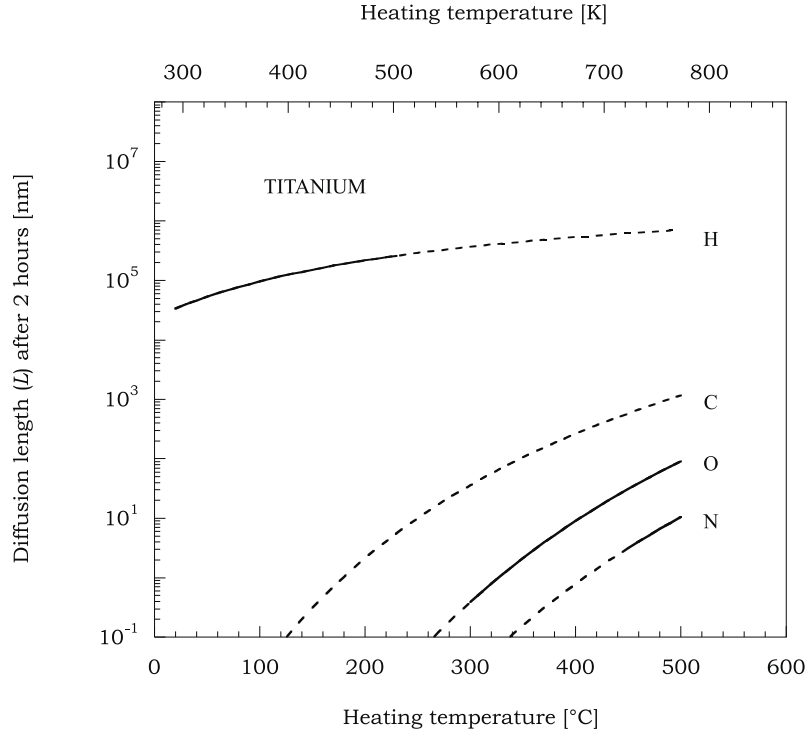


Fig. 2.11: Diffusion length after 2 hours for H, C, O and N in Ti as a function of heating temperature. The plots are realised on the basis of diffusion data taken from [45]. Extrapolated data are in dashed lines.

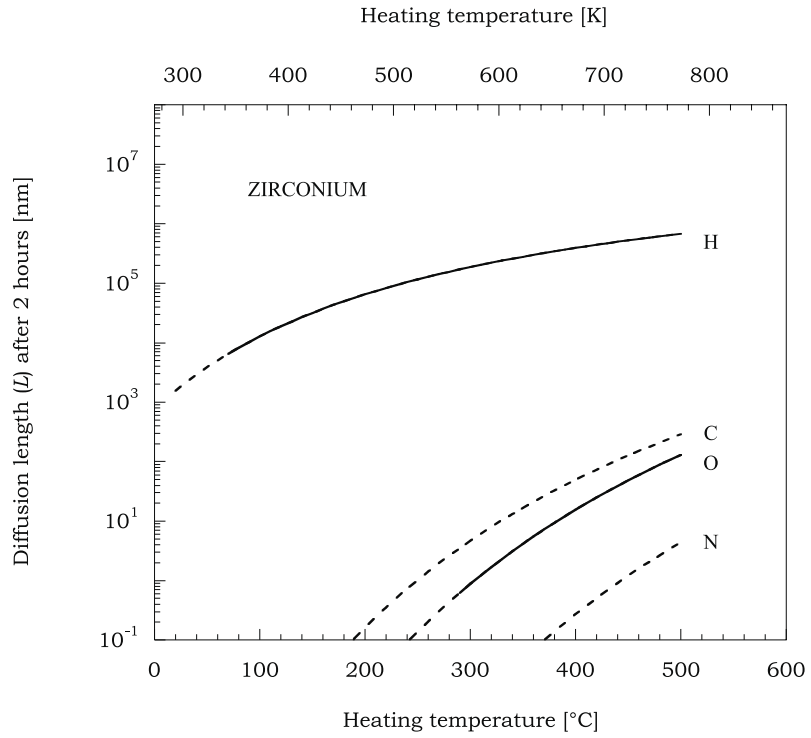


Fig. 2.12: Diffusion length after 2 hours for H, C, O and N in Zr as a function of heating temperature. The plots are realised on the basis of diffusion data taken from [45]. Extrapolated data are in dashed lines.

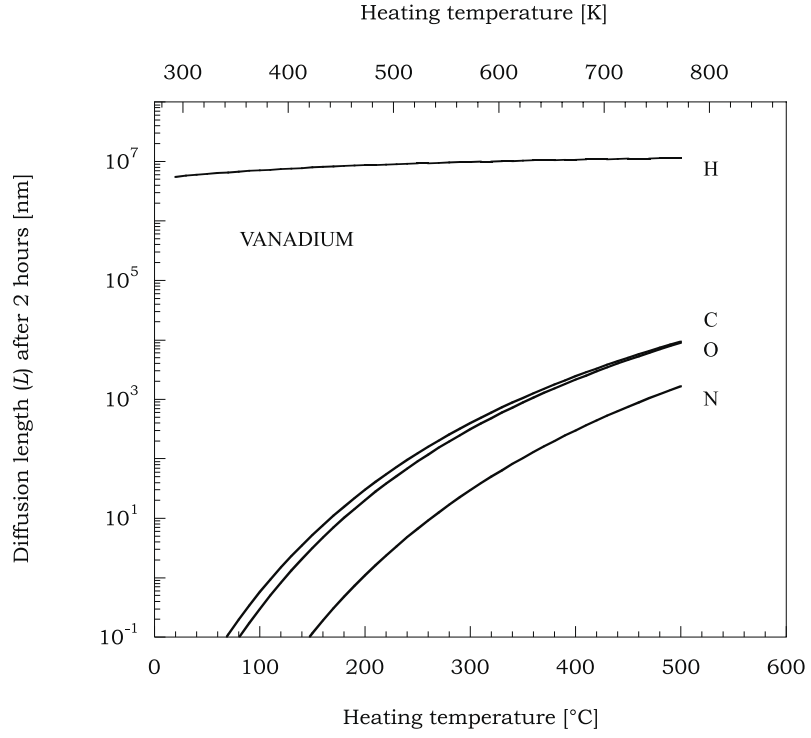


Fig. 2.13: Diffusion length after 2 hours for H, C, O and N in V as a function of heating temperature. The plots are realised on the basis of diffusion data taken from [45]. Extrapolated data are in dashed lines.

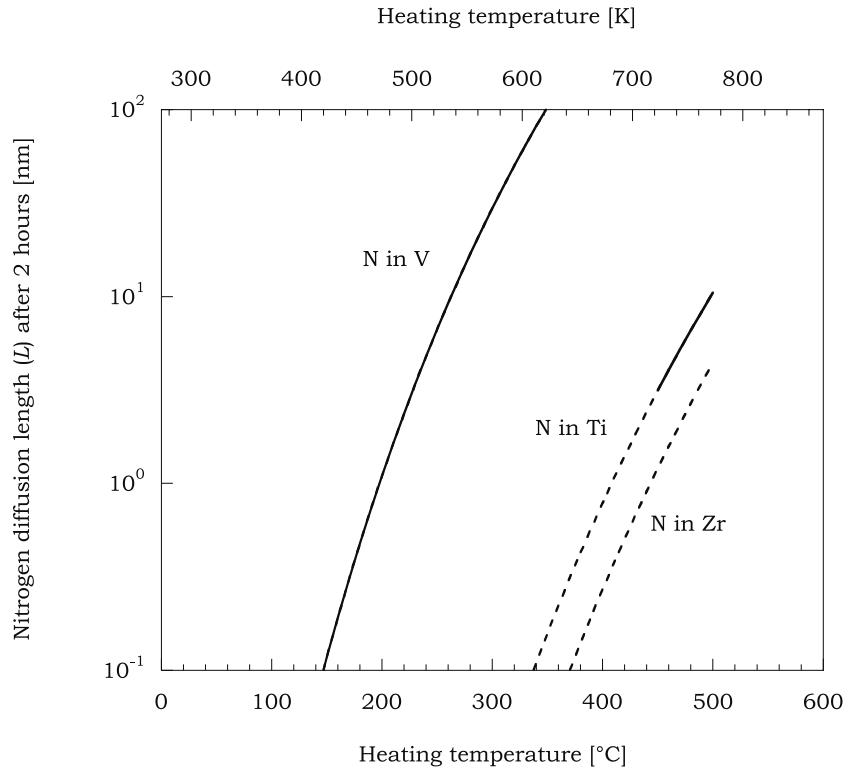


Fig. 2.14: Nitrogen diffusion length after 2 hours in Ti, Zr and V. The plots are realised on the basis of diffusion data taken from [45]. Extrapolated data are in dashed lines.



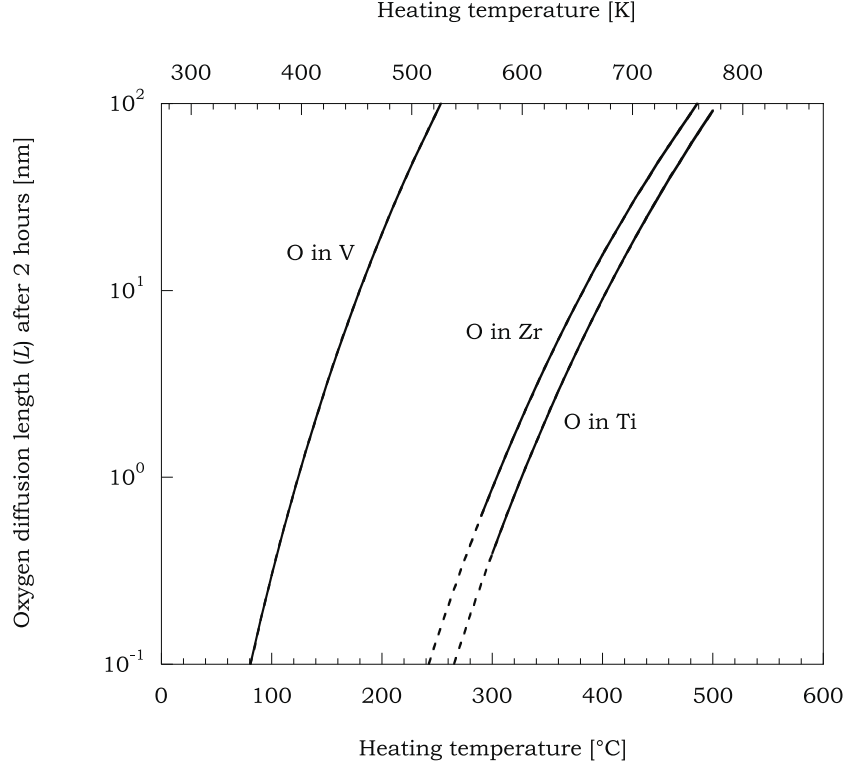


Fig. 2.15: Oxygen diffusion length after 2 hours in Ti, Zr and V. The plots are realised on the basis of diffusion data taken from [45]. Extrapolated data are in dashed lines.

At a given temperature, the diffusion length of nitrogen is about comparable in Zr and Ti and is higher for V (Fig. 2.14). The tendency is the same for oxygen as for nitrogen (Fig. 2.15).

### 2.1.3 The role of temperature and time for the activation for pure metals

A simple diffusion model, originally formulated by Munir [70], allows the evaluation of the duration of the activation process at a given temperature to dissolve completely the surface oxide layer.

Let us consider a plane source (the oxide) initially located at the surface of a semi-infinite medium (the metal). Even during heating, only those two phases coexist. For such a case, the amount of diffusing oxygen  $M_{tot}$  during the time  $t$  at a temperature  $T$  is given in Ref. [71]:

$$M_{tot} = 2 \cdot c_o \sqrt{\frac{t \cdot D(T)}{\pi}} . \quad (2.7)$$

$D(T)$  is the diffusivity of oxygen in the metal at temperature  $T$  (see Eq. (2.4)). In the particular case of oxide dissolution,  $M_{tot} = M_{oxide}$  is the total amount of oxygen contained in the oxide layer,  $c_o$  is the concentration of oxygen in the metal at the interface metal-oxide; if local equilibrium is assumed at the interface,  $c_o$  is the oxygen solubility limit ( $x_o$ ) in the metal (see data for  $x_o$  in Table 2.5).

The time ( $t_{ox}$ ) needed to dissolve the oxide layer at the temperature  $T$  is:

$$t_{ox} = \frac{\pi}{4} \cdot \left( \frac{M_{oxide}}{c_o} \right)^2 \cdot \frac{1}{D(T)} \quad (2.8)$$

For a metal Me of density  $\rho_{Me}$  [g cm<sup>-3</sup>], molecular weight  $M_{Me}$  [g mol<sup>-1</sup>] and solubility limit of oxygen  $x_o(T)$  [atomic %]:

$$c_o = x_o(T) \cdot \frac{\rho_{Me}}{M_{Me}} \cdot N_A \cdot 100 \text{ [atoms cm}^{-3}\text{]} \quad (2.9)$$

where  $N_A$  is the Avogadro constant ( $6.0221367 \times 10^{23}$  mol<sup>-1</sup>).

For an oxide Me<sub>x</sub>O<sub>y</sub> of density  $\rho_{Me_xO_y}$  [g cm<sup>-3</sup>], molecular weight  $M_{Me_xO_y}$  [g mol<sup>-1</sup>] and thickness  $h$  [cm]:

$$M_{oxide} = y \cdot N_A \cdot \frac{\rho_{Me_xO_y}}{M_{Me_xO_y}} \cdot h \text{ [atoms cm}^{-2}\text{]} \quad (2.10)$$

The following equation is used to plot  $t_{ox}$  as a function of  $T$ :

$$t_{ox} = \frac{\pi}{4} \cdot \left( \frac{y \cdot \frac{\rho_{Me_xO_y}}{M_{Me_xO_y}} \cdot h}{x_o(T) \cdot \frac{\rho_{Me}}{M_{Me}} \cdot 100} \right)^2 \cdot \frac{1}{D_o} \cdot e^{\frac{E_o}{R \cdot T}} \quad (2.11)$$

$$K_{ox} = \frac{\pi}{4} \cdot \left( \frac{y \cdot \frac{\rho_{Me_xO_y}}{M_{Me_xO_y}} \cdot h}{x_o(T) \cdot \frac{\rho_{Me}}{M_{Me}} \cdot 100} \right)^2 \quad (2.12)$$

The thickness  $h$  of the oxide layer is taken as 5 nm for all oxide types. This value has been adopted on the basis of what has been evaluated by Auger Electron Spectroscopy (AES) depth profiling (M. Taborelli, CERN, personal communication) on Ti, Zr, Nb and V.

A summary of the data needed to calculate the time ( $t_{ox}$ ) to dissolve a surface oxide layer as a function of heating temperature is given in Table 2.13. The values of diffusivity ( $D_o$ ) and solubility limit ( $x_o$ ) are valid for single crystals. The calculated time ( $t_{ox}$ ) is plotted as a function of heating temperature in Fig. 2.16.

The data reported in literature for the activation temperature are obtained by Electron Stimulated Desorption (ESD). It consists in measuring the surface outgassing induced by electron bombardment, which decreases with decreasing gas surface coverage. In the standard measuring procedure, the sample is heated for 2 hours at a given temperature (starting from 120 °C), and then cooled to ambient temperature before ESD measurement is carried out. This sequence is repeated at intervals of 40 °C or 50 °C up to a maximum temperature of 400 °C. For more details about the technique and setup, one can read Ref. [72]. The results are illustrated by presenting the variation of pressure ( $\Delta P$ ) as a function of the heating temperature (Fig. 2.17). On each graph, the coating performances are compared to that of stainless steel, the constituting material of most vacuum chambers. The activation temperature ( $T_a$ ) value is arbitrarily taken for  $\Delta P = 10^{-10}$  Torr and reported in Table 2.14.

Table 2.13: Summary of the data needed to calculate the time ( $t_{ox}$ ) to dissolve a surface oxide layer as a function of heating temperature.

	Y	Ti	Zr	Hf	V	Nb	Ta
$\rho_{Me}$ [g cm <sup>-3</sup> ]*	4.478	4.5	6.49	13.1	6.1	8.57	16.6
$M_{Me}$ [g mol <sup>-1</sup> ]	88.90585	47.867	91.224	178.49	50.9415	92.90638	180.9479
$x_o$ [atomic %]	0.5	33	29	17	4	0.4	0.58
x in Me <sub>x</sub> O <sub>y</sub>	2	1	1	1	2	2	2
y in Me <sub>x</sub> O <sub>y</sub>	3	2	2	2	5	5	5
$D_o$ [cm <sup>2</sup> s <sup>-1</sup> ]	9.40E-3	0.8	6.61E-2	0.66	1.90E-2	8.00E-2	1.14E-2
$-E_o$ [J mol <sup>-1</sup> ]	86700	200830	184100	212550	122850	116320	110940
Ref. for $D_o$ , $E_o$	[45]	[47]	[49]	[45]	[45]	[52]	[43]
$\rho_{Me_xO_y}$ [g cm <sup>-3</sup> ]*	5.03	4.23	5.68	9.68	3.35	4.6	8.2
$M_{Me_xO_y}$ [g mol <sup>-1</sup> ]	225.81	79.866	123.223	210.489	181.88	265.81	441.893
$h$ [nm]	5	5	5	5	5	5	5
$K_{ox}$	10428	24156	22143	25565	14776	13991	13344
$-E_o/R$	1.47E-6	2.86E-12	5.93E-11	1.62E-11	3.82E-9	1.35E-7	5.24E-7
Validity range [K]	1173-1733	673-1123	563-923	773-2073	333-2098	403-1073	298-1873

\* at 20°C.

Calculations show that the 5<sup>th</sup> group metals get activated faster than those of the 4<sup>th</sup> group. Within the 4<sup>th</sup> group, the first to be activated is zirconium while within the 5<sup>th</sup> group, the first to be activated is vanadium (Fig. 2.16). Then, this simple model can predict which metal has the lowest activation temperature within 4<sup>th</sup> and 5<sup>th</sup> groups, in agreement with some experimental data obtained by Electron Stimulated Desorption (ESD) (Fig. 2.17) [72], [73], [74], [75]. In particular, Zr is found to be activated after 2 hours heating at about 350 °C, a temperature not far from the calculated value (about 365 °C for 2 hours heating) (see Table 2.14).

It is important to point out that the solubility limits adopted for this calculation are extrapolated from high-temperature data found in the literature (as indicated in Table 2.5). This extrapolation may be at the origin of errors which can account for the differences between some of the measurements and the corresponding values obtained by simulation.

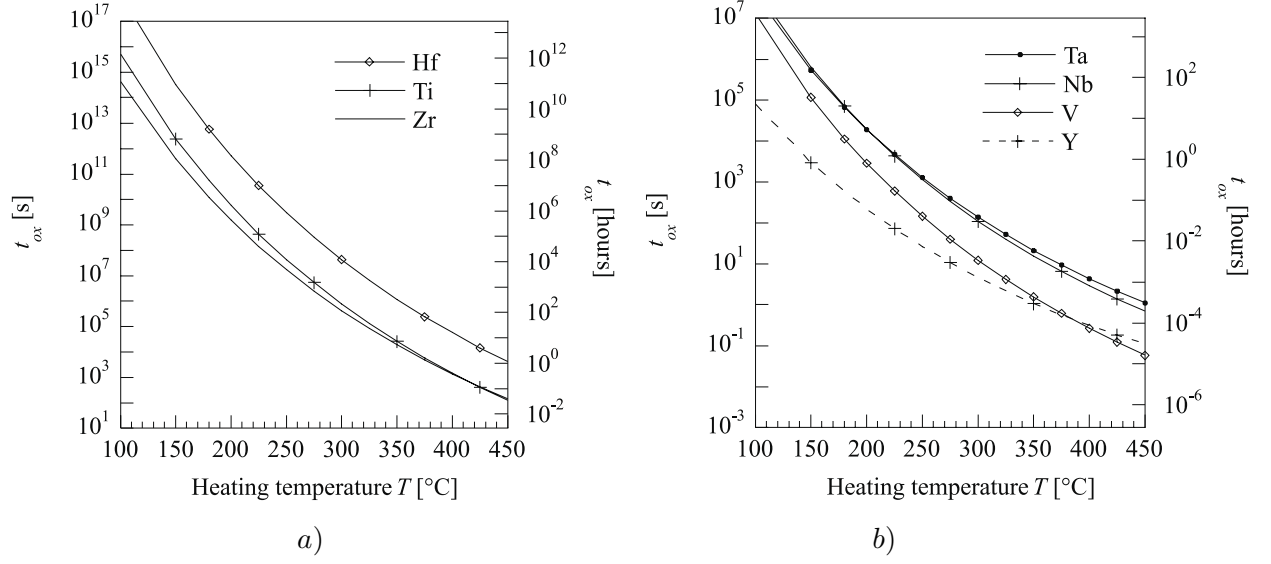


Fig. 2.16: Calculated activation time ( $t_{ox}$ ) as a function of heating temperature ( $T$ ) for metals of 4<sup>th</sup> group (a) and for metals of 5<sup>th</sup> group and Y (b).

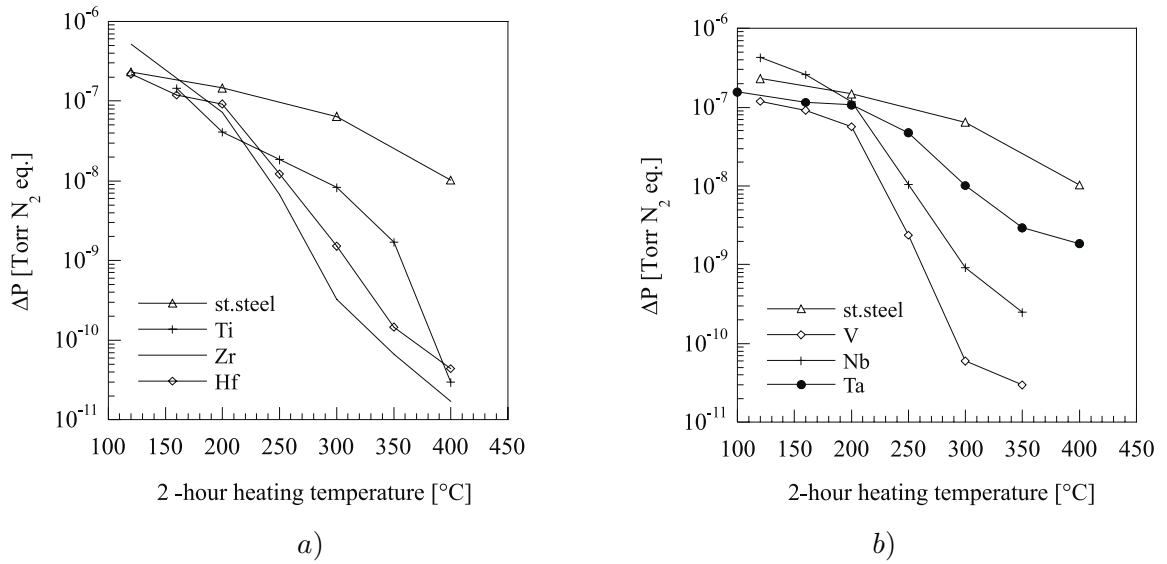


Fig. 2.17: Results of Electron Stimulated Desorption (ESD) measurements for metals of 4<sup>th</sup> group (a) and for metals of 5<sup>th</sup> group (b). Figures taken from Refs. [72], [73], [74], [75].

Table 2.14: Comparison of the activation temperature ( $T_a$ ) measured by ESD to that calculated (for a 2-hour heating).

Metal	Experimental $T_a$ [°C]	Calculated $T_a$ [°C]
Y	–	150
Ti	380	370
Zr	350	365
Hf	360	440
V	290	200
Nb	$\approx 400$	230
Ta	$> 400$	230

#### 2.1.4 Bulk or grain boundary limiting diffusion

Grain boundaries, as dislocations, are considered as short-circuits for atomic diffusion in metals [76]. At low temperatures, they can be the only possible path for atomic transport. To increase the grain boundary contribution to atomic diffusion, small grain size is an advantage [45].

In order to know if grain boundaries play an important role, we compare the diffusion length of oxygen ( $L$ ), to the average grain size of the metal itself ( $\omega$ ).

For a given temperature ( $T$ ) and duration of activation ( $t$ ), the diffusion length of oxygen ( $L$ ) is defined by Eq. (2.6):  $L = \sqrt{D(T) \cdot t}$ . When  $L$  is smaller than  $\omega$ , the configuration is that of wide grains (compared to the diffusion length). The volumetric proportion of grain boundaries is low. The diffusion occurs at grain boundaries but also within the grains ( $\omega > L$ ). When  $L$  is larger than  $\omega$ , the configuration is that of small grains (compared to the diffusion length). The volumetric proportion of grain boundaries is then high. The diffusion mainly occurs at grain boundaries ( $\omega < L$ ).

The calculation is performed with the most adequate diffusivity of oxygen [ $\text{cm}^2 \text{s}^{-1}$ ] quoted in paragraph 2.1.2 for pure, single crystal metals, namely:

Ti ( $\alpha$ )	$D = 8.0 \times 10^{-1} \cdot e^{\frac{-200830}{8.314T}}$	from 673 to 1123K	quoted from [47]
Zr ( $\alpha$ )	$D = 6.6 \times 10^{-2} \cdot e^{\frac{-184100}{8.314T}}$	from 563 to 923 K	quoted from [49]
Hf ( $\alpha$ )	$D = 6.0 \times 10^{-2} \cdot e^{\frac{-212550}{8.314T}}$	from 773 to 2073 K	quoted from [45]
V	$D = 1.90 \times 10^{-2} \cdot e^{\frac{-122850}{8.314T}}$	from 333 to 2098 K	quoted from [45]
Nb	$D = 1.38 \times 10^{-2} \cdot e^{\frac{-111530}{8.314T}}$	from 296 to 1873 K	quoted from [52]
Ta	$D = 1.14 \times 10^{-2} \cdot e^{\frac{-110940}{8.314T}}$	from 298 to 1873 K	quoted from [43]

In order to use heating conditions comparable to the experimental ones (see paragraph 4.3.4), heating durations of 2 hours are considered. The diffusion length ( $L$ ) is reported as a function of the heating temperature for metals of 4<sup>th</sup> and 5<sup>th</sup> groups (Fig. 2.18).

For Zr, Hf and Ti coatings prepared for this study, the average grain size is  $\omega = 100$  nm.

For those elements, the diffusion at grain boundaries should be negligible in the investigated temperature range (Fig. 2.18). This could explain why the simple model based on diffusion in the metal bulk allows activation temperatures similar to those obtained experimentally to be predicted. This correlation between calculation and experimentation justifies *a posteriori* that the comparison between  $L$  and  $\omega$  is a good basis to determine the type of diffusion.

In the case of Nb, the activation occurs after heating for 24 hours at 300 °C, when  $L = 3 \mu\text{m}$  (Fig. 2.18). The average grain size is anisotropic: the grains width is 100 nm and their height is the film thickness, which is usually 1  $\mu\text{m}$  [77]. Then,  $\omega < L$ , the grain boundaries play an important role in the diffusion process.

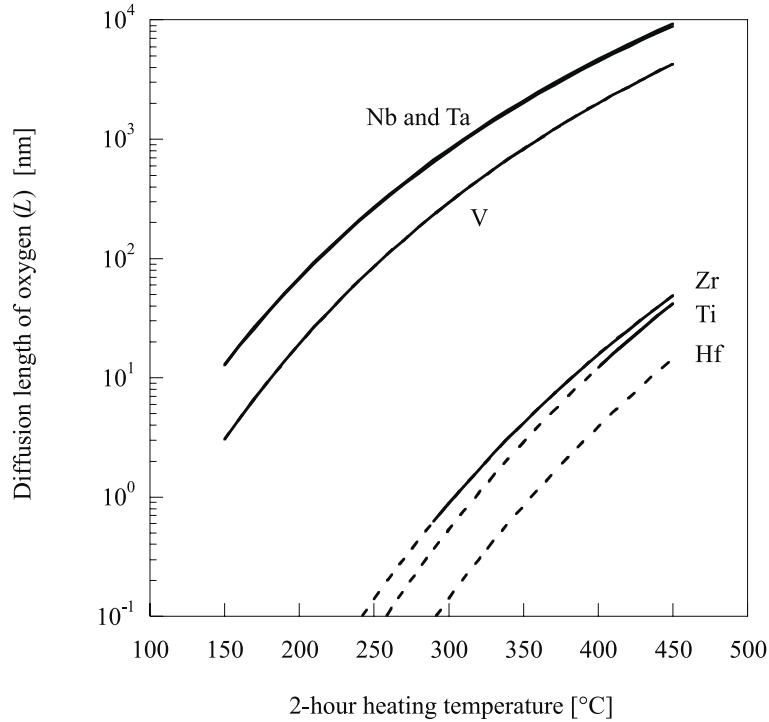


Fig. 2.18: Diffusion length ( $L$ ) vs. activation temperature (2 hours heating) for oxygen in metals of the 4<sup>th</sup> and 5<sup>th</sup> groups. The extrapolated data are in dashed lines.

The effect of the heating duration on the evolution of the diffusion length ( $L$ ) as a function of temperature is illustrated in Fig. 2.19 for V and Ti. The diffusion of oxygen over 20 nm in vanadium requires 24 hours heating at 170 °C and 2 hours at 200 °C. The diffusion of oxygen over 20 nm in titanium requires 24 hours heating at 370 °C and 2 hours at 420 °C. The variation of the heating duration necessary to reach the activation of a NEG as a function of heating temperature is also studied experimentally in the present work. Results obtained by Auger Electron Spectroscopy (AES) will be presented in Fig. 5.6 and discussed.

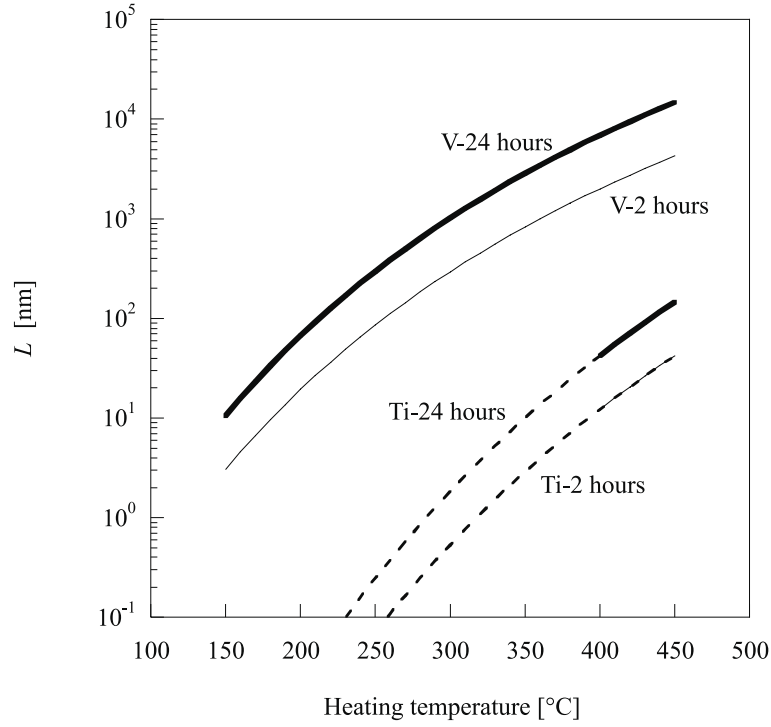


Fig. 2.19: Effect of the heating duration on the evolution of the diffusion length ( $L$ ) as a function of temperature for V and Ti.

### 2.1.5 Conclusions

The data summarised in paragraph 2.1 give us a global view about diffusivity and solubility limit in single-crystal pure metals. However, the NEG coatings under investigation are alloys and they are often of nanocrystalline structure. Neither diffusivity nor solubility limit values were found in the literature for these cases, and the models available to evaluate diffusivity and solubility limit in the case of alloys are not helpful since they are valid for single crystals. It is known that the diffusivity and solubility limit increase in the presence of grain boundaries and this trend remains qualitative.

A possible method to measure the solubility limit in the case of any thin films, is, for instance, by thermogravimetric analysis. The principle is to heat samples under controlled atmospheres (dry air, oxygen) and to measure the corresponding weight increase due to oxygen absorption. Preliminary trials failed because of the impossibility to distinguish the onset where the oxygen uptake was no longer due to increase of the concentration in solid solution but to oxidation of the metal.

## 2.2 Pumping speed and capacity

### 2.2.1 Effect of surface roughness

The rougher a surface, the larger the actual area available for pumping. In other words, roughening a surface increases the number of sites available for pumping, which is called the surface pumping capacity. It also increases the pumping speed ( $S$ ) because of multiple surface reflections, which increase the probability that the molecule is trapped.

### 2.2.2 $H_2$ absorption

The effect of  $H_2$  surface loading on non-evaporable getters has been extensively studied by R.J. Knize and J.L. Cecchi [78].  $H_2$  diffuses into the getter bulk even at room temperature so that the pumping speed at any given moment is defined by the competing action of molecular adsorption and atomic diffusion. As a result, small injected  $H_2$  quantities do not remain at the getter surface and consequently do not affect the pumping of other gases. Therefore, the effect of  $H_2$  surface loading was not studied here.

### 2.2.3 $CO$ and $N_2$ adsorption

For gases which do not diffuse at room temperature, like  $CO$  and  $N_2$ , the pumping speed  $S$  is a function of the instantaneous surface coverage  $n_a$ , the number of adsorption sites per unit area,  $n_o$ , and the initial pumping speed,  $S_o$ . According to Langmuir adsorption isotherm, if desorption does not take place and for single site adsorption [79]:

$$S = S_o \left( 1 - \frac{n_a}{n_o} \right) = S_o(1 - \Omega) \quad (2.13)$$

with  $\Omega$  the fractional coverage:

$$\Omega = \left( \frac{n_a}{n_o} \right) . \quad (2.14)$$

For many-site adsorption ( $p$  sites), the equation becomes:

$$S = S_o \left( 1 - \frac{n_a}{n_o} \right)^p = S_o(1 - \Omega)^p . \quad (2.15)$$

Because it encompasses many orders of magnitude,  $S = f(\Omega)$  is generally plotted in logarithmic scale.

The purpose of this section is to explain what are the physical parameters influencing the evolution of the pumping speed ( $S$ ) as a function of the surface coverage ( $\Omega$ ). This will facilitate the reading of that type of curves in Chapter 5. I used the Eq. (2.15) to simulate the influence of  $S_o$ , the initial pumping speed, and  $p$ , the multiplicity of adsorption sites, on  $S = f(\Omega)$ . The result of this calculation is plotted in Fig. 2.20 and Fig. 2.21, respectively. An increase of initial pumping speed ( $S_o$ ) causes a vertical translation of the  $S = f(\Omega)$  curve



in logarithmic scale to the higher  $S$  values. The higher the number of sites ( $p$ ), the lower the slope of the pumping speed  $S = f(\Omega)$  curve in logarithmic scale.

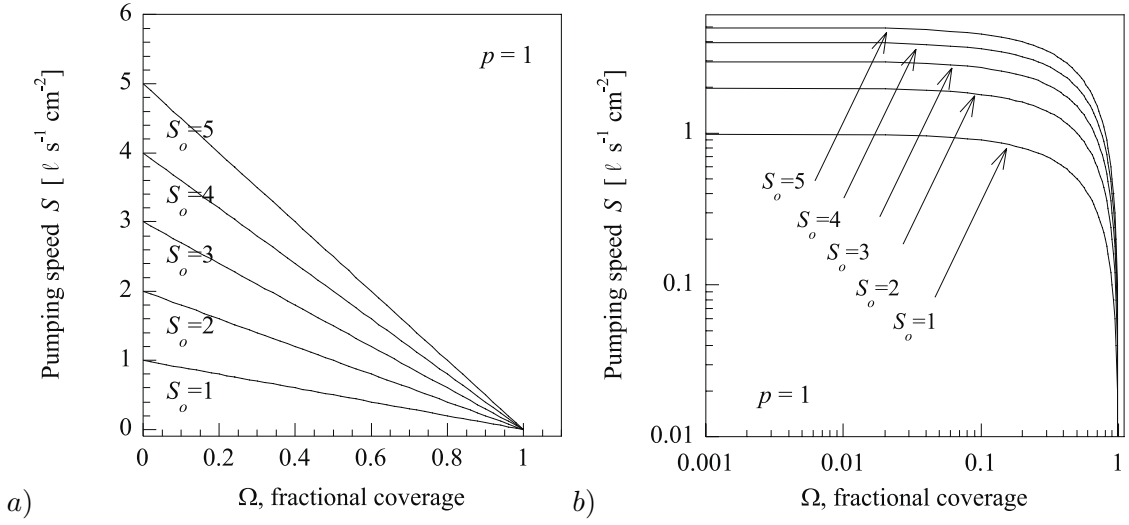


Fig. 2.20: Influence of the initial pumping speed ( $S_o$ ) on the evolution of the pumping speed as a function of the surface coverage. Calculated results presented in (a) linear scale, (b) logarithmic scale.

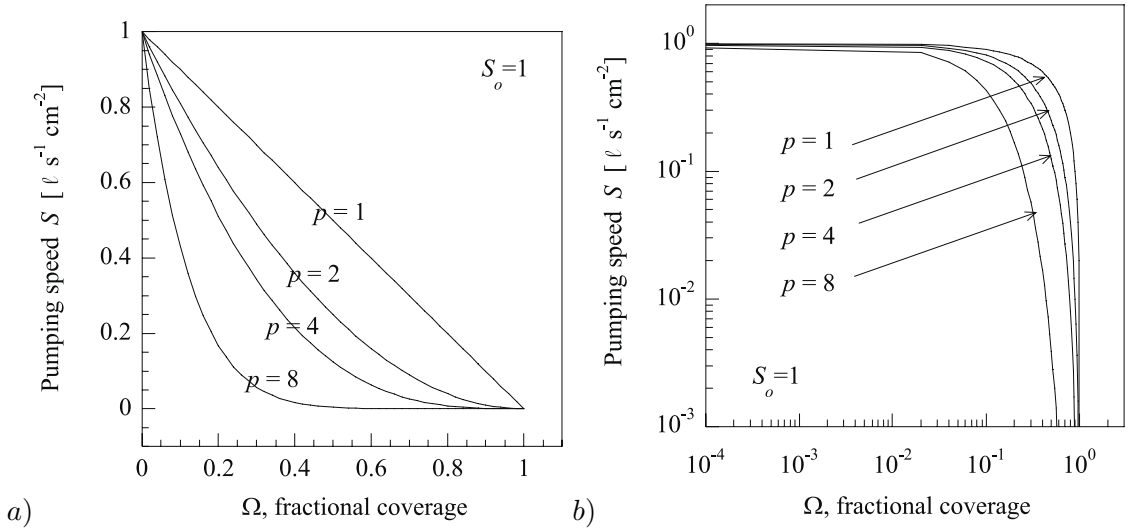


Fig. 2.21: Influence of the parameter multiplicity of adsorption sites ( $p$ ) on the evolution of the pumping speed as a function of the surface coverage. Calculated results presented in (a) linear scale, (b) logarithmic scale.

When considering porous films, the pumping speed as a function of the surface coverage can be modelled as described by C. Benvenuti and F. Francia in Refs. [80], [81]. The pumping speed is split into two contributions, one attributed to the flat surface ( $S_f$ ), the second attributed to the voids ( $S_v$ ):

$$S = S_f + S_v \quad (2.16)$$

The voids are considered to be cylindrical straight orifices. The following notation is intro-

duced for the evaluation of  $S_f$  and  $S_v$ .

$A_f$  area of the flat surface [ $\text{cm}^2$ ]

$A_v$  total area of the entrance orifices of the voids [ $\text{cm}^2$ ]

$A$  NEG coated surface =  $A_f + A_v$  [ $\text{cm}^2$ ]

$n^2$  density of the voids per  $\text{cm}^2$  of NEG coated surface

$d$  diameter of the voids [ $\text{cm}$ ]

$Q_o$  gas quantity needed to saturate the surface of the NEG which would not present any orifice on its surface per unit area [ $\text{Torr } \ell \text{ cm}^{-2}$ ]

$\alpha_f$  sticking probability on flat clean surface

$\alpha_v$  sticking probability at the entrance of the voids

$S_f$  pumping speed of the flat outer surface of the NEG per unit area [ $\ell \text{ s}^{-1} \text{ cm}^{-2}$ ]

$S_v$  pumping speed of the voids of the NEG per unit area [ $\ell \text{ s}^{-1} \text{ cm}^{-2}$ ]

$S_o$  initial pumping speed of the NEG per unit area [ $\ell \text{ s}^{-1} \text{ cm}^{-2}$ ]

$C$  conductance of an orifice of unit area [ $\ell \text{ s}^{-1} \text{ cm}^{-2}$ ]

$Q_f$  gas quantity pumped on  $A_f$

$Q_v$  gas quantity pumped on  $A_v$

$Q = Q_f + Q_v =$  gas quantity pumped for the pumping speed  $S = S_v + S_f$

With this notation,  $S_f$  may be written as:

$$S_f = \alpha_f A_f C \left[ 1 - \frac{Q_f}{Q_o \left( 1 - \frac{A_v}{A} \right)} \right] . \quad (2.17)$$

According to the Knudsen formula for molecular flow,  $S_v$  for  $\text{N}_2$  may be expressed as:

$$S_v = \alpha_v \cdot n^2 \cdot A \frac{12.5d^3}{\ell + 1.3d} . \quad (2.18)$$

The gas quantity required to saturate  $A_f$  is:

$$Q_f^{sat} = Q_o \frac{A_f}{A} . \quad (2.19)$$

And the quantity required to saturate  $A_v$  to the depth  $\ell$  is:

$$Q_v^{sat} = n^2 \pi \ell d Q_o . \quad (2.20)$$

When starting gas injection, pumping occurs mainly on the flat surface which is the most easily available from the conductance point of view. In that case,  $S = S_f + S_v \approx S_f$ . This contribution evolves, as a function of surface coverage, like the pumping speed of a smooth surface described in Fig. 2.20 and Fig. 2.21.

When the flat part of the surface is saturated, the pumping is mainly due to the voids. Then  $S = S_f + S_v \approx S_v$ . Under the assumption that the depth is much larger than the diameter, according to Ref. [81]:

$$S \approx S_v = 3.44 \times 10^4 \times \left( \frac{A_v}{A} \right)^2 \times \frac{Q_o}{Q_v^{sat}} . \quad (2.21)$$

The interest of this expression is to introduce the most relevant physical parameter when dealing about pumping by a void: the porosity  $\frac{A_v}{A}$ . Making use of Eq. (2.21), the porosity of a getter may be extracted from the pumping speed variation as a function of the adsorbed CO quantities.

The two contributions ( $S_f$  and  $S_v$ ) are added to simulate the total pumping speed ( $S$ ), as illustrated in Fig. 2.22.

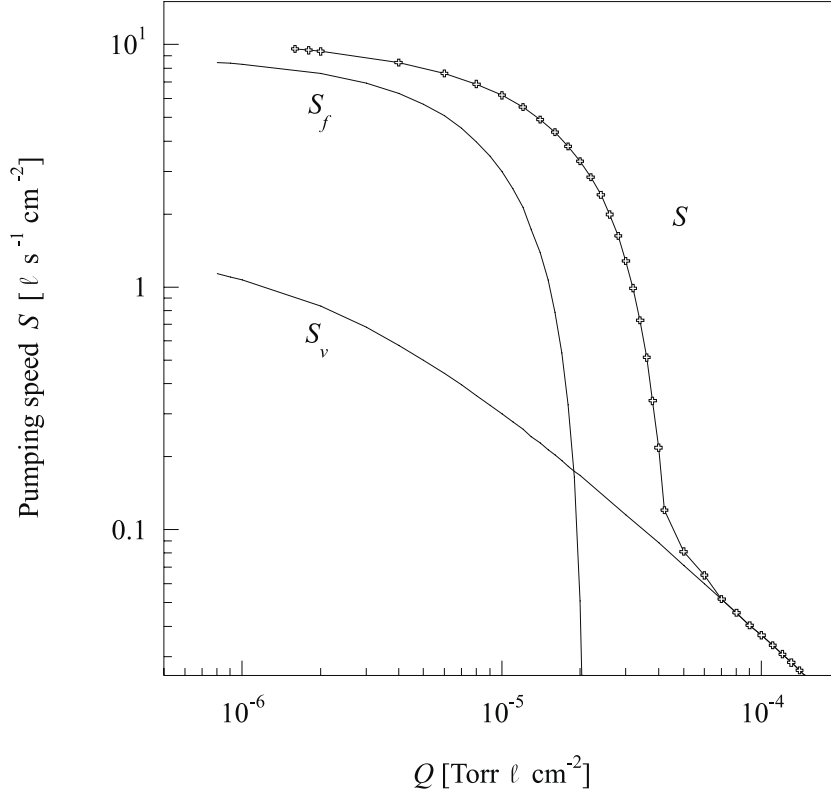


Fig. 2.22: The pumping speed  $S$  is the sum of two contributions: one attributed to the flat surface ( $S_f$ ) and the other to the voids ( $S_v$ ). Calculated curves.

### 2.2.4 Pumping of gas mixtures

- CO surface loading

Small quantities of  $N_2$  are intermittently injected while a NEG is progressively covered with CO. At low CO coverage,  $S_{N_2}$  and  $S_{CO}$  reproduce the initial part of the curves obtained individually for these gases. At large CO coverage, the pumping becomes limited by the conductance, which is the same for CO and  $N_2$ , therefore the related pumping speeds converge to the same values. An example of such a behaviour is given in Fig. 2.23 for St707 getter strip (from Ref. [80]).

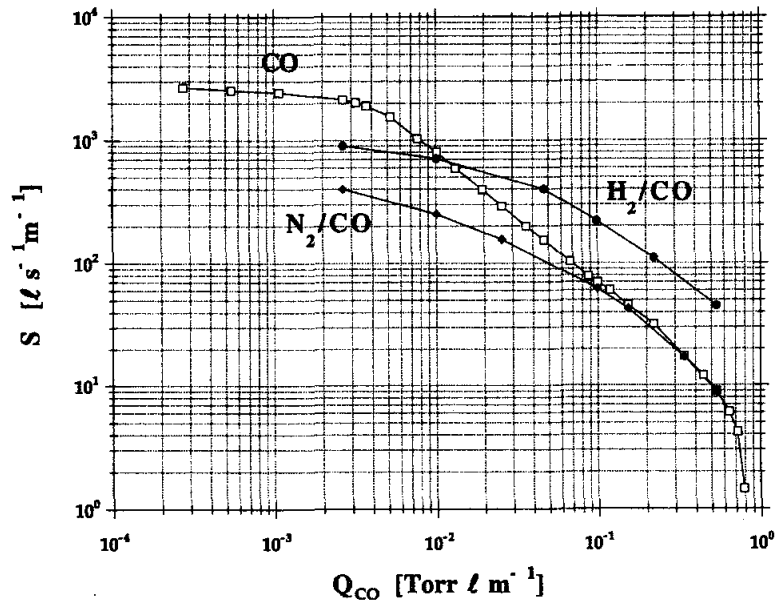


Fig. 2.23: When the pumping occurs mainly on the flat part of the surface of the St707 strip, the pumping speeds for CO and  $N_2$  differ, due to the fact that about six adsorption sites are required to pump a  $N_2$  molecule, while only one is required for CO. Once the flat part of the surface is saturated, the pumping occurs mainly in the voids. The pumping becomes limited by the conductance, which is the same for CO and  $N_2$ , therefore the related pumping speeds converge to the same value while the pumping speed for  $H_2$  is higher, according to the higher conductance for this gas. Figure taken from Ref. [80].

- $N_2$  surface loading

As illustrated in Fig. 5.24, the surface loading by  $N_2$  reduces the pumping speed of  $N_2$  while it does not affect that for CO at all. This may be due to the low surface capacity for  $N_2$ , resulting in a large population of free adsorption sites even after  $N_2$  saturation [80]. Alternatively, it may be due to the adsorption of  $N_2$  underneath the first monolayer of the surface, which therefore remains free for adsorbing CO, as already reported for Ti [82] and Zr

[83] pure metals. Such behaviour was first suggested by H.D. Shih *et al.* [82] who studied the Ti surface changes when exposed to nitrogen. The exploited information was the interfacial peaks and plasmon-decay peaks on AES spectra and the energy dependence of the peak intensity and positions on Low-Energy Electron Diffraction (LEED) spectra. These analyses revealed that the N atoms penetrate into the octahedral interstitial holes underneath the first layer of Ti atoms. This was the first ordered monoatomic underlayer found in the early stages of chemisorption of gases on metals. It was pointed out at the time that the ‘underlayer model’ explains the fact that nitrogen can be adsorbed on the surface of some metals with a surface coverage larger than unity, because bonding occurs not only in the underlayer but also with the newly uncovered Ti atoms in the top atomic layer. Later, J.S. Foord *et al.* obtained the following series of observations when injecting O<sub>2</sub>, NO and CO on a N<sub>2</sub> pre-saturated Zr surface [83]. First, a substantial attenuation of the pre-adsorbed nitrogen Auger signal took place whereas no degassing was recorded. This provides evidence that the second adsorbate had taken a position above the first adsorbate thus increasing the path to the surface for the Auger electrons from the latter and hence attenuating their intensity. A further evidence in favour of the ‘underlayer model’ is that after a N<sub>2</sub> exposure, the initial sticking probabilities for CO, O<sub>2</sub> and NO were unchanged from the clean surface value. According to J.S. Foord, it is unlikely that the second adsorbate sticks on top of the first if the latter is a chemisorbed overlayer. This is consistent with measurements proving that N, O, C atomic species diffuse readily into the metal. Zirconium carbides, nitrides and oxides have high enthalpies of formation, so providing the driving force for the disruption of the metal lattice associated with their adsorption.

# Chapter 3

## NEG coatings preparation

In this chapter, the preparation of the NEG coatings is described. Some specificities about the substrates are given: the substrate material, the substrate dimensions, the cleaning and the preparation as a function of expected properties of the coating. The choice of diode direct-current magnetron sputtering as deposition technique is discussed. Furthermore, the chapter deals with the influence of the main preparation parameters on the coatings structure. The aim is to underline the advantages of the chosen techniques with respect to the practical objectives of the NEG coatings.

### 3.1 Sputtering methods

#### 3.1.1 *Sputtering technique and deposition rate*

- Principle of sputtering deposition

If a material is subjected to ion bombardment, it is possible for its individual atoms to acquire enough energy and momentum transfer by collision to escape from the surface [84]. This process is called sputtering [85]. Unlike thermal evaporation, it does not require heating [84], [86]. Atoms ejected by sputtering from a target are deposited on surrounding surfaces progressively forming a thin film coating, in particular on a dedicated substrate.

Any energetic atomic particle impinging on a surface can cause sputtering. However, it is easier to accelerate ions than neutral particles, hence only sputtering under ion bombardment is used in practice.

The effect of ion bombardment on a material differs from that of electron and photon bombardment because the ion mass is of the same order as the mass of the atoms in the target. This permits an efficient momentum transfer to individual atoms, which is the key feature of ion sputtering. The minimum energy required to expel an atom from a target is called the *sputtering threshold* [87], [88]. It depends on the material but is quite insensitive to the mass ratio between the impinging ion and the target atoms [87], [88]. The *sputtering*

*threshold* energy is in the range of 10 to 40 eV for most materials [88], a value which is larger than the lattice binding energies (about a factor four) [89]. Some examples of the *sputtering threshold* value necessary for the sputtering of different materials with Ar and Kr ions are given in Refs. [88], [90], and summarised in Table 3.1.

Table 3.1: Examples of *sputtering threshold* values for different materials bombarded by Ar and Kr ions.

Target material-Z	<i>Sputtering threshold</i> in eV	
	Ar ions	Kr ions
Ti – 22	20	17
V – 23	23	25
Cr – 24	22	18
Cu – 29	17	16
Zr – 40	22	18
Nb – 41	25	26
Mo – 42	24	28
Ag – 47	15	15
Ta – 73	26	30
W – 74	33	30

In summary, sputtering involves direct momentum transfer from bombarding ions to the target atoms of a cathode [86] without requiring additional thermal energy input, as established by F. Stark in 1908 and supplemented by Wehner in 1950.

- Advantages of sputtering in the context of the present study

Sputtering provides the following unique combination of advantages when compared to other techniques like thermal evaporation (including pulsed laser or electron-gun).

1. The sputtering ions have energies far exceeding the strength of the chemical bond, which is a few eV [91]. Consequently, any inorganic material can be sputtered, no matter how low its vapour pressure [86].
2. With some precautions, alloys and compounds can be deposited without modifying their composition.
3. A metastable phase of the deposited film can be reached that could not be obtained otherwise.
4. A higher density of nucleation islands is obtained by sputtering than by evaporation, thus resulting in a smaller dimension of the crystal grains. It is even possible in some cases to obtain amorphous layers [92].

5. The film deposition rate can be made uniform over very large areas, resulting in composition and thickness uniformity [93].
6. The sputtering technique allows the safe production of NEG coatings from stable materials. This feature is the most useful in the case of NEG. The usual technique of their production, by compressing powder, is not suitable for low activation temperature getters because of the risk of pyrophoricity. In contrast, coatings showing good adhesion profit from the thermal capacity of the substrate which limits the getter heating resulting from exothermic gas adsorption.
7. The atoms expelled from the target acquire an energy 50 to 100 times higher in the case of sputtering compared to atoms vaporised by thermal effect [94]. Although the energy of the sputtered atoms is higher in sputtering than in other techniques, it is still low enough to avoid subsurface damage on the deposited film [95]. According to Wehner, the high energy of the atoms favours a high adhesion of the coating on the substrate [91].

- Deposition rate

The *erosion rate* of a target corresponds to the quantity of matter eroded from the target per unit of time. The *sputtering yield* is defined as the number of target atoms or particles ejected per incident ion [84], [96], [97], [98], [99]. The resulting *deposition rate* depends not only on the *sputtering yield* but also on the distance of the substrate from the cathode and on the geometry.

The angular distribution of sputtered particles from randomly oriented polycrystalline targets depends on the energy and direction of the incident ions. In the case of normal incidence, in the energy range of 1 to 3 keV, sputtered atoms are ejected from the surface in essentially a cosine distribution. At lower energies the profile tends to have an under-cosine and at higher energies an over-cosine distribution. Under oblique ion incidence, target atoms are mainly sputtered in the forward direction, that is along the direction of specular reflection of the incoming ion beam. A sketch summarising these different cases is given in Fig. 3.1 [100], [101].

The mass, the energy (due to the applied voltage), the angle of incidence and the chemical nature of the incident ion influence the *sputtering yield* value [102]. The total pressure of the vacuum system, the crystallographic structure and the temperature of the target are other parameters influencing its value [102]. For instance, the *sputtering yield*, at a fixed energy, increases with the mass of the impinging ion [84].



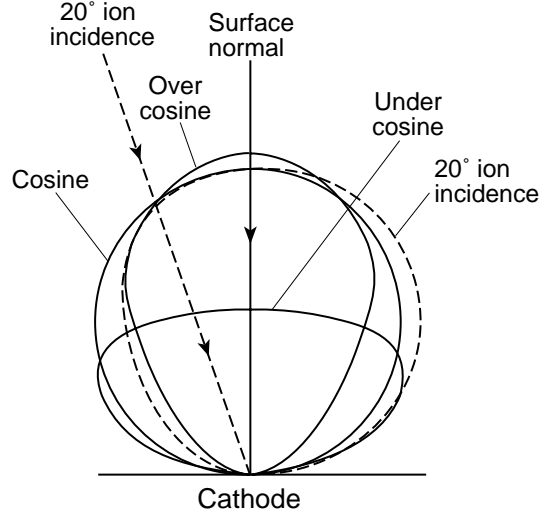


Fig. 3.1: Angular distribution of atoms sputtered from a polycrystalline target as a function of the incident ion energy and direction. Under-cosine corresponds to energy below 1 keV, cosine to energy between 1 and 3 keV, over-cosine to energy over 3 keV [101].

Table 3.2: a) *Sputtering yields* of different bulk materials for argon impinging ions with different energies at normal incidence. b) Corresponding references.

a)

Target Material	<i>Sputtering yields</i> in atoms per ion for different Ar <sup>+</sup> impinging energies:					
	0.3 keV	0.5 keV	0.5 keV	0.6 keV	1.0 keV	2.0 keV
Ti	0.35	0.45	0.5	0.55	0.8	1.0
Zr	0.45	0.5	0.65	0.75, 0.55	0.8	1.1
V	0.3	0.65	0.45	0.5	1.0	1.3
Mn	–	–	1.90	–	2.5	–
Cu	1.55	1.6	2.33	2.65	2	4
Cr	0.85	1.25	1.2	1.35	1.6	2
Y	0.5	0.65	0.68	0.75	–	–
Nb	0.4	0.5	0.6	0.6	0.9	1.1

b)

Target Material	Reference for <i>sputtering yields</i> quoted above for the following Ar <sup>+</sup> energies:					
	0.3 keV	0.5 keV	0.5 keV	0.6 keV	1.0 keV	2.0 keV
Ti	[104]	[103]	[104]	[104][108]	[103]	[103][108]
Zr	[104]	[103]	[104]	[104][109]	[103]	[103]
V	[105]	[103]	[105]	[105][98]	[103]	[103]
Mn	–	–	[110]	–	[103]	–
Cu	[104]	[103]	[104]	[104]	[103]	[103]
Cr	[104]	[103]	[104]	[104][111]	[103]	[103]
Y	[112]	[112]	[107]	[112]	–	–
Nb	[104]	[103]	[104]	[104][113]	[103]	[103]

Some literature values of *sputtering yields* of different bulk materials for argon ions (Ar<sup>+</sup>) impinging at normal incidence with different energies are given in Table 3.2 a. The target

materials are indicated in the first column. In the following columns, some *sputtering yield* values at five  $\text{Ar}^+$  impinging energies are quoted from Refs. [98], [103], [104], [105], [106], [107], [112]. When the *sputtering yield* for a given metal at a specified energy is not found in one of these references, the sign ‘–’ is indicated. The literature references from which the values are quoted are indicated in Table 3.2 *b*.

Considering the scattering in the data given in the literature, it can be concluded that it is more reliable to perform a calibration of the sputtering system used [98]. The results are presented in paragraph 3.2.2.

### 3.1.2 Plasma

A plasma (see Glossary in Chapter 8) is a partially ionised gas consisting of positive ions and negative particles (mostly electrons) in equal concentrations. The low-pressure, diffused plasma known as a glow (see Glossary in Chapter 8) discharge is especially useful in thin film processes for sputtering [114], [115]. In the sputtering process, the incident ions colliding the target are the ionised atoms of the plasma.

The deposition chamber contains the target and the substrate. The chamber is pumped to high vacuum ( $P \leq 10^{-4}$  Torr) before the gas chosen for the plasma is introduced. A potential is applied between the target and the substrate holder. An electrical discharge initiates the plasma. Electron generation by gas-phase ionisation is the main process by which plasmas are ignited and sustained [116]. Once electrons have been emitted from the cathode, they undergo collisions with the gas present in the vacuum chamber. If they have been accelerated to kinetic energy above the ionisation potential, ionisation may result; that is, for neutral gas atoms  $X$ :



with  $e^-$  an electron and  $X^+$  a singly ionised ion. This reaction generates a new electron, which also gets accelerated in the field, so that a cascade of electrons and ions occurs. This is the mechanism of gas breakdown in an electric field. For more details about the necessary pressure and electrode gap, one can read Ref. [117].

The plasma gases are chemically inert, except in the case of reactive sputtering where a reactive gas can be added [118].

In Table 3.3 some *ionisation potential* values are given for the main rare gases used for plasma. The value of the *ionisation potentials* is related to the lower limit of the voltages that can be applied to the target in the sputtering process.

Table 3.3: *Ionisation potential* of the main rare gases used for plasma, in eV, for a single ionisation [119].

Material	<i>Ionisation potential</i> in eV
Ar	15.75962
Kr	13.99961
Xe	12.12987

In the present study, the gas used in the plasma is mainly argon because it is cheaper than krypton or xenon.

The impurities contained in argon N60 are a negligible source of contamination to the coatings. Let us consider a numerical example.

The deposition rate of TiZrV is  $0.1 \text{ nm s}^{-1}$ . The average thickness of a monolayer is  $h$ :

$$h = \left( \frac{M}{\rho \times N_A} \right)^{1/3} \quad (3.2)$$

with  $\rho$  the density,  $M$  the molar mass,  $N_A$  the Avogadro constant. The number of deposited atoms per  $\text{cm}^2$  is  $N_d$  as indicated in Table 3.4:

Table 3.4: Values of  $\rho$ ,  $M$ ,  $h$  and  $N_d$  for Ti, Zr, V and TiZrV

	$\rho$ [g $\text{cm}^{-3}$ ] at 300 K	$M$ [g $\text{mol}^{-1}$ ]	Molar density [mol $\text{cm}^{-3}$ ]	Atomic density [atoms $\text{cm}^{-3}$ ]	$h$ [nm]	$N_d$ [atoms $\text{cm}^{-2}$ ]
Ti	4.50	47.90	$9.39 \times 10^{-2}$	$5.66 \times 10^{22}$	0.26	$1.47 \times 10^{15}$
Zr	6.49	91.22	$7.11 \times 10^{-2}$	$4.29 \times 10^{22}$	0.29	$1.22 \times 10^{15}$
V	5.80	50.94	$1.14 \times 10^{-1}$	$6.86 \times 10^{22}$	0.24	$1.68 \times 10^{15}$
average (i.e. for TiZrV)	5.60	63.35	$8.83 \times 10^{-2}$	$5.32 \times 10^{22}$	0.27	$1.42 \times 10^{15}$

After 3 hours of deposition, the TiZrV film is 1 micron-thick which represents 4060 monolayers, each 0.27 nm thick.

Ar N60 is 99.9999% pure so that it contains less than  $10^{-4}\%$  of total impurities (namely  $\text{O}_2$  less than 0.2 ppm,  $\text{H}_2\text{O}$  less than 0.6 ppm,  $\text{N}_2$  less than 0.3 ppm,  $\text{H}_2$  less than 0.01 ppm,  $\text{CH}_4$  less than 0.05 ppm,  $\text{CO}$  and  $\text{CO}_2$  less than 0.05 ppm). Considering a deposition at a pressure of argon  $P_{Ar} = 10^{-2}$  Torr in dynamic conditions with a pumping speed for Ar  $S_{Ar} = 2 \text{ } \ell \text{ s}^{-1}$ , the argon injection flux is

$$F_{Ar} = P_{Ar} \times S_{Ar} \quad . \quad (3.3)$$

$$F_{Ar} = 2 \times 10^{-2} [\text{Torr } \ell \text{ s}^{-1}] \quad .$$

Supposing that Ar contains  $10^{-4}\%$  of impurities (maximum allowed content), the impurities injection flux is:

$$F_{\text{impurities}} = 10^{-6} F_{\text{Ar}} = 2 \times 10^{-8} [\text{Torr } \ell \text{ s}^{-1}] \quad .$$

The total quantity of impurities injected during a deposition run of 3 hours is:

$$N_{\text{impurities}} = t \times F_{\text{impurities}} = 10800 \times 2 \times 10^{-8} = 2.2 \times 10^{-4} [\text{Torr } \ell] \quad .$$

So that:

$$N_{\text{impurities}} = 7.1 \times 10^{15} [\text{atoms}] \quad .$$

Since:

$$N [\text{atoms}] = 3.3 \times 10^{19} \times F [\text{Torr } \ell] \quad . \quad (3.4)$$

Considering that all the impurities are pumped by the getter coating, these  $N_{\text{impurities}}$  are distributed over  $900 \text{ cm}^2$  of coating. As one monolayer contains on average  $1.42 \times 10^{15} \text{ atoms cm}^{-2}$ , then  $8 \times 10^{12} \text{ atoms cm}^{-2}$  represent  $5.6 \times 10^{-3}$  monolayers of impurities which are distributed evenly amongst the whole thickness of coating (4060 monolayers). This results in less than 2 ppm atomic impurities contributed by Ar N60.

### 3.1.3 Sputtering configurations

#### • Diode

Essentially two electrode configurations exist, the diode [120] and triode [121]. The diode, the simpler of the two, is used in this project. In Fig. 3.2, a schematic description of the diode sputtering configuration is shown.

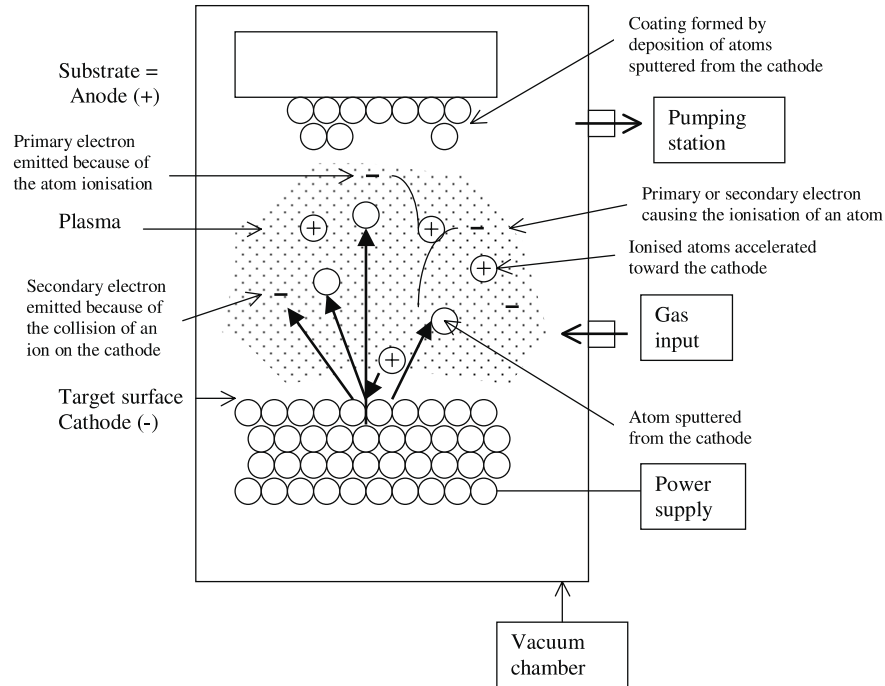


Fig. 3.2: Typical diode sputtering system [112].

- Direct-current (DC) configuration

A direct-current (DC) excitation operation is limited to electrically conducting targets which eliminate the electrical charges brought by the ions. A radio-frequency excitation (called rf sputtering) allows insulating materials to be sputtered because of capacitive coupling [122], [123]. The former is used in this project since only metals are deposited.

DC excitation requires that positive ions be extracted from the plasma by the negative potential applied to the cathode, and electrons (primary electrons) are attracted by the anode. By colliding the cathode, the ions not only sputter atoms from it but also emit secondary electrons. The primary and secondary electrons accelerated by the field go into the plasma which they maintain by colliding with argon atoms and causing ionisation. For the discharge to be self-sustained, each primary electron of the plasma must create enough ions. To do so, the cathode to anode distance has to be sufficiently large as compared to the electron mean free path.

In a self-sustained DC discharge, the transport efficiency of the cathode material to the substrate is controlled by the gas pressure, the discharge voltage, and the geometry of the apparatus.

The comparison of the distance between the electrodes and of the electron mean free path allows the working gas pressure to be fixed [124]. For instance, at  $1 \times 10^{-3}$  Torr of argon, the mean free path of an ionising electron is 300 cm which is much larger than the distance between the electrodes. Consequently, the plasma is not stable, while the discharge is self-sustained for pressures ranging from about  $5 \times 10^{-2}$  Torr to  $1 \times 10^{-1}$  Torr. However, at such high pressure, the ion mean free path is short so that they collide with atoms of the gas. During those collisions, charge transfer and energy exchange occur. The loss of kinetic energy of the sputtered atoms results in a reduction of film adhesion [125].

- Magnetron configuration

In the magnetron configuration a magnetic field is applied, which traps the electrons to increase their path before reaching the anode. The advantages of this configuration are the following.

1. The minimum self-sustaining plasma pressure is reduced (by about a factor 30 according to Ref. [126]) thanks to the magnetic confinement, providing a high electron ionisation efficiency. This feature avoids the reduction of film adhesion, loss of *deposition rate* and heating of the substrate previously described for the DC diode configuration.
2. The plasma is more intense so that the *deposition rate* is high at lower pressures [127].
3. Particular geometries can be coated, like systems with such a short distance between the electrodes that the magnetron configuration is mandatory to increase the ionising path

of the electrons and to produce enough electron multiplication to sustain sputtering discharge. This is important for the particular case of coating a cylindrical chamber with an axial cathode. By applying a radial electric field  $E$ , the electrons go straight from the cathode to the anode. By applying only an axial uniform magnetic field  $B$ , the electrons follow a helix-like path: the electrons drift along the field lines and orbit them with a Larmor radius  $R_L$ .

$$F_{\text{Lorentz}} = F_{\text{acceleration}} \Leftrightarrow e v B = \frac{m v^2}{R_L}, \quad (3.5)$$

so that

$$R_L = \frac{m v}{e B}, \quad (3.6)$$

with  $B$  the field strength,  $e$  the charge of the electron,  $m$  the mass of the electron,  $v$  the speed of the electron in the plane perpendicular to the field  $B$ .

By applying both the radial electric field  $E$  and the axial magnetic field  $B$ , the electrons follow a cycloid-like trajectory (the helix-like trajectory has a velocity component along  $\vec{E} \wedge \vec{B}$  which means that the electron-drift currents close on themselves). In this magnetron configuration, the main increase of ionising path of the electrons is due to the Larmor gyration. It was established by J. Thornton that the radius  $R_c$  of the cylindrical chamber (which is the cathode-to-anode distance) has to be at least three times larger than the gyro radius  $R_L$  of the primary electrons emitted from the cathode. With this criterion, the field strength  $B$ ,  $R_c$  and the operating voltage  $V$  are related to each other in the following way [128]:

$$B R_c > 10 V^{0.5} \text{ [G cm]}. \quad (3.7)$$

Using this equation, it is possible to adjust the magnetic field intensity so as to coat tubes of very small diameter (for instance, to coat a chamber of  $R_c = 1$  cm with an operating voltage of 500 V, the optimum  $B$  value is around 220 G =  $2.2 \times 10^{-2}$  T).

The disadvantage of magnetron sputtering is that plasma localisation can limit the uniformity of the film thickness in comparison to DC sputtering. However, the non-uniform thickness can be avoided by rotating the substrate during deposition [129].

The main two geometries that exist for magnetron sputtering are the parallel-plate and the cylindrical configurations. The latter is schematised in Fig. 3.3. They are both used in this project, as described in paragraph 3.2.2. In both cases, the cathode-to-sample distance is long in order to provide a large deposited area [130], [131] and a uniform coating composition too when using composite cathodes (see paragraph 3.1.5).

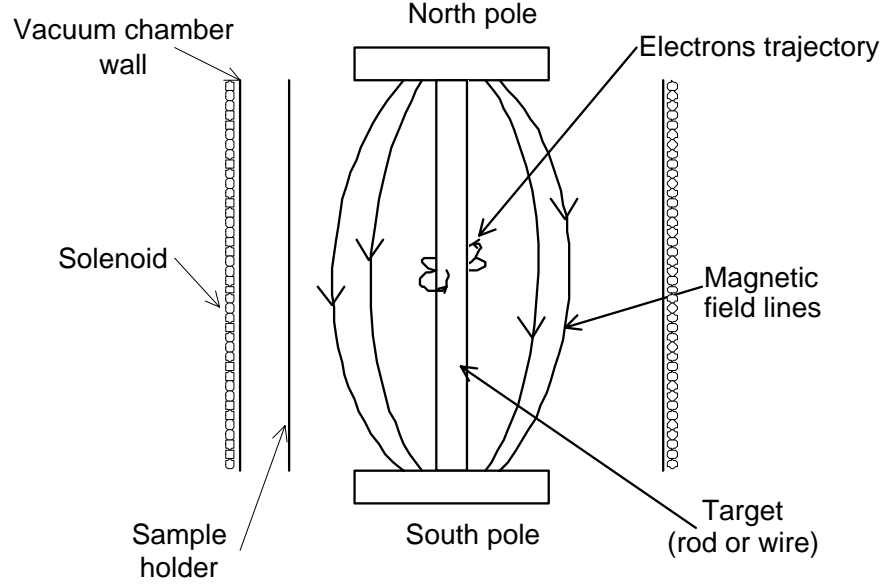


Fig. 3.3: Geometry of a typical cylindrical magnetron (from Ref. [85]).

#### 3.1.4 Influence of pressure and temperature

The type of gas used for the plasma, the discharge pressure, voltage and current, the electrode material, dimensions and spacing, the ratio of electrode dimensions to electrode spacing, as well as the *deposition rate* are important sputter deposition parameters for the coating structure [132] and properties. According to J. Thornton, the two most important parameters affecting the film morphology are the discharge pressure ( $P$ ) and the temperature of the substrate during the sputter deposition process ( $T_s$ ) normalised to the melting temperature of the target material ( $T_m$ ). He elaborated a schematic representation of the influence of the normalised substrate temperature ( $T_s/T_m$ ) and argon working pressure ( $P$ ) on the microstructure of metal coatings deposited by sputtering using cylindrical magnetron sources [133], [134], [135], [136]. This representation is called the structure zone model (see Fig. 3.4).

In Table 3.5 some values of the ratio of  $T_s$  and  $T_m$  are calculated for different metals. It appears that in the context of the present study, the pressures (1 and 10 mTorr) and normalised substrate temperatures ( $T_s/T_m$  ranging from 0.17 to 0.32) chosen to perform the coatings all belong to the same Transition Zone in the structure zone model. The microstructure is controlled by surface diffusion and is characterised by a dense fibrous structure with a smooth highly reflective surface. It forms on smooth substrates when the coating flux reaches the substrate normally to the surface, so that shadowing effects are minimised. Messier *et al.* [137] included the nanostructure to the microstructure as criteria to define the zones of their revised zone model. They made observations consistent with the microstructure zones established by Thornton, and defined subzones. In particular, within the Transition Zone several levels of structures exist which are characterised by highly anisotropic columnar structures of systematically varying column and void sizes.

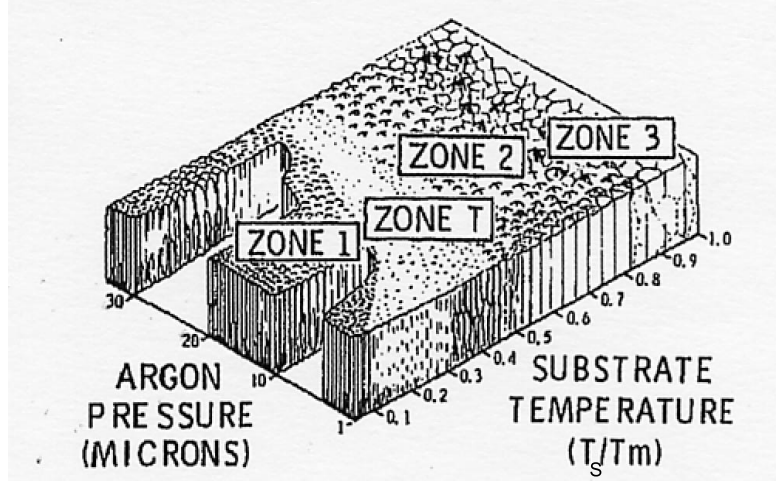


Fig. 3.4: Structure zone model established by J. Thornton modelling the film morphology of a thin film as a function of the discharge pressure ( $P$ ) and of the temperature of the substrate during the sputter deposition process ( $T_s$ ) normalised to the melting temperature of the target material ( $T_m$ ). Figure taken from [138].

Consequently, the variation of the substrate temperature  $T_s$  in the present study can originate structural changes at the nanoscale, accounting for some of the functional properties.

Table 3.5: Ratio of  $T_s$  and  $T_m$  for several values of  $T_s$  in the case of different metals

Material	$T_m[K]$	$T_s/T_m$ for $T_s = 100\text{ }^\circ\text{C}$	$T_s/T_m$ for $T_s = 200\text{ }^\circ\text{C}$	$T_s/T_m$ for $T_s = 300\text{ }^\circ\text{C}$	$T_s/T_m$ for $T_s = 350\text{ }^\circ\text{C}$
Sc	1812	0.21	0.26	0.32	0.34
Y	1799	0.21	0.26	0.32	0.35
La	1193	0.31	0.40	0.48	0.52
Ti	1943	0.19	0.24	0.29	0.32
Zr	2125	0.18	0.22	0.27	0.29
Hf	2500	0.15	0.19	0.23	0.25
V	2175	0.17	0.22	0.26	0.29
Nb	2740	0.14	0.17	0.21	0.23
Ta	3287	0.11	0.14	0.17	0.19
Cr	2130	0.18	0.22	0.27	0.29

### 3.1.5 Common cathodes for alloy deposition

A monolithic cathode consists of a bulk material of a single element or alloy. Considering a target made of an alloy of a given bulk composition, a modification of the surface composition in proportion to the *deposition rate* of the different elements occurs (only the surface is concerned since the depth of target involved in the sputtering process is of the order of tens of nm): an equilibrium establishes, which results in stoichiometric (congruent) sputtering of



multi-element materials [112]. However, this does not guarantee a stoichiometric deposit if the sticking coefficients of the sputtered species differ [91].

A composite cathode consists of a target composed of several bulk materials. It allows the deposition of compounds or alloys starting from available materials without preparing a bulk target of suitable composition. A commercially available configuration consists, for instance, of a disk in which each sector is made of a different pure metal. By rotating this target in front of the substrate while depositing, one obtains an alloy thin film. The size of the sector is about proportional to the content of the corresponding element in the deposit. The use of a composite cathode is also particularly attractive because it eliminates the problem of cathode pyrophoricity, since in a comparable morphology, the single metals studied are less reactive than their alloys, as indicated by B. Ferrario in Ref. [139].

Independent cathodes consist of several monolithic cathodes that are individually power supplied. This presents the same advantages as composite cathodes and in addition it allows the relative content of the different sputtered atom types to be exactly controlled via the control of the power applied on each target.

## 3.2 Sputtering systems and parameters

### 3.2.1 Substrate preparation

The materials employed for most substrates are stainless steel 316LN and copper OFE (Oxygen-Free Electronic copper). The reason for this choice is that they are the materials used in practical applications of NEG coatings. Nevertheless, as the activation temperature has been lowered to below 200 °C, passive activation is possible also in vacuum chambers made of aluminium. Some measurements require other substrate materials. Silicon wafers are used for Scanning Tunnelling Microscopy (STM) because of their flatness and smoothness. Coatings for thickness measurements are deposited on glass platelets and those for Transmission Electron Microscopy (TEM) require specific TEM grids. These grids, supplied by Agar Scientific, consist of copper covered by a film of formvar (polymer from polyvinyl alcohol and formaldehyde as a copolymer with polyvinyl acetate, CAS number: 63450-15-7); they are 3 mm in diameter and 0.1 mm in thickness, with a grid spacing of 200 mesh (i.e. 100  $\mu\text{m}$ ).

Two main substrate geometries are used according to the characterisation technique of the sample. The first and most common consists of platelets. The second, for pumping speed measurements, consists of 120 mm diameter disks.

These various sample parameters are summarised in Table 3.6.

Table 3.6: Summary of the substrates material, shape and dimensions for each analytical technique.

Type of analysis	Substrate dimensions		Substrate material
	Platelets [mm $\times$ mm $\times$ mm]	Disk diameter [mm]	
AES/XPS	14 $\times$ 10 $\times$ 1 or 50 $\times$ 40 $\times$ 1	–	copper or stainless steel
XRD	14 $\times$ 10 $\times$ 1	–	copper, stainless steel, glass or silicon
Pumping speed	–	120	copper
Thickness measurements	30 $\times$ 10 $\times$ 1	–	glass
TEM	–	3	copper grids
STM	14 $\times$ 10 $\times$ 1	–	silicon

- Glass

To evaluate the deposition rate of different materials as a function of the power applied on the target, thickness measurements are needed. Glass platelet substrates were chosen because of their flatness and smoothness. The cleaning is performed by degreasing and rinsing in an ultrasonic bath in alcohol. The principle of the deposition rate evaluation is to hide a part of the glass substrate with a thin mask during the deposition to create a step whose height is measured by stylus profilometry. Dividing this height by the duration of deposition gives the deposition rate of a material for a given power applied on the corresponding target. A mask of 0.1 mm turned out not to cause harmful edge effects for this measurement.

- Stainless steel

Prior to coating, stainless steel substrates are cleaned in three successive detergent aqueous solutions at 50–60 °C in an ultrasonic bath, for 15 minutes each. Afterwards, they are rinsed in de-ionised water at 70–80 °C for 10 minutes with stirring. The used detergent is the DL1 soap from Phacogene, which is dedicated to laboratory glassware and material cleaning. It is employed diluted at 5% in volume.

- Copper

Two types of copper chemical cleaning are used. They differ in the roughness they confer to the copper substrate. This was tested in the context of the study of the coating roughness, which varies among other things with that of the substrate surface prior to coating.

The copper substrates are either chemically polished or roughened before the deposition.

The polishing solution consists of sulfamic acid ( $\text{H}_3\text{NO}_3\text{S}$ ) 5 grams per litre, ammonium

citrate ( $\text{C}_6\text{H}_{14}\text{N}_2\text{O}_7$ ) 1 gram per litre, hydrogen peroxide ( $\text{H}_2\text{O}_2$ ) 5% in volume, n-butanol 5% in volume. Chemical polishing is carried out at 72 °C and is preceded and followed by washing with sulfamic acid. The final rinsing is performed with demineralized water and absolute ethanol. The process, lasting for 30 minutes, results in the dissolution of 10  $\mu\text{m}$  of copper [140]. This chemical treatment is called SUBU5 at CERN. The copper substrates prepared in this way are referred to as “smooth”. A SEM micrograph of the surface is shown in Fig. 3.5.

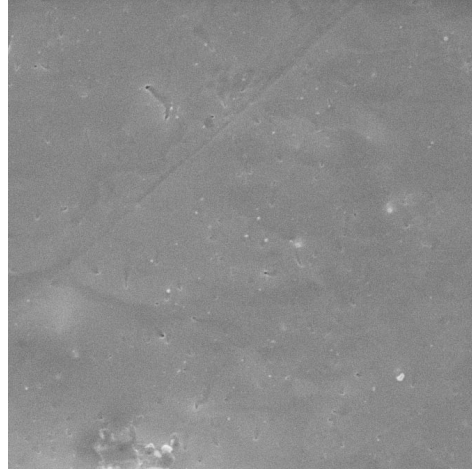


Fig. 3.5: SEM micrograph of the surface of a copper substrate chemically treated by the so-called SUBU5 process and referred to as “smooth”. Micrograph size: 15  $\mu\text{m}$   $\times$  15  $\mu\text{m}$ .

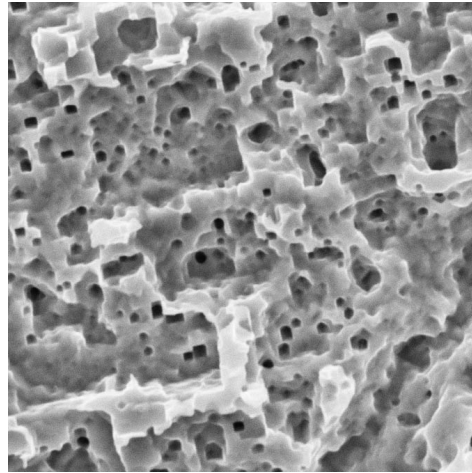


Fig. 3.6: SEM micrograph of the surface of a copper substrate chemically treated by the so-called COPPER6 process and referred to as “rough”. Micrograph size: 15  $\mu\text{m}$   $\times$  15  $\mu\text{m}$ .

In order to study the film roughness influence on the pumping speed, a chemical attack can be performed to increase the copper roughness. The aqueous solution employed consists of ammonium hydroxide  $\text{NH}_4\text{OH}$  50% in volume, hydrogen peroxide ( $\text{H}_2\text{O}_2$ ) 3% in volume, and water 47% in volume. Chemical attack is performed at room temperature for 20 minutes

with a quick stirring of the solution resulting in a dissolution speed of about  $1\text{ }\mu\text{m}$  of copper per minute. This chemical treatment is called COPPER6 at CERN. The copper substrates prepared in this way are referred to as “rough”. A SEM micrograph of the surface is shown in Fig. 3.6.

### 3.2.2 Geometries used for the sputtering systems

Two different sputtering systems have been used. In both systems, sample coatings are carried out in the DC diode magnetron sputtering configuration.

- Sputtering system A: wire cathodes

In sputtering system A, the vacuum vessel is a tube, 1 m long and 16 cm in diameter. The cathode is obtained by twisting together wires (1 or 3 mm in diameter) of source materials (Fig. 3.7). The cathode consists of two elements stretched along the chamber axis and 67 mm from each other. The magnetic field is provided by an external solenoid coaxial to the chamber. The distance between the anode and the cathodes is 27 mm. Sputtering system A is schematised in Fig. 3.8. A picture of the mounting when extracted from the vacuum deposition chamber is given in Fig. 3.9. Four copper disks can be coated simultaneously.

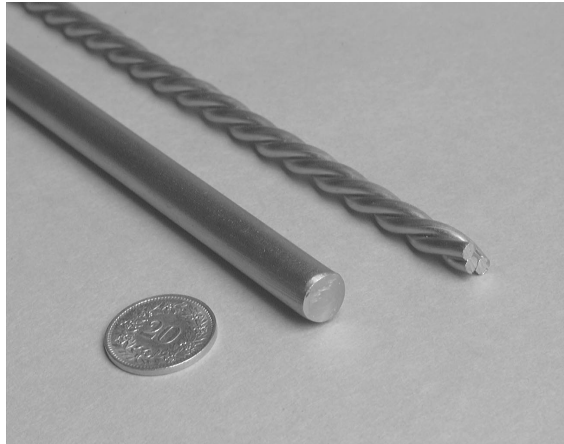


Fig. 3.7: A wire cathode made by intertwisting 3 wires and a rod cathode of comparable diameter.

The cathode made of intertwisted wires is very simple and can be applied to the deposition of thin film alloys. Its geometry is adequate for the deposition of coatings in narrow and low conductance chambers. It is remarkable that this linear and simple cathode is adapted to the final application in the beam cavity chambers.

Another advantage of the configuration is the easy control of the temperature of the substrate during deposition,  $T_s$ , by controlling the temperature of the chamber. This feature has been checked by brazing thermocouples on the samples during preliminary studies.

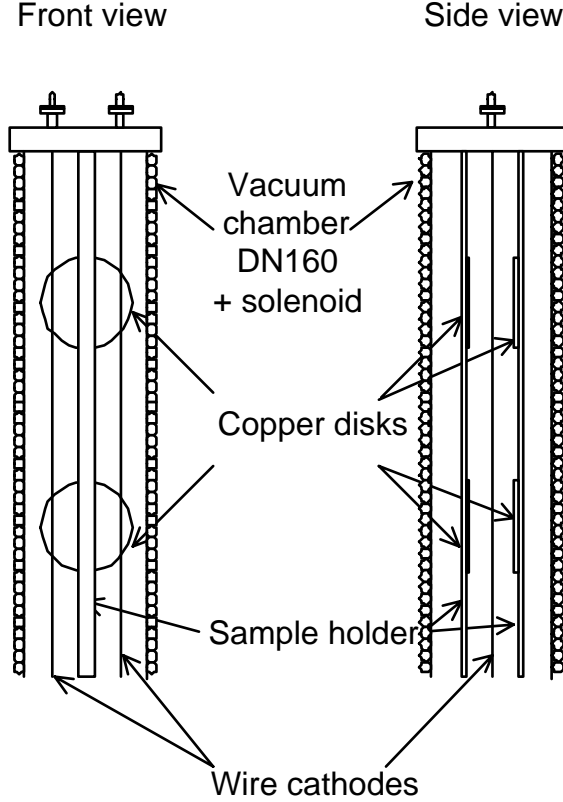


Fig. 3.8: Schematic representation of sputtering system A.

In order to test the reproducibility of the pumping speed measurements, identical samples are needed. This can be done by coating several samples during the same process. The cylindrical deposition chambers as used with wire cathodes allow four samples to be deposited along the chamber, simultaneously (see Fig. 3.9).

Together with these nice features, sputtering system A also presents some inconveniences. First, the composition of the coating can only be changed in a discontinuous way, by varying the number and/or the diameter of the wire of each element of the cathode.

Furthermore, during sputtering, the cathode is not cooled and a vapour pressure contribution may add to the *deposition rates*. Considering for instance the case of TiZrV films, above 1000 °C both Ti and V have non-negligible vapour pressures ( $P_v$ ), resulting in a higher deposition rate with respect to Zr, which has a much lower vapour pressure [141]. In Table 3.7, some vapour pressures for different metals at 1000 °C are quoted from Ref. [142]. Consequently, the composition of the three elements in the coating when using a three-wire cathode varies during the sputtering process as the cathode temperature increases. This is also the reason why the composition of the samples varies with the *deposition rate* even with an identical three-wire cathode. The higher the power applied on the cathode, the higher the temperature gets and the more pronounced the preferential vaporisation effect of high vapour pressure materials. To reduce this disadvantage, wires of large diameter could be used, so as to increase the cathode thermal losses by radiation.

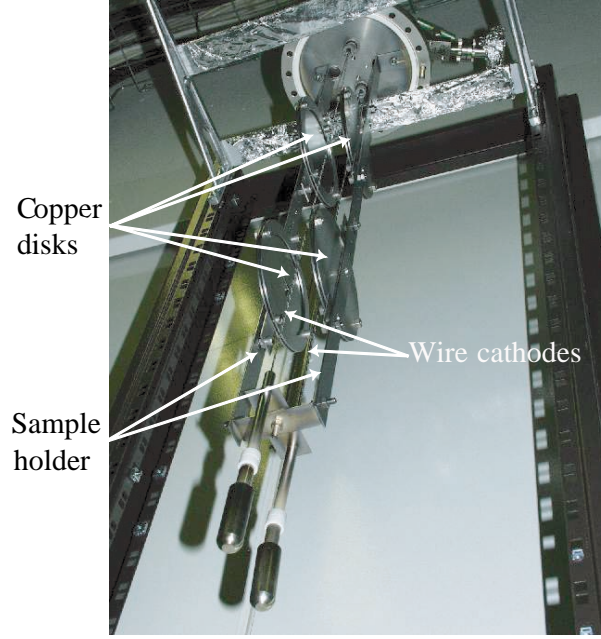


Fig. 3.9: Picture of the samples mounting in sputtering system *A*. One can notice the four copper disks mounted to be deposited simultaneously. The mounting is presented when extracted from the vacuum deposition chamber.

Table 3.7: Vapour pressures ( $P_v$ ) of different metals at 23 °C and at 1000 °C.

Material	$P_v$ in Torr at 23 °C	$P_v$ in Torr at 1000 °C
Ti	$< 10^{-11}$	$2 \times 10^{-9}$
Zr	$< 10^{-11}$	$< 10^{-11}$
V	$< 10^{-11}$	$7 \times 10^{-11}$
Y	$< 10^{-11}$	$4 \times 10^{-8}$
La	$< 10^{-11}$	$7 \times 10^{-9}$
Sc	$< 10^{-11}$	$8 \times 10^{-6}$
Cr	$< 10^{-11}$	$2 \times 10^{-6}$
Nb	$< 10^{-11}$	$< 10^{-11}$

- Sputtering system *B*: independently power supplied cathodes

This system was built at CERN to allow the composition of the coating to be varied continuously by using three cathodes which are power supplied independently. The targets are 50 mm diameter disks (2 or 3 mm thick) sealed on the cathode holder with a conducting GaIn glue. The cathode holders are made of copper and are water cooled. A schematic view of the targets of the sputtering system *B* is given in Fig. 3.10. The three targets are confocal with a tilting of 15° with respect to the axis of the system. A cross section of the magnetron and sample mounting is represented in Fig. 3.11. The distance between the anode and the cathode, respectively the substrate and the target, is 13 cm.

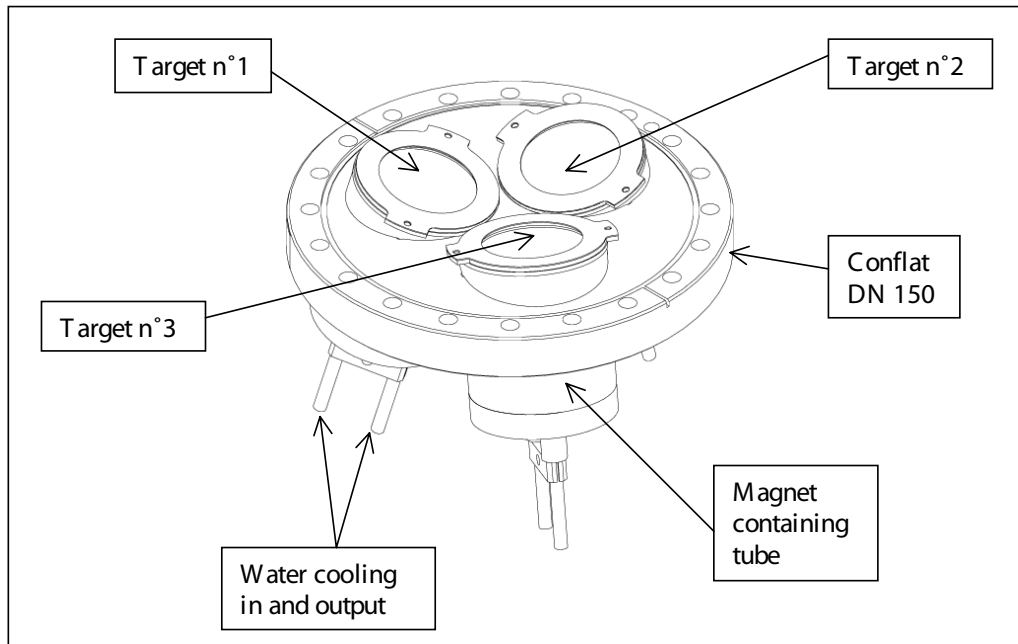


Fig. 3.10: Schematic view of the targets in sputtering system *B*.

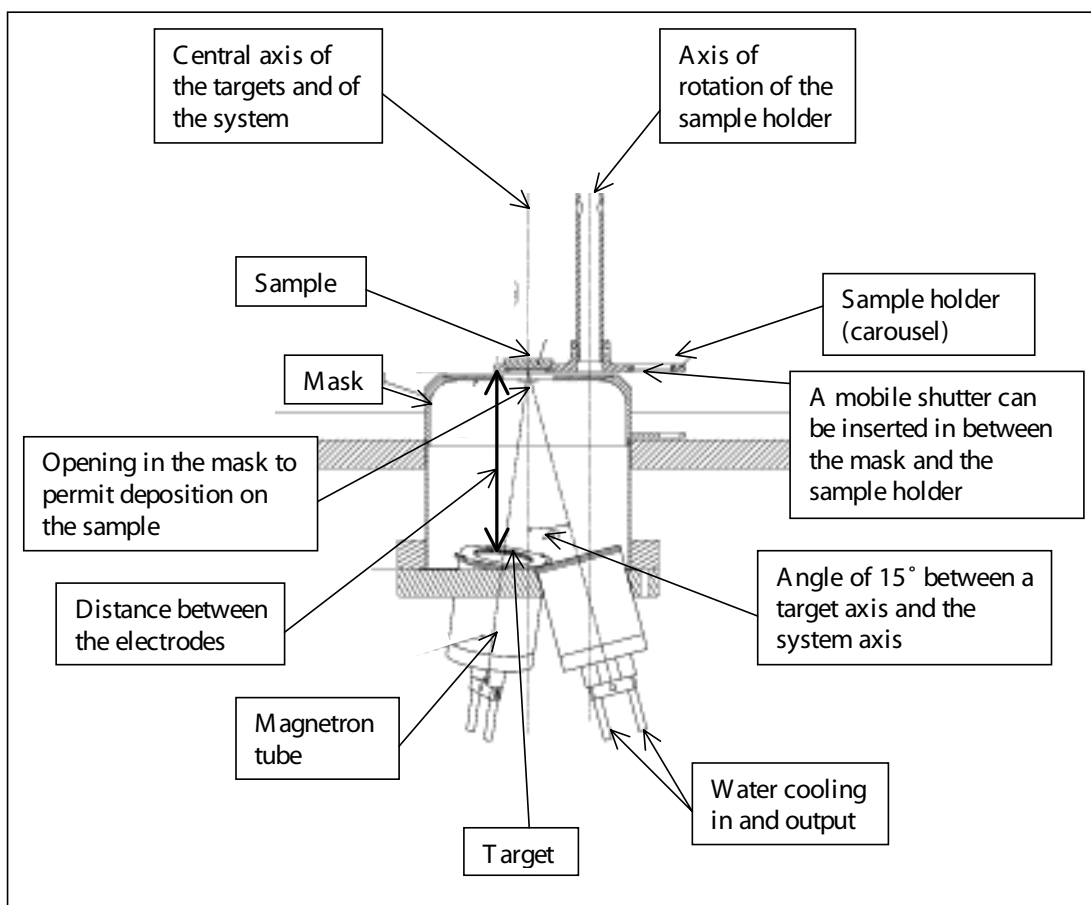


Fig. 3.11: Schematic cross section view of the magnetrons and sample mounting in sputtering system *B*.

In the deposition system *B*, a heating system allows the substrate to be heated. It is based on the use of a thermocoax heating the substrate by radiation. The advantage is that the deposition rate and the substrate temperature during deposition can be independently varied.

In the case of samples deposited on non-heated substrates, the substrate temperature remains under 90 °C for usual sputter deposition parameters. An example of measured temperature evolution of the copper substrate is reported in Fig. 3.12 as a function of the sputter deposition process duration. In this particular example, the total power applied on the targets is 400 W, and the coating composition is  $\text{Ti}_{31}\text{Zr}_{17}\text{V}_{52}$ . When aiming at a usual film thickness of 2  $\mu\text{m}$ , the process lasts 120 minutes and then the temperature is 80 °C at the end of the deposition.

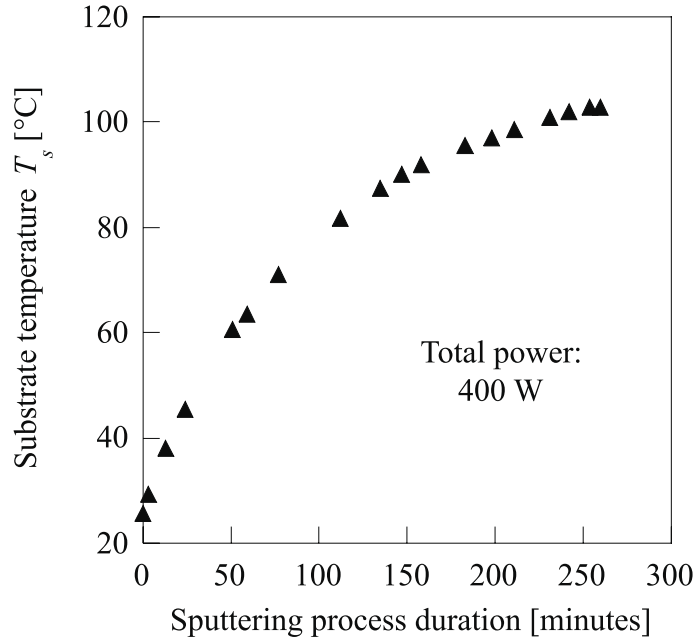


Fig. 3.12: Copper substrate temperature evolution as a function of deposition time in sputtering system *B*. The substrate is non-heated, the total power applied on the targets is 400 W, so as to reach the composition  $\text{Ti}_{31}\text{Zr}_{17}\text{V}_{52}$ . When aiming at a usual film thickness of 2  $\mu\text{m}$ , the process lasts only 120 minutes.

Small coatings of 10 mm  $\times$  14 mm can be deposited with a thickness variation of less than 0.1  $\mu\text{m}$  (verified by SEM, Scanning Electron Microscopy) and a composition variation of less than 2 atomic % (controlled by EDX, Energy Dispersive X-ray spectroscopy) over the whole deposited area. The sample holder called carousel allows 12 small samples of six different compositions to be deposited during each run (Fig. 3.13). It is made of stainless steel. After adapting the mounting, this carousel has also been used as a sample holder for the deposition of TEM grids and large samples for AES.



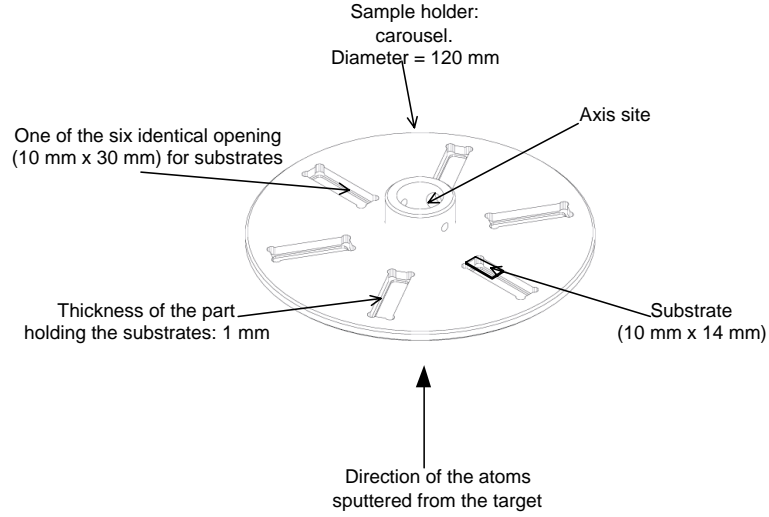


Fig. 3.13: Carousel mounting adapted for sputtering system *B*. Two substrates of 14 mm  $\times$  10 mm can be placed in each of the six windows.

Sputtering system *B* was also adapted to coat disks of 120 mm in diameter. This requires a motorization along the axis holding the sample, so as to rotate the disk while coating. In this way, a variation of less than 3 atomic % (verified by EDX) of the chosen content of any of the three elements on the whole layer is obtained. The composition variation of the coatings deposited without and with rotation of the sample holder are represented in Fig. 3.14 and Fig. 3.15, respectively; the thickness variation of the coatings in the same conditions is given in Fig. 3.16 and Fig. 3.17. The coating is a disk, 100 mm in diameter. On these four figures, the zero on the abscissa axis corresponds to the centre of the coating, which is also the position of the axis of rotation of the sample holder. The results presented were measured along one diameter of the coating.

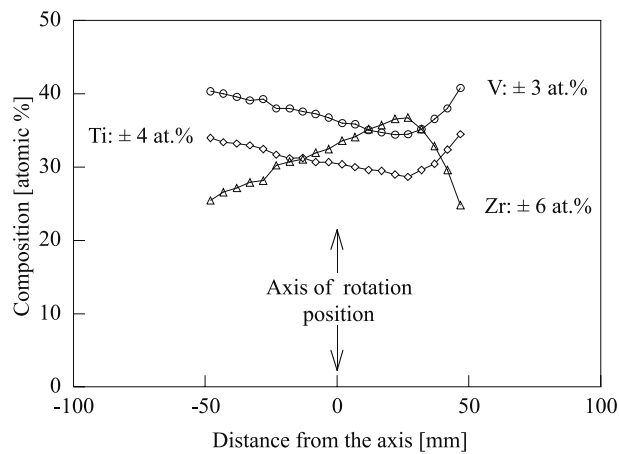


Fig. 3.14: Variation of composition of a ternary coating deposited in sputtering system *B* without rotation of the sample holder.

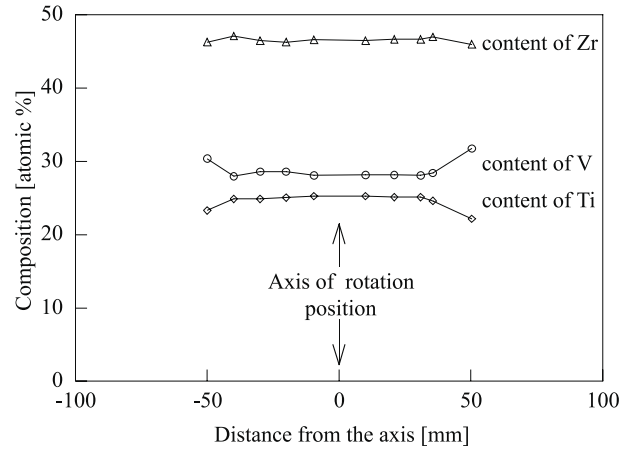


Fig. 3.15: Variation of composition of a ternary coating deposited in sputtering system *B* with rotation of the sample holder.

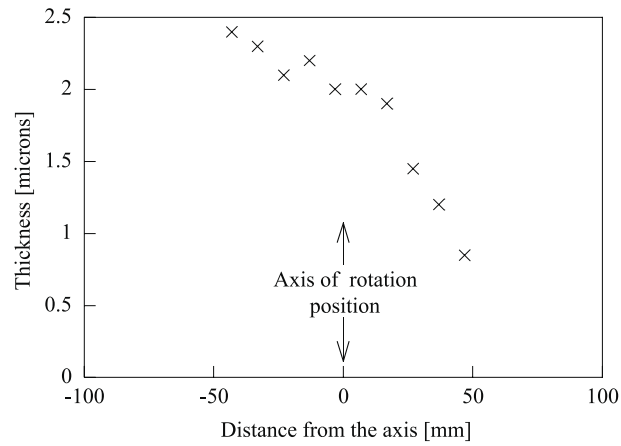


Fig. 3.16: Variation of thickness of a ternary coating deposited in sputtering system *B* without rotation of the sample holder.

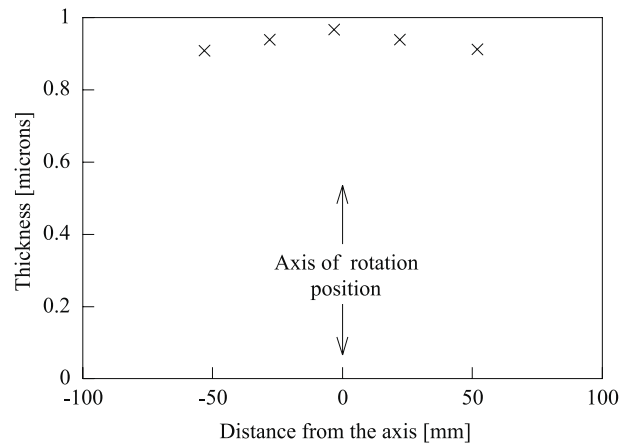


Fig. 3.17: Variation of thickness of a ternary coating deposited in sputtering system *B* with rotation of the sample holder.

As the metallic targets are exposed to air before they are settled in the sputtering machine, their surface is oxidised. The atoms sputtered from the targets at the beginning of the process are therefore a mixture of oxygen and metal atoms. In order to avoid contaminating the coating with oxygen, a mobile shutter has to mask the substrate during the first minutes of sputtering. This is called the conditioning of the targets. This is important for coatings of some nanometres (as in the case of TEM samples) in which the oxygen brought by the target is not diluted enough in the film. For instance, if a 2 nm thick layer oxide covers the target from which the 20 nm thick coating is made, the oxygen contribution cannot be neglected.

- Sputtering parameters of systems *A* and *B*

The deposition rate  $\delta_{Ti}$ ,  $\delta_{Zr}$  and  $\delta_V$  of Ti, Zr and V in the sputtering system *B* was measured for different power values (Figs. 3.18, 3.19, 3.20). The following equations resulted from the calibration:

$$\begin{aligned} \text{Power [W]} &= 16.4 \delta_{Ti} \text{ [nm s}^{-1}\text{]} \\ \text{Power [W]} &= 7.8 \delta_{Zr} \text{ [nm s}^{-1}\text{]} \\ \text{Power [W]} &= 14.6 \delta_V \text{ [nm s}^{-1}\text{]} \end{aligned} \tag{3.8}$$

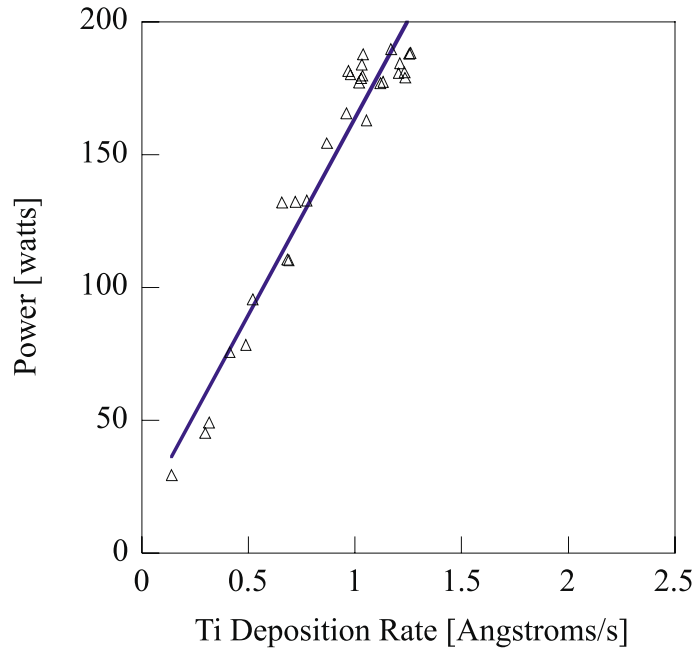


Fig. 3.18: Power required to achieve the deposition rate  $\delta_{Ti}$  of Ti indicated in the abscissa, with an argon pressure of  $5 \times 10^{-3}$  Torr, in sputtering system *B*.

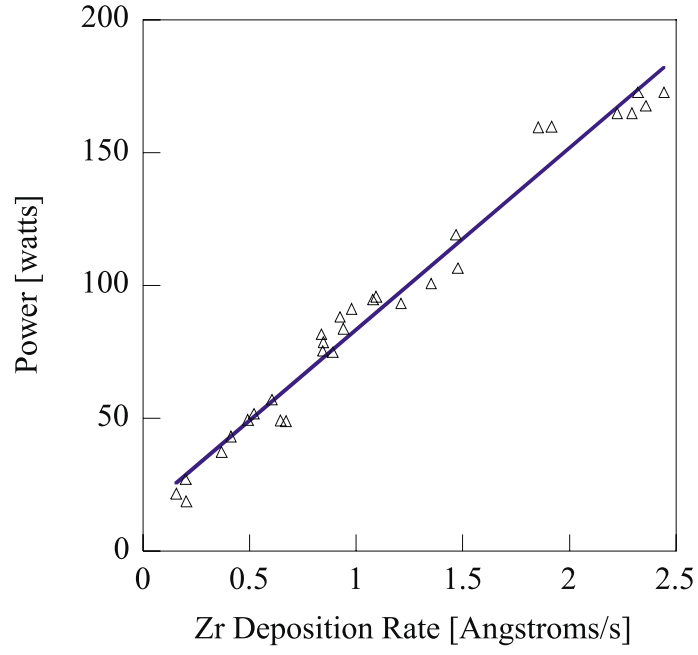


Fig. 3.19: Power required to achieve the deposition rate  $\delta_{Zr}$  of Zr indicated in the abscissa, with an argon pressure of  $5 \times 10^{-3}$  Torr, in sputtering system *B*.

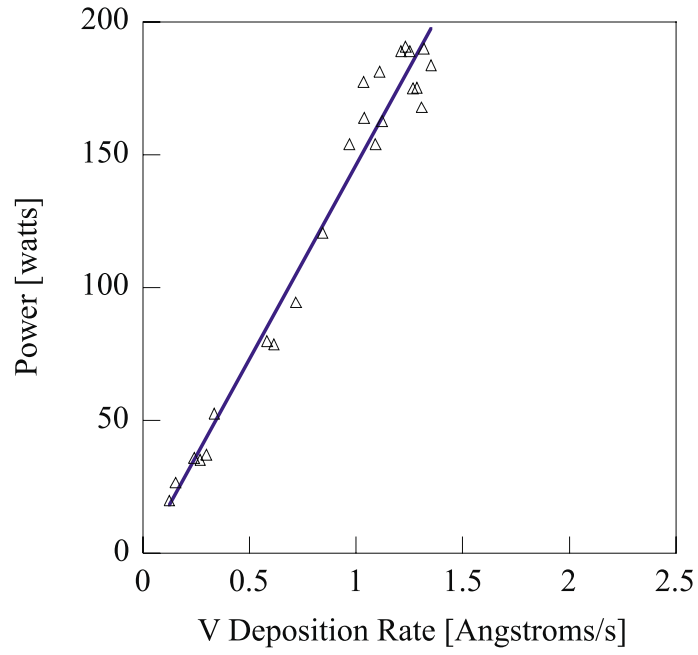


Fig. 3.20: Power required to achieve the deposition rate  $\delta_V$  of V indicated in the abscissa, with an argon pressure of  $5 \times 10^{-3}$  Torr, in sputtering system *B*.

The different deposition parameters used in the two sputtering systems are summarised in Table 3.8.

Table 3.8: Summary of the different deposition parameters used in sputtering systems *A* and *B*. The discharge voltage and current are values per cathode (two cathodes in system *A* and three cathodes in system *B*).

	System <i>A</i>	System <i>B</i>
Base pressure [Torr]	$10^{-9}$	$10^{-10}$
Cathode diameter [mm]	2–3	50
Cathode cooling	No	Yes
Discharge gas	Kr	Ar
Discharge gas pressure [Torr]	$2 \times 10^{-2}$	$5 \times 10^{-3}$
Deposition rate [ $\text{nm s}^{-1}$ ]	0.01	0.1
Discharge voltage range [V]	500	235–410
Discharge current range [mA]	40 per m	65–650
Power [W]	$\sim 40$	20–200

### 3.2.3 Purity of the cathodes

The investigated coatings contain impurities. They can be brought by (i) the gas introduced for the discharge (see 3.1.2), (ii) the degassing of the vacuum chamber walls, (iii) the pumping system, or (iv) the targets.

The methods of preparation of the targets of the main three elements concerned Ti, Zr and V can be found in the literature. The most relevant processes with respect to the presence of Cl in the coating are summarised below. The reason for this review is the possibility that the incorporation of Cl affects the properties of the NEG.

The best known method of Ti production is the Kroll process [143], [144], [145], which involves the reduction of the  $\text{TiCl}_4$  by Mg. The first step in this process discovered in 1946 is the preparation of the tetrachloride itself, which is carried out by the chlorination of a mixture of carbon with the minerals rutile or ilmenite (Example with rutile ore:  $\text{TiO}_2 + 2\text{Cl}_2 + \text{C} \rightarrow \text{TiCl}_4 + \text{CO}_2$ ). The Kroll Mg-reduction reaction takes place in a closed reactor vessel heated under an inert atmosphere (the modified process using sodium is today quite in use as well). Liquid  $\text{TiCl}_4$  is added to the liquid Mg already present in the vessel, thereby initiating the reaction  $2\text{Mg} + \text{TiCl}_4 \rightarrow 2\text{MgCl}_2 + \text{Ti}$ . The reaction products are commercially pure sponge-Ti in the form of a grey porous coke-like mass and  $\text{MgCl}_2$ , most of which is able to be drained out of the reaction chamber as a liquid. The  $\text{MgCl}_2$  is electrolytically recycled. Goodfellow, our main provider, indicates that Ti can also be obtained by reduction of the tetrachloride by calcium. The Ti sponge is densified by arc melting in a water-cooled Cu crucible (several iterations are performed of a procedure in which an arc is maintained between a consumable compacted-sponge-Ti electrode and a pool of molten sponge).

The main source of zirconium is the zirconium silicate mineral  $\text{ZrSiO}_4$ , named zircon. It is found as heavy beach sand in many parts of the world, usually in combination with

other minerals [146]. In the literature, zirconium is reported to be produced commercially by reduction of the tetrachloride with magnesium: the Kroll process [144], [146]. The first step in the manufacture is the chlorination of the sand to produce crude (Hf containing) tetrachloride and a by-product silicon tetrachloride. The industrial grades can be produced by purifying the crude tetrachloride through a simple sublimation process and then reducing it to metal using magnesium as the reductant (Kroll process). The reduction product is vacuum distilled to remove the excess magnesium and magnesium chloride leaving chunks of porous metal called sponge.

However, Goodfellow indicates that the Zr is extracted from  $\text{ZrSiO}_4$  by transformation in tetrahalide followed by a reduction with magnesium.

High-purity ductile vanadium can be obtained by reduction of vanadium trichloride with magnesium or with magnesium-sodium mixtures. Nowadays, most of the vanadium metal is produced by calcium reduction of the pentoxide  $\text{V}_2\text{O}_5$  in a pressure vessel, an adaptation of a process developed by McKechnie and Seybolt [144]. The latter is the technique employed by Goodfellow. The last step is a lamination with aluminium.

In summary, it is noticeable that one step of the purification of Ti, Zr as well as V requires chlorine. The targets of those elements can then contain chlorine, as was confirmed by Glow Discharge Mass Spectroscopy (GDMS) measurements (the technique is described in paragraph 4.1.2).

Chlorine impurities in the thin films can consequently be brought by the chlorine contained in the cathodes.

The influence of chlorine impurities on the coating properties has been studied.



# Chapter 4

## Methods for the characterisation of thin getter coatings

The characterisation of surface and bulk properties of NEG thin-films includes basic chemical and physical parameters as well as functional features related to vacuum handling.

### 4.1 Elemental composition of thin getter films

#### 4.1.1 *Energy Dispersive X-ray spectroscopy (EDX)*

In-depth elemental composition of NEG coatings was measured by Energy Dispersive X-ray spectroscopy (EDX).

The principle of EDX is described in Refs. [147], [148]. As a result of a primary electron beam bombardment, X-ray radiation of characteristic wavelengths is emitted from a specific material.

Elemental constituents are identified with the aid of Moseley's law that relates the wavelength of each observed spectral line to a specific element through the relationship:

$$\frac{1}{\lambda} = k \cdot (Z - \sigma)^{1/2} \quad , \quad (4.1)$$

where  $\lambda$  is the X-ray wavelength,  $k$  is a constant for each spectral-line series,  $Z$  is the atomic number of the element from which the X-rays originate, and  $\sigma$  is a constant associated with the atomic screening effects [149]. Light elements like C and O are badly detected by this technique, first because of their low fluorescent yield and second because of the low energy of their characteristic X-ray radiation which is easily reabsorbed by the sample itself [149].

Quantitative determination of the chemical composition can be obtained by taking into account the intensities of the characteristic X-ray line. For this purpose, conversion factors (from line intensity to concentration) are obtained by calibration with the pure bulk elements. The accuracy of the determination is better than 1 atomic %. Additional details can be found



in Ref. [150], in particular about the most widely used quantitative determination by the so-called *ZAF technique* (see Glossary in Chapter 8) [151].

The EDX equipment is in general integrated in the scanning and transmission electron microscopes. In the first case, the energy of the primary electron is of the order of some keV; this allows the extraction of information on composition from a penetration depth of the order of 1  $\mu\text{m}$ . In the latter apparatus, the samples used are thinner (some nm); as a consequence of the intersection of the thin sample with the volume of emission of photons, the composition can be obtained with a lateral resolution of the order of 1 nm [148].

The energy dispersive X-ray spectrometer integrated in a scanning electron microscope and used for this work is a LINK ISIS 300 (England). The primary electron energy for the analysis is 20 keV according to the calibration of the system. At this energy the analysis depth is larger than the film thickness, which is up to 3  $\mu\text{m}$ , as demonstrated by the fact that the signal corresponding to the substrate material is detected.

#### 4.1.2 Glow Discharge Mass Spectroscopy (GDMS)

Glow Discharge Mass Spectroscopy (GDMS) is used for the qualitative and quantitative analysis of light mass impurities. Therefore, it is a complementary technique to EDX. The principle of the technique is to analyse with a mass spectrometer the fragments created when sputtering the sample surface by glow (see Glossary in Chapter 8) discharge. The detection limit of GDMS for oxygen, carbon, argon, and chlorine (i.e. the main impurities contained in NEG films) in a metallic matrix, is 0.01 ppm in weight. The accuracy of the results is better than 20%. The sputtering rate used is faster in GDMS than in Secondary Ion Mass Spectroscopy (SIMS) so that the former technique provides information on the bulk and the latter on the surface of the sample.

The measurements were performed by Shiva Technologies, Inc., in Toulouse, France, using a High Resolution VG9000.

## 4.2 Morphology and crystallographic structure of thin getter films

#### 4.2.1 X-Ray Diffraction (XRD)

Crystalline structure and grain size are investigated by X-Ray Diffraction (XRD). This technique, based on Bragg's law, is described in detail in Refs. [147], [148], [152], [153], [154], [155], [156].

XRD measurements are in general performed in the  $\Theta-2\Theta$  configuration (Bragg-Brentano configuration). Higher signal-to-noise ratio can be achieved for thin films by means of the grazing angle technique (Fig. 4.1).

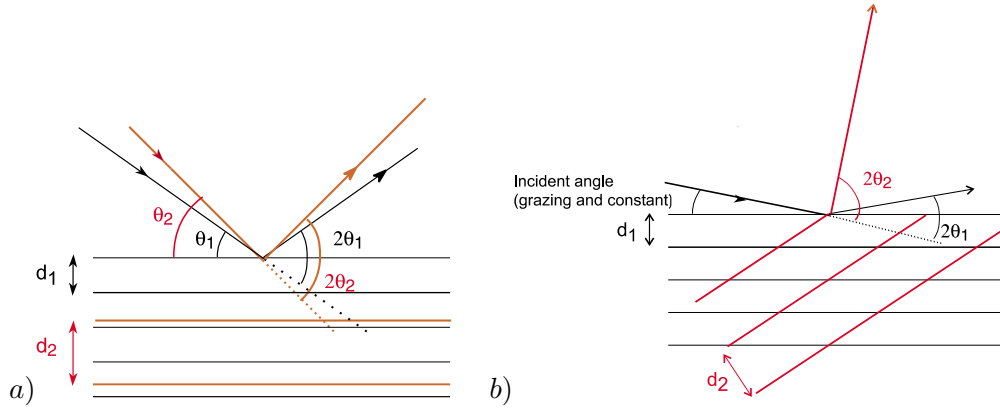


Fig. 4.1: Description of the planes observed by X-ray diffraction in a  $\Theta - 2\Theta$  mode (a) and when using a grazing angle method (b). The  $\Theta - 2\Theta$  mode corresponds to a symmetrical configuration and the grazing incidence geometry to an asymmetrical one. The thickness analysed is not the same when using grazing angles rather than a  $\Theta - 2\Theta$  mode.

Under the assumption of a homogeneous single phase and of equiaxed crystal grains, the Scherrer formula can be applied to determine the average grain size  $\omega$ :

$$\omega = \frac{k \cdot \lambda}{\Delta_c(2\Theta) \cdot \cos \Theta} \quad (4.2)$$

where  $\lambda$  is the wavelength of the source, i.e. 0.154 nm for copper  $K_\alpha$ ;  $2\Theta$  is the angular position of the recorded peak, in radians; and  $\Delta_c(2\Theta)$  is the full width at half maximum of the peak at position  $2\Theta$ , in radians. If the assumptions written above are valid, the smallest average grain size that can be evaluated precisely is 5 nm. The formula is more precisely described in paragraph 5.1.1.

The measurements in a  $\Theta - 2\Theta$  mode are performed in a diffractometer Siemens D5000, equipped with a copper X-ray source. Ni filters are used to suppress the  $K_\beta$  radiation.

In order to record diffraction lines corresponding to lattice planes by the Bragg diffraction conditions, the source beam has to be monochromatic and parallel. A monochromatic  $K_\alpha$  copper source is used, with a series of slits [157]. The equatorial divergence is limited by the aperture of the divergence slit. The axial divergence is limited by inserting two Soller collimator slits [158] in the incident and diffracted beams. Such a Soller slit consists of a number of closely spaced, parallel, and highly absorbing metal plates, which divide the X-ray beam into a number of parallel slices, each with very restricted axial divergence. In this way the radiation from an extended line source can be used without the generation of serious aberrations in the focus due to axial divergence (in other words, Soller slits lead to parallelism in one direction) [159], [160].

The background is improved by placing an antiscatter slit on the diffracted beam way, which excludes from the receiver all X-rays except those diffracted by the sample. Although the slits can be constructed of brass or nickel, it is preferable to make use of a metal of high

atomic number (e.g. molybdenum or tantalum) in order to minimise the possibility of K fluorescence, which tends to increase the background level.

The optimisation of the choice of the slits is linked to a compromise between the intensity of the signal and the angular resolution. Reducing the size of the detector diaphragm has the most impressive effect on increasing the resolution. Two Soller slits improve the resolution by leading to a more symmetrical line profile at the price of a substantial, but not prohibitive, diffracted intensity loss of about 50% [159]. This improvement is amplified at low angles. Analogous effects are observed when varying the other slits and diaphragm widths in the system: the wider the slits, the higher the intensity recorded but the lower the angular resolution. In the present case, we chose a divergence slit of 1 mm and a first Soller slit on the incident beam way. An antiscatter slit of 1 mm, a second Soller slit, and a detector diaphragm of 0.2 mm were mounted along the diffracted beam path.

Grazing angle X-ray diffraction measurements were carried out at the “Ecole Centrale de Lyon”. The latter apparatus allows *in situ* vacuum heating of the analysed samples.

#### 4.2.2 Transmission Electron Microscopy (TEM)

The principle of the Transmission Electron Microscopy (TEM) technique is described in Ref. [148]. The images result from the interaction of a primary electron beam with a thin sample. The electron beam energy is typically between 10 and 100 keV for conventional microscopes and between 1 and 3 MeV for high resolution ones. The contrasts are due to the interference of the electrons elastically diffused in the sample. The beam after interaction with the sample is recorded. If a diaphragm is placed in the way of the direct beam, the electrons transmitted without diffraction are the only ones contributing to the formation of the image. The crystallised parts appear black on a light background. This is a bright field image. When the diaphragm is centred on the  $hkl$  diffracted beam, only the rays corresponding to the selective reflexion  $hkl$  contribute to the image. The suitably oriented crystals appear light on a dark background. This is a dark field image.

The observations were performed at the Swiss Federal Institute of Technology, Lausanne (EPFL), Switzerland, and at the Institut National des Sciences Appliquées (INSA), in the Groupe d’Etude de Métallurgie Physique et de Physique des Matériaux, in Lyon, France. In the latter laboratory, two transmission electron microscopes are available: a 200 KV-200 CX JEOL, where it is possible to heat the sample *in situ* and a 2010 FEG JEOL which can provide high-resolution imaging.

#### 4.2.3 Scanning Electron Microscopy (SEM)

The Scanning Electron Microscopy (SEM) technique is described for instance in Refs. [150], [161]. SEM allows images of a sample surface to be recorded by means of secondary electrons emitted under the impact of a focused beam of electrons. The brightness of a spot on the

image is proportional to the quantity of electrons emitted. The resolution is between 3 and 10 nm.

Images of the surface of the films provided in this work were obtained in a 430I LEO microscope.

#### 4.2.4 Laser dynamic focusing

Laser dynamic focusing allows the roughness of a surface to be quantified.

The radiation emitted by a diode laser (780 nm wavelength) is focused on the surface of the sample by means of a servo-controlled lens. The lens follows the profile of the surface continuously while translating the sample horizontally. The changes in the lens position are recorded in two-dimensional coordinates. The diameter of the focused beam on the surface is  $2 \mu\text{m}$ , which corresponds to the lateral resolution of the apparatus. The vertical resolution of the lens displacements is 5 nm.

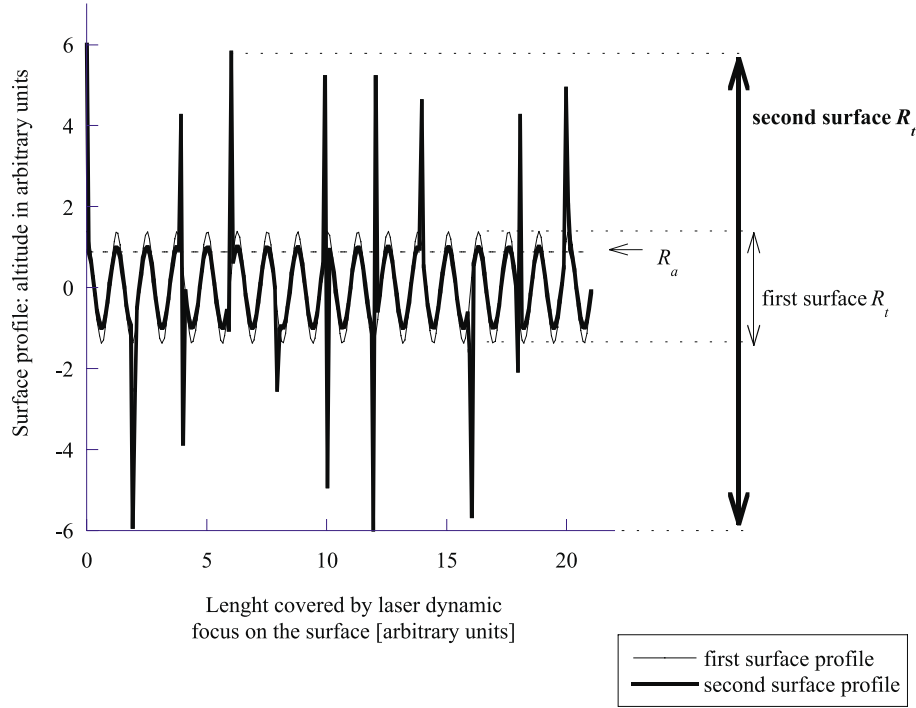


Fig. 4.2: Comparison of surfaces of identical  $R_a$  but different  $R_t$ .

Both the average roughness  $R_a$  and maximum roughness depth  $R_t$  allow the type of roughness of the surface to be defined.  $R_a$  is the arithmetic average of all vertical departures of the roughness profile from the centre line within the tested horizontal length  $\ell_m$ .

$$R_a = \frac{1}{\ell_m} \int_0^{\ell_m} |y| dx \quad . \quad (4.3)$$

$R_t$  (peak to valley height) is the vertical distance between the highest peak and the lowest

valley of the roughness profile within  $\ell_m$ . An example of two surfaces with identical  $R_a$  but different  $R_t$  is shown in Fig. 4.2.

The laser dynamic focusing apparatus is a RM 600, Rodenstock, Göttingen, Germany.

## 4.3 Thermal activation of thin getter films

### 4.3.1 Physical phenomena implied in the thermal activation

During activation, the NEG surface is progressively reduced. This is achieved by heating to a temperature high enough to decompose the oxides and to diffuse oxygen from the surface into the bulk of the getter. Hence, physical phenomena that can be correlated with the reduction of the surface oxide can be used to monitor the activation process.

### 4.3.2 Operational definition of activation temperature ( $T_a$ )

The activation temperature  $T_a$  is the lowest temperature at which a NEG has to be heated to become fully activated in a chosen time. Full activation results in a maximum for pumping speed and in a minimum for the concentration of surface contaminants.

### 4.3.3 Activation temperature evaluation by surface analytical methods

Surface analytical techniques are the fastest methods for the characterisation of NEG materials. The surface of the NEG coatings were characterised by Scanning Tunnelling Microscopy (STM), Auger Electron Spectroscopy (AES), and X-ray Photoelectron Spectroscopy (XPS).

- Scanning Tunnelling Microscopy (STM)

Scanning Tunnelling Microscopy (STM) is a technique that produces three-dimensional direct-space images of the surface of materials by means of tunnelling electrons. The principle of the technique is described in Refs. [147], [162]. The main feature of this technique is its lateral resolution at the atomic scale. The value of the tunnelling current for a given applied voltage strongly depends on the electrical properties of the surface. As a consequence, the progressive reduction of a NEG surface during the activation process can be monitored *in situ* after heating at different temperatures under vacuum.

The instrument used at EPFL operates under vacuum and allows *in situ* heating of the samples.

- Auger Electron Spectroscopy (AES)

The principle of Auger Electron Spectroscopy (AES) is described in Ref. [147]. The technique provides identification at the atomic level of all elements (except H and He) present in the outermost atomic layers of the sample. The depth resolution corresponds to few monolayers

due to the low inelastic mean free path of electrons in that energy range [163]. The lateral resolution is linked to the size of the source spot and can be as low as 5 to 15 nm in particular conditions [164].

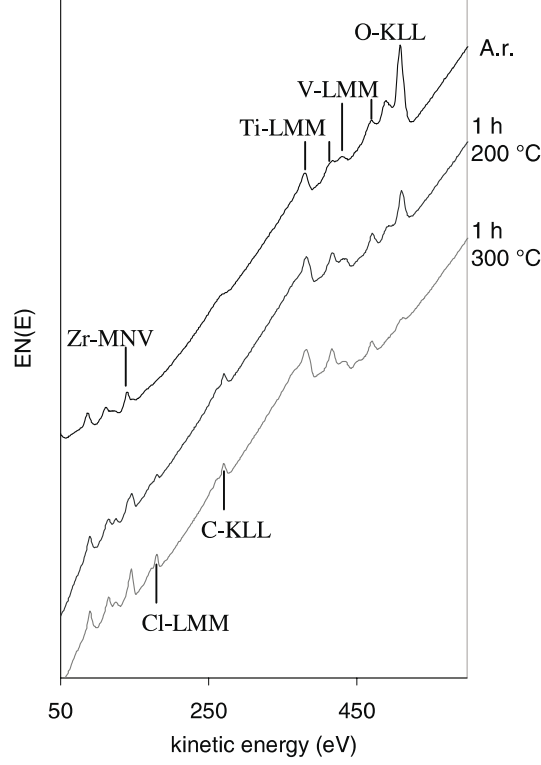


Fig. 4.3: Direct  $EN(E)$  Auger electron spectra of a  $1\ \mu\text{m}$  thick TiZrV NEG thin film on stainless steel, as-received (A.r.) and after heating for 1 hour at  $200\ ^\circ\text{C}$  and  $300\ ^\circ\text{C}$ , respectively. The  $40\ \text{mm} \times 40\ \text{mm}$  NEG thin film sample, with an in-depth composition  $\text{Ti}_{24}\text{Zr}_{54}\text{V}_{22}$  (atomic), was mounted using heater assembly of Fig. 4.5 *b*. The background increases with the energy because  $\Delta E/E$  is constant in the present configuration. This is why the resolution decreases when the energy increases. Direct  $EN(E)$  spectra reported here are normalised to the same background intensity value at 600 eV kinetic energy in order to eliminate the influence of instrumental parameters such as fluctuations in beam current and detector efficiency.

The scanning Auger electron spectrometer available at CERN is mounted on a vacuum system designed to characterise the inner wall of the four-cell cavities of the LEP collider without dissection or any deterioration [165]. The spectrometer head can be retracted from the system by means of a long bellow and maintained in an independent vacuum system when samples are changed. The spectrometer consists of a single-pass cylindrical mirror analyser (PHI 15-110B, Physical Electronics) with a coaxial electron gun. The spectra are all acquired in the direct mode with a relative energy resolution  $\Delta E/E$  of 1.2% (full width at half-maximum). The primary electron energy during the measurements is 2.5 keV and the primary beam current is typically  $1\ \mu\text{A}$ , incident normal to the sample surface. The

acquisition of one spectrum lasts about 1 minute (energy range 30–1000 eV, 1 eV step, 20 ms/step, 3 repeats). The primary electron beam diameter is approximately 0.15 mm and the electron dose, which is accumulated during the acquisition of one AES measurement lasting 1 minute, is of the order of  $10^{-3} \text{ C mm}^{-2}$ . After each measurement the sample is shifted to a new position, which was not previously exposed to electron irradiation, in order to minimise the electron-induced surface damage.

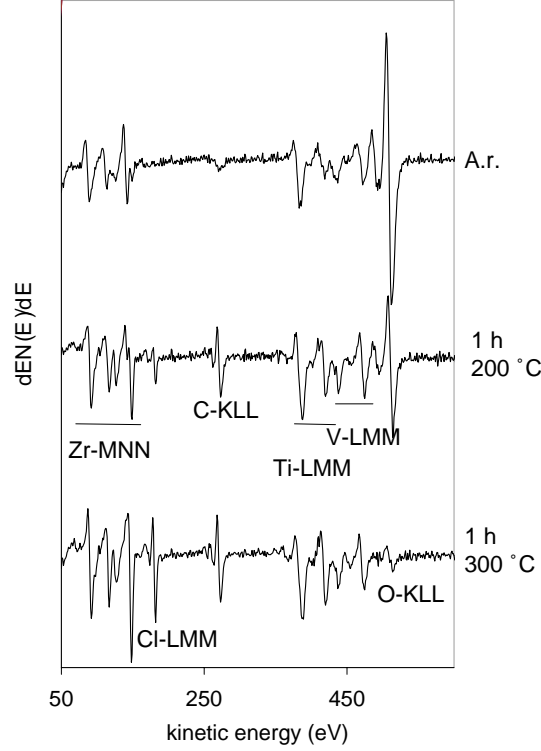


Fig. 4.4: Identical to Fig. 4.3 but in a derivative  $dEN(E)/dE$  form.

The experimental data can be presented in two ways. The relative content of each element on the surface is evaluated either by measuring the peak-to-valley height in the derivative spectra or by calculating the peak-areas from the direct spectra, as described below. Examples of direct  $EN(E)$  and derivative  $dEN(E)/dE$  spectra are presented in Fig. 4.3 and Fig. 4.4, respectively. The notation “ $EN$ ” is a way to indicate that the analyser transmission increases with the energy recorded.

Since the background subtraction on the direct spectrum is difficult due to the presence of the lines of Ti, V and O in the same energy range, the spectra are numerically differentiated and the signal intensity is measured as the peak-to-valley height in the derivative spectrum. The derivative  $dEN(E)/dE$  spectra are averaged over a 2 eV wide energy range. Numerically differentiated  $dEN(E)/dE$  spectra are used to follow the changes in the Zr MNV line-shape, which indicate the degree of activation of the TiZrV surface. The peak at 147 eV (corre-

sponding to Zr in metal) grows when the surface oxide is progressively reduced, whereas the component at 141 eV, characteristic for Zr in  $\text{ZrO}_2$  [166], decreases.

Peak-areas are calculated from the direct spectra by subtracting, as a first approximation, a linear background (between 499–518 eV, 200–285 eV, 174–186 eV and 81–98 eV for O-KLL, C-KLL, Cl-LMM and Zr-MNN peak areas, respectively).

Sample heating in the spectrometers (for AES and XPS) is achieved by radiation from a hot filament. Electron bombardment is avoided, because the electron-stimulated desorption would degrade the vacuum even more. The sample plate temperature is measured by a K-type thermocouple. The maximum heating temperature which can be reached in this way is 350 °C. The sample heater was designed in order to allow sample temperature measurements with an accuracy of  $\pm 3$  °C. Therefore, the samples are tightly clamped to an OFE copper sample plate by means of four screws so that a good thermal contact between the sample plate and the samples is assured. Two different sample mountings *a* and *b* were designed for the Auger electron spectrometer. Schematic views are shown in Fig. 4.5.

- a* Two samples with the dimensions 14 mm  $\times$  10 mm  $\times$  1 mm are clamped to the heatable OFE copper plate by means of a copper mask, which partly covers the sample surface. For some measurements the copper mask has been entirely coated by a TiZrV thin film.
- b* One sample with the dimensions 50 mm  $\times$  40 mm  $\times$  1 mm is directly fixed to the sample plate by means of four screws.

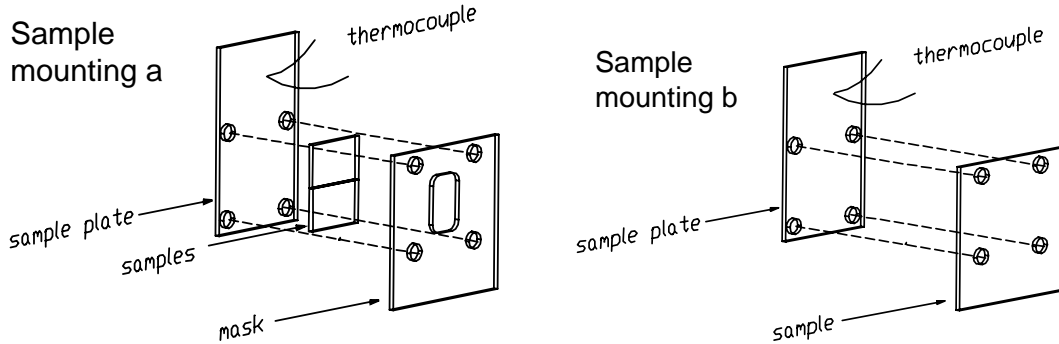


Fig. 4.5: Schematic view of the two different sample mountings *a* and *b* used for sample heating in the Auger electron spectrometer. Sample mounting *a* allows two samples with the dimensions 14 mm  $\times$  10 mm  $\times$  1 mm to be clamped to the sample plate by means of a mask, which covers the sample edges. With mounting *b*, only one sample with the dimensions 50 mm  $\times$  40 mm  $\times$  1 mm is fixed to the sample plate using four screws.

The rate at which the sample temperature is raised up to the set value is about 10 °C min<sup>-1</sup>. The surface analysis measurements were carried out as a function of heating time at constant



temperature, or more frequently as a function of heating temperature, which is kept constant during 1 h. In the latter case, the surface of the NEG alloys are first analysed in the as-received state (after deposition and an air exposure for about 1 h) and then after *in situ* heating for 1 h at a given temperature. The heating temperatures are 120 °C, 160 °C, 200 °C, 250 °C, 300 °C and 350 °C, respectively. The surface analysis measurements are carried out immediately at the end of each heating step. Two samples are heated and measured during the same run in configuration *a* and only one in configuration *b*.

The UHV system of the Auger electron spectrometer is pumped by a combination of a turbomolecular pump and sputter ion pumps. In addition a Ti sublimation pump with an estimated effective pumping speed of about  $1000 \ell \text{ s}^{-1}$  for  $\text{N}_2$  was installed in order to reduce the residual contamination during sample heating. Compared to the global pumping speed of the system, the pumping speed of the activated NEG samples is negligibly small.

The vacuum chamber of the Auger electron spectrometer is unbaked in order to keep the initial sample conditions. The total base pressure before the surface treatments is  $10^{-9}$  Torr ( $\text{N}_2$  equivalent),  $\text{H}_2$  being the dominant gas followed by water vapour (about  $2 \times 10^{-10}$  Torr). During sample heating the total pressure in the experimental vacuum chamber increases to about  $4 \times 10^{-8}$  Torr at 350 °C, again with  $\text{H}_2$  as the main gas followed by  $\text{H}_2\text{O}$  (about  $4 \times 10^{-9}$  Torr) and  $\text{CH}_4$  (about  $4 \times 10^{-9}$  Torr). The partial pressures of CO and  $\text{CO}_2$  during sample heating at 350 °C are of the order of  $10^{-9}$  Torr. Baking the UHV system would not significantly reduce the sample contamination, since most of the outgassing during thermal treatment is generated by the sample heater.

- X-ray Photoelectron Spectroscopy (XPS)

The X-ray Photoelectron Spectroscopy (XPS) principle is described in Ref. [147]. The lateral resolution is at best 1  $\mu\text{m}$ . As for AES, the depth resolution corresponds to few monolayers owing to the low inelastic mean free path of electrons in the energy range concerned [163]. XPS allows elemental identification of surface elements by evaluation of the characteristic binding energy of the electrons escaping from the sample submitted to X-ray radiations. All elements except hydrogen can be identified from their characteristic photoelectron peaks. The detection limit is typically 1 atomic %. Additionally, it provides information on the chemical state of the electron emitting elements.

XPS measurements are carried out with a PHI ESCA 5400 spectrometer. The PHI model 10-360 spherical sector electron spectrometer is operated with fixed pass energy (fixed analyser transmission mode) and the transmitted electrons are detected with a position-sensitive detector. A non monochromated  $\text{Mg K}_\alpha$  X-ray source ( $h\nu = 1253.6 \text{ eV}$ , with  $h = 6.6257 \times 10^{-34} \text{ J s}$ , the Planck constant and  $\nu$  the frequency of the photons) excites photoelectrons. The spectra are acquired at  $45^\circ$  emission angle relative to the sample normal.

The binding energy scale was calibrated on *in situ* sputter-cleaned Au and Cu sam-

ples [167]. The Zr 3d deconvolution is realised with asymmetrical Gaussian–Lorentzian functions.

For XPS measurements the sample mounting *a*, described for AES measurements is used (Fig. 4.5).

#### 4.3.4 Evaluation of gettering properties by pumping speed measurements

The pumping speed of a given pump is defined as the ratio between the flux of gas pumped and the pressure of the same gas at the aperture of the pump itself. The pumping speed of a NEG depends on its gas surface coverage, i.e. the quantity of gas already pumped. The pumping speed measured for a negligible gas load is named the initial pumping speed.

- Set-up

Pumping is measured by means of a standard Fischer–Mommson measuring dome [169] schematised in Fig. 4.6. The flux of gas is measured recording the pressure drop across a known conductance (see paragraph 1.2) that separates two chambers. The geometrical shape of the dome was calculated in order to give pressure readings equal to those of a spherical system having a perfect Maxwellian distribution of gas molecule velocity. In the specific case of this work the lower chamber, in which the gases are injected, is referred to as chamber 1. The upper chamber, which is pumped by both the NEG (area 78 cm<sup>2</sup>) and a turbomolecular pumping unit (to avoid accumulation of CH<sub>4</sub> and rare gases) is referred to as chamber 2. The turbomolecular pump provides an effective pumping speed in the dome of 10 ℓ s<sup>−1</sup> and 2.7 ℓ s<sup>−1</sup> for H<sub>2</sub> and CO, respectively. For a gas *i*, this pumping speed is designated by  $S_i^{turbo}$ . The conductance that separates the two chambers has an aperture of 0.78 cm<sup>2</sup> so that at room temperature:

$$C_{H_2} = 44.18 \text{ ℓ s}^{-1} \text{ cm}^{-2} \times 0.78 \text{ cm}^2 = 34.4 \text{ ℓ s}^{-1} \quad (4.4)$$

$$C_{CO} = C_{N_2} = 11.70 \text{ s}^{-1} \text{ cm}^{-2} \times 0.78 \text{ cm}^2 = 9.1 \text{ ℓ s}^{-1}$$

Pressure measurements were performed by means of two Bayard–Alpert gauges. They were calibrated *in situ* by comparing their readings to those of a previously calibrated gauge.

In order to limit the contamination sources to a minimum, the system is not equipped with a residual gas analyser (indeed, some degassing from the analyser filament would unduly load the getter surface).

- Samples

The samples are 120 mm diameter copper disks coated on one side only on a 100 mm diameter surface. After 24 hours dry air venting in the sputtering vessel, the coated copper disk is clamped between the Conflat flanges of the measuring dome pump opening. The disk can be

heated up to 400 °C by means of an external heater. The disk temperature is measured by means of three E-type thermocouples, pressed between the steel flanges and the disk.

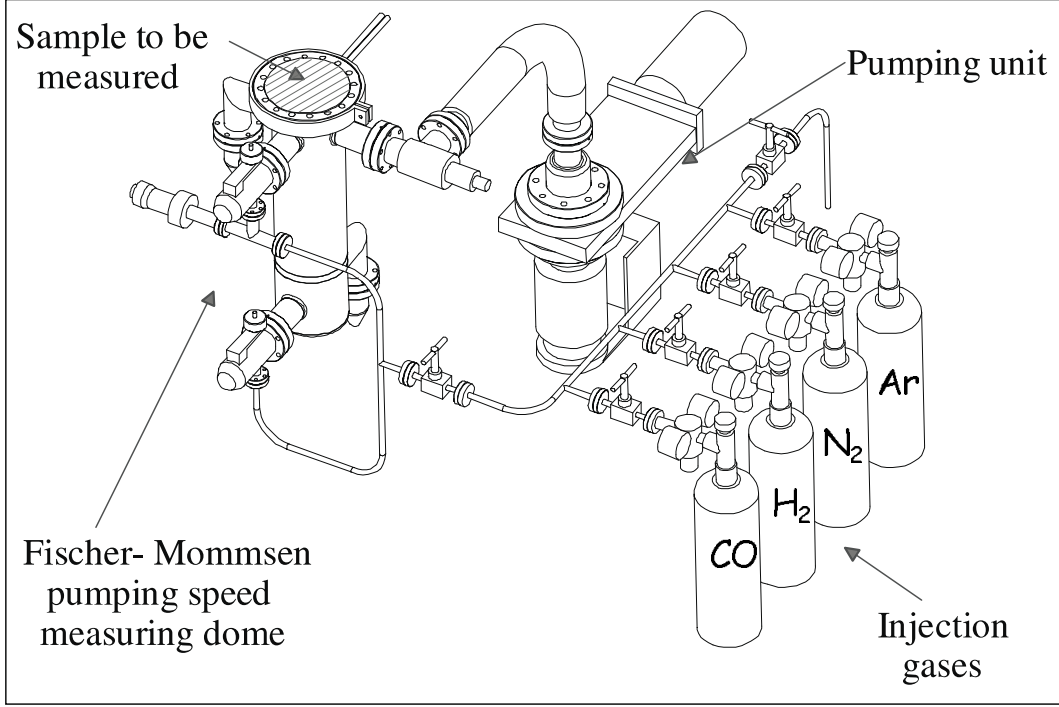


Fig. 4.6: Schematic view of a standard Fischer–Mommsen measuring dome.

- Experimental procedure

After pump-down, the measuring system is baked at 250 °C for 20 hours. During bake-out, the copper disk is maintained at a temperature lower than 80 °C by water cooling to avoid the NEG activation and, hence, undue pumping of the gas released during the bakeout. Just before the end of the bakeout, the sample is heated at 120 °C for 2 hours while the heating temperature of the rest of the system is gradually decreased. During bakeout, the total pressure is monitored by a standard Penning ionisation gauge. The base pressure obtained after cooling at room temperature is in the  $10^{-10}$  Torr range.

In a standard measuring cycle, the samples are heated to a given temperature  $T$  for 2 hours (unless otherwise indicated) (heating rate of 100 °C per hour) and the pumping speeds  $S_i^{NEG}$  for individual gas  $i$  are measured after cooling down the sample to room temperature. The investigated temperature range spans from 120 °C to 325 °C in steps of 25 °C or 30 °C without intermediate air venting. The temperatures are chosen so that one step should not interfere with the next.

During the measurement, a gas is injected in chamber 1 at a pressure in the  $10^{-8}$  Torr range, but pressures two orders of magnitude higher can be applied when surface saturation has to be achieved.

- How to evaluate the pumping speed from the pressure reading

The injected flux of gas  $i$ ,  $F_i$  [Torr  $\ell^{-1}$  s $^{-1}$ ] can be expressed in two ways:

$$\begin{aligned} F_i &= C_i(\Delta P_2 - \Delta P_1) \\ F_i &= \Delta P_2(S_i^{NEG} + S_i^{turbo}) \end{aligned} \quad (4.5)$$

where  $\Delta P_1$  and  $\Delta P_2$  are the pressure variation during the injection in chamber 1 and chamber 2, respectively.

The getter pumping speed for the gas  $i$ ,  $S_i^{NEG}$ , in  $\ell$  s $^{-1}$  is:

$$S_i^{NEG} = C_i \left( \frac{\Delta P_1}{\Delta P_2} - 1 \right) - S_i^{turbo} . \quad (4.6)$$

To study the way the pumping speed progressively reduces with increasing the quantity of the gas adsorbed ( $Q_i$ ), the injection flux is maintained constant and the pumping speed is periodically measured. This type of measurement ends when the pumping speed is negligible (i.e. when the getter is saturated); the quantity of the gas then adsorbed is the surface pumping capacity. The quantity of gas  $i$  pumped by the getter is obtained by integrating the pumping flux with time:

$$Q_i = \int_0^t S_i^{NEG} \cdot \Delta P_2 \cdot dt . \quad (4.7)$$

It is expressed per unit area in Torr  $\ell$  cm $^{-2}$  or molecules cm $^{-2}$ .

Some measurements were performed in order to assess how the surface load of a gas influences the NEG film pumping speed for other gases. To do this, the pumping speed of a gas is recorded after injection of defined quantities of another gas.

- Reliability of the pumping speed measuring apparatus

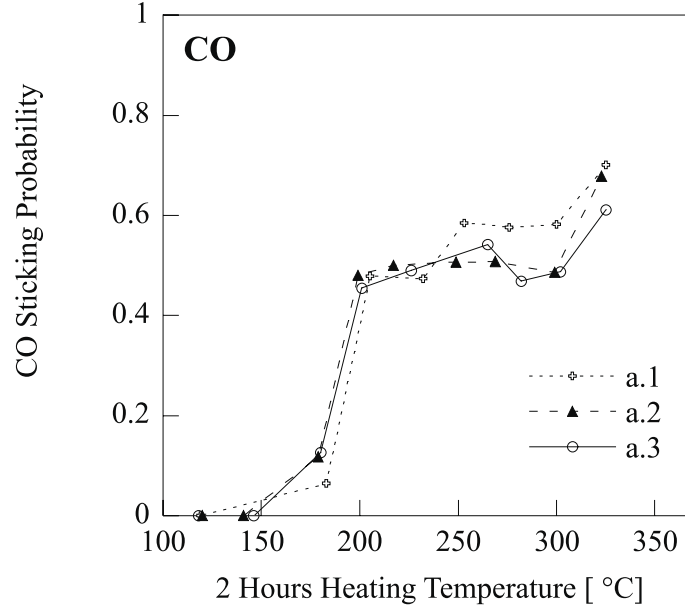
In order to test the reliability of the pumping speed measuring apparatus, three samples produced during the same coating process were measured. The samples, Ti<sub>32</sub>Zr<sub>16</sub>V<sub>52</sub> (atomic), were deposited in sputtering system *A*, by using a cathode made of intertwined 1 mm wires. The spread of pumping speed of these three identical samples for CO and H<sub>2</sub> as a function of the heating temperature is shown in Fig. 4.7 *a* and *b*, respectively.

The onset of the CO pumping speed is between 150 °C and 180 °C and a large increase is observed between 180 °C and 200 °C up to a value corresponding to a sticking probability of about 0.5. Then the CO pumping speed remains nearly constant up to 300 °C, and finally it keeps increasing again above 325 °C. The highest values of the sticking probability are close to 0.75.

Measurable sticking probabilities for H<sub>2</sub> are always obtained after 2 hours heating at a temperature between 180 °C and 200 °C. This is in agreement with data obtained with long coated chambers [170] when considering the different heating time. The maximum of the

pumping speed for  $\text{H}_2$  is obtained between 230 °C and 250 °C and it corresponds to a value of the sticking probability close to  $1 \times 10^{-2}$ . For higher heating temperatures, up to 300 °C, the pumping speed decreases to about one half of the attained maximum value, and then it increases again above 325 °C.

a)



b)

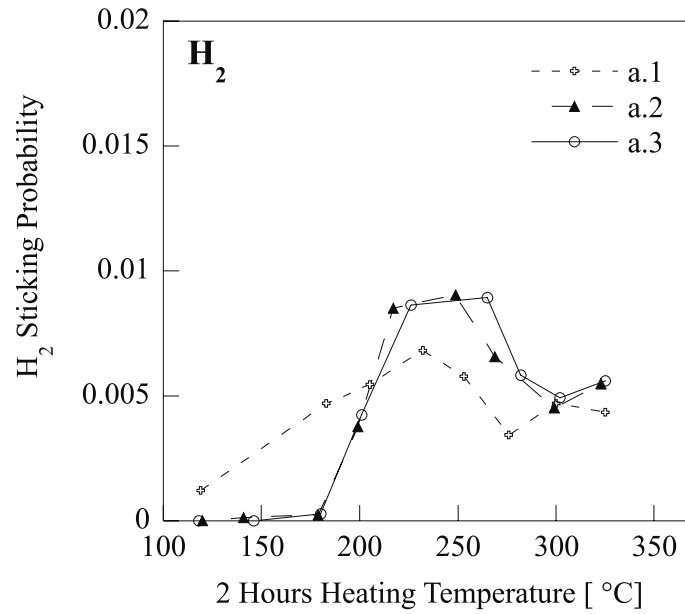


Fig. 4.7: *a*: Pumping speed of CO as a function of the heating temperature for samples of composition  $\text{Ti}_{32}\text{Zr}_{16}\text{V}_{52}$  (atomic). Three samples produced during the same coating process were measured in order to test the reliability of the pumping speed measuring apparatus. *b*: Pumping speed of  $\text{H}_2$  as a function of the heating temperature for the same samples as in Fig. 4.7 *a*.

# Chapter 5

## Results

The parameters that influence the getter properties are numerous and interconnected. Accordingly, the results are presented in five main sections: the influence of the TiZrV coating composition, of the substrate, of the substrate temperature during the deposition ( $T_s$ ), of the surface load of a gas and the effects of air venting.

### 5.1 Influence of the TiZrV film composition

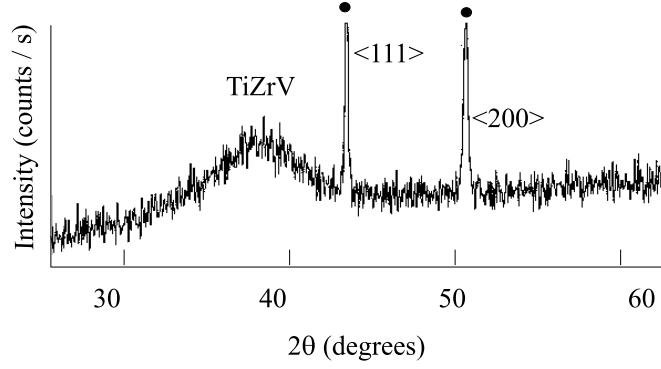
#### 5.1.1 Film crystallinity

XRD was performed on samples of more than 50 different TiZrV compositions. Two kinds of film structures can be distinguished using the  $\Theta - 2\Theta$  configuration, each one with a typical XRD diffractogram, represented in Fig. 5.1 *a* and *b*. In diffractogram *a*, a broad peak around  $38^\circ$  is present whereas in diffractogram *b* a sharp diffraction peak at  $36^\circ$  due to the film can be distinguished. In both cases no other peaks are observed at larger diffraction angles, except those of the substrate.

Under the assumption that the film coating is made up of a single ternary phase, the position of the peaks (independently of their sharpness) can be predicted by Vegard's law. This law states that the lattice parameter of a solid solution is an average of the lattice parameters of each of the constituting elements weighted by the respective atomic concentration [171], [172]. In spite of the fact that Vegard's law [173]–[181] is applicable only to elements that present similar crystal lattices, successful applications to elements that crystallise in hexagonal close-packed (hcp) and face centred-cubic (fcc) lattices [182], or in hexagonal close-packed and body-centred cubic (bcc) lattices, as for Ti and V [183], have been reported on the entire mixing range of the elements. As both Ti-Zr and Ti-V follow Vegard's law, the same result is assumed for Ti-Zr-V. Vegard's law is applied to Ti-Zr-V alloys using the EDX data for the composition; the  $2\Theta$  positions for the main  $K_\alpha$  peaks is calculated for a direction which is equivalent in hcp and bcc lattices, using namely:  $\langle 002 \rangle$  at  $38.404^\circ$  for Ti hcp (JCPDF n°44-1294),  $\langle 002 \rangle$  at  $34.840^\circ$  for Zr hcp (JCPDF n°5-665) and  $\langle 110 \rangle$  at  $42.171^\circ$  for V bcc

(JCPDF n°22-1058). The Bragg relation allows one to calculate the equivalent of the  $2\Theta$  position in lattice parameter  $d_{002}$  for the ternary alloy. The results obtained are summarised in Table 5.1.

a)



b)

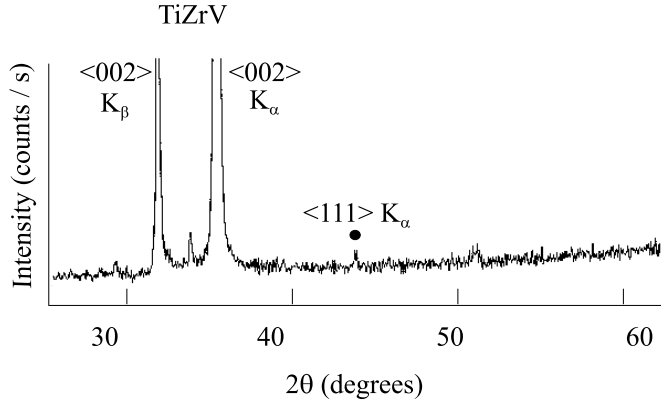


Fig. 5.1: XRD spectra of two TiZrV thin films measured with the same acquisition time. The intensity is indicated in linear scale. The broad peak of diffractogram *a* (Cu  $K_\alpha$  source) measured at  $2\Theta \approx 38^\circ$  for  $\text{Ti}_{19}\text{Zr}_{35}\text{V}_{46}$  is typical of the nanocrystalline structure. The sharp peaks in diffractogram *b* at  $2\Theta \approx 36^\circ$  (Cu  $K_\alpha$  and  $K_\beta$  source) correspond to the  $\langle 002 \rangle$  reflections of the well crystallised film of  $\text{Ti}_{10}\text{Zr}_{80}\text{V}_{10}$ . The peaks marked with • originate from the stainless steel substrate. The spectra are not smoothened.  $2\Theta$  varies from  $25^\circ$  to  $145^\circ$  with  $0.01^\circ$  steps and each step lasting for 3 s.

Under the assumption of a single homogeneous phase, the Scherrer equation is used to determine the average size  $\omega$  of the crystallites in a direction perpendicular to the surface of the specimen according to Eq. (4.2) [184],[185],[186]:

$$\omega = \frac{k \cdot \lambda}{\Delta_c(2\Theta) \cdot \cos \Theta} \quad ,$$

$\lambda$  is the wavelength of the source, i.e. 0.154 nm for copper  $K_\alpha$ .  $2\Theta$  is the position of the X-ray recorded peak, in radians.  $\Delta_c(2\Theta)$  is the contribution to the full width at half maximum due to small crystallite size, in radians;  $k$  is a constant named shape factor, which is related both

to the way in which  $\omega$  and  $\Delta_c(2\Theta)$  are defined and to the crystallite shape and structure [186], [187], [188], [189]. The Scherrer equation was first determined for the particular case of crystals of cubic crystalline structure and cubic geometric shape (for which  $k = 0.94$ ). However, the formula is now frequently used also to estimate the crystallite sizes of other structures. The constant  $k$  has been determined to vary between 0.89 and 1.42 [186]. It is usually taken as close to unity. Since the precision of crystallite size analysis by this method is, at best, about  $\pm 10\%$ , the assumption that  $k = 1.0$  is generally justified [186].

Table 5.1: Comparison of theoretical (predicted by Vegard's law) and experimental (estimated by Gaussian fitting with a standard deviation lower than  $0.04^\circ$ ) main diffraction peak  $2\Theta$  position for various Ti-Zr-V compositions. The  $d_{002}$  equivalent to the  $2\Theta$  evaluated by Vegard's law is calculated.

Sample reference number	Composition [atomic %]	$2\Theta[^\circ]$ calculated with Vegard's law	Calculated $d_{002}[\text{\AA}]$	$2\Theta[^\circ]$ experimental
22	Ti <sub>56</sub> Zr <sub>44</sub>	36.8	2.44	36.9
24	Ti <sub>18</sub> Zr <sub>82</sub>	35.5	2.53	35.5
26	Ti <sub>53</sub> V <sub>47</sub>	40.2	2.24	40.2
34	Ti <sub>30</sub> Zr <sub>19</sub> V <sub>51</sub>	39.6	2.27	39.4
42	Ti <sub>21</sub> Zr <sub>57</sub> V <sub>22</sub>	37.2	2.41	36.7
48	Ti <sub>38</sub> Zr <sub>31</sub> V <sub>31</sub>	38.5	2.34	37.5
70	Ti <sub>48</sub> Zr <sub>52</sub>	36.5	2.46	36.5

The total full width at half maximum  $\Delta(2\Theta)$  has three contributions:  $\Delta_i(2\Theta)$  is due to the instrument,  $\Delta_c(2\Theta)$  is due to the small crystallite size (when it is below 500 nm),  $\Delta_s(2\Theta)$  is due to the strain. As the peaks have a Gaussian profile, according to Ref. [185]:

$$\Delta_c(2\Theta) = \sqrt{\Delta^2(2\Theta) - \Delta_i^2(2\Theta)} - \Delta_s(2\Theta) . \quad (5.1)$$

The latter contribution  $\Delta_s$  increases rapidly with increasing  $\Theta$ ; it is negligible in our case since the only peak due to the thin film is always below  $\Theta = 20^\circ$  [185]. The experiment to evaluate the instrumental broadening was performed with bulk Al annealed for 24 hours at  $375^\circ\text{C}$ ;  $\Delta_i(2\Theta)$  has been evaluated to be  $0.05^\circ$  at  $2\Theta = 38.475^\circ$ . It comes out that:

$$\Delta_c(2\Theta) = \sqrt{\Delta^2(2\Theta) - 0.0025} . \quad (5.2)$$

Considering the precision of the full width at half maximum evaluation:

$$\Delta_c(2\Theta) \approx \Delta(2\Theta) . \quad (5.3)$$

In the present case, the measurements in non-symmetrical grazing angle configuration have led to the same diffraction patterns as the symmetrical  $\Theta - 2\Theta$  configuration. Consequently, the grains are considered as equiaxed so that  $\omega$  is the average size of the grains. Some values obtained are summarised in Table 5.2 [190].



Table 5.2: Average grain size ( $\omega$ ) evaluated with the Scherrer formula for various Ti-Zr-V compositions. The instrumental peak broadening has been neglected.

Samples reference number	Composition [atomic %]	$2\Theta[^\circ]$ calculated with Vegard's law	$2\Theta[^\circ]$ experimental	Average grain size $\omega$ [nm]
38	Ti <sub>19</sub> Zr <sub>40</sub> V <sub>41</sub>	38.52	38.0	< 5
42	Ti <sub>21</sub> Zr <sub>57</sub> V <sub>22</sub>	37.20	36.65	< 5
44	Ti <sub>29</sub> Zr <sub>28</sub> V <sub>43</sub>	39.00	37.90	< 5
40	Ti <sub>58</sub> Zr <sub>22</sub> V <sub>20</sub>	38.36	38.70	191
50	Ti <sub>10</sub> Zr <sub>11</sub> V <sub>79</sub>	40.98	41.40	169
65	Ti <sub>47</sub> Zr <sub>9</sub> V <sub>44</sub>	39.74	40.45	224

The samples can be separated into two classes according to their grain size: polycrystalline films, with crystallite size over 100 nm (Fig. 5.1 *b*), and nanocrystalline films with crystallite size below 5 nm (Fig. 5.1 *a*). In addition, two films did not reveal any diffraction peak within the sensitivity of the present measurements and appear to be amorphous at the resolution scale of the XRD. The XRD results are summarised on a Ti-Zr-V ternary diagram in Fig. 5.2, where the average grain size is represented as a function of the sample composition. It is also to be noticed that the described structures are homogeneous over the whole thickness of the as-deposited films. This can be deduced from grazing angle measurements (angles of incidence of  $0.4^\circ$  and  $3^\circ$ ) which exhibit full width at half maximum for the unique peak equal to that obtained in the  $\Theta - 2\Theta$  configuration.

Another interpretation of the diffraction line broadening could be that the films are composed of crystallites (which could be typically about 1  $\mu\text{m}$  in size), with different lattice spacings [191]. Peak broadening also occurs by elastic deformation of individual large grains (about 1  $\mu\text{m}$  in size) [191]. Microscopic investigations confirm that the broadening of the diffraction peak is due to the small grain size. Scanning Tunnelling Microscopy (STM) of an as-deposited Ti<sub>21</sub>Zr<sub>57</sub>V<sub>22</sub> coating on silicon shows a surface made of grains with an average size of about 4 nm (Fig. 5.3). Transmission Electron Microscopy (TEM) of an as-deposited Ti<sub>28</sub>Zr<sub>25</sub>V<sub>47</sub> film stripped off from its glass substrate allows one to distinguish some grains with an average size of 2 nm (Fig. 5.4 *a*, *b*). In both analyses, the getter thin films are heated *in situ* (in vacuum) up to more than 300 °C for some hours and no structural changes are observed. The grain sizes measured by XRD (crystalline planes parallel to the surface, see Fig. 5.1 *a*) are in agreement with those observed by TEM (crystalline planes perpendicular to the surface, see Fig. 5.4 *a*), so that the grains are isotropic.

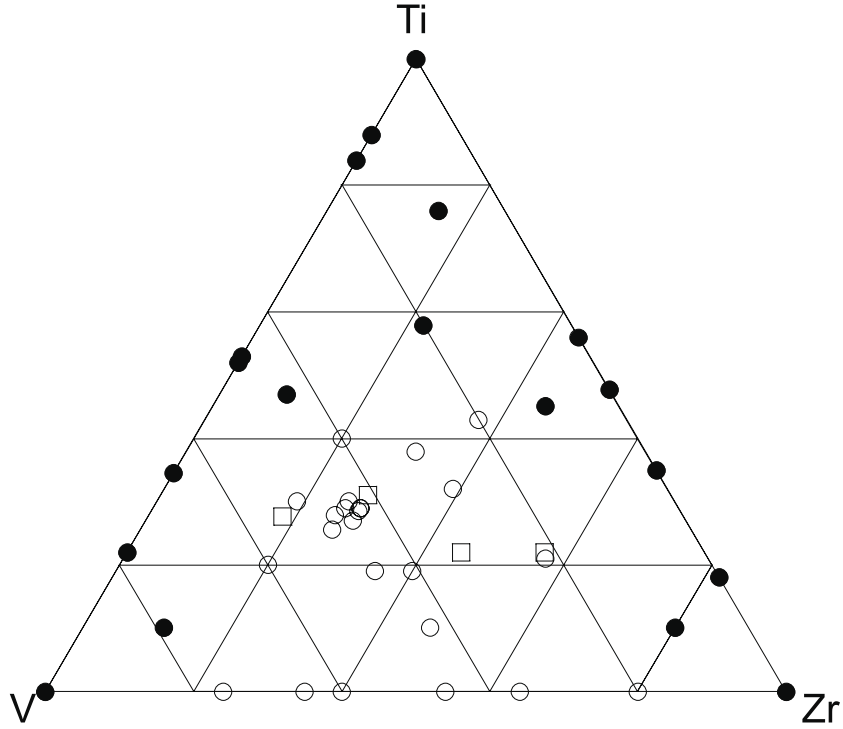


Fig. 5.2: Structure composition map of TiZrV films based on the crystal average grain size. The black symbols represent the samples with grains larger than 100 nm, and the open ones represent samples with a grain size below 5 nm. The circles correspond to stainless steel substrates and the squares to copper.

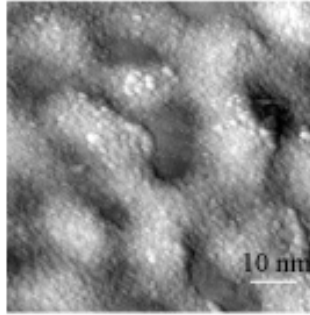


Fig. 5.3: Scanning Tunneling Microscopy (STM) image of the surface of an as-deposited  $\text{Ti}_{21}\text{Zr}_{57}\text{V}_{22}$  coating on silicon. The scanned surface measures  $100 \text{ nm} \times 100 \text{ nm}$ . The grains on the surface have an average size of about 4 nm. Courtesy of R. Sanjinès from EPFL.

EDX measurements were performed in a Transmission Electron Microscope on sample n° 216. Sequences were realised on a fixed location of the film with an increasing probe diameter from 10 nm to 480 nm and with a fixed probe diameter of 10 nm on different locations of the film. The analysed depth is the film thickness, which is of the order of 20 nm. The evaluated thin film composition is 26.6 atomic % of Ti, 49.7 atomic % of Zr, 23.6 atomic % of V with standard deviation of 0.4, 0.7, 0.5 respectively. The composition homogeneity does not exclude the possibility that the system is constituted by a single phase.

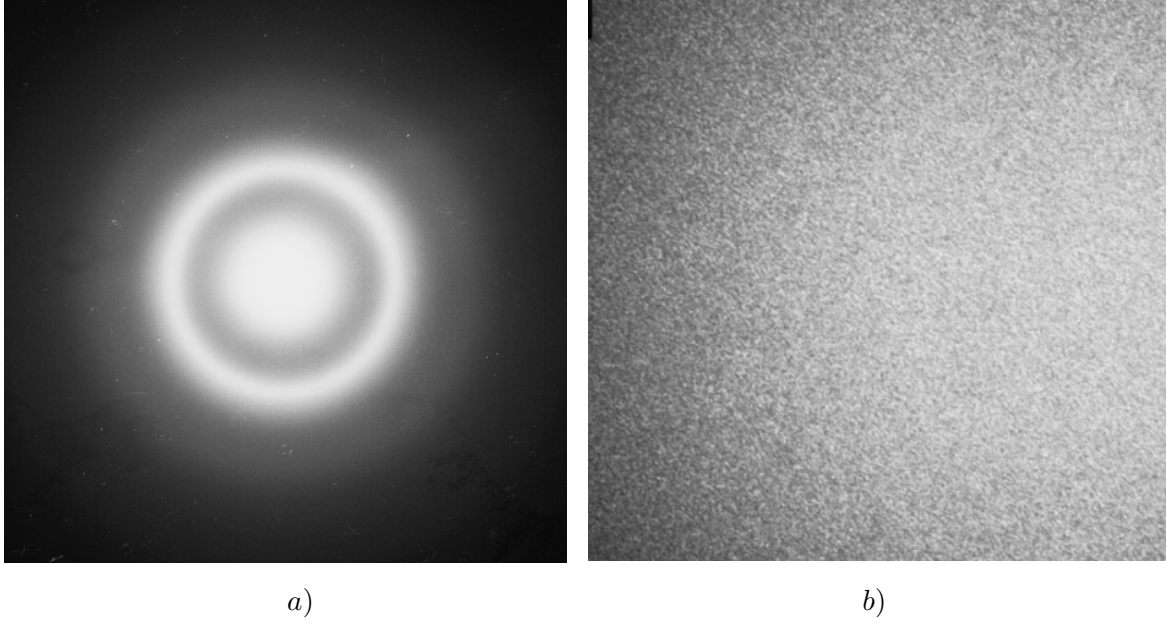


Fig. 5.4: Transmission Electron Microscopy (TEM) of an as-deposited  $\text{Ti}_{28}\text{Zr}_{25}\text{V}_{47}$  film stripped off from its glass substrate. *a* shows a diffraction pattern in which the small size of the grains induces relaxation of the conditions of diffraction causing the enlargement of the diffraction spots (form effect). *b* exhibits a dark field image made for grains in diffraction conditions on one of the diffraction rings of graph *a*; those grains represent a small fraction of the grains on the trajectory of the beam and they appear as white spots on black background. The image width is 270 nm. Grains can be distinguished, excluding that the film could be amorphous. The direct image is not shown because the large quantity of grains along the beam makes it difficult to interpret.

### 5.1.2 Activation temperature

- Surface analysis

The surface of the NEG samples was analysed by AES, first in the as-received state (typically after less than 15 minutes air exposure) and then after *in situ* heating for 1 hour at a given temperature. An example of direct and derivative Auger spectra is given in Fig. 4.3 and Fig. 4.4 respectively, for a 1  $\mu\text{m}$ -thick film coating deposited on stainless steel, with an in-depth composition of  $\text{Ti}_{24}\text{Zr}_{54}\text{V}_{22}$  (atomic) as determined by EDX. These AES spectra are a representative example showing the surface composition variation of a TiZrV film during the activation process. On the as-received TiZrV surface, the detected elements are Zr, V and Ti together with C and O. During the vacuum heat treatment, chlorine appears, the C-KLL and Zr-MNV peak shapes are significantly modified, while the oxygen signal vanishes almost entirely. No trace of elements belonging to the substrate was detected, suggesting that the film is free of large uncoated areas. A similar trend is observed also in the AES signals of the St707 bulk getter (from SAES-Getters, Milan, Italy) but at higher temperatures [192] (idem by XPS [193]).

The intensity of the oxygen line at 512 eV exhibits a progressive decrease while heating up

to 300 °C, as expected for a reduction of the surface oxide. Therefore, the degree of activation of different NEG samples can be assessed from the evolution of the O-KLL peak intensity with heating temperature. The apparent residual intensity of the O-KLL line remaining after heating at 300 °C is partly due to the contribution of V, whose  $L_3M_{45}M_{45}$  line overlaps with the O-KLL peak. In Fig. 5.5 it can be seen that NEG films with different composition show different kinetics of the reduction of the surface oxide. Materials with a low activation temperature can be clearly distinguished from materials with a higher activation temperature.

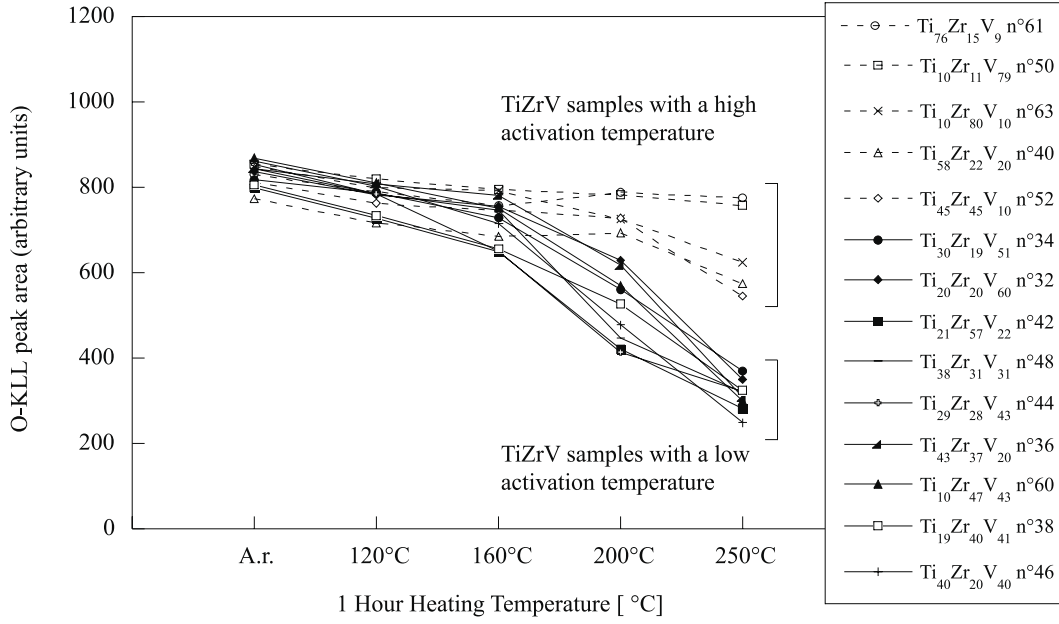


Fig. 5.5: O-KLL peak-area evolution on TiZrV NEG thin film coatings of various composition as a function of heating temperature. Two groups of NEG samples exhibiting different activation temperatures can be clearly distinguished from the slope with which the oxygen peak intensity decreases in the temperature intervals 160–200 °C and 200–250 °C.

It is to be noted that the degree of activation of NEG samples depends on both the heating time and heating temperature. Consequently, the degree of activation can also be assessed from the O-KLL intensity evolution with heating time at a fixed temperature. This is illustrated in Fig. 5.6, where the O-KLL peak intensity variation as a function of the square root of time ( $\sqrt{t}$ ) for several TiZrV samples is given for different constant temperatures. For samples that reach activation at the lowest heating temperatures, the reduction by half of the O-KLL signal requires 1 hour heating at 200 °C or 1 day at 170 °C.

After heating at 200 °C for 1 hour, the carbon line C-KLL at 272 eV changes its shape (Fig. 4.3) as a result of the modification of the chemical state of carbon from graphite or adsorbed hydrocarbons into carbide [194], [195]. The carbon concentration is obtained from the peak area of the C-KLL peak in the  $EN(E)$  spectra; the measurement of the peak-to-

peak height of the C-KLL line on the derivative spectra resulted in an important overestimate of the C concentration when the adsorbed hydrocarbons are transformed into carbide. For most samples, the evolution of the C-KLL peak-area shows that the carbon concentration already increases after heating at 120 °C for 1 hour with respect to the value for the as-received sample and starts to decrease above 250 °C only. However, by changing the heater assembly and the mounting of the samples (Fig. 4.5), it was observed that the strong carbon concentration increase after 1 hour heating at 120 °C does not occur anymore, as shown in Fig. 4.3. It was determined that some carbon contamination is trapped between samples and mask after the sample mounting in air. Consequently, the C-KLL peak variations are an instrumental artefact [192]. Then, modifications of carbon concentration cannot be exploited to monitor the NEG activation.

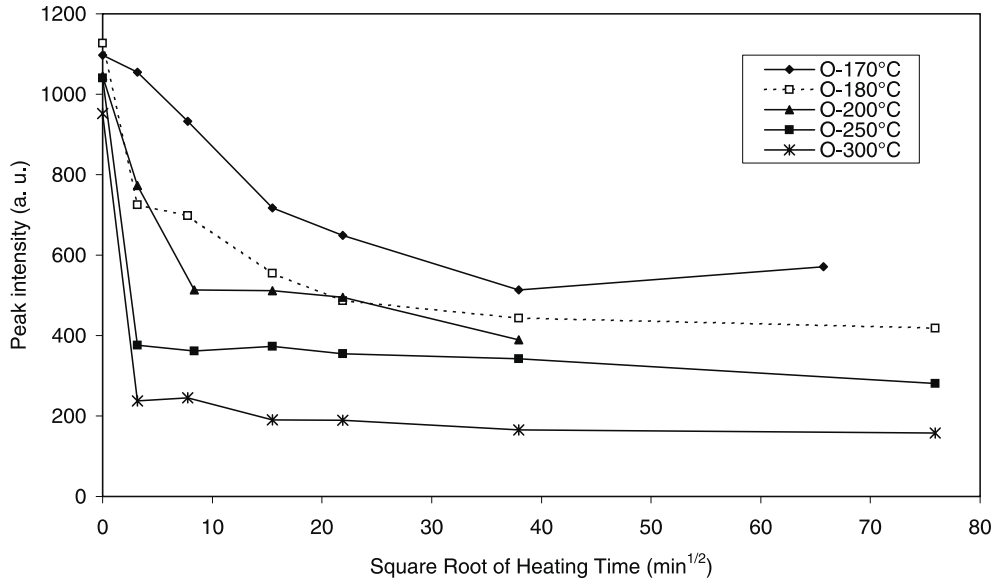


Fig. 5.6: O-KLL peak intensity variation as a function of the square root of time for TiZrV samples measured by AES at different constant temperatures. The sample heated at 170 °C is  $\text{Ti}_{43}\text{Zr}_{37}\text{V}_{20}$ , 180 °C is  $\text{Zr}_{53}\text{V}_{47}$ , 200 °C is  $\text{Ti}_{20}\text{Zr}_{20}\text{V}_{60}$ , 250 °C is  $\text{Ti}_{29}\text{Zr}_{28}\text{V}_{43}$ , and 300 °C is  $\text{Ti}_{21}\text{Zr}_{57}\text{V}_{22}$ : these sample compositions belong to the zone corresponding to activation at the lowest temperatures (Fig. 5.8) so that the result of their activation process is comparable.

A chlorine peak (Cl-LMM at 181 eV) appears at 200 °C and its intensity increases continuously upon heating. This element is known to segregate to the surface of refractory metals like titanium [196]. The Cl-LMM intensity variation as a function of heating time at constant temperature was also measured. It turns out that the Cl-LMM intensity increases with heating temperature and time. At temperatures up to 250 °C the Cl-LMM intensity shows an approximately linear increase with the square root of the heating time ( $\sqrt{t}$ ), as expected for surface segregation of impurities controlled by bulk diffusion. At 300 °C the Cl-LMM intensity strongly deviates from the  $\sqrt{t}$  dependency: it increases slower than if it was following ( $\sqrt{t}$ ) evolution [192].

In the present study, Cl has been detected on every heated NEG sample. The lower the activation temperature the lower the temperature at which Cl segregation occurs on the NEG surface. On the St707 strips from SAES-Getters (Milan, Italy) made of  $\text{Zr}_{70}\text{V}_{24.6}\text{Fe}_{5.4}$  (weight), Cl appears on the surface after 1 hour heating at 300 °C [192].

In addition to the oxygen peak decrease, the oxide reduction is also indicated by the variation of the peak shape of the metallic elements. In particular, Tomita *et al.* [197] found that the shape of the Zr-MNV peak correlates with the amount of oxygen adsorbed onto the surface of Zr. The variations of the Zr-MNV peak shape during the NEG activation process are resolved by the Auger electron spectrometer used; the variations clearly appear in the derivative spectra (Fig. 4.4). The Zr-MNV Auger peak component at 141 eV is typical for Zr in  $\text{ZrO}_2$  [198]. During the  $\text{ZrO}_2$  reduction, the peak component at 147 eV (attributed to Zr metal) increases with respect to the 141 eV component (Fig. 5.7). On the  $\text{Ti}_{24}\text{Zr}_{54}\text{V}_{22}$  NEG thin-film example, strong Zr-MNV peak shape variations already occur after 1 hour heating at 160 °C.  $R$  is defined as the ratio of the peak-to-valley height of the Zr component at 147 eV to the peak-to-valley height of the Zr component at 141 eV. This quantity  $R$  was used to characterise the activation behaviour of TiZrV films of different composition. In other words, a high  $R$  value indicates a high degree of activation. Moreover, the calculation of  $R$  requires neither previous calibration, nor normalisation, nor background subtraction. The  $R$  activation criterion is applied to each sample, for each temperature of the thermal treatment. The largest difference between the various samples is found at 200 °C. At higher temperatures (250 °C heating for 1 hour) most of the samples are already almost completely metallic and at lower temperature (160 °C heating for 1 hour) most of them just start to be reduced so that no distinction is possible. In Fig. 5.8, the AES results for all samples at 200 °C are shown on a ternary diagram as a function of their composition, using a threshold  $R$  value of 0.5. The samples are separated into two groups, i.e. those which exhibited an  $R$  value above a threshold (open symbols) and the others (filled symbols). Samples which do not contain Zr are also included in Fig. 5.8. Their state of oxidation is estimated from the evolution of the oxygen intensity in comparison with that measured for samples containing zirconium. They all unambiguously belong to the category of samples which have not started to activate at 200 °C. All the samples corresponding to activation at the lowest temperatures have compositions belonging to the same zone of the diagram. Figure 5.8 can be considered as a quality map for TiZrV coatings of different composition with respect to the chosen criterion.

A similar quality criterion could be obtained by exploiting the splitting between the metal and oxide Auger peak of Ti-LMV [199]. However, because of the high kinetic energy of the Ti-LMV electrons the two peaks cannot be resolved with the energy analyser used for the present study. Similarly, the energy shift between metal and oxide LMV transition of V is narrower than the resolution of the analyser at the corresponding kinetic energy [200].

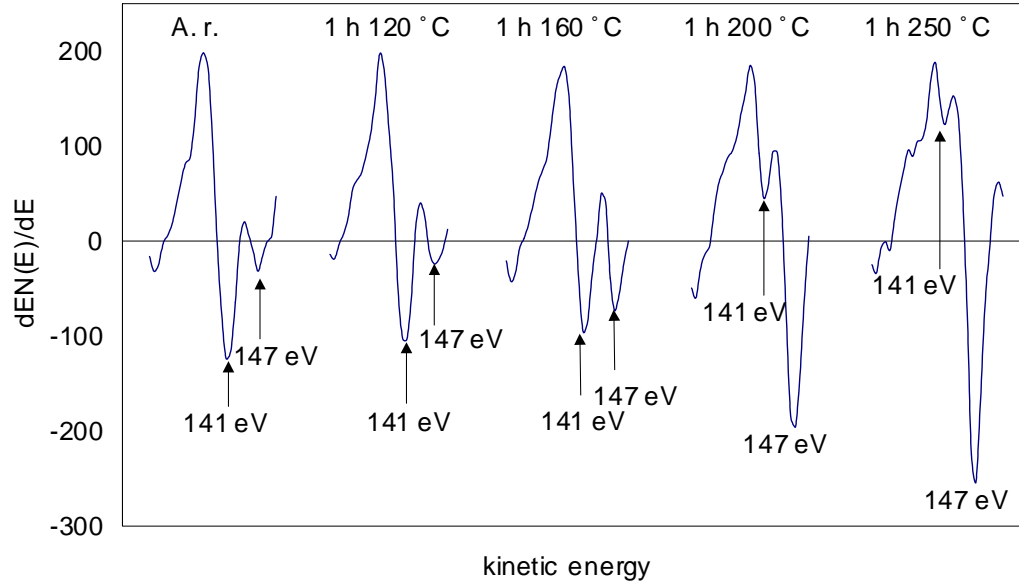


Fig. 5.7: Zr-M<sub>4,5</sub>N<sub>2,3</sub>N<sub>4,5</sub> line shape changes as a function of heating temperature of the Ti<sub>24</sub>Zr<sub>54</sub>V<sub>22</sub> (atomic) thin film, which survey spectra are shown in Fig. 4.4. With increasing heating temperature the peak component at 147 eV increases with respect to the one at 141 eV, indicating the progressive reduction of ZrO<sub>2</sub>.

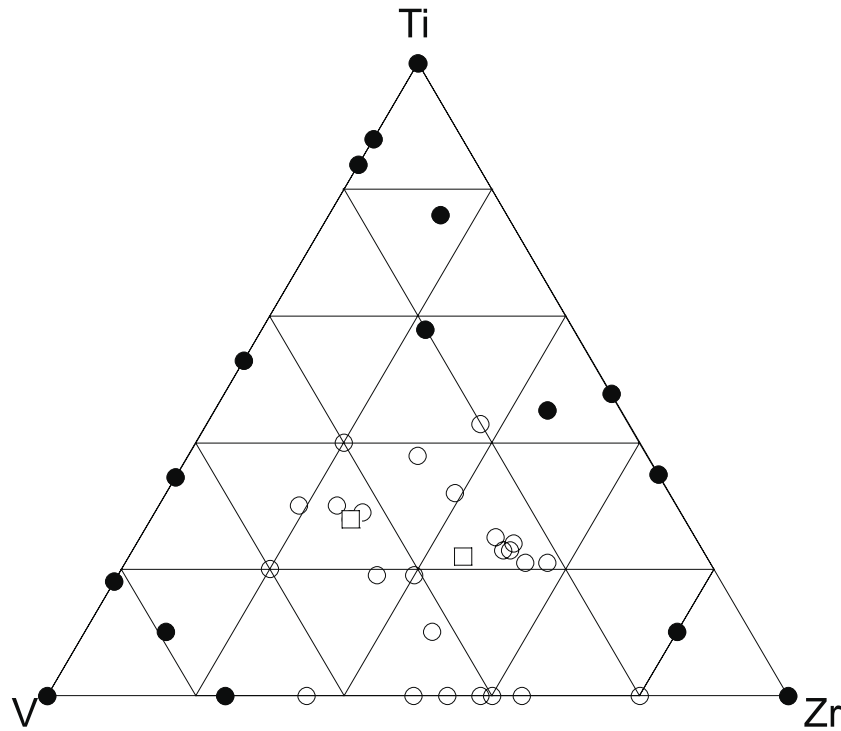


Fig. 5.8: Quality-composition map of TiZrV films based on the “*R* criterion” as a function of the in-depth elemental composition measured by EDX. The samples with *R* > 0.5 after 200 °C heating for 1 hour are indicated by empty symbols and the others by black symbols. The circles correspond to stainless steel substrates and the squares to copper.

- Pumping speed results

Pumping speed measurements for CO and H<sub>2</sub> as a function of the heating temperature were performed for samples of five different TiZrV compositions. The heating cycle is described in paragraph 4.3.4. The samples are deposited with sputtering system *B*, at a sputtering rate of about 0.1 nm s<sup>-1</sup>, on copper substrates chemically smoothened. The composition of the coatings is reported in Table 5.3 and their position in the TiZrV ternary diagram is shown in Fig. 5.9. They all belong to the zone corresponding to activation at the lowest temperatures (Fig. 5.8). The description of the samples is given in Appendix 9.1.

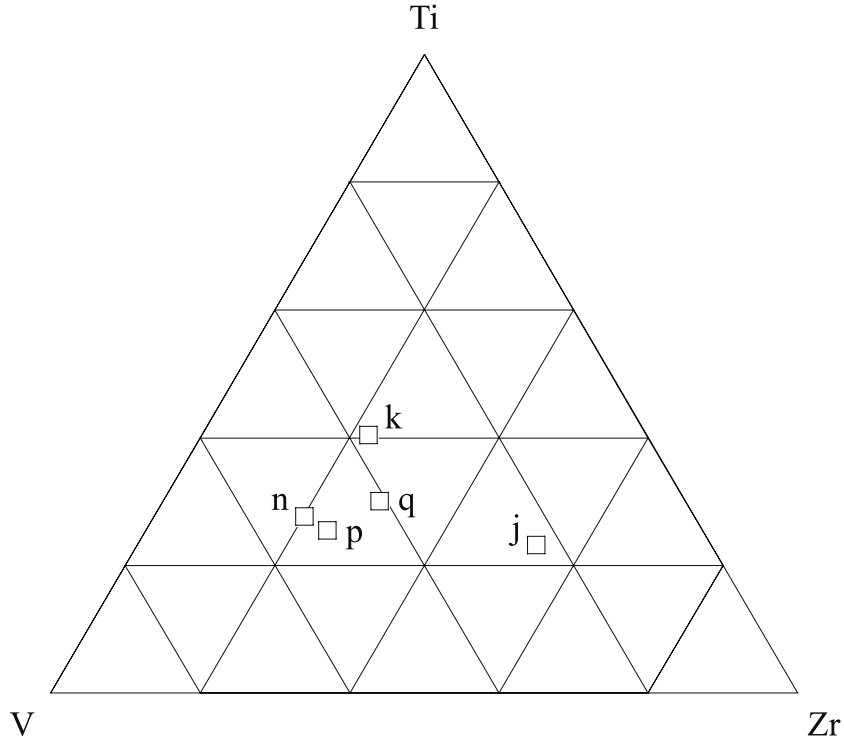


Fig. 5.9: The composition of five samples deposited for pumping speed measurements is indicated in the TiZrV ternary diagram. The films are deposited on copper substrates.

Remember (see paragraphs 1.2 and 4.3.4) that the pumping speed per unit area  $S$  is linked to the sticking probability  $\alpha$  by Eq. (1.2):

$$S = \alpha C \text{ [}\ell \text{ s}^{-1} \text{ cm}^{-2}\text{]}$$

The conductance  $C$  is calculated as expressed in Eq. (1.3):

$$C = 3.64 \sqrt{\frac{T}{M}} \text{ [}\ell \text{ s}^{-1} \text{ cm}^{-2}\text{]}$$

where  $T$  is the absolute temperature in Kelvin and  $M$  the molecular weight. At the temperature of measurement, which is room temperature,  $C_{H_2} = 44.18 \ell \text{ s}^{-1} \text{ cm}^{-2}$  and  $C_{CO} = C_{N_2} = 11.70 \ell \text{ s}^{-1} \text{ cm}^{-2}$ .



Table 5.3: Maximum values of the sticking probabilities (and related activation temperatures) for H<sub>2</sub> and for CO of five samples of different composition.

Samples reference	j	k	n	p	q
Composition (EDX) [atomic %]	Ti <sub>24</sub> Zr <sub>53</sub> V <sub>23</sub>	Ti <sub>41</sub> Zr <sub>22</sub> V <sub>37</sub>	Ti <sub>28</sub> Zr <sub>20</sub> V <sub>52</sub>	Ti <sub>26</sub> Zr <sub>24</sub> V <sub>50</sub>	Ti <sub>30</sub> Zr <sub>29</sub> V <sub>41</sub>
Maximum sticking probability for H <sub>2</sub>	$7.3 \times 10^{-3}$	$9.7 \times 10^{-3}$	$6.8 \times 10^{-3}$	$6.4 \times 10^{-3}$	$1.5 \times 10^{-2}$
$T$ [°C] of the maximum pumping for H <sub>2</sub>	297	280	317	199	319
Maximum sticking probability for CO	0.59	0.69	0.60	0.52	0.55
$T$ [°C] of the maximum pumping for CO	242	260	317	249	250

The effect of increasing temperature on the CO sticking probability ( $\alpha_{CO}$ ) is similar for all the disks (See Fig. 5.10). The onset of the CO pumping speed is between 150 °C and 180 °C and a large increase is observed between 180 °C and 200 °C up to the maximum value reached after 2 hours heating at about 250 °C. The value of the maximum sticking probability ranges between 0.5 and 0.7. Heating at temperatures higher than 250 °C results in a slight decrease of the CO pumping speed. Compared to the other disks, sample n shows a lower CO pumping speed up to 275 °C and reaches the maximum above 300 °C. It is to be noted that sample n composition is at the limit of the zone corresponding to activation at the lowest temperatures (see Fig. 5.8).

The evolution of the H<sub>2</sub> sticking probability ( $\alpha_{H_2}$ ) as a function of the heating temperature is shown in Fig. 5.11. An H<sub>2</sub> sticking probability higher than the detection limit is always obtained after a 2-hour heating at a temperature between 150 °C and 200 °C. The maximum H<sub>2</sub> sticking probability as well as the temperature at which it is attained depend on the NEG composition (see Table 5.3). Among the tested compositions, the three films reaching the highest H<sub>2</sub> sticking probability after 2 hours heating at 200 °C ( $\alpha_{H_2} = 6 \times 10^{-3}$ ) are those which correspond to samples n, p and q. For the latter, a value of  $\alpha_{H_2}$  as high as 0.015 is reached, but only after heating at 325 °C for 2 hours.

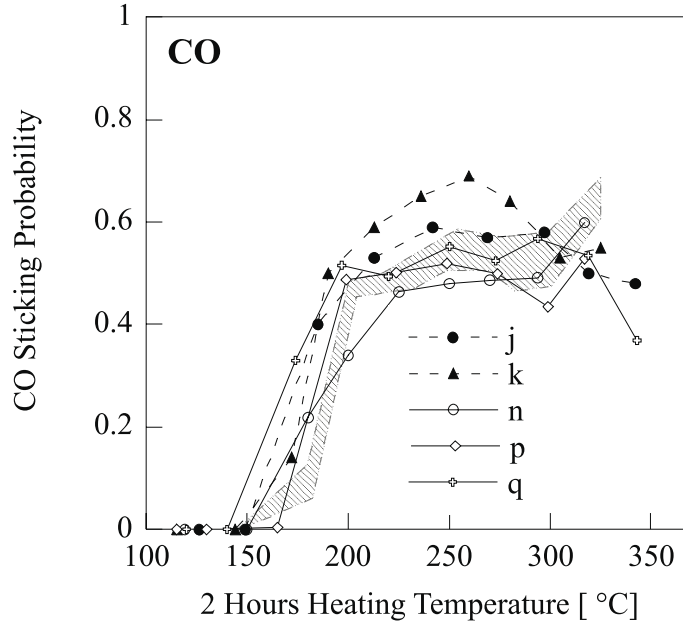


Fig. 5.10: CO sticking probability ( $\alpha_{CO}$ ) as a function of the heating temperature for five TiZrV compositions. The NEG thin films are deposited in sputtering system *B* on smooth copper. The typical spreading of results for identical disks is indicated by a hatched band. The spreading is reported from Fig. 4.7 *a*.

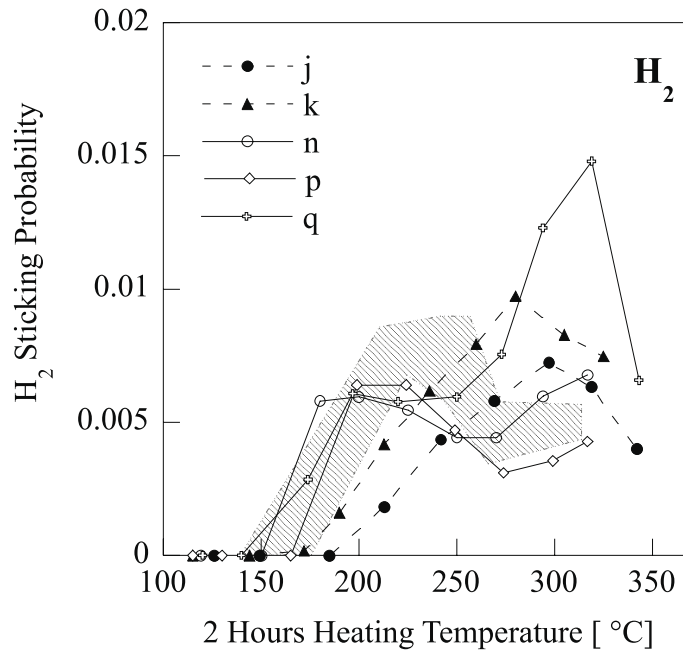


Fig. 5.11: H<sub>2</sub> sticking probability ( $\alpha_{H_2}$ ) as a function of the heating temperature for the same samples as in Fig. 5.10. The typical spreading of results for identical disks is indicated by a hatched band. The spreading is reported from Fig. 4.7 *b*.

## 5.2 Influence of the substrate

### 5.2.1 Material of the substrate

Stainless steel 316LN, copper and aluminium are the usual construction materials for vacuum chambers. The first chambers of the experimental zone in TAS (see Glossary in Chapter 8) at CERN are made of Glidcop<sup>®</sup> (copper strengthened by alumina  $\text{Al}_2\text{O}_3$  particles made by an internal oxidation technique; registered trademark SCM Metal Products, Inc). The Front End injector for the Spallation Neutron Source at the Lawrence Berkeley National Laboratory is made of a combination of Glidcop<sup>®</sup> with oxygen-free copper [201]. The central beam pipe of the LHC detectors is in beryllium, as some vacuum pipes in PEP-II of the Stanford Linear Accelerator Center [202]. The baseline for the CMS experiment is a 4.5 m long beryllium chamber [203], [204]. Be-Al has been proposed for use for the 12 m long baseline of the LHCb experiment [203], [204]. It is then of practical interest to study the effects induced by the material of the substrate on the morphology, the crystallinity, and the activation process of TiZrV coatings. NEG thin films deposited with the same sputtering parameters on several of the following substrates were compared: stainless steel 316LN, copper (rough, smooth or electrolytically deposited), Glidcop<sup>®</sup>, aluminium, beryllium, glass, and Be-Al. The type of characterisation performed on the NEG coatings according to the substrate material are summarised in Table 5.4.

Table 5.4: Summary of the characterisation performed on the NEG coatings according to the substrate material.

Substrate material	Morphology	Crystal structure	Activation temperature
Glass	X		
Stainless steel	X	X	X
Copper	X	X	X
Aluminium	X		
Glidcop <sup>®</sup>	X	X	X
Beryllium	X		
Al-Be		X	X

- Influence on the film morphology

The influence of the substrate material on the morphology of TiZrV thin films was tested for stainless steel 316LN, smooth copper, Glidcop<sup>®</sup>, glass, aluminium and beryllium substrates. SEM micrographs of the coatings on these substrates are shown in Fig. 5.12. It is observed that the films are all smooth except for those deposited on beryllium and aluminium, which appear with coarse grains.

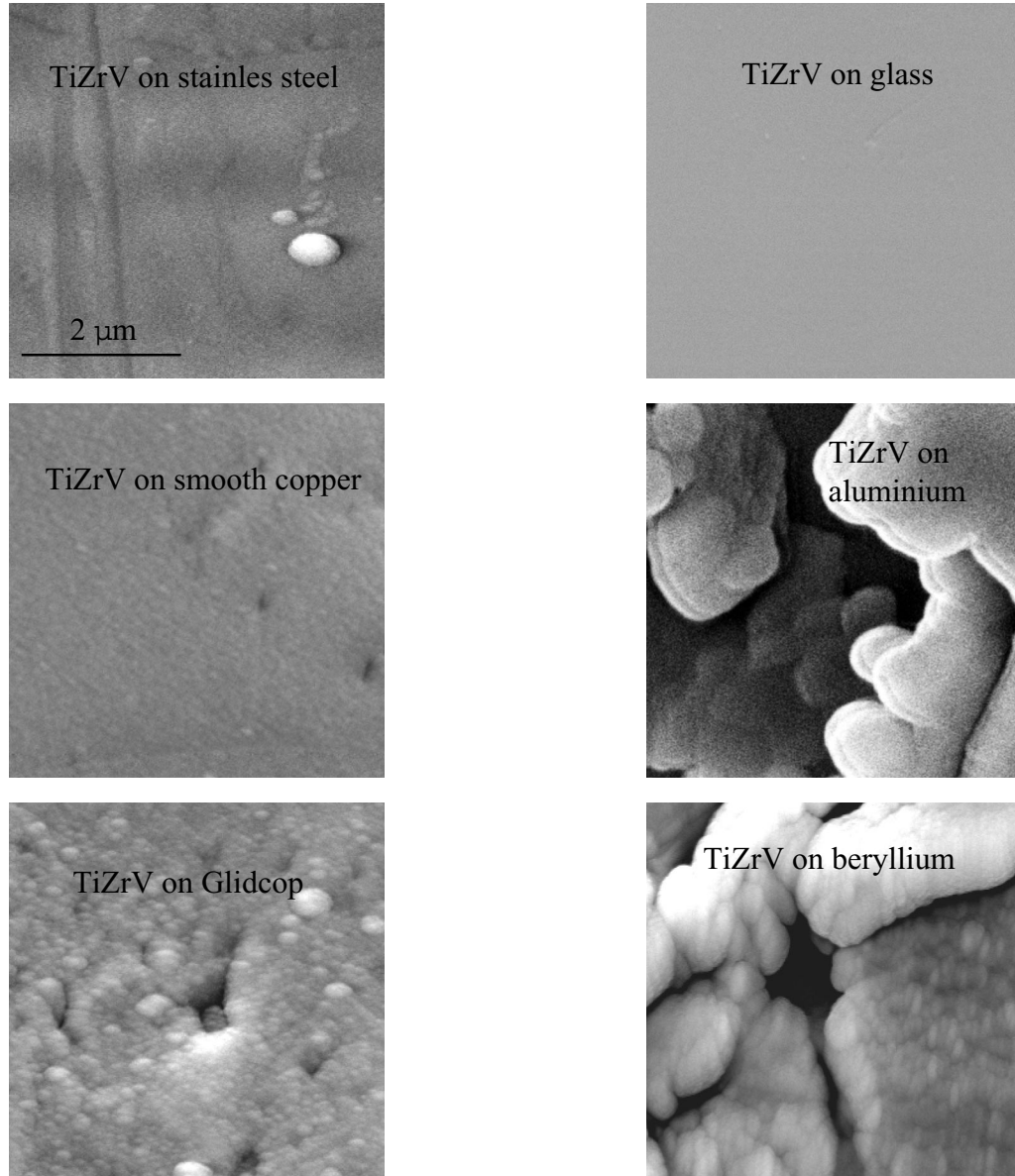


Fig. 5.12: Micrographs obtained by SEM of TiZrV thin films deposited on different substrates: stainless steel 316LN, smooth copper, Glidcop<sup>®</sup>, glass, aluminium, and beryllium. The indicated scale is the same for the six micrographs.

- Influence on the film crystallinity

A set of  $\text{Ti}_{30}\text{Zr}_{15}\text{V}_{55}$  thin films deposited simultaneously in sputtering system *A*, at the substrate temperature  $T_s = 100\text{ }^{\circ}\text{C}$ , on stainless steel 316LN, copper (rough, smooth or electrolytically deposited), Glidcop<sup>®</sup> and Be-Al was characterised by XRD. The measured X-ray diffraction patterns are similar and so no difference of crystallinity can be detected<sup>1</sup> (Fig. 5.13). Some of these results have already been included in Fig. 5.2, which is a structure composition map of TiZrV films based on the crystal grain size. As already described, the

<sup>1</sup>This result holds for films deposited by both diode and magnetron sputtering.

black symbols represent the samples with grains larger than 100 nm, and the empty ones represent samples with a grain size below 5 nm. The circles correspond to stainless steel substrates and the squares to copper.

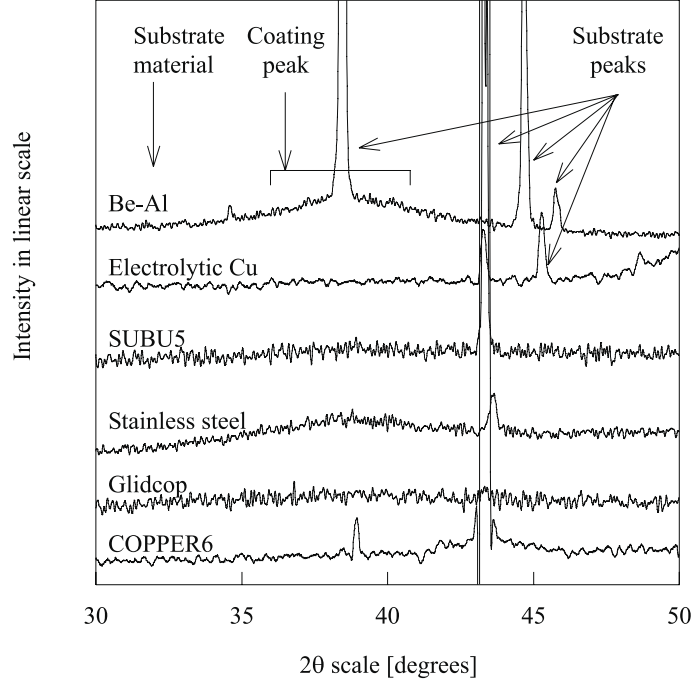


Fig. 5.13: XRD diffractograms for a set of  $\text{Ti}_{30}\text{Zr}_{15}\text{V}_{55}$  thin films deposited on different substrate materials.

- Influence on the activation temperature  $T_a$

The activation process of identical  $\text{TiZrV}$  films deposited on copper and stainless steel substrates was analysed by AES. Similar results have been obtained, independently of the substrate material. Some results have already been included in Fig. 5.8, which is a quality-composition map of  $\text{TiZrV}$  films based on the “ $R$  criterion” as a function of the in-depth elemental composition. As already described, the samples with  $R > 0.5$  after 200 °C heating for 1 hour are indicated by empty symbols and the others by black symbols. The dots correspond to stainless steel substrates and the squares to copper.

The crystallinity of a set of  $\text{Ti}_{30}\text{Zr}_{15}\text{V}_{55}$  thin films was described above. The same samples were also characterised by XPS. The evolution of the O 1s peak intensity is represented as a function of heating temperature in Fig. 5.14. Considering the accuracy of the evaluation of the O 1s peak intensity, it is concluded that the measurements reported are equivalent, especially as the main indication of the activation is the slope of the curve in a given interval of temperatures.

In summary, no effect on the activation process of a  $\text{TiZrV}$  thin film due to the material of the substrate can be detected either by AES or by XPS.

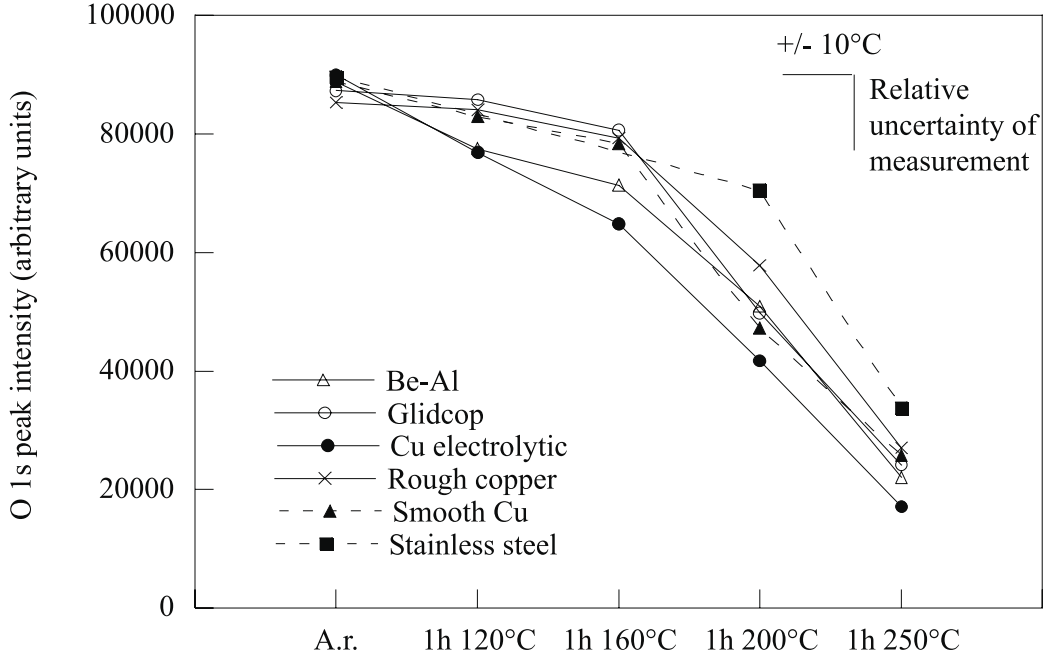


Fig. 5.14: Comparison of the evolution of the O 1s peak intensity as a function of the heating temperature for  $\text{Ti}_{30}\text{Zr}_{15}\text{V}_{55}$  (atomic) coatings on various substrates. All samples are deposited simultaneously in the sputtering system A at the substrate temperature  $T_s = 100^\circ\text{C}$ .

### 5.2.2 Substrate roughness

- Influence on the film morphology

Laser dynamic focusing was applied to measure the roughness of chemically attacked and smoothened copper substrates coated or not coated. The preparation of smooth copper substrates with SUBU5 and of rough copper substrates by chemical attack with COPPER6 is described in paragraph 3.2.1. SEM micrographs of the surface of smooth and rough copper substrates are given in Fig. 3.5 and Fig. 3.6, respectively. The results of laser dynamic focusing measurements are summarised in Fig. 5.15. The samples are described in Appendix 9.1. The average roughness, as defined in paragraph 4.2.4, is measured over a distance  $\ell_m$  of 5.60 mm for all the samples. The result is  $R_a = 0.16 \mu\text{m}$  and  $R_t = 1.46 \mu\text{m}$  for thin films on smooth copper substrates. The values are more than three times higher for thin films on rough copper ( $R_a = 0.53 \mu\text{m}$  and  $R_t = 4.48 \mu\text{m}$ ). By XRD, using the  $\Theta - 2\Theta$  configuration, no difference of crystallinity is observed for thin films on rough or on smooth copper substrates.

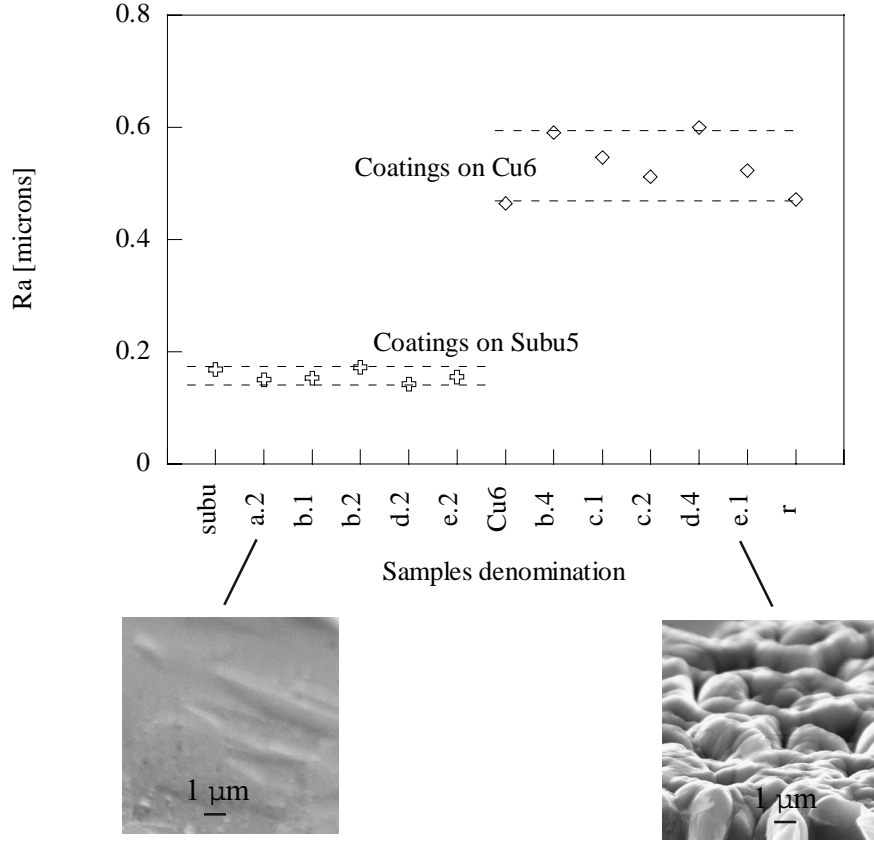


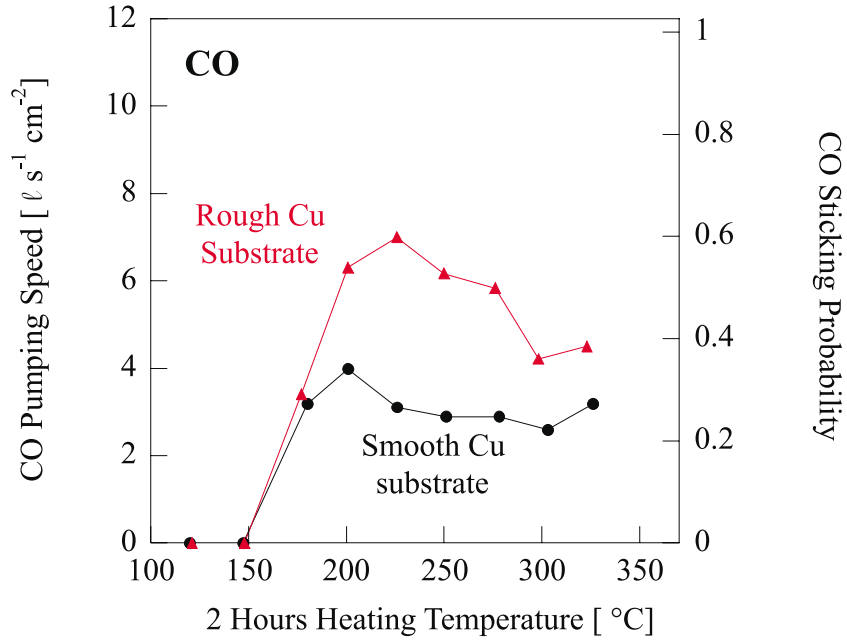
Fig. 5.15: Roughness of several TiZrV coatings on copper substrates compared to the roughness of the substrates. SEM micrographs of thin films on rough and smooth copper substrates.

- Influence on pumping speed

The roughness of a substrate influences the pumping characteristics of the coating. As an example, the pumping characteristics of two samples made of a  $\text{Ti}_{30}\text{Zr}_{15}\text{V}_{55}$  thin film deposited simultaneously on rough and smooth copper substrates are compared. The sticking probability of CO and  $\text{H}_2$  as a function of heating temperature is given in Fig. 5.16 for both samples. The heating cycle is described in paragraph 4.3.4. CO pumping speed as a function of  $Q_{\text{CO}}$ , the quantity of the same gas adsorbed on the NEG coating at room temperature, after 2 hours heating at 325 °C, is shown in Fig. 5.17 for both samples. The onset for the pumping of CO appears after 2 hours heating at 180 °C for both samples: a sticking probability  $\alpha_{\text{CO}}$  of 0.28 is then reached (Fig. 5.16 a). Then, for the NEG deposited on smooth copper, the value remains stable up to the last heating step at 325 °C. The evolution of the sticking probability of CO is different for the NEG deposited on rough copper:  $\alpha_{\text{CO}}$  reaches a maximum of 0.60 after 2 hours heating at 225 °C and progressively decreases by 30% when progressively increasing the heating temperature to 325 °C. The sticking probability of  $\text{H}_2$ ,  $\alpha_{\text{H}_2}$ , (Fig. 5.16 b) evolves in a similar way for both samples, with a pumping onset after 2 hours heating at 180 °C and a maximum sticking probability reached after 2 hours heating at 200 °C. The difference is that the sticking probability is much higher in the case of the

film deposited on a rough copper substrate (for instance 9 times higher for the heating step at 200 °C).

a)



b)

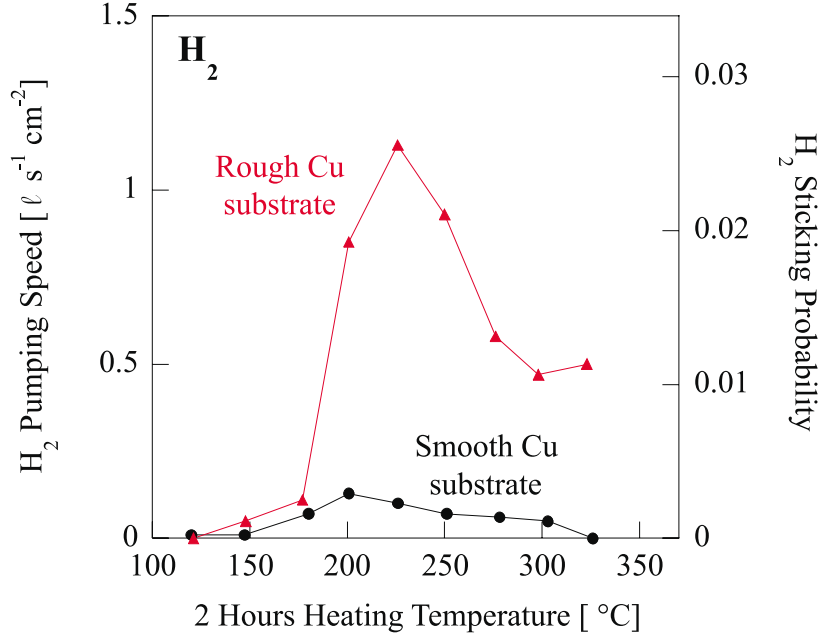


Fig. 5.16: Comparison of the sticking probability of CO,  $\alpha_{\text{CO}}$ , (a) as a function of the heating temperature for identical NEG thin films deposited on rough and smooth copper substrates. Idem for the sticking probability of  $\text{H}_2$ ,  $\alpha_{\text{H}_2}$  (b). (Substrate temperature:  $T_s = 150^{\circ}\text{C}$ ).

It is interesting to observe that the two sets of samples are very different also with respect



to the surface capacity for CO (see Fig. 5.17). When pumping CO, the pumping speed  $S_{CO}$  progressively decreases when the surface gets progressively covered and  $S_{CO}$  approaches zero when the surface is saturated:  $Q_{CO}$  is then the total number of molecules which may be chemisorbed on the getter surface (surface pumping capacity). Both saturation curves have the same aspect, except that the surface pumping capacity for CO is six times higher for the NEG deposited on a rough copper substrate than on a smooth one.

Therefore, it can be concluded that an increased surface roughness does not accelerate the activation process, but clearly increases pumping speed and surface pumping capacity.

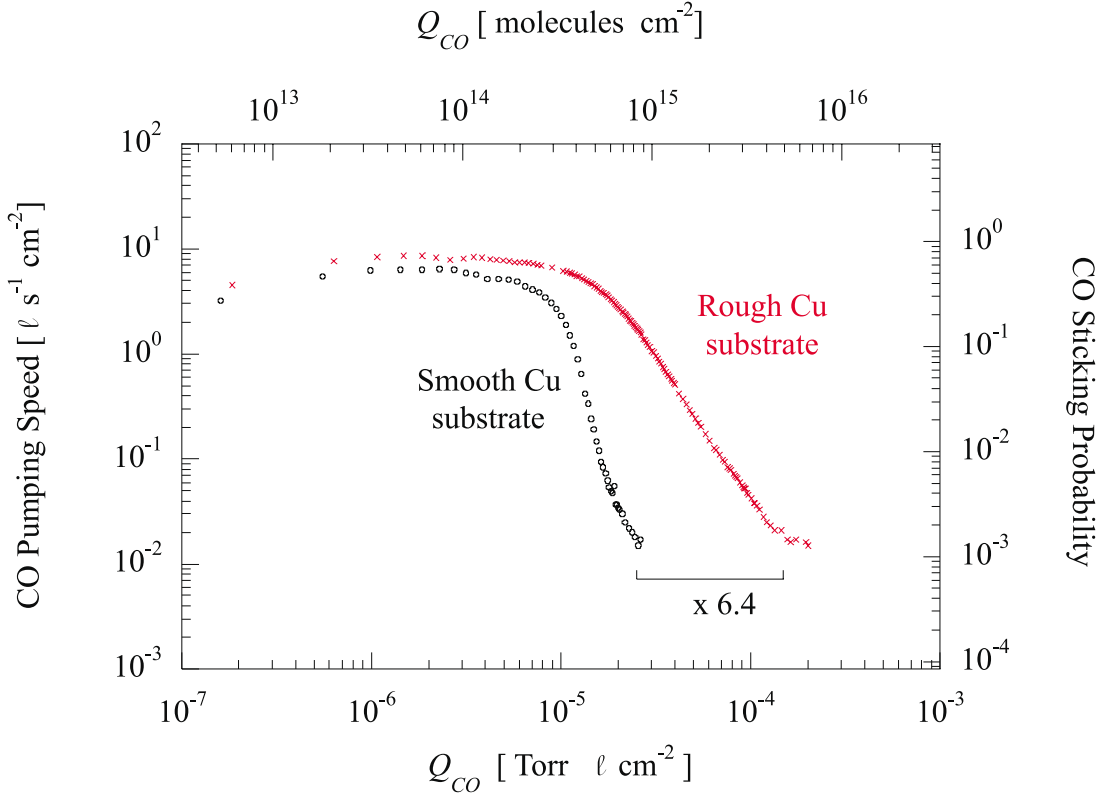


Fig. 5.17: CO pumping speed as a function of the quantity of the same gas adsorbed on the NEG coating after 2 hours heating at 325 °C. The results obtained for two identical NEG thin films deposited on rough and smooth copper substrates are compared.

### 5.3 Influence of the substrate temperature $T_s$

In order to study the influence of the substrate temperature,  $T_s$ , on the film morphology, crystallinity and pumping characteristics, some samples were coated at different temperatures whilst maintaining all the other sputtering parameters identical (40 mA per meter of each of the two cathodes of 1 mm in diameter in sputtering system A, 500 V between the cathodes and the anode, the krypton discharge pressure  $P$  aimed at). Substrate temperatures ranging from 100 to 350 °C in steps of 50 °C were applied. The sample parameters are reported in Table 5.5.

Table 5.5: Samples deposited with different substrate temperature  $T_s$ . During each deposition run (qualified by the letter), four samples were deposited simultaneously and are distinguished by the notation  $x = 1, 2, 3$ , or  $4$ . See Appendix 9.1 for more details about the samples. For each deposition run, two coatings are deposited on rough copper substrates and two on smooth ones, except for the series of samples a.x, all four being deposited on smooth copper substrates.

Name	$T_s$ [°C]	Ti [at. %]	Zr [at. %]	V [at. %]	Deposition Rate [ $\mu\text{m}/\text{h}$ ]	$P$ [Torr]
a.x	100	33	16	51	0.08	$2.2 \times 10^{-2}$
f.x	100	26	18	56	0.08	$1.9 \times 10^{-2}$
g.x	150	24	20	56	0.06	$2.3 \times 10^{-2}$
e.x	200	24	17	59	0.07	$3.0 \times 10^{-2}$
d.x	250	28	17	55	0.11	$3.4 \times 10^{-2}$
b.x	300	32	16	52	0.08	$3.2 \times 10^{-2}$
c.x	350	22	15	65	0.07	$5.0 \times 10^{-2}$

### 5.3.1 Film morphology

The variation of the substrate temperature,  $T_s$ , induces significant changes on the film morphology. Above a substrate temperature  $T_s$  of 200 °C, the film roughness increases, as can be observed by SEM (Fig. 5.18 and Fig. 9.1 *a*). This phenomenon is in agreement with the results that G.S. Bales and A. Zangwill have published in Ref. [205]: enhanced mobility favours coalescence which in turn results in rough structures. The scale of variation of the roughness is out of the resolution of the laser dynamic focusing method. The increase of substrate roughness was already presented as a way to increase the roughness of coatings. The effects of roughening the substrate and increasing the substrate temperature were combined. The results are illustrated in Fig. 5.19 and Fig. 9.1 *b*.

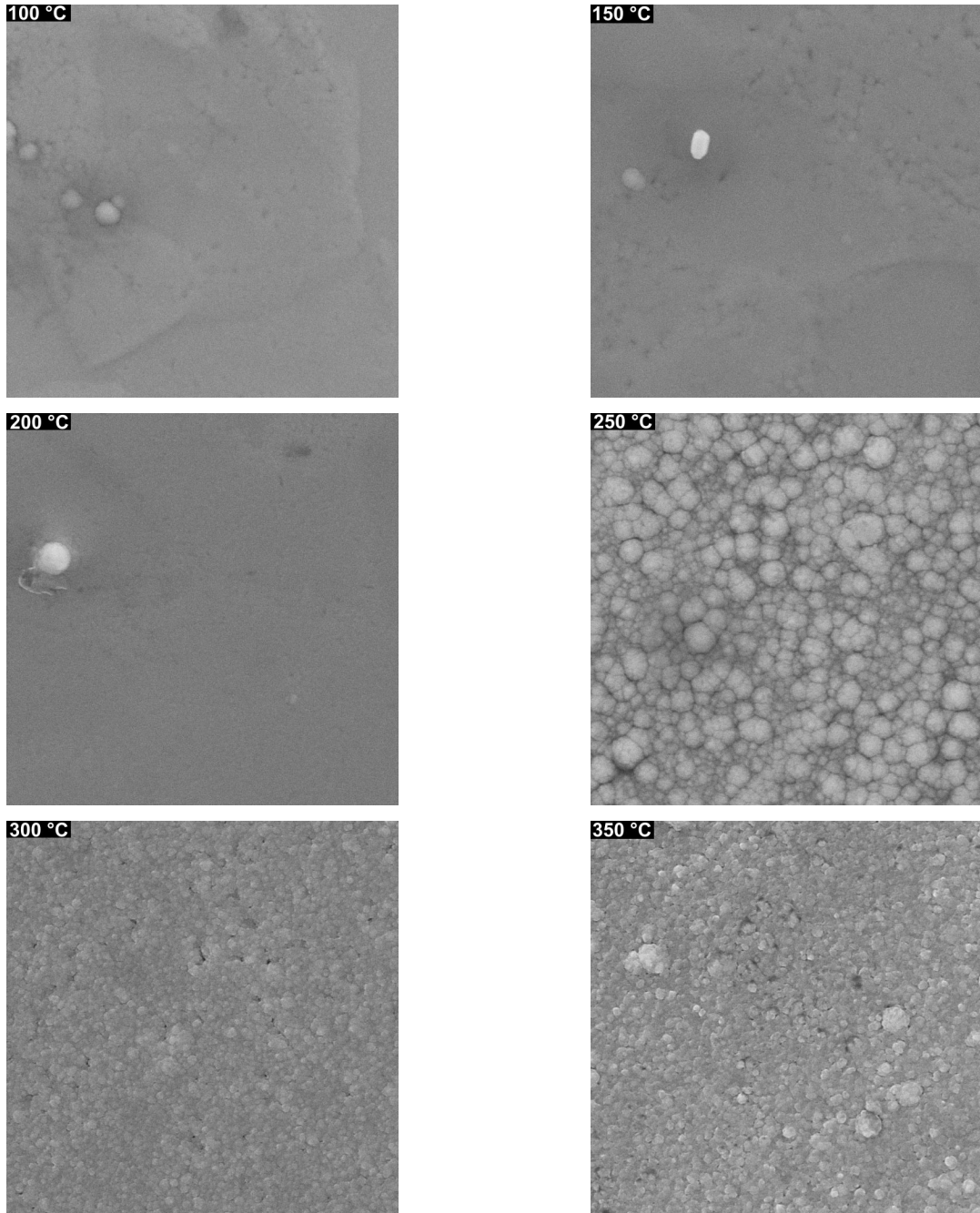


Fig. 5.18: SEM micrographs of TiZrV thin films sputtered on smooth copper substrates at substrate temperatures ranging from 100 to 350 °C in steps of 50 °C. Micrographs size: 15  $\mu\text{m}$   $\times$  15  $\mu\text{m}$ .

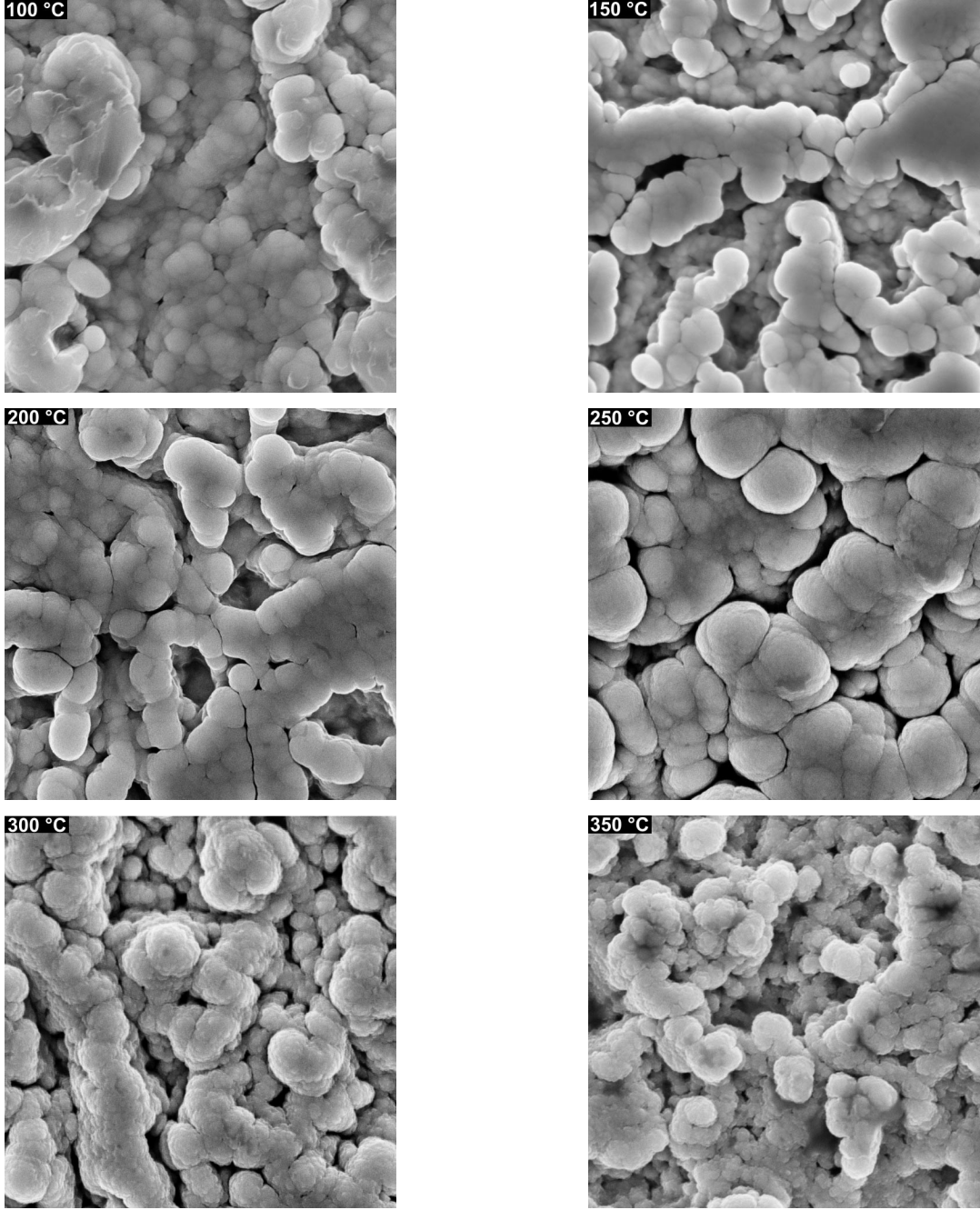


Fig. 5.19: SEM micrographs of TiZrV thin films sputtered on rough copper substrates at substrate temperatures ranging from 100 to 350 °C in steps of 50 °C. Micrographs size: 15  $\mu\text{m}$   $\times$  15  $\mu\text{m}$ .

### 5.3.2 Film crystallinity

X-ray diffraction was performed in the  $\Theta - 2\Theta$  geometry on each of the TiZrV films deposited at different substrate temperatures as reported in Table 5.5. The diffractograms obtained are given in Fig. 5.20. Only one diffraction peak related to the film is detected. The evaluation of the average grain size ( $\omega$ ) according to the Scherrer equation indicates that up to a substrate temperature  $T_s = 250$  °C, the grain size is below 5 nm (see Table 5.6). For higher substrate

temperatures the grain size increases ( $\omega = 9$  nm for  $T_s = 300$  °C,  $\omega = 11$  nm for  $T_s = 350$  °C). Thus, 250 °C is the highest substrate temperature at which a grain size below the threshold value of 5 nm is still preserved. The results are independent of whether the copper substrate is rough or smooth.

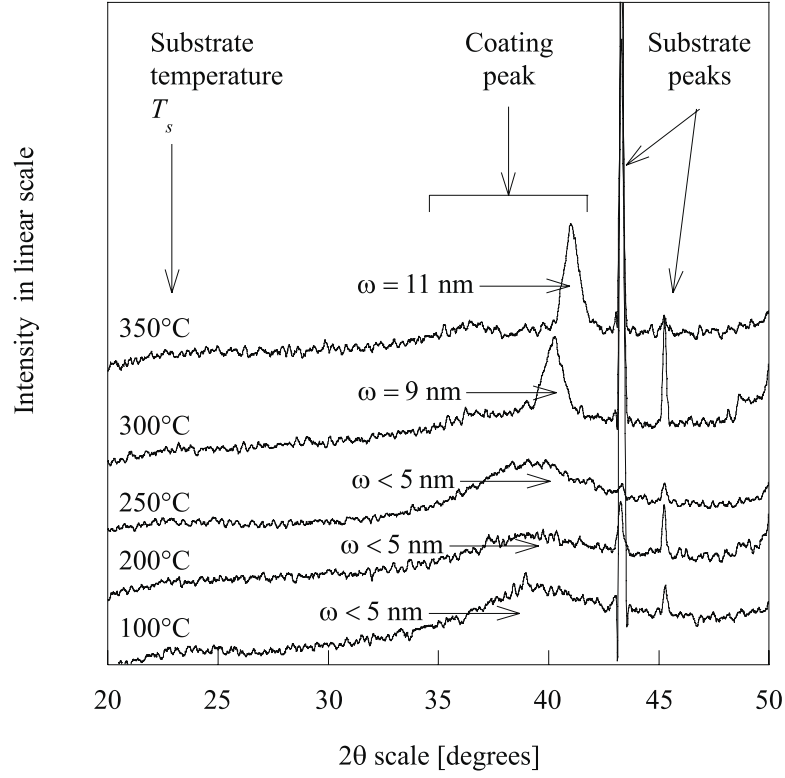


Fig. 5.20: XRD diffractograms obtained in the  $\Theta - 2\Theta$  geometry for TiZrV thin films sputtered at different substrate temperatures ranging from 100 °C to 350 °C in steps of 50 °C.

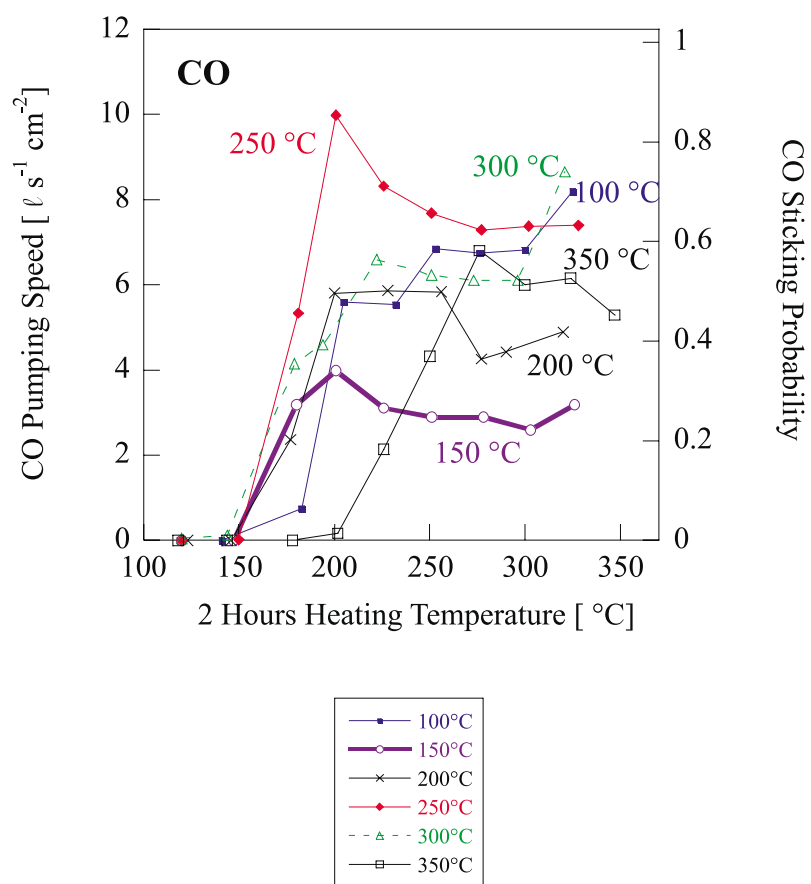
Table 5.6: Average grain size ( $\omega$ ) evolution as a function of substrate temperature ( $T_s$ ).

Samples	$T_s$ [°C]	Composition [atomic %]	$2\Theta$ [°] from Vegard's law	$2\Theta$ [°] experimental	Average grain size $\omega$ [nm]
a	100	Ti <sub>33</sub> Zr <sub>16</sub> V <sub>51</sub>	39.75	39.1	< 5
e	200	Ti <sub>24</sub> Zr <sub>17</sub> V <sub>59</sub>	40.02	39.0	< 5
d	250	Ti <sub>28</sub> Zr <sub>17</sub> V <sub>55</sub>	39.87	39.4	< 5
b	300	Ti <sub>32</sub> Zr <sub>16</sub> V <sub>52</sub>	39.79	40.2	9.4
c	350	Ti <sub>22</sub> Zr <sub>15</sub> V <sub>65</sub>	41.09	41.1	10.8

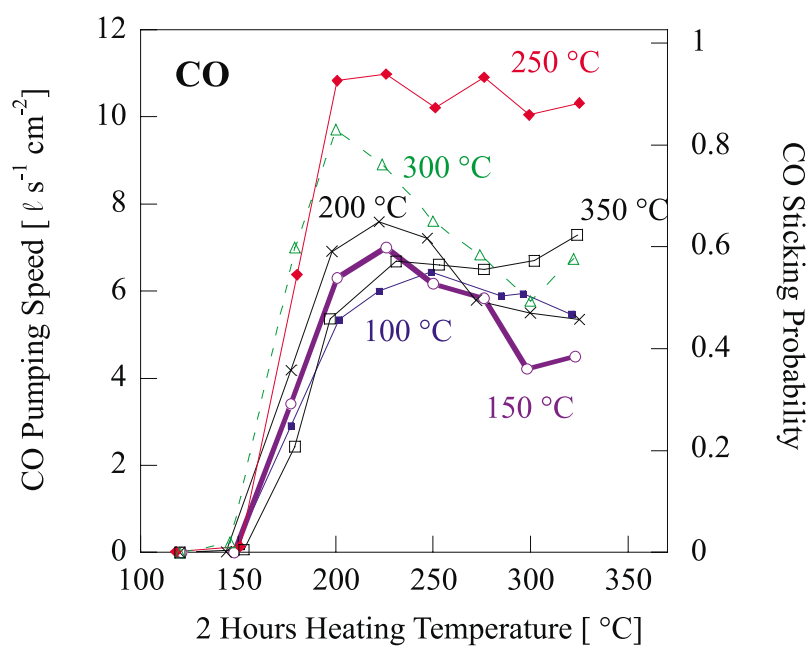
### 5.3.3 Pumping speed for CO and H<sub>2</sub> and surface pumping capacity

Pumping speed values of TiZrV thin films change as a function of substrate temperature ( $T_s$ ) as shown for CO and H<sub>2</sub> in Fig. 5.21 and Fig. 5.22, respectively. The surface pumping capacity for CO is also strongly affected by the substrate temperature (Fig. 5.23).

a)



b)



c)

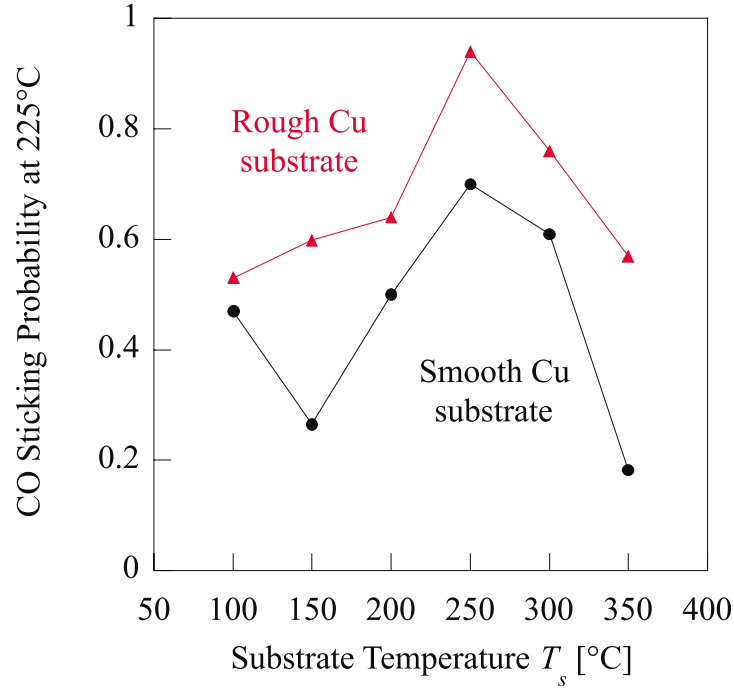


Fig. 5.21: Comparison of the CO sticking probabilities ( $\alpha_{CO}$ ) as a function of the heating temperature for NEG thin films deposited at different substrate temperatures ranging from 100 °C to 350 °C in steps of 50 °C, on smooth (a) and on rough (b) copper substrates. Summary of the sticking probabilities of CO ( $\alpha_{CO}$ ) obtained for the same samples after 2 hours heating at 225 °C (c).

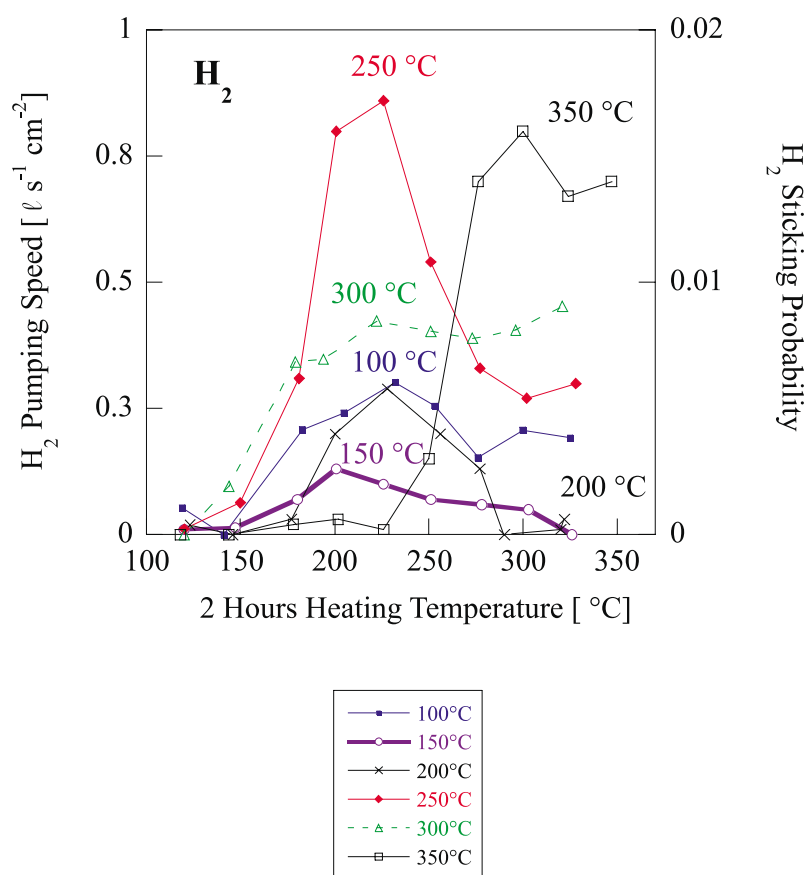
The onset of pumping for both H<sub>2</sub> and CO is obtained after heating at temperatures ranging between 150 °C and 180 °C (for 2 hours) independently of the substrate temperature ( $T_s$ ).

The highest CO sticking probability reached amongst the tested TiZrV thin films is  $\alpha_{CO} = 0.9$ . It was obtained for samples coated at  $T_s = 250$  °C for both smooth (Fig. 5.21 a) and rough (Fig. 5.21 b) copper substrates. This value is recorded after 2 hours heating at 200 °C.

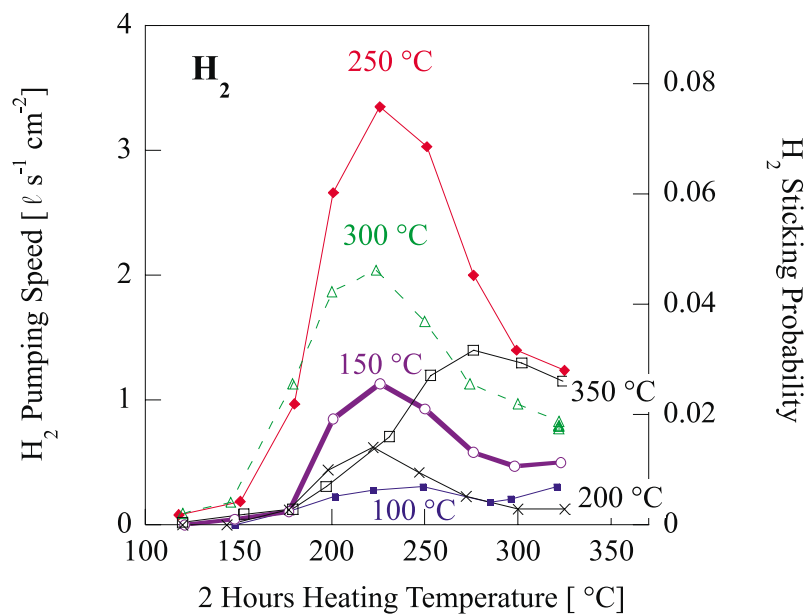
For H<sub>2</sub> as for CO, the maximum pumping speed is reached for the sample coated at  $T_s = 250$  °C. This value, obtained after 2 hours heating at 225 °C, is equal to 0.02 in the case of the smooth copper substrates (Fig. 5.22 a) and to 0.08 in the case of the rough ones (Fig. 5.22 b). The presence of a maximum of H<sub>2</sub> and CO pumping speed as a function of heating temperature will be the main subject of discussion in next chapter.

The surface pumping capacity for CO increases with the substrate temperature up to 300 °C in the case of the smooth copper substrates (Fig. 5.23 a) and up to 250 °C in the case of rough ones (Fig. 5.23 b). The highest surface pumping capacity in the latter case equals  $2 \times 10^{16}$  molecules cm<sup>-2</sup> which means more than three times higher than that measured in the case of smooth substrates.

a)



b)





c)

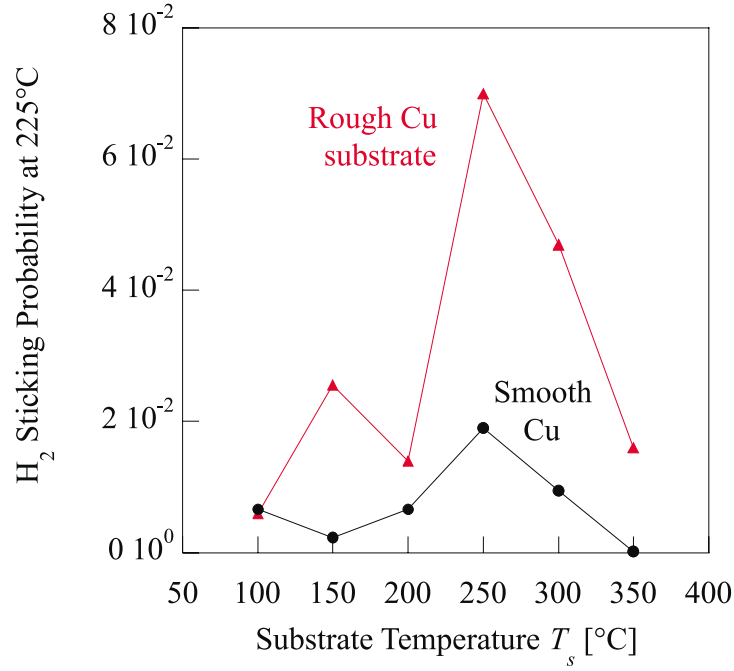
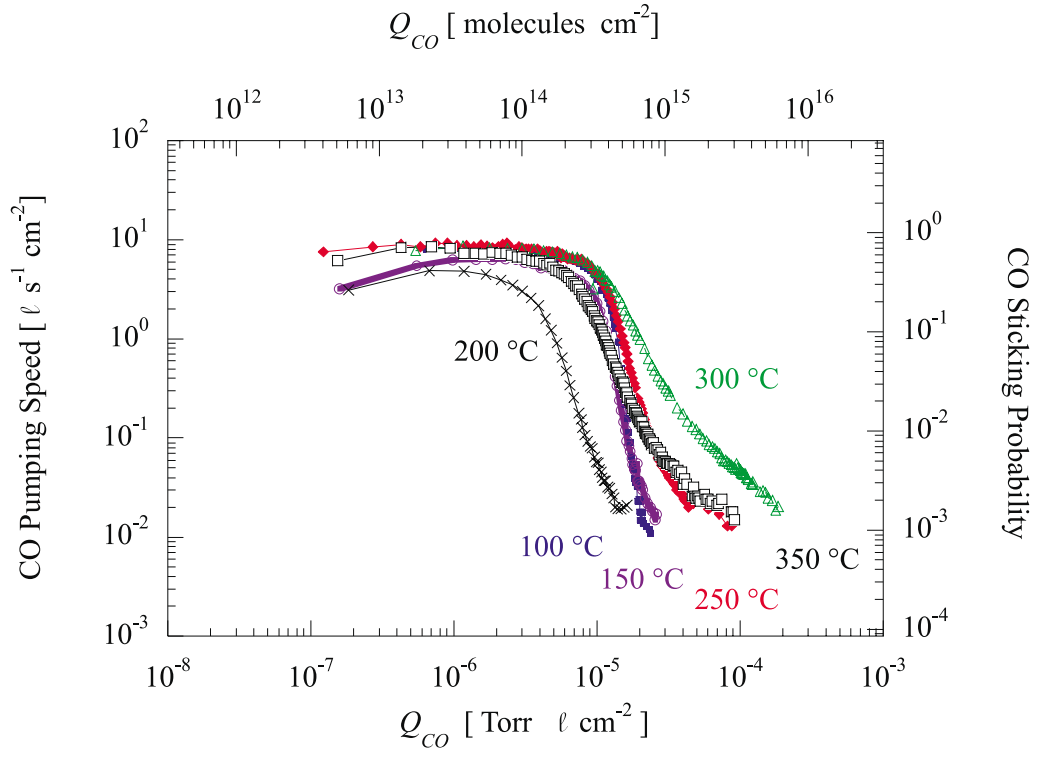


Fig. 5.22: Comparison of the H<sub>2</sub> sticking probabilities ( $\alpha_{H_2}$ ) as a function of the heating temperature for NEG thin films deposited at different substrate temperatures ranging from 100 °C to 350 °C in steps of 50 °C, on smooth (a) and on rough (b) copper substrates. Summary of the sticking probabilities of H<sub>2</sub> obtained after 2 hours heating at 225 °C (c).

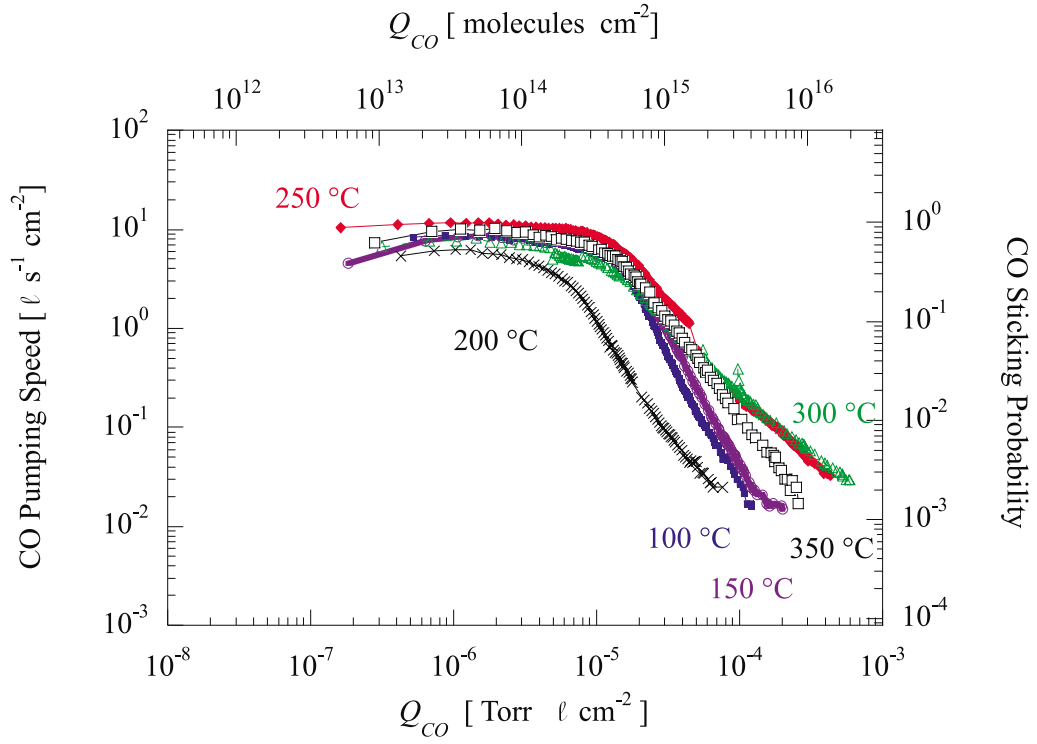
The sticking probability measured after 2 hours heating at 225 °C for the six substrate temperatures tested is summarised in Fig. 5.21 c for CO and in Fig. 5.22 c for H<sub>2</sub>. For the same samples, the surface pumping capacities for CO after 2 hours heating at 325 °C are summarised in Fig. 5.23 c. In these three comparisons, the curve corresponding to the rough substrates follows the curve corresponding to the smooth ones but it is translated to higher pumping speed and pumping capacity values, respectively. This means that the roughness of the substrate does not change the general pumping properties of NEG coatings but increases their values and amplifies their variations.

It appears clearly that the optimum substrate temperature in terms of sticking probability for CO and for H<sub>2</sub> is  $T_s = 250$  °C. It is also the case for surface pumping capacity for CO on rough substrates. The reasons of both these effects may be found in the rough structure of the getter films, as discussed in paragraph 2.2.

a)



b)



c)

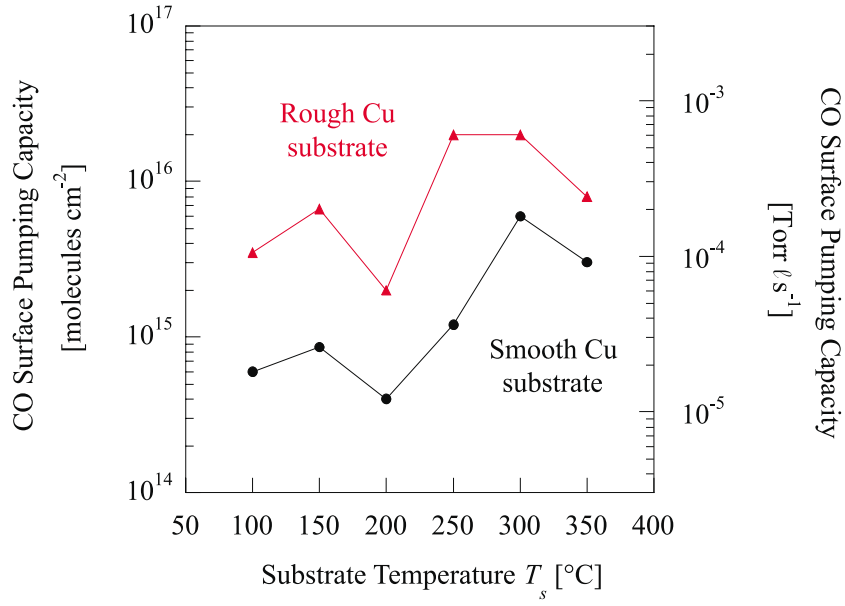


Fig. 5.23: CO pumping speed as a function of the quantity of the same gas adsorbed on the NEG coating after 2 hours heating at 325 °C for different substrate temperatures ranging from 100 °C to 350 °C in steps of 50 °C, on smooth (a) and on rough (b) copper substrates. Summary of the surface pumping capacities for CO for the same samples (c).

## 5.4 Influence of the surface load of a gas on the pumping speed for other gases

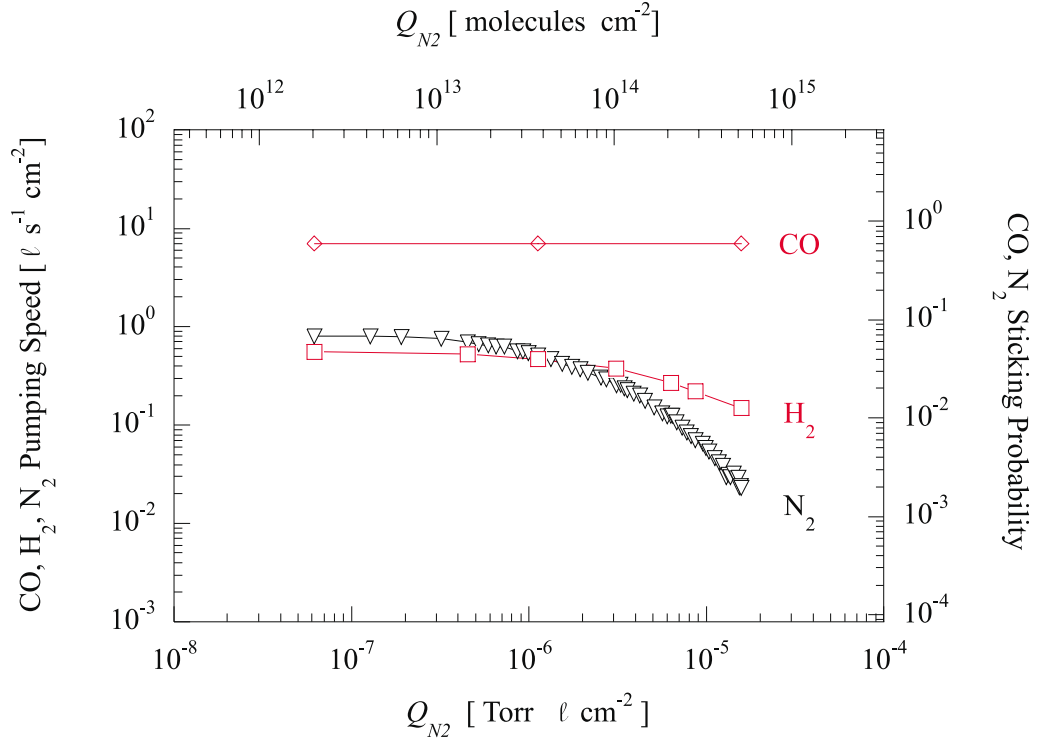
In real vacuum systems, many different gas species are pumped simultaneously. It is therefore of great practical importance to assess how the surface load of a gas influences the NEG film pumping speed for other gases. Two distinct cases are studied: the influence of the injection of N<sub>2</sub> on the pumping of H<sub>2</sub> and CO, and the influence of the injection of CO on the pumping of H<sub>2</sub> and N<sub>2</sub>.

The effect of H<sub>2</sub> loading was not studied because it is well known that H<sub>2</sub> diffuses into the bulk of getter materials even at room temperature. Therefore, it does not affect the pumping of other gases [204], as explained in paragraph 2.2.2.

### 5.4.1 Influence of N<sub>2</sub> surface load on the pumping speed of H<sub>2</sub> and CO

The influence of N<sub>2</sub> surface load on the pumping speed of H<sub>2</sub> and CO is shown in Fig. 5.24 a. This particular example is that of sample r (deposited on a rough copper substrate). The sample is activated at 350 °C for 2 hours before surface loading with N<sub>2</sub> at room temperature. According to the technique described in paragraph 4.3.4, the evolution of the pumping speed of N<sub>2</sub> as a function of the quantity of the same gas pumped on the surface ( $Q_{N_2}$ ) is measured.

a)



b)

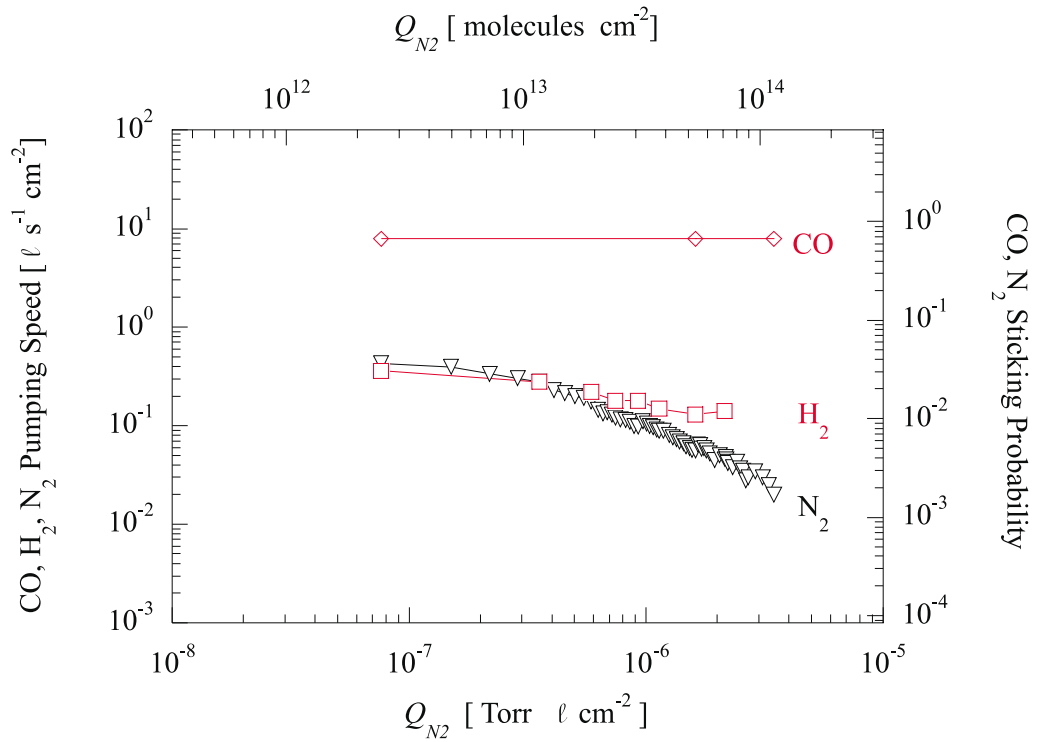


Fig. 5.24: Pumping speeds of N<sub>2</sub>, H<sub>2</sub>, and CO as a function of the quantities of N<sub>2</sub> pumped  $Q_{N_2}$  (after heating at 325 °C for 2 hours). *a*: sample r which consists of a Ti<sub>31</sub>Zr<sub>17</sub>V<sub>52</sub> (atomic) thin film deposited on a rough copper substrate, at  $T_s < 100$  °C. *b*: sample a.2 which consists of a Ti<sub>33</sub>Zr<sub>16</sub>V<sub>51</sub> (atomic) thin film deposited on a smooth copper substrate, at  $T_s = 100$  °C.

The injection of  $N_2$  is interrupted several times and replaced by injections of  $H_2$  and  $CO$  (in quantities negligible compared to that of  $N_2$ ), so as to measure the pumping speeds of  $H_2$  and  $CO$  as a function of the quantity of  $N_2$  pumped ( $Q_{N_2}$ ). The surface loading of  $5 \times 10^{14}$   $N_2$  molecules  $cm^{-2}$  reduces by a factor of about 30 the pumping speed of  $N_2$  while the pumping speed of  $H_2$  is reduced only by a factor 3.5 (from a pumping speed  $S_{H_2}$  of 0.54 down to  $0.15 \ell s^{-1} cm^{-2}$ ).  $N_2$  does not affect the  $CO$  pumping at all since  $S_{CO}$  remains constant whatever the quantity of  $N_2$  pumped. This behaviour has already been reported for St101 and St707 getter strips [206]. It may be due to  $N_2$  adsorbed underneath the first monolayer of the surface, which therefore remains free for adsorbing  $CO$  (as already reported for Ti [207] and Zr [208] pure metals) and/or to the low surface capacity for  $N_2$ , resulting in a large population of free adsorption sites even after  $N_2$  saturation [209]. This hypothesis is discussed in paragraph 2.2.4.

Another measurement obtained with sample a.2 (Fig. 5.24 b) shows that the previous result is independent of the substrate roughness. In the case of sample a.2, deposited on a smooth copper substrate, the surface loading by  $1 \times 10^{14}$  molecules  $cm^{-2}$  is enough to reduce the pumping speed of  $H_2$  and  $N_2$  by a factor of two, while that of  $CO$  is only slightly reduced.

#### 5.4.2 Influence of the $CO$ surface load on the pumping speed of $H_2$ , $CO$ and $N_2$

In the same way, Fig. 5.25 shows the effect of  $CO$  surface loading on the pumping speeds of  $N_2$ ,  $CO$  and  $H_2$ . The measurement is performed on sample b.1,  $Ti_{32}Zr_{16}V_{52}$  (atomic), deposited on a smooth copper substrate at  $T_s = 300$  °C. The sample is activated at 325 °C for 2 hours before loading with  $CO$  at room temperature. The results clearly indicate that this gas appreciably reduces the pumping speed of the other gases as already observed for St101 and St707 getter strips [206], [210]. The surface load by  $2 \times 10^{14}$  molecules  $cm^{-2}$  is enough to reduce the pumping speed of  $H_2$  and  $N_2$  by 40%.

At large coverage,  $CO$  and  $N_2$  have the same pumping speed curves. As they have the same molecular mass, they experience the same conductance ( $C_{CO} = C_{N_2} = 11.70 \ell s^{-1} cm^{-2}$ ) (see paragraph 1.2, Eq. (1.3)). This reveals that the conductance of the voids in the film is the limiting factor of the pumping speed at large coverage (see paragraph 2.2.4) [209].

After complete saturation with  $CO$ , a NEG thin film can be conditioned by heating to restore the initial pumping speed (according to the definition given in Ref. [209]). An example is shown in Fig. 5.26 (a and b) for sample b.4. In that particular case, heating up to 250 °C is required to completely restore the pumping performance.

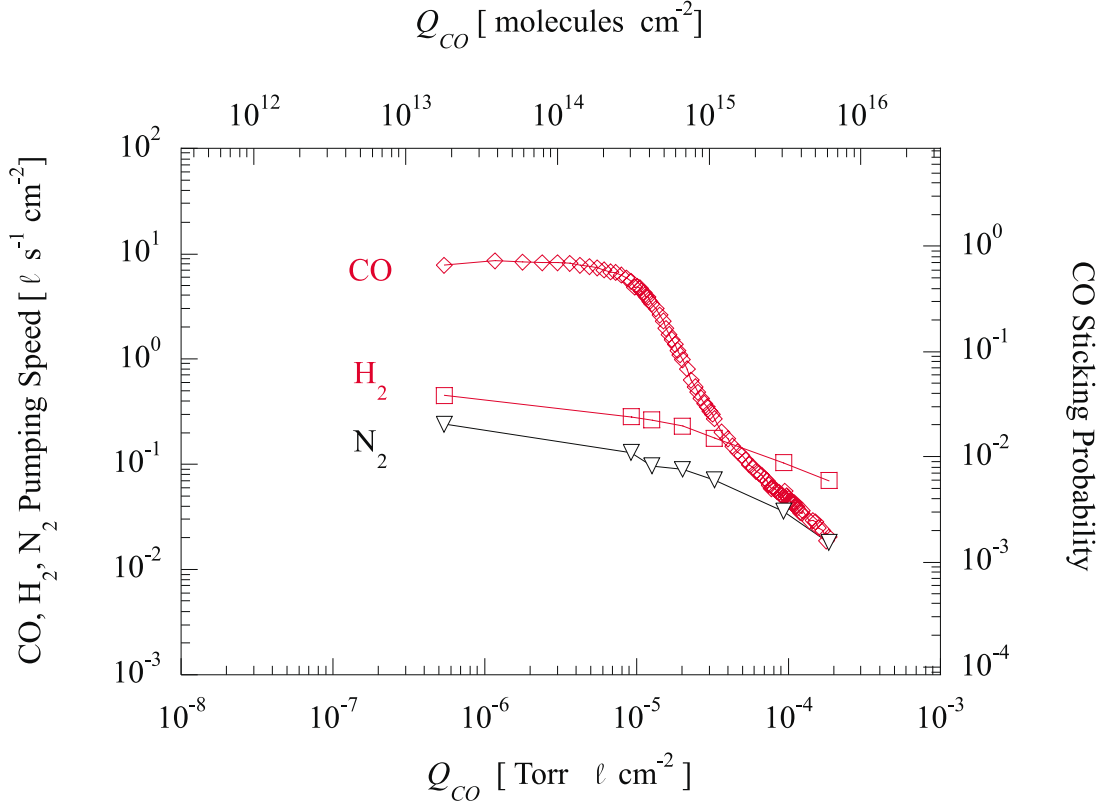


Fig. 5.25: Pumping speeds of  $N_2$ ,  $H_2$ , and  $CO$  as a function of the quantity of  $CO$  pumped ( $Q_{CO}$ ) measured for a  $Ti_{32}Zr_{16}V_{52}$  (atomic) thin film after heating at  $325^\circ C$  for 2 hours (sample is b.1 deposited on a smooth copper substrate, at  $T_s = 300^\circ C$ ).

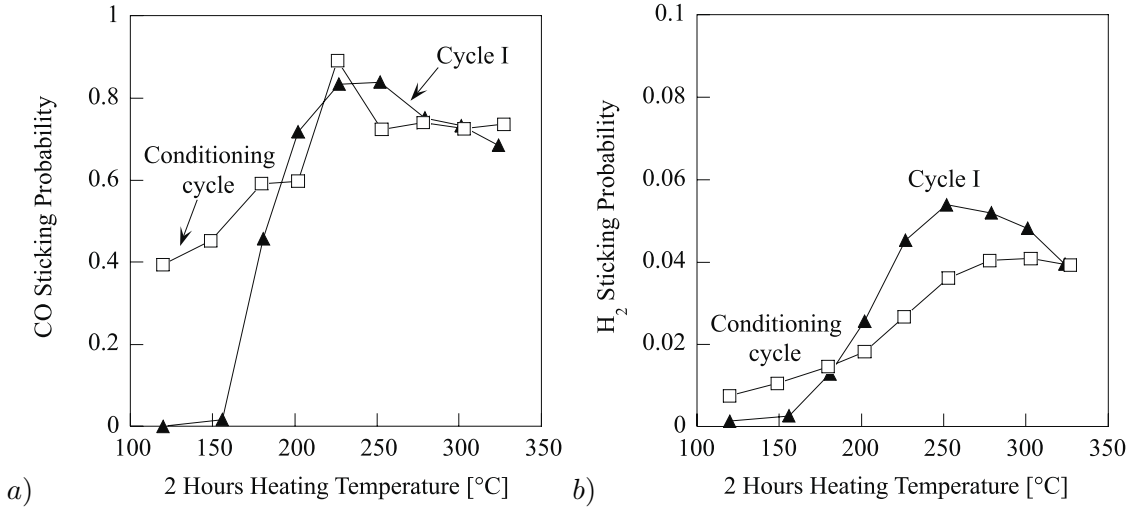


Fig. 5.26: Influence of  $CO$  saturation on the evolution of sticking probability of  $CO$   $\alpha_{CO}$  (a) and of  $H_2$   $\alpha_{H_2}$  (b) as a function of the heating temperature. The example is that of sample b.4,  $Ti_{32}Zr_{16}V_{52}$ , deposited on a rough copper substrate, at  $T_s = 300^\circ C$ .

To be more descriptive, during the first heating cycle (referred to as cycle I in the figure), the onset of  $H_2$  pumping speed is between  $150^\circ C$  and  $180^\circ C$  (Fig. 5.26 b). A large increase

is observed until a maximum value is reached after 2 hours heating at 250 °C. Then, the H<sub>2</sub> sticking probability decreases slightly down to  $\alpha_{H_2} = 0.04$  (reached at 325 °C). After this heating step, saturation with CO is undertaken. An identical sequence of heating treatments and pumping speed measurements is performed again (results referred to as conditioning cycle on the graph). The maximum disappears on the curve of H<sub>2</sub> pumping speed in this conditioning cycle. The highest H<sub>2</sub> sticking probability measured is reached at 275 °C and remains constant until 325 °C. Its value is 0.04, which is also the value recorded at the end of the previous cycle.

## 5.5 Effects of intermediate air venting on the pumping speed of H<sub>2</sub> and CO (ageing)

In real vacuum systems, air ventings are unavoidable. It is therefore of great practical importance to assess how this influences the NEG film pumping speed for H<sub>2</sub> and CO.

During the activation progress, the oxygen present in the surface passivation layer is diffused inside the getter film. Owing to the small film thickness (micrometre range) each activation process results in a non-negligible increase of the oxygen concentration in the film, which in turn may produce a deterioration of film performance (reduced pumping speed, reduced surface pumping capacity, and increased activation temperature). The effect of repeated activation/air venting cycles on the sticking probability of H<sub>2</sub> ( $\alpha_{H_2}$ ) is already reported in Ref. [141].

In the present study, the deterioration of the pumping performances of TiZrV-coated Cu disks was studied after a second air venting/activation cycle. The first example is that of sample g.2 ( $T_s = 150$  °C). The CO saturation curves are shown in Fig. 5.27. It turns out that the surface pumping capacity for CO is three times lower after the additional venting/activation cycle. Similar results were obtained with disks coated at higher temperature (see Fig. 5.28 and Fig. 5.29). After venting, the surface pumping capacity is reduced by a factor three for sample d.3 deposited at  $T_s = 250$  °C, and a factor six for sample b.3 deposited at  $T_s = 300$  °C (Fig. 5.28). Sample b.4 ( $T_s = 300$  °C) shows a decrease of surface pumping capacity from  $1.8 \times 10^{16}$  CO molecules cm<sup>-2</sup> for the first cycle (referred to as “I” on Fig. 5.29) to three times lower after air venting (referred to as “II” on the graph).

To be more precise about the experiments performed on sample b.4, it is important to describe the additional CO saturations that were done compared to the procedure used to obtain results of Fig. 5.27 and Fig. 5.28. The CO saturation performed after 2 hours heating at 325 °C is followed by a 1-hour dry air venting, and the saturation experiment is repeated five times at increasing activation temperatures: 200 °C, 225 °C, 250 °C, 300 °C, 325 °C. Then, the global result given previously can be supplemented by the fact that 2 hours heating at 200 °C leads to a surface pumping capacity of  $3.5 \times 10^{15}$  molecules cm<sup>-2</sup> and the progressive

increase of the heating temperature raises the pumping capacity up to  $6 \times 10^{15}$  molecules  $\text{cm}^{-2}$ , a capacity which is three times lower than the one obtained at the end of the first saturation. There is then no loss of surface pumping capacity due to pumping of CO whereas the deterioration is clear after air venting.

The initial pumping speeds for  $\text{H}_2$  and CO measured for sample b.4 are shown in Fig. 5.30 *a* and *b* respectively, before (cycle I) and after (cycle II) the additional venting/activation cycle. The  $\text{H}_2$  pumping speed evolution as a function of temperature has a maximum after dry air venting, as in the first cycle, excepted that it is translated to higher temperature and to lower sticking probability values. A less detrimental effect is observed for the initial pumping speed of CO.

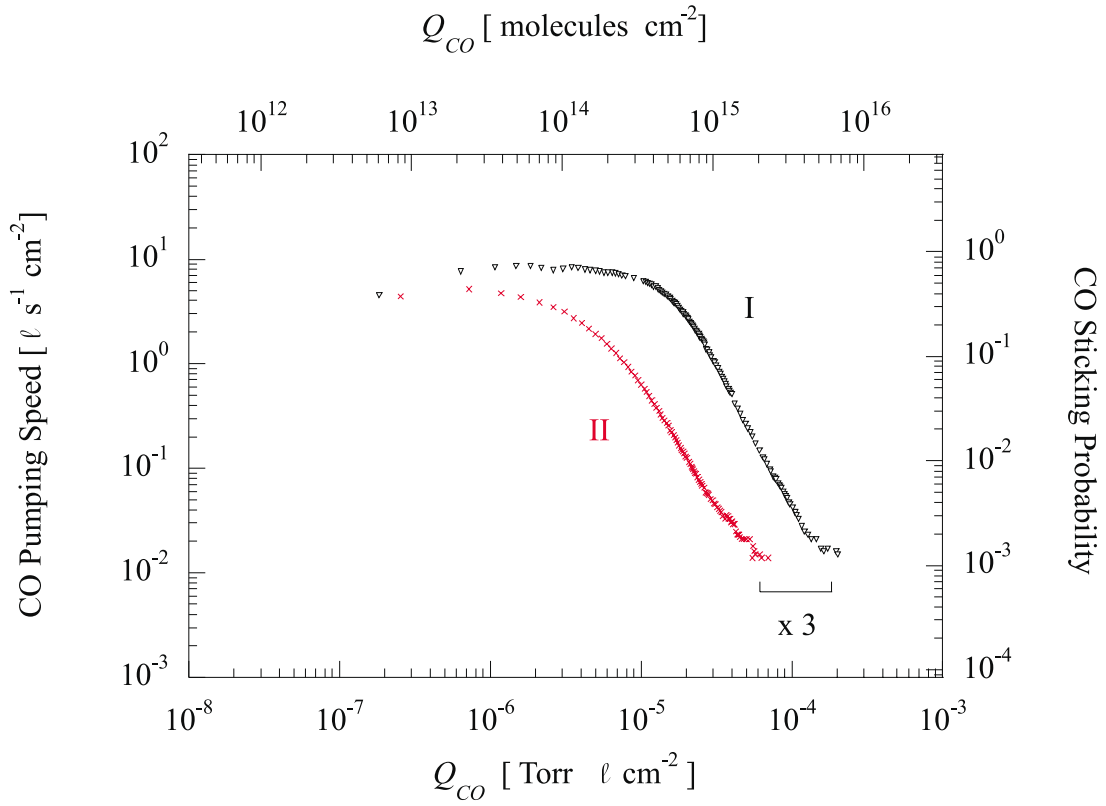


Fig. 5.27: Influence of air venting on the quantities of CO pumped  $Q_{CO}$  for a  $\text{Ti}_{24}\text{Zr}_{20}\text{V}_{56}$  (atomic) thin film after heating at  $325^\circ\text{C}$  for 2 hours (the sample is g.2 deposited on a rough copper substrate, at  $T_s = 150^\circ\text{C}$ ). “I” refers to the measurement performed before the air venting and “II” the one performed after the air venting.



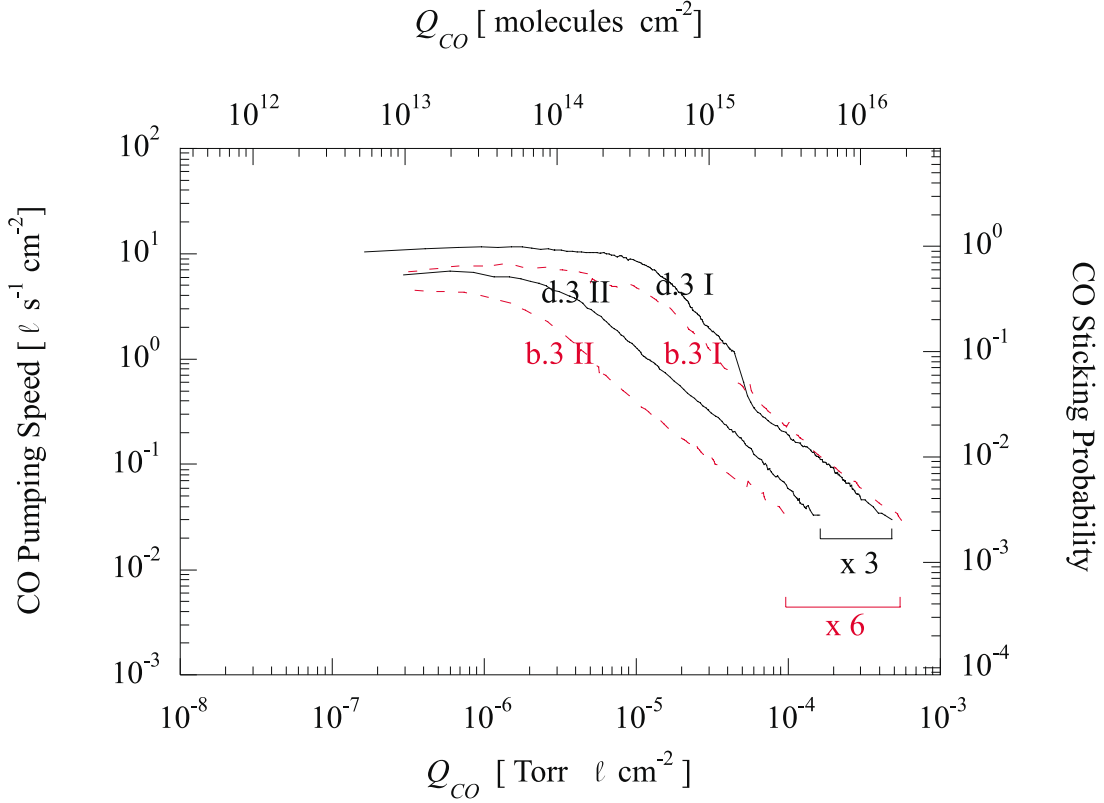


Fig. 5.28: Influence of air venting on the quantities of CO pumped  $Q_{CO}$  for a thin film after heating at 325 °C for 2 hours (the samples are b.3  $\text{Ti}_{32}\text{Zr}_{16}\text{V}_{52}$  (atomic) and d.3  $\text{Ti}_{28}\text{Zr}_{16}\text{V}_{56}$  (atomic) deposited on a rough copper substrate, at  $T_s = 300$  °C and 250 °C, respectively). “I” refers to the measurements performed before the air venting and “II” to those performed after the air venting.

The highest heating temperatures during the first cycle do not influence the ageing of the NEG, as shown in Fig. 5.31. Indeed, the O-KLL intensity measured by AES as a function of heating temperature always decreases more slowly after any additional air venting/activation cycle. This indicates an increase in activation temperature. This degradation of the activation is comparable for samples heated up to 350 °C (samples n°123, 161A, 161B, 44B) and up to 200 °C (samples n°165A and 165B) during the first cycle.

The deterioration of pumping speed consequent to exceeding a given heating temperature is a feature which has already been observed for other NEGs (namely the St707) (by K. Ichimura in Refs. [211], [212], [213], M. Sancrotti *et al.* in Ref. [214] and by C. Benvenuti *et al.* in Ref. [210]).

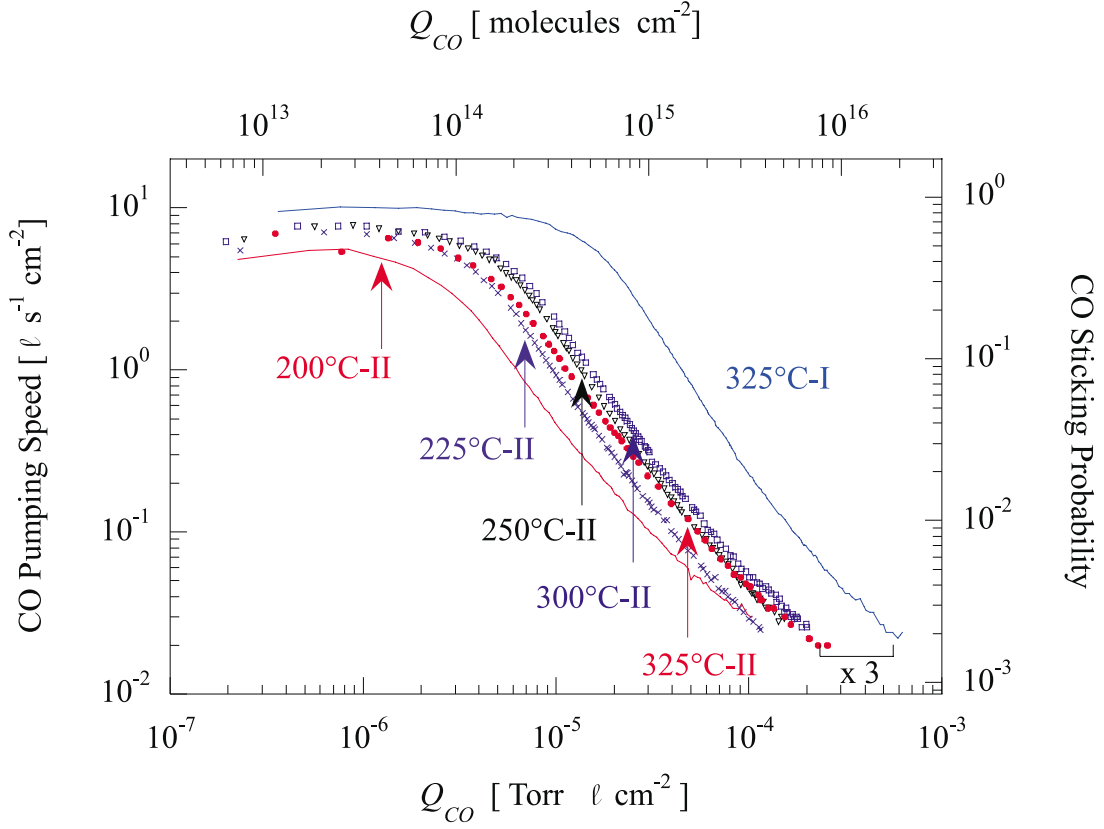


Fig. 5.29: Influence of air venting on the quantities of CO pumped  $Q_{CO}$  after heating at progressively increasing temperatures from 200 to 325 °C for 2 hours. “I” refers to the measurement performed before the air venting and “II” to those performed after the air venting. The example is the same as in Fig. 5.26 (sample b.4,  $Ti_{32}Zr_{16}V_{52}$ , deposited on a rough copper substrate, at  $T_s = 300$  °C).

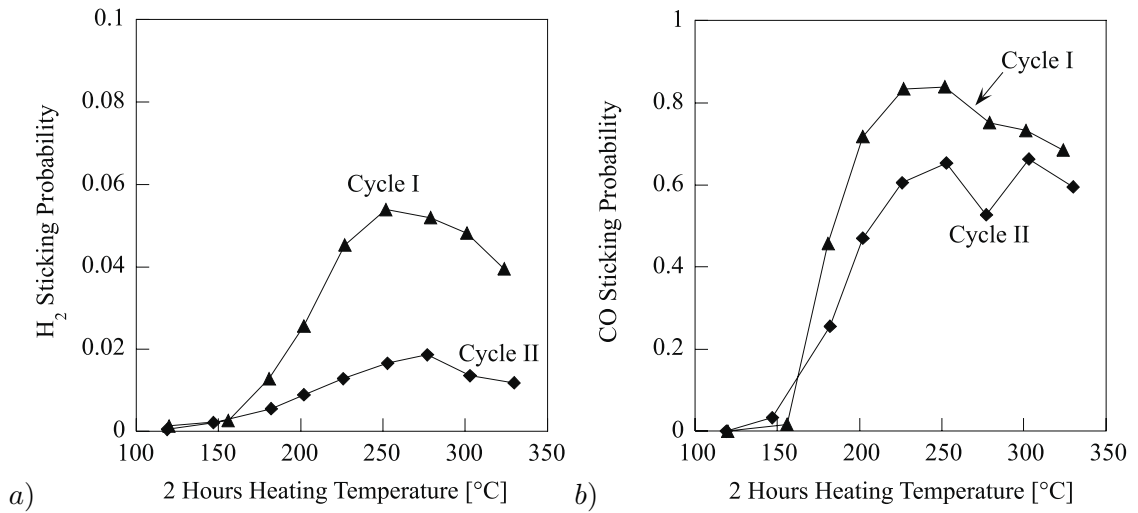


Fig. 5.30: Influence of air venting on the evolution of sticking probability of  $H_2$   $\alpha_{H_2}$  (a) and of CO  $\alpha_{CO}$  (b) as a function of the heating temperature. The sample is the same as in Fig. 5.26

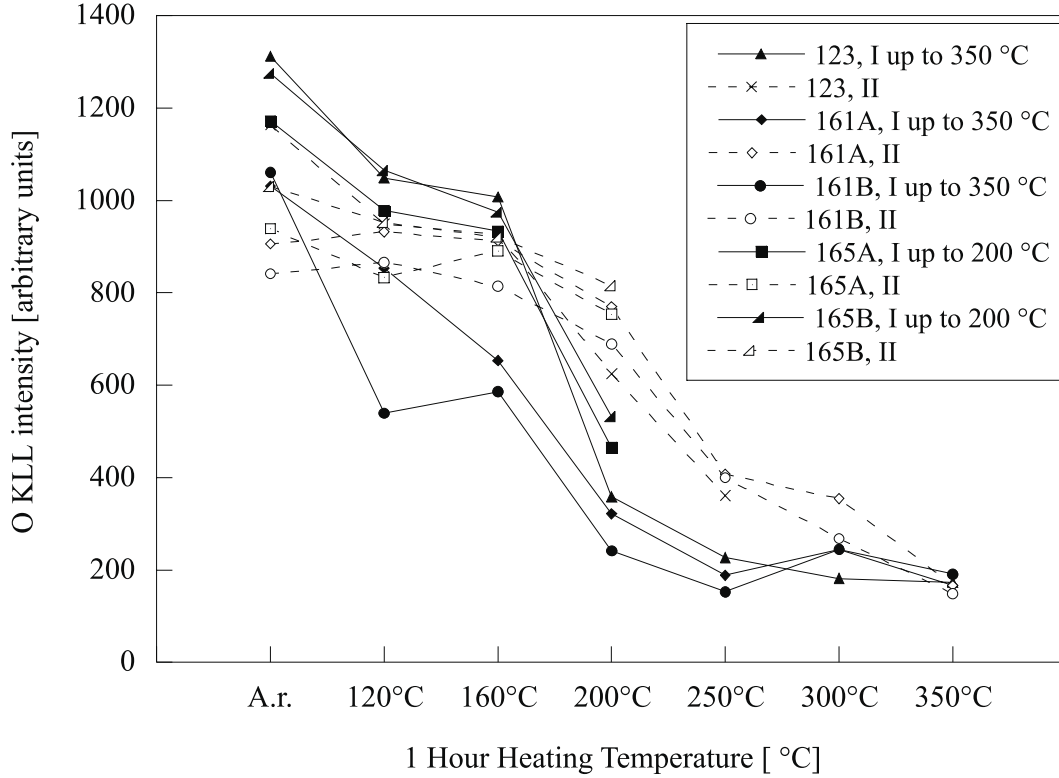


Fig. 5.31: Influence of air venting and of the high heating temperatures on the O-KLL intensities (AES measurements) variation as a function of the activation temperature. On the legend, “I” stands for first activation (before air venting) and “II” for second activation (after air venting).

## 5.6 Intermediate conclusions

From this study, we can conclude that the parameter mostly influencing the non-evaporable TiZrV getter coating properties is the substrate temperature during the sputter deposition process ( $T_s$ ). Several values of substrate temperatures ranging from less than 100 °C to 350 °C in steps of 50 °C have been tested. The properties of the coatings produced in these different conditions have been measured. As long as pumping speed for H<sub>2</sub> and CO, and surface pumping capacity for CO are concerned,  $T_s = 250$  °C is the optimum coating temperature for TiZrV NEG films on copper substrates.

TiZrV compositions corresponding to samples of low activation temperature ( $T_a$ ) are identified in a zone of the ternary diagram. The most significant result in this investigation is the correspondence of the low grain size (< 5 nm) in the TiZrV NEG coatings with the low activation temperature of those NEGs ( $T_a < 200$  °C for a 2-hour heating). It is striking that all the TiZrV NEG films (whatever the nature and roughness of the substrate) found to activate at low temperatures have an average grain size below 5 nm.

## 5.7 Summary of the results

The results described in this chapter show that the general laws governing the behaviour of the bulk getters ([206], [210]) also apply to NEG thin films of low activation temperature.

- a- Room temperature pumping of CO blocks the surface and inhibits the pumping of other gases (paragraph 5.4.2), while the blocking by N<sub>2</sub> is marginal (paragraph 5.4.1) and that of H<sub>2</sub> non existing (paragraph 2.2.2).
- b- The pumping speed variation as a function of the pumped quantity of a given gas also follows the bulk NEG behaviour, as described in the literature [206], showing the importance of NEG roughness and porosity (paragraph 5.2.2).

While for bulk NEG<sub>s</sub>, produced by pressing a NEG powder on a metal substrate, the pumping speed and surface capacity vary on a very narrow range only, the surface capacity of NEG thin films may be increased by almost two orders of magnitude by varying the production conditions. Very rough coatings have been produced by raising the substrate temperature, while coating, to about 250 °C (paragraph 5.3). By combining high coating temperature and chemical etching of the substrate prior to coating, surface capacities as high as those of the bulk NEG<sub>s</sub> have been achieved, in spite of a 50 times smaller NEG-film thickness (paragraph 5.3.3).

- c- The surface morphology of TiZrV coatings has been found to be affected by the chemical nature of the substrate material, but not their crystalline structure (paragraph 5.2.1).
- d- It has been shown that temperatures of activation as low as 180 °C may be obtained over a wide range of compositions. More important, coatings produced from cathodes made of intertwisted Ti, Zr, and V wires provide a composition within this range. This fact is of major practical relevance, because it allows NEG coatings to be produced in a very simple way, making use of pure metal wires available from the market (paragraph 5.1.2).
- e- The crystalline structure has been found to depend on the NEG film composition and to be linked to the activation temperature. More precisely, all the coatings which display a low activation temperature are of nanocrystalline structure (grain size smaller than 5 nm) (paragraphs 5.1.1 and 5.1.2).
- f- Finally, TiZrV coatings undergo a pumping speed decrease when heated for activation above 250 °C. This behaviour is similar to that of the St707 bulk NEG (although taking place in a different temperature range).

Points e and f, which are the most striking, will be discussed in Chapter 6.



# Chapter 6

## Discussion

Considering the conclusions formulated in the previous chapter in agreement with what is already known about getters, the two following questions remain open.

- Why do some TiZrV compositions provide a lower activation temperature? Is this related to the crystallinity? What is the origin of the nanocrystallinity?
- Why does the TiZrV NEG coatings pumping speed decrease when heated above 250 °C?

### 6.1 Influence of the crystalline state on the activation temperature

As previously announced, TiZrV coatings of different composition can be grouped into two families according to their grain size, i.e. those with a grain size above 100 nm and the so-called nanocrystalline films, which have a grain size below 5 nm. The grain size difference of about two orders of magnitude as a function of composition is striking and difficult to justify. Since a low activation temperature is a major asset for NEG's use, and the TiZrV coatings with low activation temperature all belong to the small grain size family, we will focus on the possible origin of such nanocrystalline structures.

#### 6.1.1 *The nanocrystalline structure of TiZrV*

Nanocrystallinity, in the sense of grains of less than 5 nm size, was found to be important for the activation behaviour. We analyse here the possible origins of this type of structure.

From first principle theories, it is difficult to predict the structures and the properties of alloys and solid solutions. Relevant factors which have been known to metallurgists as, for example, chemical affinity, electronegativity or the difference of atomic sizes are considered semi-empirically. Empirical rules have been formulated by Hume and Rothery concerning the limits of solid solubility based on atomic size, electronegativity and number of valence electrons [215]. These rules are only valid for thermodynamic equilibrium. The first rule states that if the difference between the atomic sizes of the component elements forming an alloy

exceeds about 14–15%, solid solubility should become restricted. Theoretical justification for the “ $\pm 15\%$ ” rule has been obtained from considerations of elastic strain energy in a solid solution. It is important to underline that within the favourable size zone, additional factors (electronegativity and number of valence electrons) will determine the extent of solid solubility.

The atomic radii of elements of the 3<sup>rd</sup>, 4<sup>th</sup> and 5<sup>th</sup> groups are summarised in Table 6.1 as well as the indication of the “ $\pm 15\%$ ” rule. This law does not exclude the possibility to form Ti-Zr solid solution and Ti-V solid solution but excludes the Zr-V one. This information is in agreement with the phase diagrams which show the existence of intermetallic compounds for the Zr-V system and extended solubility for the other two (see Fig. 6.1, Fig. 6.2, Fig. 6.3).

Table 6.1: Lattice parameters of elements of the 3<sup>rd</sup>, 4<sup>th</sup> and 5<sup>th</sup> groups and calculation of the radius of those elements in metallic lattice as well as the “ $\pm 15\%$ ” rule.

	Lattice parameter [Å]	Atomic radius [Å]	+15%	−15%
Sc	3.31	1.66	1.90	1.41
Y	3.65	1.83	2.10	1.55
La	3.75	1.88	2.16	1.59
Ti	2.95	1.48	1.70	1.25
Zr	3.23	1.62	1.86	1.37
Hf	3.20	1.60	1.84	1.36
V	3.02	1.31	1.50	1.11
Nb	3.30	1.43	1.64	1.21
Ta	3.31	1.43	1.65	1.22
Cr	2.88	1.25	1.43	1.06

Additional aspects should be considered for sputter deposited films: the stress induced in the layer and the difficulty to obtain a structure in thermodynamic equilibrium. The available phase diagrams are given for standard conditions ( $P = 1$  atm) and the respective existence domains for the various phases might be shifted in temperature and concentration as a function of stress. No measurements of stress were performed in the present investigation.

In the case of sputter deposition, the equilibrium structure is hardly obtained because of kinetic constraints. The time allowed to the atoms for surface diffusion is determined by the deposition rate. Therefore, the fact that several phases can nucleate simultaneously combined with the limited time for surface diffusion could hinder the formation of large ordered regions, as large crystalline grains. For a Ti-Zr layer, the elements exhibit a miscibility in the entire composition range and the same lattice type (hcp). Therefore, during deposition, only one lattice type can nucleate and the grains, the size of which is limited by diffusion, can reach a larger size than in Zr-V. In the case of Zr-V, we expect nucleation of a V rich phase with bcc structure (or Zr rich with hcp structure if we deposit a Zr rich layer) and in

principle a  $\text{ZrV}_2$  Laves phase which has a complicated and large unit cell. The simultaneous growth of such incompatible (not miscible and different lattice) phases one close to the other combined with a limited diffusion is expected to limit naturally the grain size. This is also observed experimentally since the TiZr and ZrV samples analysed by XRD in the present work are crystalline and nanocrystalline respectively (Fig. 5.2). A limitation of this simple model consists in the difficulty to estimate the diffusion rate of the atoms on the surface during deposition. Surface diffusion depends on the material and on the temperature. The appropriate temperature is difficult to evaluate since the atoms reach the surface with a very high kinetic energy compared to the thermal energy at the substrate temperature and the energy loss process is rather complicated.

For the TiZrV ternary films, the nanocrystallinity region is found for the compositions which have low Ti content. This fact shows that the crucial ingredient for the nanocrystallinity is the ZrV combination.

It is interesting to remark that the ternary phase diagram (at 750 °C) for TiZrV (see Fig. 6.4 taken from Ref. [216]) shows a region of miscibility of Ti, Zr, V for a Ti rich composition roughly corresponding to the region of samples of large grain size analysed in the present work. Moreover, for the composition range where nanocrystalline films are produced, the phase diagram predicts several different compounds. This is in agreement with the arguments developed above for the phase diagrams of binary systems.

The sharpness in the transition between grains of less than 5 nm diameter and grains of more than 100 nm diameter as a function of composition cannot be explained with the simple model presented so far.

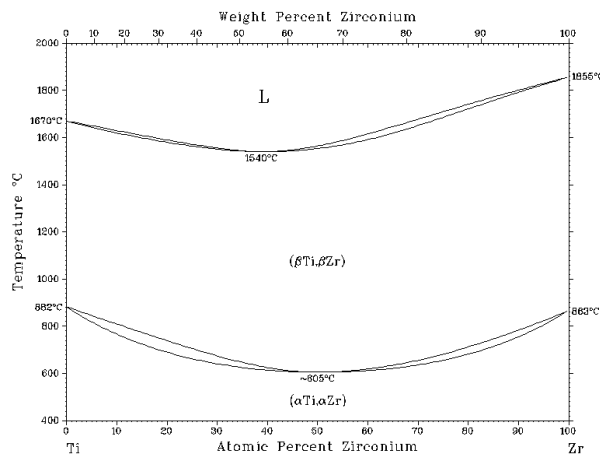


Fig. 6.1: Phase diagram of the binary alloy of Ti and Zr [217].

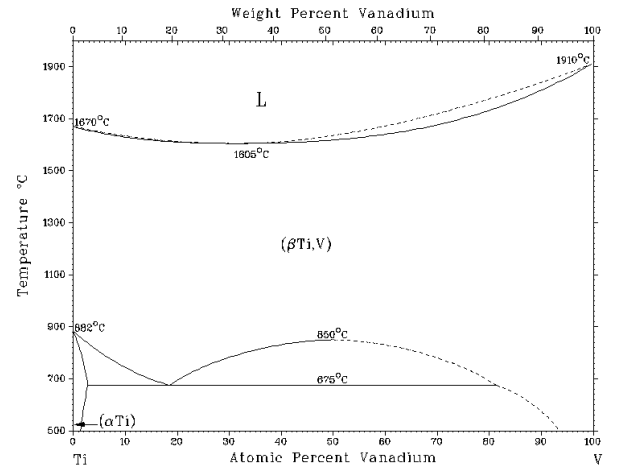


Fig. 6.2: Phase diagram of the binary alloy of Ti and V [217].



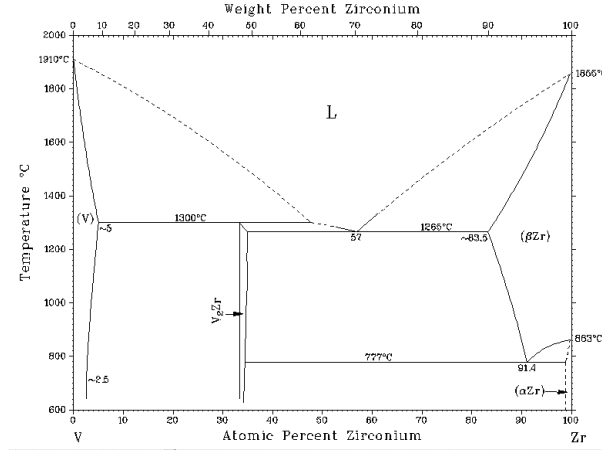


Fig. 6.3: Phase diagram of the binary alloy of V and Zr [217].

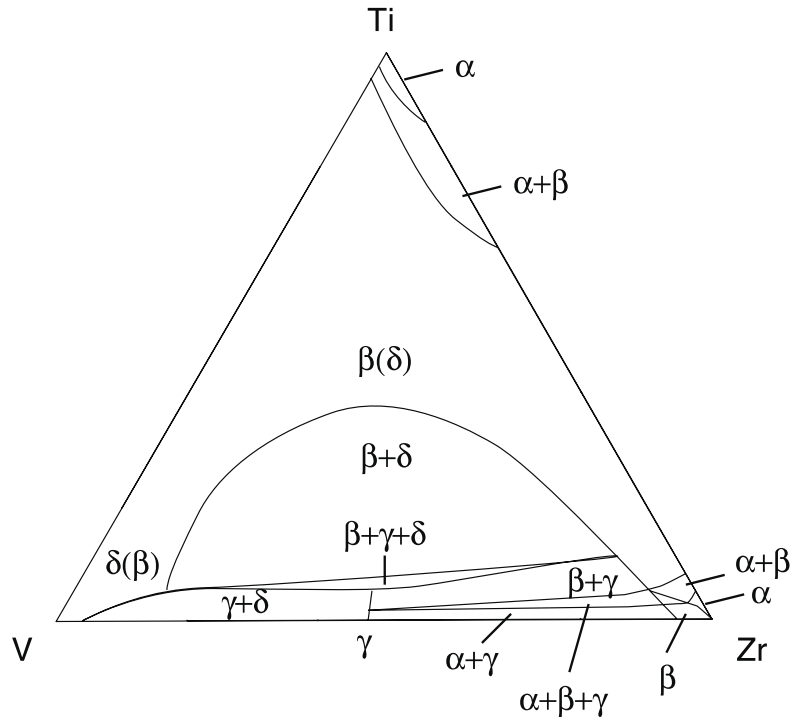


Fig. 6.4: Phase diagram of the ternary alloy of Ti, Zr and V for  $750\text{ }^{\circ}\text{C} < T < 850\text{ }^{\circ}\text{C}$  [216].

### 6.1.2 Activation of TiZrV compared to TiZrCr, TiZrNb

The average grain size of the investigated TiZrV coatings are reported as a function of the composition in Fig. 5.2 and are given in Table 5.2. The activation behaviour as evaluated by AES (using the  $R$  criterion defined in paragraph 5.1.2) is illustrated as a function of the composition in Fig. 5.8. The comparison of the two series of results shows that all the NEG coatings with low activation temperature (high  $R$  value) have an average grain size smaller than 5 nm (those samples are said to be nanocrystalline in this document). Nevertheless, inversely, one TiZrV coating with an average grain size lower than 5 nm has a high activation

temperature, as measured by AES. It corresponds to the composition:  $\text{Zr}_{24}\text{V}_{76}$ .

The role of a component in the TiZrV alloys was investigated by replacing it with other elements. The first choice is to replace V by Cr, an element characterised by an atomic radius smaller than that of V, which should also hinder the solubility and induce nanocrystallinity, in view of the first Hume–Rothery rule and of the arguments developed in paragraph 6.1 (see Fig. 6.5, and Fig. 6.6). In contrast, when V is replaced by Nb of larger atomic size, the formation of solid solution of Ti–Nb and Zr–Nb are not excluded as suggested by the phase diagrams (See Fig. 6.7, and Fig. 6.8).

The activation behaviour of TiZrNb films has been analysed by the standard AES test. The composition of those films as well as their crystallinity are reported in Fig. 6.9. The reduction of  $\text{ZrO}_2$  reveals the same activation behaviour independently of the Nb concentration in the investigated range (Fig. 6.10). The  $R$  value is always lower, and the activation temperature higher, than those corresponding to the easily activated TiZrV samples. All the TiZrNb films have a crystallite size larger than 200 nm (Fig. 6.9), in agreement with the above considerations from the phase diagrams. This result provides further evidence of the need of nanocrystallinity in obtaining low activation temperatures (see paragraph 5.1.2). XRD analysis reveals that TiZrCr layers of several compositions have nanocrystalline structure (Fig. 6.11). However, despite their crystallite size lower than 5 nm, all TiZrCr film compositions tested appear to activate at higher temperatures than the easily activated TiZrV samples (Fig. 6.12). This, again, provides evidence that the nanocrystallinity of the films is not enough to guarantee low activation temperature.

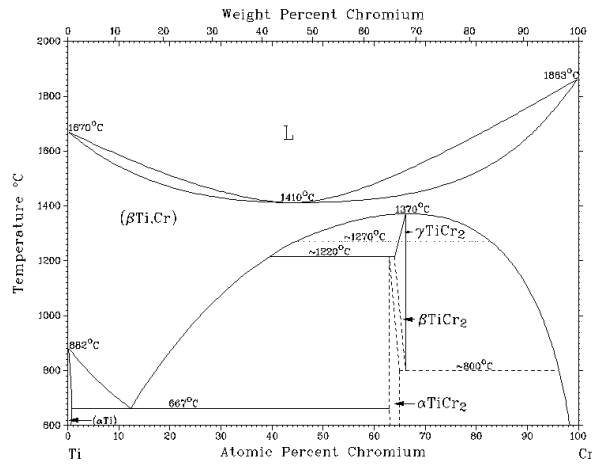
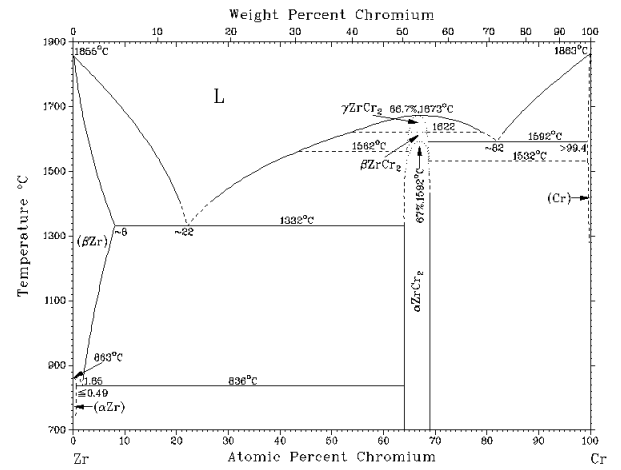


Fig. 6.5: Phase diagram of the binary alloy of Ti and Cr [217].



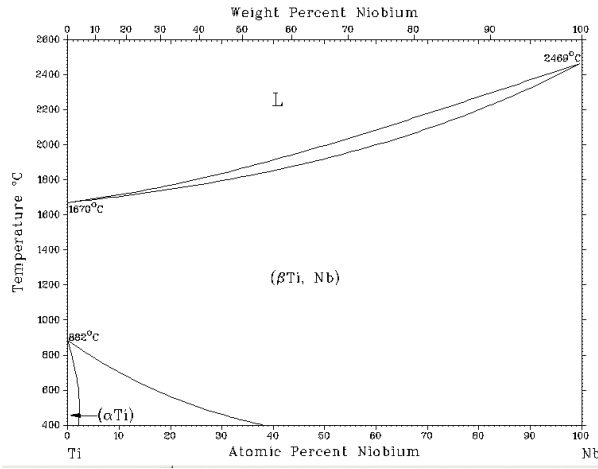


Fig. 6.7: Phase diagram of the binary alloy of Ti and Nb [217].

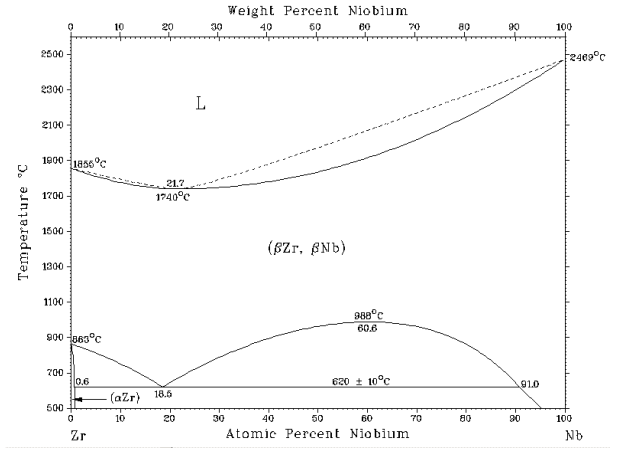


Fig. 6.8: Phase diagram of the binary alloy of Zr and Nb [217].

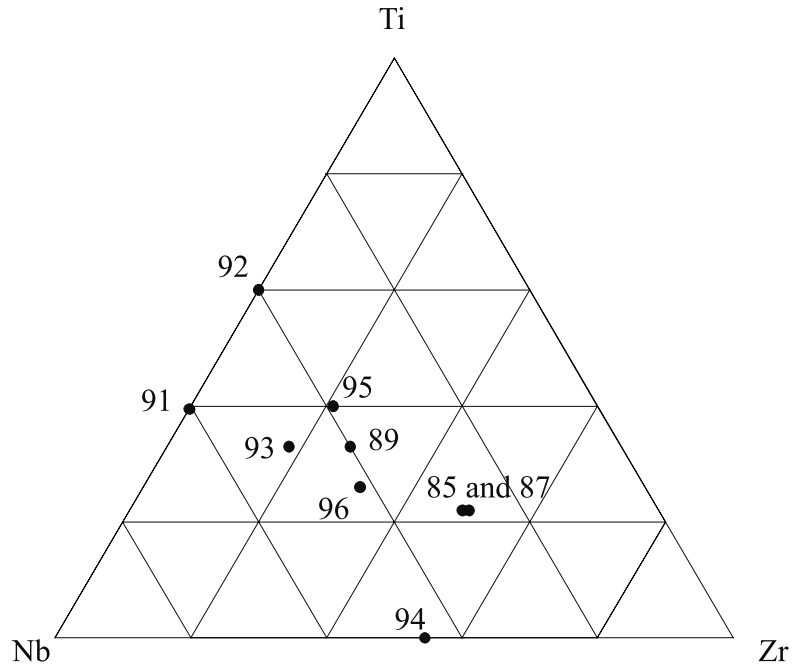


Fig. 6.9: Indication on a ternary diagram of the TiZrNb compositions tested by XRD. All samples present a grain size larger than 100 nm.

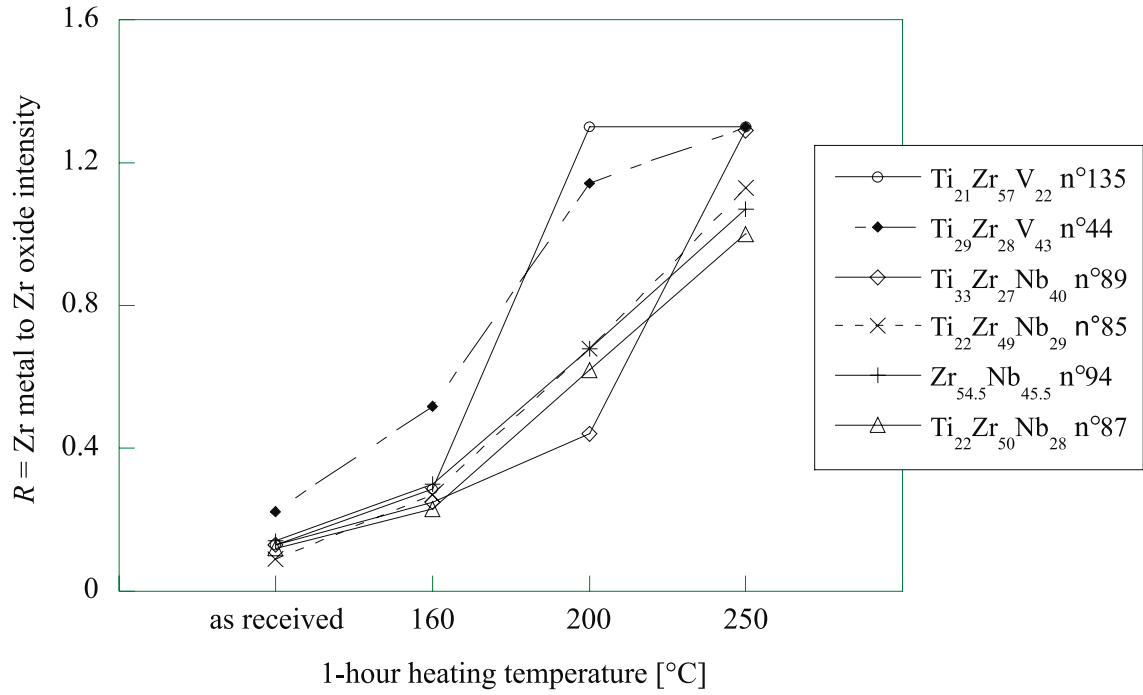


Fig. 6.10: AES results obtained for TiZrNb coatings and presented using the  $R$  criterion (see paragraph 5.1.2). A high  $R$  value indicates a high degree of activation. The crystallinity of the samples is indicated in Fig. 6.9. Some TiZrV samples are added for comparison.

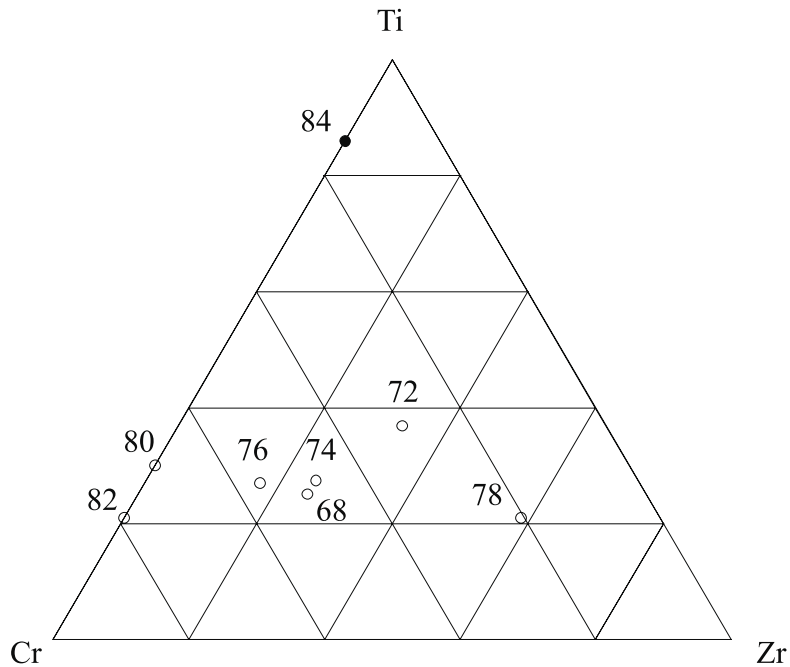


Fig. 6.11: Indication on a ternary diagram of the TiZrCr compositions tested by XRD. The black symbols represent the samples with grains larger than 100 nm, and the open ones represent samples with a grain size below 5 nm.

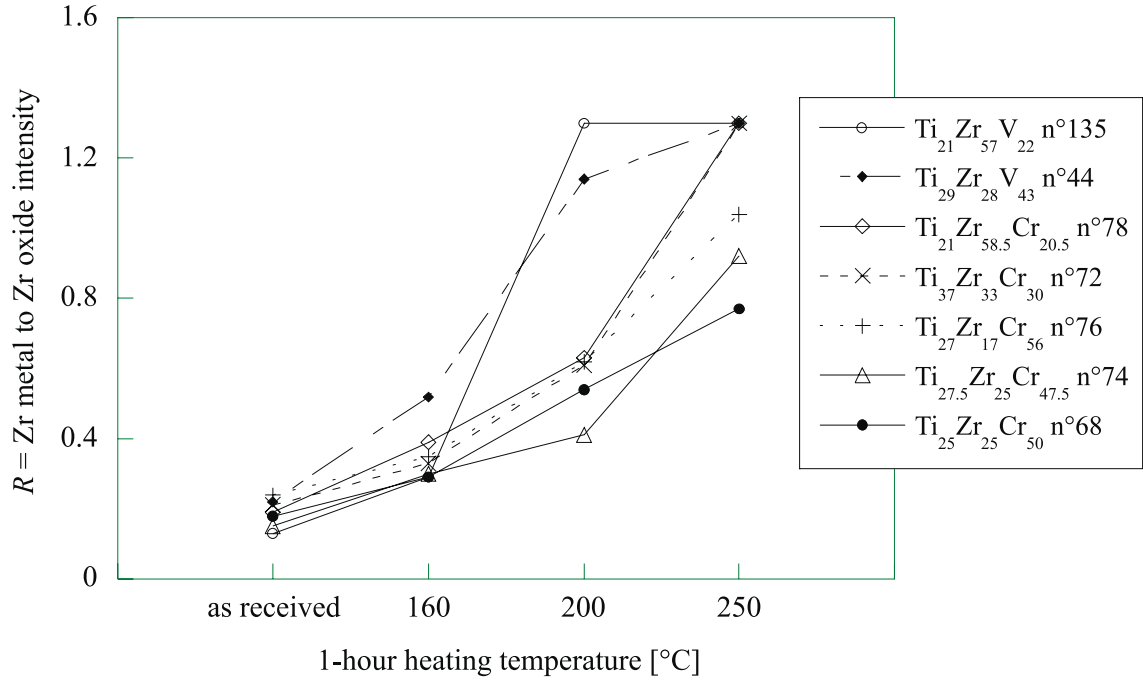


Fig. 6.12: AES results obtained for TiZrCr coatings and presented using the  $R$  criterion (see paragraph 5.1.2). A high  $R$  value indicates a high degree of activation. The crystallinity of the samples is indicated in Fig. 6.11. Some TiZrV samples are added for comparison.

During activation, oxygen must diffuse out from the surface. Since the diffusion along grain boundaries is faster than that in the lattice (see paragraph 2.1.2), the presence of a large amount of grain boundaries per unit volume should favour the activation. This means that small grains, as in nanocrystalline films, favour diffusion and hence a faster activation or a lower activation temperature. In the same way, the solubility might be increased in the case of small grains because the grain boundaries may retain considerable amounts of oxygen. While these considerations may justify the benefits of a small grain structure, they do not help understanding why some nanocrystalline materials display a high activation temperature. Actually, they do not take into account the different stabilities of the oxides present on the surface. The Cr oxides are very stable (see Fig. 2.1) and their reduction more difficult compared to that of the oxides of V.

### 6.1.3 Conclusions

Small crystals (a few nanometers large, or nanocrystals) have a positive role to obtain low activation temperatures NEG films. However, there is also evidence that the nanocrystallinity is not sufficient to account fully for this effect.

## 6.2 Decrease of pumping speed at $T \geq 250$ °C

The pumping speeds recorded for CO as well as for H<sub>2</sub> generally present a maximum as a function of heating temperature (see for example Fig. 5.16, Fig. 5.21, Fig. 5.22). The irreversible decrease of pumping speed is an handicap in view of the applications. For instance, it may be required to heat the NEG coating above 250 °C in case of a contamination with hydrocarbons, or in order to reduce the SEY. Additionally, both time and temperature contribute to define the activation, so that a limitation in heating temperature may result in a limitation of the heating duration (even at temperatures lower than 250 °C). Therefore, the irreversible deterioration of the NEG coatings is an issue which needs to be clarified. Some possible causes of this behaviour are discussed. Among these, I consider the thermal stability of the crystalline structure, the possible pollution of the NEG coating due to the substrate, and the pollution by a gas.

### 6.2.1 Crystallisation

In view of the role of the crystallites a few nanometers in size for a low activation temperature (see paragraphs 5.1.2 and 6.1), one could try to justify the decrease of the pumping speed by an increase of the grain size during the activation.

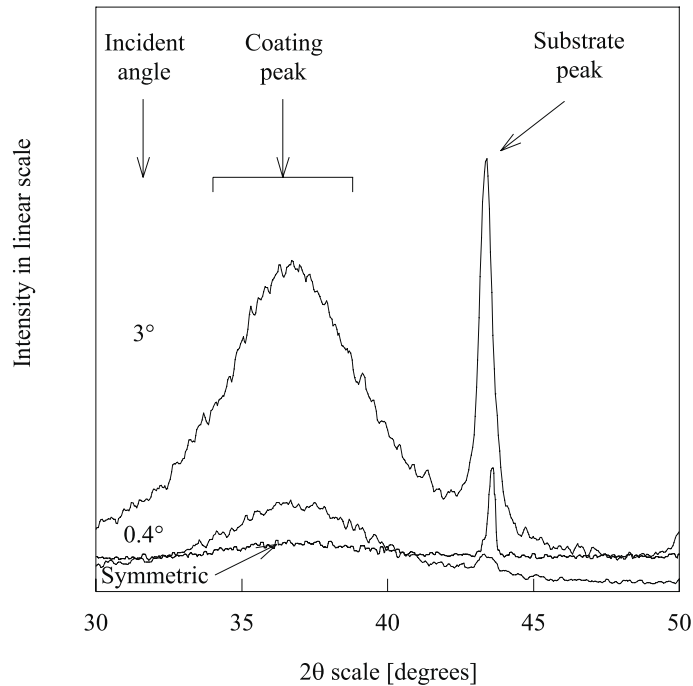


Fig. 6.13: XRD spectra obtained on a Ti<sub>23</sub>Zr<sub>46</sub>V<sub>31</sub> thin film (1 μm thick) in the as-received state. “Symmetric” stands for  $\Theta - 2\Theta$  geometry. The grazing angle characterisation is performed with two different angles of incidence: 0.4° and 3°. Courtesy of H. Jaffrezic from the Ecole Centrale de Lyon.

The XRD spectra of the samples after pumping speed measurements indicate that the average grain size remains smaller than 15 nm after any heating treatment.

In order to improve the sensitivity to the influence of the effect of the thermal treatment on the crystalline structure of NEG thin films, XRD measurements have been performed at grazing incidence. A  $\text{Ti}_{23}\text{Zr}_{46}\text{V}_{31}$  sample has been analysed by XRD before and after a thermal treatment. In order to check the homogeneity of the structure over the whole thickness of the film, the analysis has been repeated using different angles of incidence:  $0.4^\circ$  and  $3^\circ$ . The same sample was also characterised in the  $\Theta - 2\Theta$  geometry for comparison.

The spectra measured in the as-received state are shown in Fig. 6.13. The peaks at  $36^\circ$  have different intensities when measured at different angles of incidence ( $0.4^\circ$  and  $3^\circ$ ). This effect, due to the geometry of the scattering and not to the distribution of the grains, is a consequence of the X-ray penetration. With an angle of incidence of  $0.4^\circ$ , 50 nm of the films are analysed whereas at  $3^\circ$  incidence, a thickness of 500 nm is tested (estimated values). The peak at  $36^\circ$  keeps the same position in angle and the same width at half maximum when measured at both angles of incidence of  $0.4^\circ$  or of  $3^\circ$ . Using the Scherrer formula (see Eq. (4.2)), the average grain size evaluated in both cases is then the same (about 2 nm). This result indicates that the thin film before heating has a homogeneous distribution of crystallites with same grain sizes.

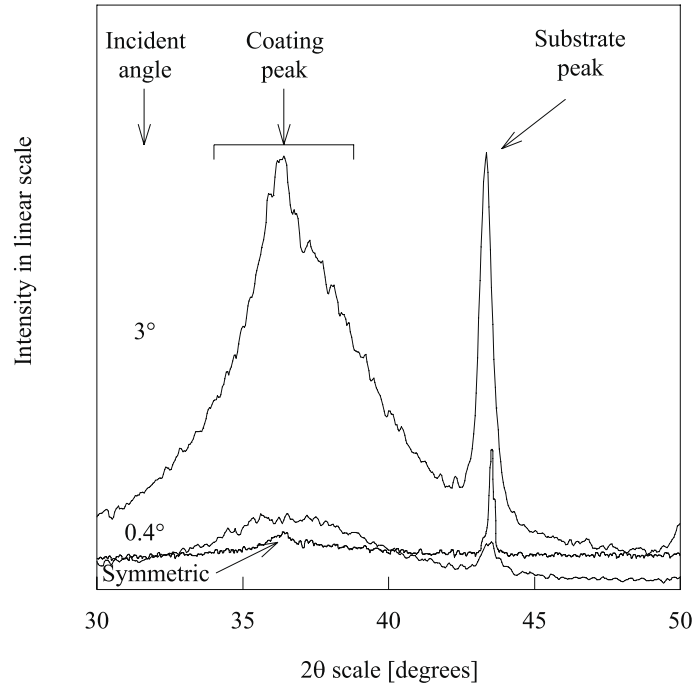


Fig. 6.14: As Fig. 6.13, for the same sample heated for 2 hours at  $300^\circ\text{C}$  plus 2 hours at  $350^\circ\text{C}$ .

The spectra obtained for the same sample after the heat treatment are shown in Fig. 6.14. The signal corresponding to the surface (angle of incidence:  $0.4^\circ$ ) is the same for the heated and the as-received sample. But in the case of the analysis at grazing incidence angle of  $3^\circ$ , the peak at  $36^\circ$  becomes sharper after heating. This reveals a crystalline growth initiated at the film–substrate interface. The average grain size evaluated with the Scherrer formula

is about 2.5 nm over the 500 nm analysed. As it is known that the grain size next to the surface is about 2 nm (thanks to the analysis at 0.4°), the grain size must be much higher than 2.5 nm in the film at the interface with the substrate.

The accuracy on the average grain size is low in the range of few nanometres, so that we should not focus on their absolute values. The interest is in the relative comparison of the line shapes to monitor the grains growth when increasing the heating temperature.

According to the measurements performed in grazing angle geometry, it is possible to detect a growth of the crystallites initiated at the film–substrate interface. Since no change of grain size is observed on the surface of the sample this cannot have any influence on the pumping speed measurements.

A sample consisting of  $\text{Ti}_{24}\text{Zr}_{50}\text{V}_{27}$ , was heated *in situ* under vacuum in a transmission electron microscope for 2 hours up to 430 °C. No change of grain size was measured. The hypothesis that thermally induced crystalline changes could be the cause of the decrease of pumping speed become therefore weakened by the TEM results.

### 6.2.2 Poisoning from the substrate

In this study, the NEG coatings are always deposited on copper substrates (2 mm thick) for measurements of pumping speed. The amount of oxygen diffusing from the copper substrate to the film during the heating cycle is evaluated in order to check if pollution by oxygen could justify the decrease of pumping speed.

As a first approximation, I consider the diffusion length of oxygen in copper as a function of the heating temperature as already defined in Eq. (2.6).

$$L = \sqrt{D(T) \cdot t} \quad .$$

with  $D = 0.011 \times e^{-412000/8.314T} [\text{cm}^2 \text{ s}^{-1}]$  and  $t = 2$  hours.

Table 6.2: Calculation of the diffusion length of oxygen in copper as a function of the heating temperature (for 2 hours).

$T$ [°C]	$D$ [ $\text{cm}^2 \text{ s}^{-1}$ ]	$L$ [cm]
120	$3.60 \times 10^{-8}$	0.016
180	$1.92 \times 10^{-7}$	0.037
200	$3.05 \times 10^{-7}$	0.047
250	$8.31 \times 10^{-7}$	0.077
275	$1.28 \times 10^{-6}$	0.096
300	$1.90 \times 10^{-6}$	0.117

After 2 hours at 300 °C, the oxygen already diffused through more than half the thickness of the copper substrate (see Table 6.2).



More precisely, the calculation is performed using the model defined by Crank [218] for one-dimensional diffusion in a medium between two parallel plates, assuming an initial uniform concentration of oxygen in copper substrate (i.e.  $c = c_o$  from  $x = 0$  mm to  $x = 2$  mm). The OFE copper contains 5 ppm (weight) of oxygen which corresponds to  $c_o = 10^{18}$  atoms  $\text{cm}^{-3}$ . The thickness of the substrate is  $\ell = 2$  mm. At the NEG-copper substrate interface (at  $x = 2$  mm), the TiZrV film is considered to be initially free of oxygen.

If  $M_t$  denotes the total amount of diffusing oxygen which has left the copper sheet at time  $t$  and  $M_\infty$  the corresponding total quantity:

$$\frac{M_t}{M_\infty} = 1 - \sum_{n=0}^{\infty} \frac{8}{(2n+1)^2 \Pi^2} \cdot \exp\left(\frac{-D(2n+1)^2 \Pi^2 \cdot t}{4\ell^2}\right) \quad (6.1)$$

$$\frac{c - c_o}{-c_o} = \sum_{n=0}^{\infty} (-1)^n \operatorname{erfc} \frac{(2n+1)\ell - x}{2\sqrt{Dt}} + \sum_{n=0}^{\infty} (-1)^n \operatorname{erfc} \frac{(2n+1)\ell + x}{2\sqrt{Dt}}. \quad (6.2)$$

From Eq. (6.1), the  $M_t/M_{tot}$  value is plotted as a function of the heating temperature in Fig. 6.15 and transformed to an equivalent number of air exposures assuming that exposure to air provides  $N = 7 \times 10^{15}$  oxygen atoms per  $\text{cm}^2$  via oxide formation.

From Eq. (6.2), the  $c/c_o$  profile across the copper thickness is also obtained for different heating temperatures (Fig. 6.16).

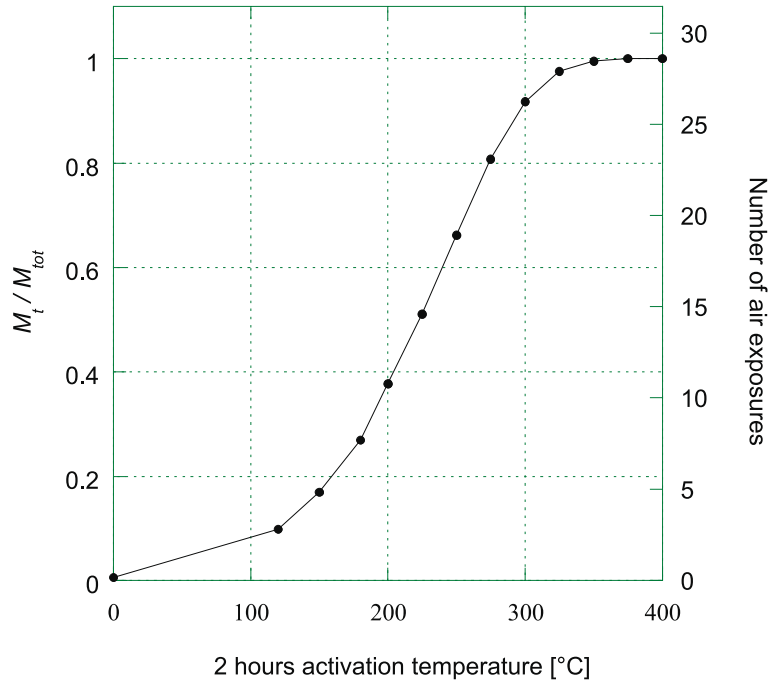


Fig. 6.15:  $M_t/M_{tot}$  for oxygen in a 2 mm thick copper substrate as a function of temperature for successive 2-hour heatings. The evolution as a function of temperature of the oxygen (in number of air exposures equivalence) brought in  $1 \mu\text{m}$  of TiZrV by a 2 mm copper substrate initially containing  $c_o = 10^{18}$  atoms  $\text{cm}^{-3}$  of oxygen is indicated.

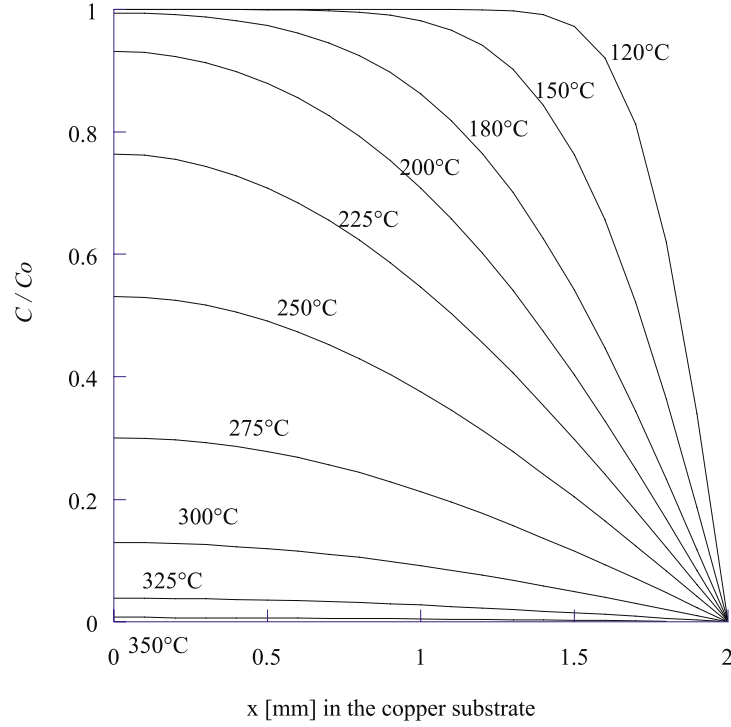


Fig. 6.16:  $c/c_o$  profile for oxygen in a 2 mm thick copper substrate after 2 hours of activation at various temperatures. The interface air–substrate is located at  $x = 0$  mm. The substrate is between  $x = 0$  mm and  $x = 2$  mm. The interface substrate–NEG is located at  $x = 2$  mm. The initial oxygen concentration is  $c/c_o = 1$  in the substrate. One hypothesis of the model is that the oxygen concentration remains negligible in the NEG during the whole heating treatment.

These results could be alarming since half of the oxygen has already diffused from the copper substrate to the NEG coating after 2 hours of heating at 250 °C. However, the decrease of pumping speed was recorded also for NEG coatings on stainless steel. The diffusion of oxygen in the latter material is six times slower than in copper, but the pumping speed decrease takes place at about the same temperature (between 250 °C and 300 °C). Consequently, the observed effect cannot be due to the diffusion of oxygen from the substrate.

Another hypothesis could be an interdiffusion of the substrate component and the coating material during the heating cycle. The diffusion length of copper in Ti is compared to that of O, C and H for a 2-hour heating at increasing temperatures (Fig. 6.17). The same calculation has been done for Zr (Fig. 6.18). It comes out that the diffusion of copper in Zr and Ti is of the same order of magnitude as that of oxygen. This result could be alarming, but it would take more than 10 days at 350 °C for copper to reach the surface of a Zr film 1  $\mu\text{m}$  thick (Fig. 6.19) and about 40 days at 450 °C for copper to reach the surface of a Ti film 1  $\mu\text{m}$  thick. Consequently, in practice, the surface of the NEG is never polluted by copper in the conditions in which they are used.

In agreement with this calculation, the AES spectra taken on the thermally treated films (more than 200) have never shown any trace of copper.

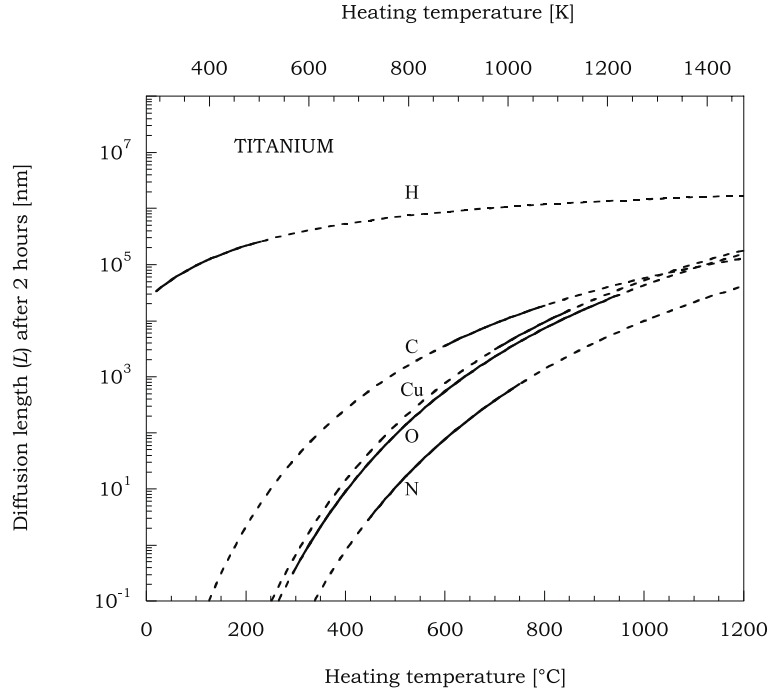


Fig. 6.17: Diffusion length of Cu in Ti compared to that of O, C and H for a 2-hour heating at different temperatures. The diffusion coefficient of Cu in Ti ( $\alpha$ ) from 980 to 1120 K is  $D = 0.38 \times e^{-195000/8.314T}$  [ $\text{cm}^2 \text{s}^{-1}$ ] [219]. The diffusion coefficient of O, C and H in Ti are taken from [45]. Extrapolated data are in dashed lines.

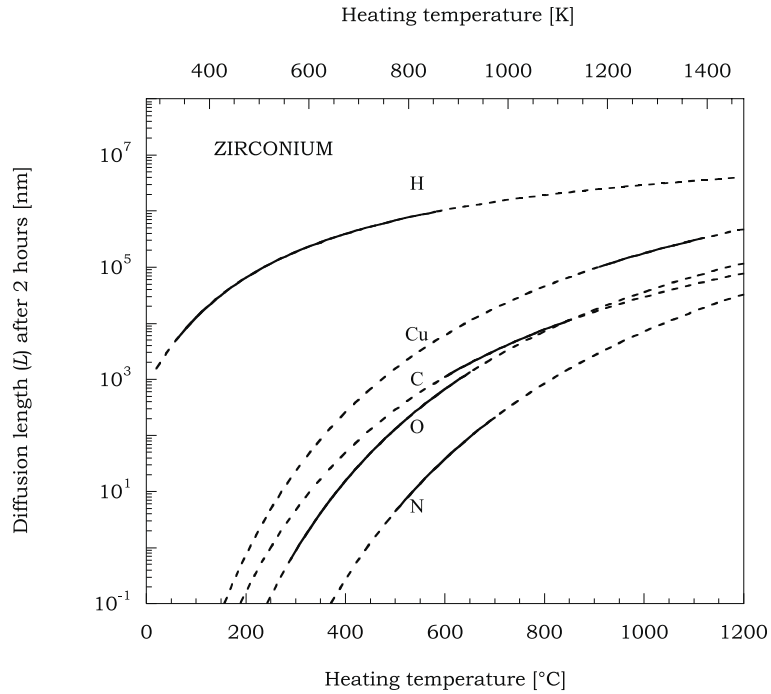


Fig. 6.18: As Fig. 6.17 for Zr. The diffusion coefficient of Cu in Zr ( $\beta$ ) from 1173 to 1290 K is  $D = 0.1 \times e^{-155000/8.314T}$  [ $\text{cm}^2 \text{s}^{-1}$ ] [219]. The diffusion coefficient of O, C and H in Zr are taken from [45]. Extrapolated data are in dashed lines.

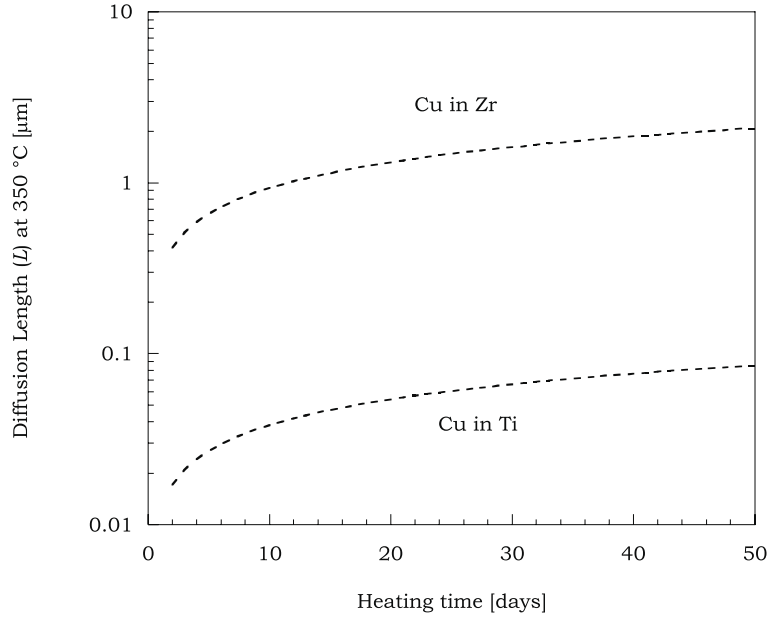


Fig. 6.19: Diffusion length of Cu in Ti and Zr as a function of heating time for a constant heating temperature of 350 °C. The diffusion data used are the same as in Figs. 6.17 and 6.18.

### 6.2.3 Poisoning by gas

A possible cause of the decrease of pumping speed when heating at  $T \geq 250$  °C could be a poisoning of the NEG surface by a gas. This contaminant gas could be released during heating by the vacuum system. In order to simulate the effect of a contaminant gas on the NEG, the following experiment was undertaken. The CO and H<sub>2</sub> pumping speeds were measured for two identical NEG samples after heating for 2 hours at increasing temperatures (according to the heating treatment described in paragraph 4.3.4). CO saturations were performed periodically on one of the samples in order to check if the resulting pumping speed is lowered.

For sample b.3, the onset of the CO pumping speed is between 150 °C and 180 °C and a large increase is observed afterwards up to a maximum value ( $\alpha_{co} = 0.8$ ) reached after 2 hours heating at 225 °C (Fig. 6.20 a). Heating at temperatures higher than 225 °C results in a decrease of the CO pumping speed. The evolution of the H<sub>2</sub> sticking probability as a function of the heating temperature is shown in Fig. 6.20 b. A H<sub>2</sub> sticking probability higher than the detection limit is obtained after 2 hours heating at a temperature of about 150 °C. The H<sub>2</sub> sticking probability increases up to a maximum value reached after 2 hours of heating at 225 °C ( $\alpha_{H_2} = 4.6 \times 10^{-2}$ ) and decreases down to  $\alpha_{H_2} = 1.8 \times 10^{-2}$  when heating to 325 °C.

For the second and identical sample (b.4), the CO and H<sub>2</sub> pumping speeds measured are the same as for b.3 up to 2 hours heating at 225 °C. At higher temperatures, the decrease of pumping speed is limited by the intermediate CO saturations.

It is consequently very improbable that the pollution by a gas during bakeout could be

at the origin of the NEG poisoning. On the contrary, successive saturations with CO do not deteriorate the pumping speed, but rather help to maintain it close to its maximum value.

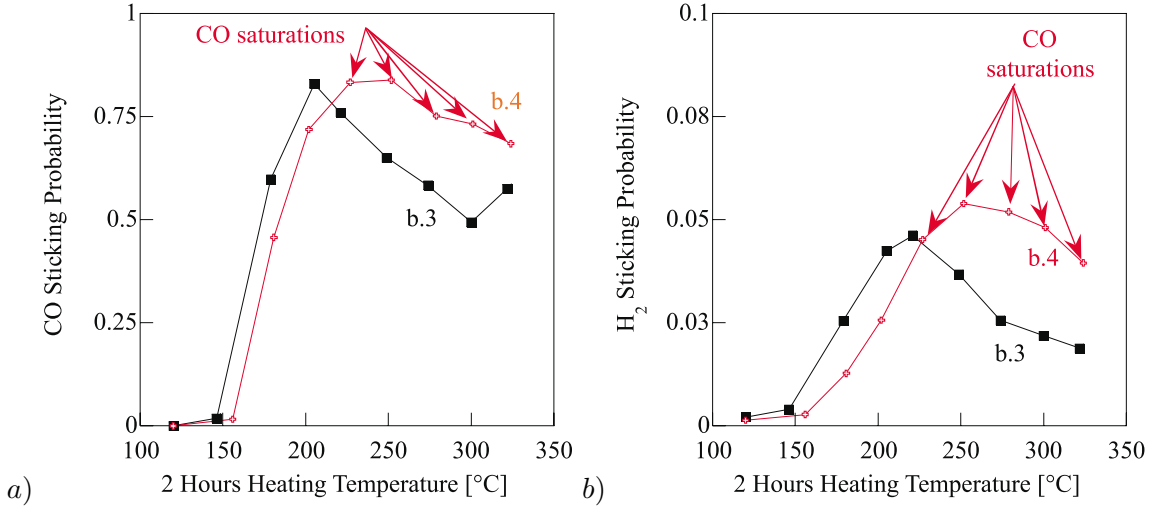


Fig. 6.20: Comparison of the sticking probabilities of identical NEG films, one of the two being periodically saturated with CO. CO (a) and H<sub>2</sub> (b) results for samples b.3 and b.4, Ti<sub>32</sub>Zr<sub>16</sub>V<sub>52</sub>, deposited on a rough copper substrate, with  $T_s = 300$  °C. Note that adding CO limits the pumping speed decrease consequent to heating above 225 °C.

#### 6.2.4 Conclusions

We have examined the following possible causes of the decrease of the pumping speeds with increasing temperature of heating above the maximum generally recorded for CO as well as for H<sub>2</sub> at 225 °C: thermal instability of the crystalline structure, pollution of the NEG coating due to the substrate, pollution by a gas. These disturbing effects do not appear to be relevant for the deterioration of the NEG properties.

Whatever the real cause could be, it must be compatible with two important experimental facts, namely:

- it is undetectable by all the analytical tools which have been used for this work.
- it is counteracted by the addition of CO during the heating sequence (see Fig. 6.20).

It is known that impurities may hinder the atomic mobility and grain growth. Therefore, one may speculate that added carbon atoms prevent the formation of unfavourable surface phases or inhibit the annealing of crystal defects and/or nanoprotusions.

# Chapter 7

## Conclusions

Getters are solid materials capable of chemisorbing gas molecules on their surface: getters are chemical pumps. They are widely used in a variety of applications such as in particle accelerators, vacuum tubes, field-emission display (FED), inert gas purification systems, H<sub>2</sub> plasma purification, hydrogen species recycling as in the Tokamak Fusion Test Reactor. Among the different Non-Evaporable Getter (NEG) materials tested, the TiZrV alloys have the lowest activation temperature. For this reason, the TiZrV coatings were the object of this work. In particular, the aim of this investigation was to understand how to optimise three important properties of TiZrV coatings: to achieve the lowest possible activation temperature ( $T_a$ ), and to obtain the highest pumping speed and surface pumping capacity. This objective is important in the context of the LHC accelerator, since for the experimental regions, aluminium alloys will be used for the manufacturing of some vacuum chambers, which then could not be heated above 200 °C.

In the present investigation, TiZrV coatings (250 samples) of various compositions have been deposited by DC (Direct-Current) diode magnetron sputtering. The influence of the substrate material, substrate roughness, substrate temperature ( $T_s$ ), film composition, on the activation temperature and pumping properties have been investigated in order to optimise the deposition parameters for vacuum applications.

The characterisation of the films has been carried out by Auger Electron Spectroscopy (AES), X-ray Photoelectron Spectroscopy (XPS) and Energy Dispersive X-ray spectroscopy (EDX) for the surface and bulk chemical composition, respectively, and by X-Ray Diffraction (XRD), Scanning Electron Microscopy (SEM), Transmission Electron Microscopy (TEM) and Scanning Tunnelling Microscopy (STM) for the morphology and crystallinity. The performances of the best coatings selected through the above mentioned methods have been investigated by pumping speed measurements of H<sub>2</sub>, CO and N<sub>2</sub>.

The main results of this investigation are the following.

XRD measurements prove that depending on their composition, the TiZrV coatings can

be grouped into two families which are sharply separated with respect to their grain size: polycrystalline films, with grain size above 100 nm and nanocrystalline films with grain size below 5 nm. TEM images clearly reveal grains with sizes in the nanometer range for the tested samples of the second family.

The surface of the NEG TiZrV getter coatings was analysed by AES, first in the as-received state (typically after less than 15 minutes air exposure) and then after *in situ* heating for 1 hour at a given temperature in order to monitor their activation behaviour. A quality criterion ( $R$ ) was defined to quantify the degree of activation of TiZrV films.  $R$  is the ratio of the peak-to-valley height of the Zr–AES component at 147 eV (corresponding to a Zr metallic component) to the peak-to-valley height of the Zr–AES component at 141 eV (corresponding to Zr in ZrO<sub>2</sub>) measured at 200 °C. A high  $R$  value indicates a high degree of reduction of the oxide and hence a high degree of the activation. According to AES results, TiZrV coatings of different compositions can be divided into two groups: one group of high activation temperature ( $T_a > 200$  °C for 1 hour heating) and one of low activation temperature ( $T_a < 200$  °C for 1 hour heating).

For the first time, a clear relation between morphology and activation has been found: without exception, the TiZrV NEG films with low activation temperature are among the coatings crystallising with small grain size (below 5 nm).

Pumping properties were studied for TiZrV coatings of low activation temperature.

For TiZrV coatings sputtered in identical conditions, different substrate materials (stainless steel 316LN, copper –rough, smooth or electrolytically deposited–, Glidcop<sup>®</sup>, aluminium, beryllium, glass, and Be-Al) were found to induce different morphologies (possibly affecting the pumping capacity), but identical crystallinity (grain size below 5 nm) and activation temperature.

The roughness of the copper substrate obtained by various chemical treatments was found to be reproduced by the coating. The increased surface roughness does not accelerate the activation process, but clearly increases pumping speed and surface pumping capacity.

The substrate temperature during sputter deposition ( $T_s$ ) was found to be a sensitive parameter to increase the roughness of a coating on copper without changing its crystallinity up to 250 °C. It appears clearly that the ideal copper-substrate temperature is  $T_s = 250$  °C in terms of sticking probability for CO and for H<sub>2</sub>. This temperature yields also the best surface pumping capacity for CO on rough substrates. Indeed, by combining this coating temperature ( $T_s = 250$  °C) with a rough substrate, the surface pumping capacity results improved by a factor of 100 compared to a film of identical composition deposited at 100 °C on smooth copper. The pumping speed is correspondingly enhanced. In conclusion, the improvement of the NEG films obtained by selecting the best deposition parameters consists in achieving the same level of pumping capacity for a 2 µm thick coating as for the available commercial NEG films more than 100 µm thick.

The vacuum performance of the best NEG TiZrV coatings for the main gases found in Ultra High Vacuum (UHV) systems have been studied according to standard pumping speed evaluation procedures. It includes the mutual influence of a gas load on the pumping speed and the study of a pumping speed decrease generally recorded when increasing temperature of heating above 250 °C.

N<sub>2</sub> load affects only slightly the H<sub>2</sub> pumping and does not affect the CO pumping at all. CO load reduces appreciably the pumping speed of the other gases as already observed for St101 and St707.

In the case of TiZrV coatings, a pumping speed decrease with increasing temperature of heating above 250 °C is generally recorded for CO as well as for H<sub>2</sub>. This feature had already been observed, although in a different temperature range, for other NEGs (namely the St707). We have explored the following possible causes for this phenomenon: thermal instability of the crystalline structure, pollution of the NEG coating due to the substrate, pollution by a gas. These disturbing effects do not appear to be relevant for the deterioration of the NEG properties. The possibility of other types of surface modifications (formation of unsuitable surface phases by segregation, removal of lattice defects and/or nanoprotusions) which could not be detected by means of the available investigation methods, remains open.

A new phenomenon has been discovered in relation with this decrease of pumping speed. When saturations with CO are performed before heating above 225 °C the NEG for a new pumping speed measurement, the value of the pumping speed is increased compared to the case of an identical sample which was not subjected to the injections of CO. This indicates that under these conditions carbon adsorption improves the pumping speed of the TiZrV films. No clear explanation has been found for this phenomenon yet.

As a conclusion, the preparation of the best TiZrV NEG coatings, as resulting from this investigation, corresponds to the following procedure.

- The films are deposited by DC diode magnetron sputtering using either Ar or Kr as discharge gas. We found that a large zone of compositions within the TiZrV ternary diagram provide equivalently good properties. A cathode made of three intertwined wires (one of Ti, one of V and the third of Zr) provides a composition of low activation temperature. This is an important feature for the coating of long vacuum tubes (like those for the LHC).
- In the case of a cathode made of intertwined wires, the adopted discharge pressure is  $3 \times 10^{-2}$  Torr, the discharge voltage is 500 V, and the discharge current is 40 mA m<sup>-1</sup>, the field applied is 200 G ( $= 2 \times 10^{-2}$  T), resulting in a film growth rate of 0.1 μm h<sup>-1</sup>. Higher coating rates (up to 0.5 μm h<sup>-1</sup>) are also possible.
- The substrate must be cleaned by one of the chemical treatments described previously



depending of its nature. If the experiment allows it, the copper substrates are roughened by a chemical attack in view of increasing the actual surface available for pumping.

- The optimum substrate temperature during the sputter deposition process, both in terms of sticking probabilities and of surface pumping capacity, is  $T_s = 250\text{ }^{\circ}\text{C}$ .

In conclusion, the present study has largely improved the knowledge of the properties of TiZrV getter films. Coatings of optimised characteristics may be reliably produced on vacuum chambers made of different materials. The acquired knowledge is sufficient to adopt this solution for the LHC accelerator at CERN, where about 5 km of this machine will be coated as well as the intersection vacuum chambers for the physic experiments. Meanwhile, TiZrV coated chambers have already been successfully used as a solution in several specific cases such as at the European Synchrotron Radiation Facility (ESRF) (Grenoble, France) and at Elettra (Trieste, Italy) to keep a low dynamic pressure in the undulator aluminium vacuum chambers.

# Chapter 8

## Glossary

### **Gettering rate**

The gettering rate represents the number of gaseous atoms or molecules that are removed from the gaseous phase by the getter per unit time [220].

### **Glow**

During the sputtering process, some of the sputtered atoms collide with high-energy electrons or metastable atoms of the plasma and are excited to high-energy states. When they then de-excite they emit a photon, which create a 'glow'.

### **Ionisation potential**

The ionisation potential is the amount of energy required to remove an electron from an isolated atom or molecule [221].

### **Molecular flow**

Transport phenomena in the molecular state are not determined by molecular collisions or viscosity of the gas. In this case, molecules condense on a surface, rest on it for a given time and then re-evaporate in arbitrary directions [222].

### **Plasma**

In a progression of increasingly energetic states, a plasma can be thought of as the fourth state of matter, starting with solids with their fixed atom positions. Adding energy to this first state allows the atoms to move around each other as a liquid and then to separate completely as a gas. Adding even more energy causes gas atoms to separate into the ions and free electrons of a plasma, although there is no abrupt phase change as there is in going from solid to liquid to a gas [221].

### Secondary electron emission

When an ion approaches a surface at any energy and at any angle, it will be neutralised before impact by interaction with the lattice electrons of the surface. This interaction occurs within less than an atomic diameter of the surface and actually may involve two lattice electrons. One lattice electron is captured by the ion as an orbital electron, thus neutralising the ion. The second electron acquires the excess energy and momentum given up by the neutralising electron and may, as a result, be ejected from the surface. The probability of ejection depends on the type of ion and the type of material making up the surface. The ejection process is referred to as secondary emission. The electrons ejected in this process are referred to as secondary electrons.

### Sievert's law

When considering a chemical reaction [223], the Gibbs free energy change ( $\Delta G$ ) is composed of an enthalpy term ( $\Delta H$ ) and an entropy term ( $\Delta S$ ) according to :

$$\Delta G = \Delta H - T \cdot \Delta S \quad . \quad (8.1)$$

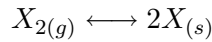
The Gibbs free energy change  $\Delta G$  is related to the equilibrium constant  $K$  for the reaction such as:

$$\Delta G = -k \cdot T \cdot \ln K \quad . \quad (8.2)$$

with  $T$  the temperature and  $k$  the Boltzman constant. From Eqs. (8.1) and (8.2):

$$K = e^{-\frac{\Delta H}{k \cdot T}} \cdot e^{\frac{\Delta S}{k}} \quad . \quad (8.3)$$

In the case of the dissociation of a diatomic gas molecule  $X_2$  on a metallic surface, there is evidence that the solutes generally exist in monoatomic form  $X$ .



where  $g$  and  $s$  denote gas phase and solid solution, respectively. The solubility of the gases studied ( $O_2$ ,  $H_2$ ,  $N_2$ ) is often small enough for Henry's law to apply (the interaction between solute atoms can be neglected). Considering  $P_{X_2}$  the pressure of  $X_{2(g)}$  and  $c$  the concentration of the solid solution, then:

$$K = \frac{c^2}{P_{X_2}} \quad . \quad (8.4)$$

From Eqs. (8.3) and (8.4):

$$P_{X_2} = e^{-\frac{\Delta S}{k}} \cdot c^2 \cdot e^{\frac{\Delta H}{kT}} \quad . \quad (8.5)$$

Setting down:

$$A = e^{-\frac{\Delta S}{k}} \quad . \quad (8.6)$$

$A$  is a constant parameter depending on the getter material, which can be determined experimentally.  $A$  includes the entropic contribution of energy of the dissociation of  $X_{2(g)}$ .

The most common form of Sievert’s law [224], [225] relating the gas concentration to the gas pressure and to the getter temperature results from Eqs. (8.5) and (8.6):

$$P_{X_2} = A \cdot c^2 \cdot e^{\frac{\Delta H}{kT}} \quad (8.7)$$

### **Solubility limit**

Solid solubility limit is the maximum content of solute that can be solved in the solvent at a given temperature, while the solution is still single phase with the structure of the pure solvent [226].

### **TAS**

The front quadrupole absorbers (TAS) are required to absorb the flux of forward high-energy charged and neutral particles that are produced at the high-luminosity IPs 1 and 5 of the LHC, thereby preventing these particles from quenching the inner triplet superconducting quadrupoles and localising the induced activation to the absorber and surrounding shielding.

### **Throughput**

Throughput is defined as the amount of gas flowing per unit time at a fixed temperature across a specified cross section near the pump intake [227], [228]. The gas quantity can be expressed in pressure-volume units or in the number of molecules; the resulting throughput is in Torr  $\ell$  s<sup>−1</sup> or molecules s<sup>−1</sup> respectively.

### **Work function**

The work function of the uniform surface of a metal is defined as the difference in potential energy of an electron between the vacuum level and the Fermi level [229]. The vacuum level is the energy of an electron at rest at a point sufficiently far outside the surface so that the electrostatic image force on the electron may be neglected — more than 10 nm from the surface. The Fermi level is the electrochemical potential of the electrons in the metal.

### **ZAF technique**

The *ZAF* correction allows one to lower errors on the quantitative evaluations made by EDX. *Z* is a correction factor depending on the atomic number of the sample, *A* depends on the absorption of X-rays and *F* corrects the X-rays fluorescence, as described in [230]. As some reference samples allow the calibration of the composition determination, the precision on the concentrations is assumed to be 1% atomic and the minimum detectable concentration is around the same value [231].



# Chapter 9

## Appendix

### 9.1 Sample description and labelling

The small samples dedicated to surface analysis are designated by a number. This number was attributed chronologically each time a new sample was sputter deposited. Remember that two identical samples are always deposited simultaneously. If it is necessary to distinguish between the two samples, they are designated as “number.A” and “number.B”. Otherwise, the letter is dropped.

The large samples dedicated to pumping speed measurements are labelled by a letter. Four identical samples are deposited simultaneously in sputtering system *A*. These four samples are distinguished by using the notation: “letter.x”, with  $x = 1, 2, 3$  or  $4$ . The samples deposited in sputtering system *A*, with a wire cathode made by intertwisting three wires (one of Ti, one of Zr and one of V) of 1 mm in diameter each, using krypton plasma, are described in Table 9.1. Those deposited in sputtering system *B*, using argon plasma, are described in Table 9.2. The chemical treatment applied to the copper substrate before the deposition is designated by Subu5 or Cu6, as described in paragraph 3.2.1.  $T_s$  is the substrate temperature during deposition. The composition indicated is measured by EDX and is given in atomic per cents. In this summary, the reference of the samples as used during the experiments is indicated as former reference of samples. As the notation was too heavy, it was simplified to a new sample labelling system which is the one used in the text.

Table 9.1: Description and labelling of samples deposited in sputtering system *A*.

Sample labelling	Former reference of samples	Deposition run number	Chemical attack of Cu substrate	$T_s$ [°C]	Composition (atomic % )
a.x	Disk-wire3.1, 3.2	35	Subu5	100	Ti <sub>33</sub> Zr <sub>16</sub> V <sub>51</sub>
	Disk-wire3.3, 3.4	35	Subu5	100	Ti <sub>33</sub> Zr <sub>16</sub> V <sub>51</sub>
b.x	Disk-wire4.1, 4.2	44	Subu5	300	~ Ti <sub>32</sub> Zr <sub>16</sub> V <sub>52</sub>
	Disk-wire4.3, 4.4	44	Cu6	300	~ Ti <sub>32</sub> Zr <sub>16</sub> V <sub>52</sub>
c.x	Disk-wire5.1, 5.2	64	Cu6	350	Ti <sub>21</sub> Zr <sub>15</sub> V <sub>64</sub>
	Disk-wire5.3, 5.4	64	Subu5	350	Ti <sub>22</sub> Zr <sub>15</sub> V <sub>65</sub>
d.x	Disk-wire6.1, 6.2	71	Subu5	250	Ti <sub>28</sub> Zr <sub>17</sub> V <sub>55</sub>
	Disk-wire6.3, 6.4	71	Cu6	250	Ti <sub>28</sub> Zr <sub>16</sub> V <sub>56</sub>
e.x	Disk-wire7.1, 7.3	85	Cu6	200	Ti <sub>24</sub> Zr <sub>17</sub> V <sub>59</sub>
	Disk-wire7.2, 7.4	85	Subu5	200	Ti <sub>24</sub> Zr <sub>17</sub> V <sub>59</sub>
f.x	Disk-wire8.1, 8.2	92	Cu6	100	Ti <sub>26</sub> Zr <sub>18</sub> V <sub>56</sub>
	Disk-wire8.3, 8.4	92	Subu5	100	
	Disk-wire9.1, 9.2	97	Subu5	200	Ti <sub>28</sub> Zr <sub>23</sub> V <sub>49</sub>
	Disk-wire9.3, 9.4	97	Cu6	200	
g.x	Disk-wire10.1, 10.3	102	Subu5	150	Ti <sub>24</sub> Zr <sub>20</sub> V <sub>56</sub>
	Disk-wire10.2, 10.4	102	Cu6	150	
h.x	Disk-wire11	109		200	

Table 9.2: Description and labelling of samples deposited in sputtering system *B*.

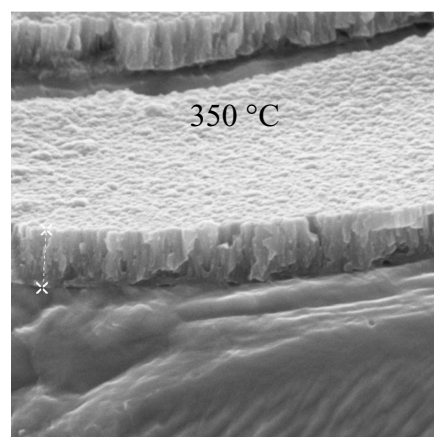
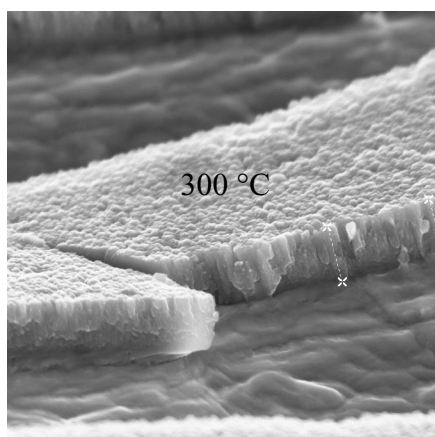
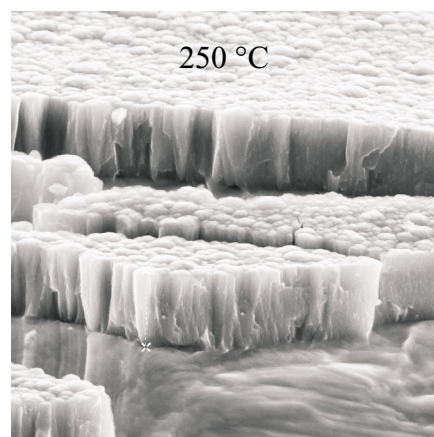
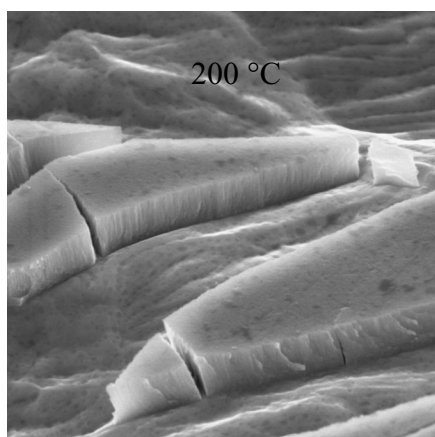
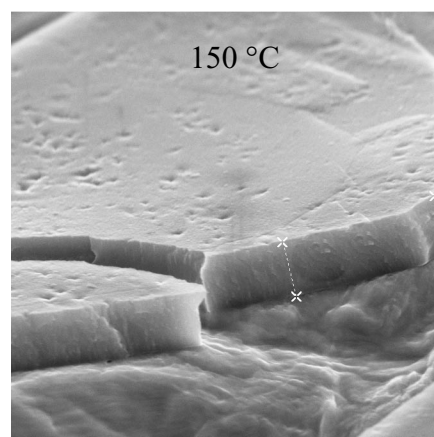
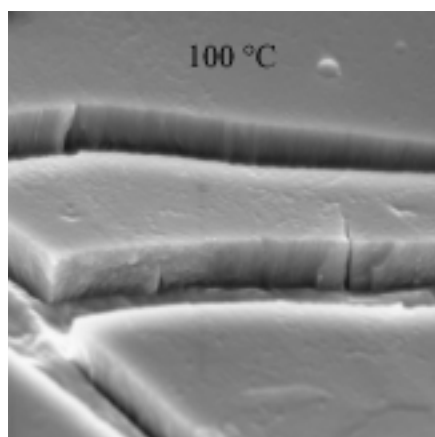
Sample labelling	Former reference of samples	Chemical Attack of Cu substrate	$T_s$ [°C]	Composition (atomic %)
i	Disk1	Subu5	< 100	Ti <sub>25</sub> Zr <sub>47</sub> V <sub>28</sub>
j	Disk2	Subu5	< 100	Ti <sub>24</sub> Zr <sub>53</sub> V <sub>23</sub>
k	Disk3	Subu5	< 100	Ti <sub>41</sub> Zr <sub>22</sub> V <sub>37</sub>
l	Disk4	Subu5	< 100	Ti <sub>26</sub> Zr <sub>19</sub> V <sub>55</sub>
m	Disk5	Subu5	< 100	Zr
n	Disk6	Subu5	< 100	Ti <sub>28</sub> Zr <sub>20</sub> V <sub>52</sub>
o	Disk7	–	< 100	–
p	Disk8	Subu5	< 100	Ti <sub>26</sub> Zr <sub>24</sub> V <sub>50</sub>
q	Disk9	Subu5	< 100	Ti <sub>30</sub> Zr <sub>29</sub> V <sub>41</sub>
r	Disk10	Cu6	< 100	Ti <sub>31</sub> Zr <sub>17</sub> V <sub>52</sub>
s	Disk11	Cu6	< 100	Ti <sub>32</sub> Zr <sub>17</sub> V <sub>51</sub>
t	Disk12	Subu5	< 100	–
u	Disk15	Degreased	< 100	TiZrY
v	Disk16	Subu5	< 100	TiZrY
w	Disk17	Cu6	< 100	TiZrY/Ti
x	Disk18	Subu5	< 100	TiZr/TiZrY/Ti

## 9.2 SEM micrographs of NEG coatings deposited at different substrate temperatures ( $T_s$ )

As a complement to Figs. 5.18 and 5.19 other SEM micrographs of the same samples are shown in Fig. 9.1. The copper substrate is visible on both series of micrographs because the samples were bent so as to see the film profile (to do this, the samples were dipped in liquid  $N_2$  and bent in order to tear the film). The interest of those micrographs is to exhibit the increase of the coating roughness when increasing both the substrate temperature ( $T_s$ ) and the substrate roughness by chemical treatment.



a)



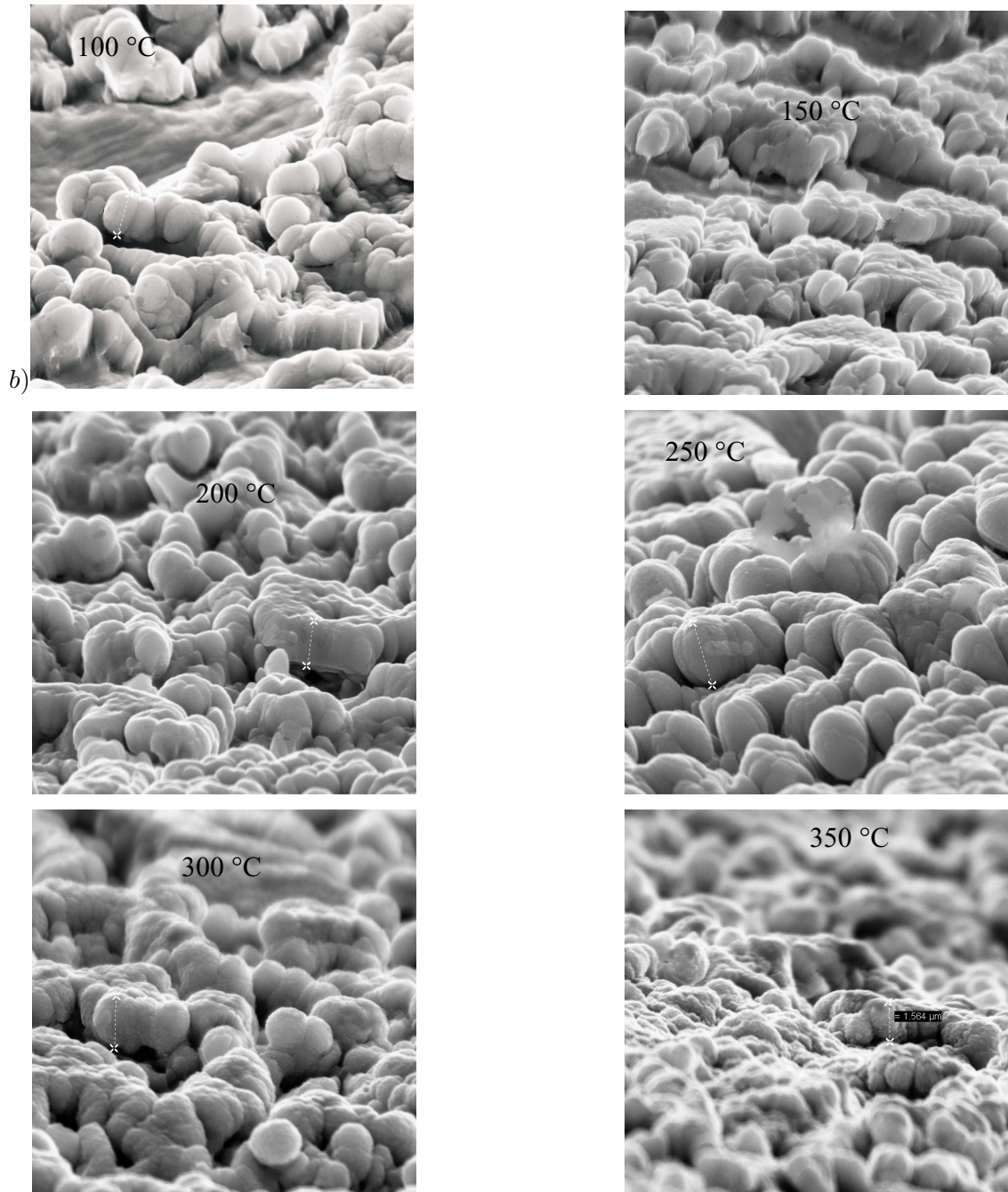


Fig. 9.1: SEM micrographs of TiZrV thin films sputtered on smooth copper substrates at substrate temperatures ranging from 100 to 350 °C in steps of 50 °C (a). Idem on rough copper substrates (b). Micrographs size: 15  $\mu\text{m}$   $\times$  15  $\mu\text{m}$ .



# Bibliography

## Bibliography Chapter 1

- [1] C. Benvenuti, “A New Pumping Approach for the Large Electron Positron Collider (LEP)”, Nuclear Instruments and Methods, vol. 205, pp. 391–401 (1983).
- [2] High Vacuum Series, “The Physical Basis of Ultrahigh Vacuum”, edited by P. Redhead, J. Hobson, E. Kornelsen, published by Chapman and Hall, London (1968), p. 78.
- [3] C. Benvenuti, “Molecular Surface Pumping: the Getter Pump”, in “Vacuum Technology”, Proceedings of the CERN Accelerator School, Scanticon Conference Centre, Snekersten, Denmark, 28 May – 3 June 1999, CERN report 99-05, edited by S. Turner (1999).
- [4] “Traité des Matériaux, vol. 1: Introduction à la Science des Matériaux”, edited by W. Kurz, J.-P. Mercier, G. Zambelli, published by Presses Polytechniques et Universitaires Romandes Lausanne, Second Edition (1995).
- [5] N. Marquardt, “Introduction to the Principles of Vacuum Physics”, in the same book as Ref. [3] above.
- [6] “Foundations of Vacuum Science and Technology”, edited by J. Lafferty, published by John Wiley and Sons, Inc., New York, (1998), p. 262.
- [7] Idem as [6] p. 511.
- [8] P. Redhead, “The Ultimate Vacuum”, Vacuum, vol. 53, n° 1–2, pp. 137–149 (1999).
- [9] “Notions de Base en Technique du Vide”, edited by G. Rommel, published by Société Française du Vide, supplément à la revue “Le Vide: Science, Technique et Applications”, n° 277, Juillet, Aout, Septembre (1995), p. 128.
- [10] Idem as [6] p. 267.
- [11] R. Swalin, “The Science and Technology of Materials, vol. 3: Thermodynamics of Solids”, published by Wiley-Interscience, New York, Second Edition (1972), p. 177.
- [12] C. Benvenuti, “Non Evaporable Getters: from Pumping Strips to Thin Film Coatings”. Internal Report.

- [13] C. Benvenuti, R. Calder, O. Gröbner, “Vacuum for Particle Accelerators and Storage Rings”, *Vacuum*, vol. 37, n° 8–9, p. 699-707 (1987).
- [14] C. Benvenuti, P. Chiggiato, “Obtention of Pressures in the  $10^{-14}$  Torr Range by Means of a Zr-V-Fe Non Evaporable Getter”, *Vacuum*, vol. 44, n° 5–7, pp. 511–513 (1993).
- [15] P. della Porta, “Present Knowledge on Residual Gases in Electron Tubes”, in *Advances in Electron Tube Techniques*, edited by D. Slater, Proceedings of the Sixth National Conference, Sept. 1962, Macmillan, New York (1963).
- [16] M. Amiotti, S. Tominetti, “Getters Boost Lifetimes of Field-Emission Displays”, *Vacuum Solutions*, n° 10, pp. 25–29 (1999).
- [17] “A Stronger Suck”, *The Economist*, September 12<sup>th</sup> 1998.
- [18] L. Rosai, M. Borghi, “Purification of Rare Gases and the Measurement of Low Residual Impurity Levels”, *Journal of Vacuum Science & Technology A: Vacuum, Surfaces and Films*, vol. 11, n° 1, pp. 347–349 (1974).
- [19] J.L. Cecchi, “Impurity Control in TFTR”, *Journal of Nuclear Materials*, vol. 93-94, pp. 28–43 (1980).
- [20] G.M. McCracken and P.E. Stott, *Nuclear Fusion*, vol. 19, p. 889 (1979).
- [21] H.F. Dylla, *Journal of Nuclear Materials*, vol. 93–94, p. 61 (1980).
- [22] F. Waelbroeck, P. Wienhold, J. Winter, “Thermally Activated Processes in Hydrogen Recycling”, *Journal of Nuclear Materials*, vol. 111–112, pp.185-188 (1982).
- [23] E.S. Marmar, *Journal of Nuclear Materials*, vol. 76–77, p. 59 (1978).
- [24] C. Benvenuti, J. M. Cazeneuve, P. Chiggiato, F. Cicoira, A. Escudeiro Santana, V. Johaneck, V. Ruzinov, J. Fraxedas, “A Novel Route to Extreme Vacuum: the Non-Evaporable Getter Thin Film Coatings”, *Vacuum*, vol. 53, n° 1–2, p. 219–225 (1999).
- [25] C. Benvenuti, P. Chiggiato, F. Cicoira, Y. L’Aminot, “Nonevaporable Getter Films for Ultrahigh Vacuum Applications”, *Journal of Vacuum Science & Technology A: Vacuum, Surfaces and Films*, vol. 16, n° 1, pp. 148–154 (1998).
- [26] C. Benvenuti, P. Chiggiato, “Pumping Characteristics of the St707 Nonevaporable Getter (Zr 70 V 24.6-Fe 5.4 wt % )”, *Journal of Vacuum Science & Technology A: Vacuum, Surfaces and Films*, vol. 14, n° 6, pp. 3278–3283 (1996).
- [27] C. Benvenuti, P. Chiggiato, P. Costa Pinto, A. Escudeiro Santana, T. Hedley, A. Mongelluzzo, V. Ruzinov, I. Wevers, “Vacuum Properties of TiZrV Non-Evaporable Getter Films”, *Vacuum*, vol. 60, n° 1–2, pp. 57–65 (2001).

- [28] C. Benvenuti, “Recent Advances in Vacuum Techniques for Accelerators”, Proceedings of the Tenth International Conference on Cyclotrons and their Applications, East Lansing, MI, USA, 30 April-3 May 1984, pp. 540–546 (1984).
- [29] P. Chiggiato, R. Kersevan, “Synchrotron Radiation-Induced Desorption from a NEG-Coated Vacuum Chamber”, *Vacuum*, vol. 60, n° 1-2, pp. 67–72 (2001).
- [30] F. Zimmermann, “Discussion: Electron Clouds Effects, Vacuum”. Proceedings of the 11<sup>th</sup> Chamonix Workshop, 15–19 January 2001, Chamonix, France, pp. 176–177 (2001).
- [31] G. Rumolo, F. Zimmermann, “Theory and Simulation of the Electron Cloud Instability”. Proceedings of the 11<sup>th</sup> Chamonix Workshop, 15–19 January 2001, Chamonix, France, pp. 166–175 (2001).
- [32] F. Zimmermann, “Electron-Cloud Simulations: an Update”, Proceedings of the 11<sup>th</sup> Chamonix Workshop, 15–19 January 2001, Chamonix, France, pp. 144–159 (2001).
- [33] H. Lengeler, “Modern Technologies in RF Superconductivity”, Proceedings of the CERN Accelerator School Fifth General Accelerator Physics Course, CERN Report 94-01, edited by S. Turner, vol. 2, pp. 791–805 (1994).
- [34] F. Ruggiero, “Electron Cloud Effects, Vacuum (SPS+LHC). Summary”, Proceedings of the 11<sup>th</sup> Chamonix Workshop, 15–19 January 2001, Chamonix, France, pp. 10–13 (2001).
- [35] G. Rumolo, F. Zimmermann, “Simulation of Single Bunch Instabilities Driven by Electron Cloud in the SPS”, Proceedings of 2001 Particle Accelerator Conference, Chicago, IL, USA, 18–22 June 2001, vol. 3, pp. 1886–8 (2001).
- [36] V. Baglin, O. Brüning, R. Calder, F. Caspers, I. Collins, O. Gröbner, N. Hilleret, J.-M. Laurent, M. Morvillo, M. Pivi, F. Ruggiero, “Beam-Induced Electron Cloud in the LHC and Possible Remedies”, Proceedings of the 6<sup>th</sup> European Particle Accelerator Conference, Stockholm, Sweden, 22–26 Jun 1998, IOP Publishing Ltd, Bristol, pp. 359–361 (1999).
- [37] B. Henrist, N. Hilleret, C. Scheuerlein, M. Taborrelli, “The Secondary Electron Yield of TiZr and TiZrV Non-Evaporable Getter Thin Film Coatings”, *Applied Surface Science*, vol. 172, pp. 95–102 (2001).
- [38] I. Bojko, N. Hilleret, C. Scheuerlein, “Influence of Air Exposures and Thermal Treatments on the Secondary Electron Yield of Copper”, *Journal of Vacuum Science & Technology A: Vacuum, Surfaces and Films*, vol. 18, n° 3, pp. 972–979 (2000).

## Bibliography Chapter 2

- [39] E.A. Brandes, G.B. Brooks, “Smithells Metals Reference Book”, Seventh Edition, Butterworth Heinemann, Oxford (1992).
- [40] D. Lide, H. Kehiaian, “CRC Handbook of Thermophysical and Thermochemical Data”, CRC Press, Boca Raton (1994).
- [41] “Tugoplavkie metally i splavy (Refractory Metals and Alloys)”, Ed. G.S. Burhanov, Moscow (1986).
- [42] G. Hörz, H. Speck, E. Fromm, H. Jehn “Physics Data. Gases and Carbon in Metals (Thermodynamics, Kinetics, and Properties)” vol. 5-7, “Part VII: Group V A Metals (1): (V)” (1981).
- [43] G. Hörz, H. Speck, E. Fromm, H. Jehn “Physics Data. Gases and Carbon in Metals (Thermodynamics, Kinetics, and Properties)” vol. 5-9, “Part IX: Group V A Metals (3): (Ta)” (1981).
- [44] ASM International, The Materials Information Society, “Binary Alloy Phase Diagrams”, Second Edition Plus Updates, published on CD by the National Institute of Standards and Technology (1996).
- [45] H. Bakker, H. P. Bonzel, C. M. Bruff, M.A. Dayananda, W. Gust, J. Horváth, I. Kaur, G. Kidson, A. LeClair, H. Mehrer, G. Murch, G. Neumann, N. Stolica, N. A. Stolica, N. Stolwijk, “Landolt Börnstein”, New series, Group III “Condensed Matter”, n° 26 “Diffusion in Solid Metals and Alloys”, published by Springer-Verlag, Berlin, edited by H. Mehrer (1990), Chapter 8: “Diffusion of C, N, and O in metals” (A. LeClair), Chapter 9: “The Diffusion of H, D, and T in Metals” (G. Kidson).
- [46] E. Fromm, H. Jehn, G. Hörz, “Physics Data. Gases and Carbon in Metals (Thermodynamics, Kinetics, and Properties)” vol. 5-3, “Part III: Group III A Metals. Rare Earth Metals (Sc, Y, La, Ce, Pr, Nd, Sm, Eu, Gd, Tb, Dy, Ho, Er, Tm, Yb, Lu)” (1978).
- [47] H. Jehn, E. Fromm, G. Hörz, “Physics Data. Gases and Carbon in Metals (Thermodynamics, Kinetics, and Properties)” vol. 5-5, “Part V: Group IV A Metals (1): (Ti)” (1979).
- [48] S. Mozhaev, L. Sokiryanskii, “Some Laws of Oxygen Diffusion in Titanium” in “Mobility of Atoms in Crystal Lattices”, edited by V. N. Svechnikov, Kiev (1965), translated into English by the Israel Program for Scientific Translations (1970).
- [49] H. Jehn, H. Speck, E. Fromm, G. Hörz, “Physics Data. Gases and Carbon in Metals (Thermodynamics, Kinetics, and Properties)” vol. 5-6, “Part VI: Group IV A Metals (2): (Zr, Hf)” (1979).

- [50] E. Samsonov, “Handbook of the Physicochemical Properties of the Elements”, Translated from Russian, Plenum, New York (1968).
- [51] D. Fisher, “Defects and Diffusion in Metal. Five Years of Research and Annual Retrospective I”, Scitec Publications (1999).
- [52] G. Hörz, H. Speck, E. Fromm, H. Jehn “Physics Data. Gases and Carbon in Metals (Thermodynamics, Kinetics, and Properties)” vol. 5-8, “ Part VIII: Group V A Metals (2): (Nb)” (1981).
- [53] “Diffusion Data. A Continuous Compilation of New Reference Data on Diffusion Process in Inorganic Solids and their Melts”, vol. 3, published by The Diffusion Information Center, Cleveland (1969).
- [54] B. Predel “Landolt Börnstein”, New series, Group IV “Macroscopic Properties of Matter”, n° 5 “Phase Equilibria, Crystallographic and Thermodynamic Data of Binary Alloys”, published by Springer-Verlag, Berlin, edited by O. Madelung (1990).
- [55] “Alloy Phase Diagrams”, edited by H. Baker, ASM Handbook n° 3, ASM International, The Materials Information Society (1992).
- [56] P. Waldner, “Modelling of Oxygen Solubility in Titanium”, Scripta Materialia, vol. 40, n° 8, pp. 969–974 (1999).
- [57] S.A. Raspopov, A.G. Gusakov, A.G. Voropayev, M.L. Zheludkevich, A.S. Gritsovet, A.A. Vecher and V.K. Grishin, “Interactions of Zirconium with Atomic and Diatomic Oxygen”, Journal of the Chemical Soc. Faraday Trans., vol. 93, pp. 2113-2116 (1997).
- [58] H. Jehn, E. Fromm, “Oxygen Solubility in the Va-Metals Vanadium, Niobium, and Tantalum”, Metallwissenschaft und Technik, vol. 26, n° 10, pp. 1007-1011 (1972).
- [59] D.L. Smith, “Solubility of Oxygen in Vanadium”, Journal of Less-Common Metals, vol. 31, n° 3, pp. 345–358 (1973).
- [60] R. Bryant, “The Solubility of Oxygen in Transition Metal Alloys”, Journal of the Less-Common Metals, vol. 4, pp. 62–68 (1962).
- [61] “ASM Handbook (Formerly Ninth Edition, Metals Handbook), vol. 13, Corrosion, edited by J. Davis, ASM International, The Material Information Society (1993).
- [62] F. T. Sisco, E. Epremian, “Columbium and Tantalum”, in “Wiley Series on the Science and Technology of Materials”, published by John Wiley and Sons, Inc., New York (1963).
- [63] C. Benvenuti, S. Calatroni, V. Ruzinov, “Diffusion of Oxygen in Niobium During Bake-Out”, SRF2001, Tsukuba, The 10<sup>th</sup> Workshop on RF Superconductivity, September 6–11 (2001).



- [64] A.U. Seybolt, “Solid Solubility of Oxygen in Columbium”, *Journal of Metals*, vol. 6, pp. 774–776 (1954).
- [65] A.Taylor, N. J. Doyle, “Solid-Solubility of Oxygen in Nb and Nb rich Nb-Hf, Nb-Mo and Nb-W Alloys. Part I: The Nb-O System”, *Journal of the Less-Common Metals*, vol. 13, pp. 313–330 (1967).
- [66] S. Stecura, “Observation of Oxide Particles Below the Apparent Oxygen Solubility Limit in Tantalum”, *Metallurgical Transactions*, vol. 5, pp. 1337–1340 (1974).
- [67] R.J. Wasilewski, “The Solubility of Oxygen in, and the Oxides of, Tantalum”, *Journal of the American Ceramic Society*, vol. 75, pp. 1001–1002 (1953).
- [68] M. Parkman, R. Pape, R. McRae, D. Brayton, L. Reed, “Solubility and Diffusion of Oxygen in Tantalum”, *Metallurgy and Metallography*, published by NASA, National Aeronautics and Space Administration, San Carlos (1969).
- [69] Y. Adda, J. Philibert “La diffusion dans les solides”, Presses Universitaires de France, Paris (1966).
- [70] Z.A. Munir, “Analytical Treatment of the Role of Surface Oxide Layers in the Sintering of Metals”, *Journal of Materials Science*, vol. 14, pp. 2733–2740 (1979).
- [71] J. Crank, “The Mathematics of Diffusion”, Clarendon Press, Oxford, Second Edition (1975), p. 32.
- [72] C. Benvenuti, P. Chiggiato, F. Cicoira, Y. L’Aminot, “Nonevaporable Getter Films for Ultrahigh Vacuum Applications”, *Journal of Vacuum Science & Technology A: Vacuum, Surfaces and Films*, vol. 16, n° 1, pp. 148–154 (1998).
- [73] C. Benvenuti, P. Chiggiato, F. Cicoira, V. Ruzinov, “Decreasing Surface Outgassing by Thin Film Getter Coatings”, *Vacuum*, vol. 50, n° 1–2, pp. 57–63 (1998).
- [74] C. Benvenuti, J. M. Cazeneuve, P. Chiggiato, F. Cicoira, A. Escudeiro Santana, V. Johaneck, V. Ruzinov, J. Fraxedas, “A Novel Route to Extreme Vacuum: the Non-Evaporable Getter Thin Film Coatings”, *Vacuum*, vol. 53, n° 1–2, pp. 219–225 (1999).
- [75] C. Benvenuti, “Non Evaporable Getters: from Pumping Strips to Thin Film Coatings”. Internal Report.
- [76] J. Philibert, Chapitre VII “Diffusion dans les Milieux Limités”, dans “Diffusion et Transport de Matière dans les Solides”, Les Editions de Physique, Les Ulis (1985).
- [77] S. Calatroni, “Correlation Between the Grain Size, the Resistivity and  $H_{c1}/H_{c2}$  for Niobium Films Grown on Oxidised and Oxide-Free Copper”, *Proceedings of*

the 10<sup>th</sup> Workshop on RF Superconductivity SRF2001, September 6–11 2001, Epochal Tsukuba International Congress Center, Tsukuba City, only online version: <http://conference.kek.jp/SRF2001>.

- [78] R. J. Knize, J. L. Cecchi, “Theory of Bulk Gettering”, *Journal of Applied Physics*, vol. 54, n° 6, pp. 3183–9 (1983).
- [79] “Foundations of Vacuum Science and Technology”, edited by J. Lafferty, published by John Wiley and Sons, Inc., New York (1998)
- [80] C. Benvenuti, F. Francia, “Room-Temperature Pumping Characteristics of a Zr-Al Nonevaporable Getter for Individual Gases”, *Journal of Vacuum Science & Technology A: Vacuum, Surfaces and Films*, vol. 6, n° 4, pp. 2528–2534 (1988).
- [81] C. Benvenuti, F. Francia, “Room Temperature Pumping Characteristics for Gas Mixtures of a Zr-Al Nonevaporable Getter”, *Journal of Vacuum Science & Technology A: Vacuum, Surfaces and Films*, vol. 8, n° 5, pp. 3864–3869 (1990).
- [82] H. Shih, F. Jona, D. Jepsen; P. Marcus, “Atomic Underlayer Formation During the Reaction of Ti 0001 with Nitrogen”, *Surface Science*, vol. 60, n° 2, pp. 445–465 (1976).
- [83] J. Foord, P. Goddard, R. Lambert, “Adsorption and Absorption of Diatomic Gases by Zirconium: Studies of the Dissociation and the Diffusion of CO, NO, N<sub>2</sub>, O<sub>2</sub> and D<sub>2</sub>”, *Surface Science*, vol. 94, n°2–3, pp. 339–354 (1980).

### Bibliography Chapter 3

- [84] E. Kay, *Techniques of Metals Research*, vol. 1, Chapter 31, “Thin Film Sputtering Techniques”, pp. 1269–1309, published by Interscience, New York (1968). (Published a second time as proceedings: E. Kay, “Physics of Sputtering Processes”, pp. 18–59, published by London MRC Materials Research Co in *Transactions of the Conference and School on the Elements, Techniques and Applications of Sputtering*, October 20–22, 1969, Grand Hotel, Brighton.).
- [85] D. Smith, “Thin-film Deposition. Principles and Practice”, McGraw-Hill, Inc., New York (1995) p. 401.
- [86] Idem as [85] p. 371.
- [87] Idem as [84] p. 1274.
- [88] R. Stuart, G. Wehner, “Sputtering Yields at Very Low Bombarding Ion Energies”, *Journal of Applied Physics*, vol. 33, n° 7, pp. 2345–2352 (1962).

- [89] R. Stuart, “Vacuum Technology, Thin Films, and Sputtering. An Introduction”, Academic Press, Inc. Orlando, Florida, 32887 (1983) pp. 91–135.
- [90] Y. Crassin, “Les Techniques de Dépôt par Pulvérisation Cathodique”, Alcatel CIT, Annecy, France, (Mars 1995) p. 4.5.
- [91] Idem as [85] p. 373.
- [92] Idem as [90] 3.6 c.
- [93] Idem as [85] p. 432.
- [94] J. Bessot, “Techniques du Vide, Pulvérisation Cathodique: Procédés, Appareillage, Applications”, Alcatel (1972), p. 3.
- [95] Idem as [85] pp. 402, 411, 412, 431, 432.
- [96] Idem as [89] p. 114.
- [97] Idem as [85] pp. 435–444.
- [98] N. Matsunami, Y. Yamamura, Y. Itikawa, N. Itoh, Y. Kazumata, S. Miyagawa, K. Morita, R. Shimizu, H. Tawara, “Energy Dependence of the Ion-Induced Sputtering Yields of Monatomic Solids”, Atomic Data and Nuclear Data Tables, vol. 31, pp. 1–80 (1984).
- [99] N. Matsunami, Y. Yamamura, N. Itoh, H. Tawara, T. Kawamura, “Energy Dependence of Ion-Induced Sputtering Yields of Monatomic Solids in the Low Energy Region”, Report: IPPJ-AM-52 Nagoya University, Japan (1987).
- [100] Idem as [89] pp. 94–95.
- [101] Idem as [84] pp. 1275–8.
- [102] Idem as [84] pp. 1271–5.
- [103] Idem as [85] p. 592.
- [104] Idem as [89] p. 115.
- [105] G. K. Wehner, “Sputtering Yield Data in the 100–600 eV”, General Mills Report 2309 (July 15, 1962), General Mills, Inc., Minneapolis, Minnesota (1962).
- [106] Idem as [84] p. 1273.
- [107] C. Schwebel, Cours d’Enseignement des Techniques du Vide, Session Obtention des Couches Minces, vol. 1, “Techniques de Dépôt de Couches Minces”, Société Française du Vide, 20–31 Mars 1995 (1995).

- [108] Idem as [98] p. 24.
- [109] Idem as [98] p. 44.
- [110] Idem as [107] p. 10.
- [111] Idem as [98] p. 28.
- [112] A. Richardt, A.-M. Durand, “Le Vide: Les Couches Minces, Les Couches Dures”, edited by In Fine (1994) pp. 231–232.
- [113] Idem as [98] p. 47.
- [114] Idem as [85] p. 374.
- [115] Idem as [89] p. 96.
- [116] Idem as [85] pp. 379–382.
- [117] Idem as [85] p. 380.
- [118] Idem as [112] pp. 249–252.
- [119] D. Lide, “Handbook of Chemistry and Physics”, 1913–1995, CRS Press, Special Student Edition (1995) pp. 10–205.
- [120] Idem as [112] p. 236.
- [121] Idem as [112] p. 238.
- [122] G. Jackson, “R.F. Sputtering”, Thin Solid Films, vol. 5, n° 4, pp. 209–246 (1970).
- [123] Idem as [112] p. 240.
- [124] Idem as [112] p. 237.
- [125] Idem as [85] p. 477.
- [126] Idem as [85] p. 381.
- [127] Idem as [112] p. 240.
- [128] J. Thornton, A. Penfold, “Cylindrical Magnetron Sputtering”, in Thin Film Processes, edited by J. Vossen and W. Kern, Academic Press, New York (1978) p. 92.
- [129] Idem as [85] p. 487.
- [130] C. Benvenuti, J.-M. Cazeneuve, P. Chiggiato, F. Cicoira, A. Escudeiro Santana, V. Johaneck, V. Ruzinov, J. Fraxedas, “A Novel Route to Extreme Vacuum: the Non-Evaporable Getter Thin Film Coatings”, Vacuum, vol. 53, n° 1–2, pp. 219–225 (1999).

- [131] C. Benvenuti, P. Chiggiato, F. Cicoira, Y. L'Aminot, "Nonevaporable Getter Films for Ultrahigh Vacuum Applications", *Journal of Vacuum Science & Technology A: Vacuum, Surfaces and Films*, vol. 16, n° 1, pp. 148–154 (1998).
- [132] Idem as [89] p. 97.
- [133] Idem as [128] pp. 105–107.
- [134] Idem as [112] pp. 243–245.
- [135] Idem as [85] pp. 159–161.
- [136] J. Thornton, D. Hoffman, "Stress-Related Effects in Thin Films", *Thin Solid Films*, vol. 171, pp. 5–31 (1989).
- [137] R. Messier, A. Giri, R. Roy, "Revised Structure Zone Model for Thin Film Physical Structure", *Journal of Vacuum Science & Technology A: Vacuum, Surfaces and Films*, vol. 2, n° 2 (1984).
- [138] J. Thornton, "High Rate Thick Film Growth", *Annual Review of Material Sciences*, vol. 7, pp. 239–260 (1977).
- [139] B. Ferrario, "Introduzione alla Tecnologia del Vuoto", Seconda Edizione Riveduta ed Ampliata da A. Calcatelli, Pàtron editore, Quarto inferiore, Bologna (1999).
- [140] S. Calatroni, J.-P. Bacher, C. Benvenuti, R. Cosso, J.-M. Dalin, J. Guérin, D. Lacarrère, A. Lasserre, G. Orlandi, E. Radicioni, F. Scalambryn, M. Taufer, "Influence of Copper Substrate Treatments on Properties of Niobium Coatings", *Proceedings of 6<sup>th</sup> Workshop on Radio Frequency Superconductivity*, Newport News, VI, USA, 4–11 Oct 1993, pp. 687–695 (1993).
- [141] C. Benvenuti, P. Chiggiato, P. Costa Pinto, A. Escudeiro Santana, T. Hedley, A. Mongelluzzo, V. Ruzinov, I. Wevers, "Vacuum properties of TiZrV non-evaporable getter films", *Vacuum*, vol. 60, n° 1–2, pp. 57–65 (2001).
- [142] "Foundations of Vacuum Science and Technology", edited by J. Lafferty, published by John Wiley and Sons, Inc., New York, (1998) pp. 709–713.
- [143] E. Collings, *ASM Series in Metal Processing* vol. 3: "The Physical Metallurgy of Titanium Alloys", American Society for Metals, Metals Park, OH (1984) pp. 4–5.
- [144] Idem as [119] pp. 4–31, p. 4–32, p. 4–34.
- [145] M. Donachie Jr, "Titanium: a Technical Guide", ASM International, Metals Park, OH, 2<sup>nd</sup> Edition (1988) p. 38.

- [146] J. Schemel, “ASTM Manual on Zirconium and Hafnium”, edited by American Society for Testing and Materials, Philadelphia (1977), pp. 56–57.

#### **Bibliography Chapter 4**

- [147] “Concise Encyclopedia of Materials Characterization”, edited by R. Cahn, E. Lifshin, Series: Advances in Materials Science and Engineering, Oxford, Pergamon Press Ltd. (1993).
- [148] J.-P. Eberhart, “Analyse Structurale et Chimique des Matériaux”, Dunod, Paris (1989).
- [149] Idem as [148] pp. 109–111.
- [150] J.I. Golstein, D.E. Newbury, P. Echlin, D.C. Joy, A.D. Romig, C.E. Lyman, C. Fiory, E. Lifshin, “Scanning Electron Microscopy and X-Ray Microanalysis. A Text for Biologists, Materials Scientists, and Geologists”, Plenum Press, New York, Second Edition (1992).
- [151] Idem as [150] pp. 417–436.
- [152] N. Cusack, “The Physics of Structurally Disordered Matter: an Introduction”, IOP Publishing Ltd, Bristol (1987).
- [153] D. Brandon, W. Kaplan, “Microstructural Characterization of Materials”, published by John Wiley & Sons Ltd, Chichester (1999).
- [154] J.-P. Lauriat, “Introduction à la Cristallographie et à la Diffraction Rayons X - Neutrons”, edited by Paris Onze Edition, Orsay (1996).
- [155] C. Suryanarayana, M. Grant Norton, “X-Ray Diffraction: a Practical Approach”, New York, Plenum Press (1998).
- [156] L. Dent Glasser, “Crystallography and its Applications”, published by Van Nostrand Reinhold Company, New York (1977).
- [157] H. Klug, L. Alexander, “X-ray Diffraction Procedures: for Polycrystalline and Amorphous Materials”, New York, Wiley Interscience publication, Second Edition (1974), p. 275.
- [158] W. Parrish, “Role of Axial Divergence in Powder Diffractometry”, Zeitschrift für Kristallographie, vol. 127, pp. 200–212 (1968).
- [159] Idem as [148] p. 135.
- [160] H. Lipson, H. Steeple, “Interpretation of X-ray Powder Diffraction Patterns”, published by Macmillan, London (1970), pp. 94–97 and p. 178.

- [161] Idem as [148], Chapter 20.
- [162] H. J. Mathieu, “Analyse des Surfaces”, Cours destiné aux étudiants en Science des Matériaux, 4ème année, à l’EPFL, Lausanne (1997), pp. 117–141.
- [163] J. Watts, “An Introduction to Surface Analysis by Electron Spectroscopy”, Oxford University Press (1990).
- [164] M. Seah, “Quantification of AES and XPS”, in “Practical Surface Analysis, vol. 1: Auger and X-Ray Photoelectron Spectroscopy”, edited by D. Briggs, M. Seah, published by John Wiley & Sons, New York, Second Edition (1995).
- [165] C. Benvenuti, R. Cosso, J. Genest, M. Hauer, D. Lacarrère, A. Rijllart, R. Saban, “A Scanning Auger Electron Spectrometer for Internal Surface Analysis of Large Electron Positron 2 Superconducting Radio-Frequency Cavities”, Review of Scientific Instruments, vol. 67, n° 8, pp. 2788–2795 (1996).
- [166] B. Jungblut, G. Sicking, T. Papachristos, “The Oxidation of Zirconium as Observed by Auger Electron Spectroscopy: a Comparison of Experiment and Density of State Calculations”, Surface and Interface Analysis, vol. 13, pp. 135–141 (1988).
- [167] M.P. Seah, G.C. Smith, “Spectrometer Energy Scale Calibration”, in the same book as Ref. [164].
- [168] Idem as [162] pp. 83–116.
- [169] E. Fischer, H. Mommsen, “Monte Carlo Computations on Molecular Flow in Pumping Speed Test Domes”, Vacuum, vol. 17, n° 6, pp. 309–315 (1967).
- [170] C. Benvenuti, J. M. Cazeneuve, P. Chiggiato, F. Cicoira, A. Escudeiro Santana, V. Johaneck, V. Ruzinov, J. Fraxedas, “A Novel Route to Extreme Vacuum: the Non-Evaporable Getter Thin Film Coatings”, Vacuum, vol. 53, n° 1–2, pp. 219–225 (1999).

## Bibliography Chapter 5

- [171] C. Suryanarayana, M. Grant Norton, “X-Ray Diffraction: a Practical Approach”, Plenum Press, New York (1998), p. 176.
- [172] H. Klug, L. Alexander, “X-ray Diffraction Procedures: for Polycrystalline and Amorphous Materials”, Wiley Interscience, New York, second edition (1974), p. 562.
- [173] V. Urusov, “A Geometric Model of Deviations from Vegard’s Rule”, Journal of Solid State Chemistry, vol. 98, n° 2, pp. 223–236 (1992).
- [174] A. Denton, N. Ashcroft, “Vegard’s Law”, Physical Review A (Statistical Physics, Plasmas, Fluids, and Related Interdisciplinary Topics), vol. 43, n° 6, pp. 3161–3164 (1991).

- [175] A. Cox, M. Sangster, “Vegard’s Rule and Volumes of Formation for Impurity Ions”, *Journal of Physics C (Solid State Physics)*, vol. 18, n° 36, pp. L1123–6 (1985).
- [176] L. De Caro, C. Giannini, L. Tapfer, H. Schönherr, L. Däweritz, K. Ploog, “Validity of Vegard’s Rule for the Lattice Parameter and the Stiffness Elastic Constant Ratios of the AlGaAs Ternary Compound”, *Solid State Communications*, vol. 108, n° 8, pp. 599–603 (1998).
- [177] T. Massalski, “The Lattice-Spacing Relationships in Alloys”, *Metallurgical Reviews*, vol. 3, n° 9, pp. 45–79 (1958).
- [178] J. Friedel, “Deviations from Vegard’s Law”, *Philosophical Magazine*, vol. 46, pp. 514–516 (1955).
- [179] I. McColm, S. Wilson, “Vegard Relationships in Cubic Oxide Bronzes with the Perovskite Structure”, *Journal of Solid State Chemistry*, vol. 41, n° 2, pp. 227–80 (1982).
- [180] D. J. Lee, J. K. Lee, “On Coherency-Induced Ordering in Substitutional Alloys. I. Analytical”, *Acta Materialia*, vol. 48, n° 15, pp. 3847–55 (2000).
- [181] L. Vegard, “Die Konstitution der Mischkristalle und die Raumfüllung der atome”, in *Zeitschrift für Kristallographie, Kristallgeometrie, Kristallphysik, Kristallchemie*, Frankfurt, pp. 17–26 (1977).
- [182] Idem as [171], p. 177.
- [183] V. D. Dobroel’skii, S. M. Karal’nuk, A. V. Koval’, *Metallofizika*, “X-Ray Spectral Study of Various Alloys”, Kiev (Akademiya Nauk Ukrainskoi SSR Institut Metallofiziki) vol. 41, n° 73 (1972).
- [184] Idem as [172], Chapter 9.2.
- [185] Idem as [171], Part II, Module 6.
- [186] H. Lipson, H. Steeple, “Interpretation of X-Ray Powder Diffraction Patterns”, Macmillan, London (1970), pp. 246–263.
- [187] Idem as [172], pp. 656–659.
- [188] J. Schultz, “Diffraction for Materials Scientists”, *International Series in the Physical and Chemical Engineering Sciences*, Edited by N. Amundson, published by Prentice-Hall, Inc., Englewood Cliffs, New Jersey, (1982) p. 266.
- [189] Idem as [171], p. 213.
- [190] M. Fassone, CERN Internal Report n° 99/01/04 (1999).



- [191] Idem as [172], p. 643.
- [192] A.E. Prodromides, C. Scheuerlein, M. Taborelli, “The Characterisation of Non-Evaporable Getters by Auger Electron Spectroscopy: Analytical Potential and Artifacts”, *Applied Surface Science*, vol. 191, n° 1–4, pp. 300–312 (2002).
- [193] F. Meli, Z. Sheng, I. Vedel, L. Schlapbach, “XPS Analysis of the Getter Mechanism and Getter Activation Process”, *Vacuum*, vol. 1, n° 7–9, pp. 1938–1940 (1990).
- [194] T. Haas, J. Grant, G. Dooley, “Chemical Effects in Auger Electron Spectroscopy”, *Journal of Applied Physics*, vol. 43, n° 4, pp. 1853–60 (1972).
- [195] H. Mathieu, J. Mathieu, D. McClure, D. Landolt, “Beam Effects in Auger Electron Spectroscopy Analysis of Titanium Oxide Films”, *Journal of Vacuum Science & Technology*, vol. 14, n° 4, pp. 1023–1028 (1977).
- [196] M. Jobin, M. Taborelli, P. Descouts, “Surface Properties of Electropolished Titanium and Vanadium”, *Applied Surface Science*, vol. 72, pp. 363–372 (1993).
- [197] M. Tomita, T. Tanabe, S. Imoto, “An AES Study of Surface Oxidation of Zirconium”, *Surface Science*, vol. 209, pp. 173–182 (1989).
- [198] B. Jungblut, G. Sicking, T. Papachristos, “The Oxidation of Zirconium as Observed by Auger Electron Spectroscopy: a Comparison of Experiment and Density of State Calculations”, *Surface and Interface Analysis*, vol. 13, pp. 135–141 (1988).
- [199] V. Henrich, G. Dresselhaus, H. Zeiger, “Surface Defects and the Electronic Structure of  $\text{SrTiO}_3$  Surfaces”, *Physical Review B*, vol. 17, n° 12, pp. 4908–4921 (1978).
- [200] F. Szalkowski, G. Somorjai, “Auger Electron Spectroscopy Investigations of the Surface Chemical Composition of Vanadium, the Vanadium Oxides, and Oxidized Vanadium: Chemical Shift and Peak Intensity Analysis”, *Journal of Chemical Physics*, vol. 56, n° 12, pp. 6097–6103 (1972).
- [201] A. Ratti, R. Gough, M. Hoff, R. Keller, K. Kennedy, R. MacGill, J. Staples, S. Virostek, R. Yourd, “The SNS RFQ Prototype Module”, *Proceedings of the 1999 Particle Accelerator Conference*, New York, NY, USA, 27 March–2 April 1999, IEEE, Piscataway (1999), vol. 2, pp. 884–886 (1999).
- [202] X. Lin, C. Ng, K. Ko, “HOM Heating at the PEP-II B-Factory IR Beryllium Vacuum Pipe”, *Proceedings of the 1997 Particle Accelerator Conference*, Vancouver, BC, Canada, 12–16 May 1997, vol. 1, pp. 387–9 (1998).
- [203] Minutes of the LHC Experimental Beampipes, 15<sup>th</sup> February (2001).

- [204] R. Knize, J. Cecchi, “Theory of Bulk Gettering”, *Journal of Applied Physics*, vol. 54, n° 6, pp. 3183–3189 (1983).
- [205] G.S. Bales, A. Zangwill, “Macroscopic Model for Columnar Growth of Amorphous Films by Sputter Deposition”, *Journal of Vacuum Science & Technology A*, vol. 8, n° 61 (1991).
- [206] C. Benvenuti, F. Francia, “Room Temperature Pumping Characteristics for Gas Mixtures of a Zr-Al Nonevaporable Getter”, *Journal of Vacuum Science & Technology A: Vacuum, Surfaces and Films*, vol. 8, n° 5, pp. 3864–3869 (1990).
- [207] H. Shih, F. Jona, D. Jepsen; P. Marcus, “Atomic Underlayer Formation During the Reaction of Ti 0001 with Nitrogen”, *Surface Science*, vol. 60, n° 2, pp. 445–465 (1976).
- [208] J. Foord, P. Goddard, R. Lambert, “Adsorption and Absorption of Diatomic Gases by Zirconium: Studies of the Dissociation and the Diffusion of CO, NO, N<sub>2</sub>, O<sub>2</sub> and D<sub>2</sub>”, *Surface Science*, vol. 94, n° 2–3, pp. 339–354 (1980).
- [209] C. Benvenuti, F. Francia, “Room-Temperature Pumping Characteristics of a Zr-Al Nonevaporable Getter for Individual Gases”, *Journal of Vacuum Science & Technology A: Vacuum, Surfaces and Films*, vol. 6, n° 4, pp. 528–2534 (1988).
- [210] C. Benvenuti, P. Chiggiato, “Pumping Characteristics of the St707 Nonevaporable Getter (Zr 70 V 24.6-Fe 5.4 wt Journal of Vacuum Science & Technology A: Vacuum, Surfaces and Films, vol. 14, n° 6, pp. 3278–3283 (1996).
- [211] K. Ichimura, K. Ashida, K. Watanabe, “Surface Characterization of a Zr-V-Fe Getter by XPS-SIMS-Activation Process and D<sub>2</sub>O Exposure”, *Journal of Vacuum Science & Technology A: Vacuum, Surfaces, and Films*, vol. 3, n° 2, pp.346–50 (1985).
- [212] K. Ichimura, N. Inoue, K. Ashida, K. Watanabe, T. Takeuchi, “Activation Process and Absorption/Desorption of D<sub>2</sub>O for Zr-V-Fe Getter”, *Proceedings of the Sixth International Conference on Plasma Surface Interactions in Controlled Fusion Devices*, Nagoya, Japan, 14-18 May 1984, *Journal of Nuclear Materials*, vol. 128–129, pp. 876–880 (1984).
- [213] K. Ichimura, M. Matsuyama, K. Watanabe, “Alloying Effect on the Activation Processes of Zr-Alloy Getters”, *Journal of Vacuum Science & Technology A: Vacuum, Surfaces, and Films*, vol. 5, n° 2, pp. 220–225 (1987).
- [214] M. Sancrotti, G. Trezzi, P. Manini, “An X-Ray Photoemission Spectroscopy Investigation of Thermal Activation Induced Changes in Surface Composition and Chemical Bonds of Two Gettering Alloys: Zr<sub>2</sub>Fe Versus Zr<sub>57</sub>V<sub>36</sub>Fe<sub>7</sub>”, *Journal of Vacuum Science & Technology A: Vacuum, Surfaces, and Films*, vol. 9, n° 2, pp. 182–189 (1991).

## Bibliography Chapter 6

- [215] R. W. Cahn, P. Hassen, “Physical Metallurgy”, vol. 1, Third, Revised and Enlarged Edition, Elsevier Science Publishers, Amsterdam (1983), where it is quoted: W. Hume-Rothery, J. Inst. Metals, vol. 35, pp. 295 (1926).
- [216] A. Nowikow, H. G. Baer, “Das Dreistoffsystem Titan-Vanaddin-Zirkon”, Z. Metalkde, vol. 49, n° 4, pp. 195–199 (1958).
- [217] ASM International, The Materials Information Society, “Binary Alloy Phase Diagrams”, Second Edition Plus Updates, published on CD by the National Institute of Standards and Technology (1996).
- [218] J. Crank, “The Mathematics of Diffusion”, Clarendon Press, Oxford, Second Edition (1975).
- [219] D. Fisher, “Defects and Diffusion in Metal. Five Years of Research and Annual Retrospective I”, Scitec Publications (1999).

## Bibliography Chapter 8

- [220] “Foundations of Vacuum Science and Technology”, edited by J. Lafferty, published by John Wiley and Sons, Inc., New York, (1998), p. 262.
- [221] D. Smith, “Thin-film Deposition. Principles and Practice”, McGraw-Hill, Inc., New York (1995), p. 379.
- [222] Proceedings of the CERN Accelerator School, Scanticon Conference Centre, Snekersten, Denmark, 28 May – 3 June 1999, CERN Report 99-05, edited by S. Turner (1999), p. 19.
- [223] R. Swalin, “The Science and Technology of Materials vol. 3: Thermodynamics of Solids”, published by Wiley-Interscience, New York, Second Edition (1972) p. 107.
- [224] Idem as [223] p. 177.
- [225] Idem as [220] p. 267.
- [226] H. Bakker, “Materials Science Foundations, vol. 1: Enthalpies in Alloys, Miedema’s Semi-Empirical Model”, edited by M. Magnini, F. H. Wöhlbier, published by Tans Tech Publications Ltd (1998), p. 11.
- [227] Idem as [222] p. 11
- [228] Idem as [223] p. 6.

- [229] C. Kittel, “Introduction to Solid State Physics”, 7<sup>th</sup>, John Wiley and Son Inc., New York (1996), pp. 560–561.
- [230] J.I. Golstein, D.E. Newbury, P. Echlin, D.C. Joy, A.D. Romig, C.E. Lyman, C. Fiory, E. Lifshin, “Scanning Electron Microscopy and X-Ray Microanalysis. A Text for Biologists, Materials Scientists, and Geologists”, Plenum Press, New York, Second Edition (1992), pp. 417–436.
- [231] M. Esnouf, P. H. Jouneau, “Microscopie Electronique en Sciences des Matériaux”, Course at CERN (Mars 2001).

### Bibliography Chapter 9

- [232] C. Benvenuti, P. Chiggiato, F. Cicaira, Y. L’Aminot, “Nonevaporable Getter Films for Ultrahigh Vacuum Applications”, *Journal of Vacuum Science & Technology A: Vacuum, Surfaces and Films*, vol. 16, n° 1, pp. 148–154 (1998).
- [233] C. Benvenuti, P. Chiggiato, “Pumping Characteristics of the St707 Nonevaporable Getter (Zr 70 V 24.6-Fe 5.4 wt % )”, *Journal of Vacuum Science & Technology A: Vacuum, Surfaces and Films*, vol. 14, n° 6, pp. 3278–3283 (1996).
- [234] C. Benvenuti, P. Chiggiato, F. Cicaira, V. Ruzinov, Decreasing Surface Outgassing by Thin Film Getter Coatings, *Vacuum*, vol. 50, n° 1–2, p. 57 (1998).
- [235] C. Benvenuti, J. M. Cazeneuve, P. Chiggiato, F. Cicaira, A. Escudeiro Santana, V. Johaneck, V. Ruzinov, J. Fraxedas, “A Novel Route to Extreme Vacuum: the Non-Evaporable Getter Thin Film Coatings”, *Vacuum*, vol. 53, n° 1–2, pp. 219–225 (1999).
- [236] C. Benvenuti, P. Chiggiato, “Obtention of Pressures in the  $10^{-14}$  Torr Range by Means of a Zr-V-Fe Non Evaporable Getter”, *Vacuum*, vol. 44, n° 5–7, pp. 511–513 (1993).
- [237] “Foundations of Vacuum Science and Technology”, edited by J. Lafferty, published by John Wiley and Sons, Inc., New York (1998).
- [238] C. Benvenuti, J.P. Bojon, P. Chiggiato, G. Losch, “Ultimate Pressures of the Large Electron Positron Collider (LEP) Vacuum System”, *Vacuum*, vol. 44, n° 5–7, p. 507 (1993).
- [239] C. Benvenuti, “Non Evaporable Getters: from Pumping Strips to Thin Film Coatings”. Internal Report.
- [240] C. Benvenuti, P. Chiggiato, P. Costa Pinto, A. Escudeiro Santana, T. Hedley, A. Mongelluzzo, V. Ruzinov, I. Wevers, “Vacuum Properties of TiZrV Non-Evaporable Getter Films”, *Vacuum*, vol. 60, n° 1–2, pp. 57–65 (2001).

- [241] “Vacuum Technology”, Proceedings of the CERN Accelerator School, Scanticon Conference Centre, Snekersten, Denmark, 28 May – 3 June 1999, CERN Report 99-05, edited by S. Turner (1999).
- [242] I. Halley-Demoulin, Ph-D thesis, Université de Bourgogne, Dijon, France (1992).
- [243] T. Nakajama, F. Shoji, E. Yagi, Transactions of the Japanese Institute of Metals, vol. 5, p. 231 (1986).

# Acknowledgments

In the first place, I would like to acknowledge the persons that gave me the unique opportunity to do this work:

F. Lévy, the leader of the Laboratoire de physique des couches minces, who supervised the thesis at EPFL, without the support of who this project would not have been feasible. His confidence in my work provided me an appreciated freedom in my research.

C. Benvenuti, the leader of the Surface and Materials group at CERN, who offered me daily his time, experience and advises in a countless manner.

The financial support of the Swiss national science foundation and of CERN are greatly acknowledged.

Many colleagues at CERN have contributed in an important way to the realisation of this work. I would like to express my gratitude in particular to:

M. Taborelli and C. Scheuerlein for their XPS and AES measurements, for all their precious advises about surface analysis and for their constant enthusiasm.

P. Chiggiato, for sharing his experience about NEG vacuum properties and about vacuum technologies.

S. Calatroni for giving me some keys about sputtering.

I am also indebted to:

S. Sgobba, for the pertinent discussions, for instance about XRD.

G. Jesse, for SEM and EDX analysis.

P. Costa Pinto, for the deposition of some of the coatings.

W. Vollenberg for his advises and technical assistance on the sputtering system.

T. Mongelluzzo for his technical help on the Fischer–Mommsen dome.

M. Remskar (EPFL) and C. Esnouf (INSA) for the TEM experiments.

H. Jaffrezic (Ecole Centrale de Lyon) for the XRD at grazing angles.

I. Canon, for transmitting her experience and passion about LATEX program.

Thank you to all of you for all the interesting discussions we frequently had during those four years.



Alexandra PRODROMIDES  
29 years old, french, single  
alexandra@prodromides.net

**Materials  
engineer**

## EDUCATION:

- 1998-2002 **Ph-D** at **CERN**, the European laboratory for particle physics (Switzerland) and **EPFL**, École Polytechnique Fédérale de Lausanne, about Non Evaporable Getter films. The **production parameters** of these patented materials were improved in view of **large scale** production.
- 1997: **Master degree** in material sciences (University of Caen, France).
- 1994-97: **Engineering school** in material sciences (Caen, France).
- 1991-94: Specialized-studies to prepare the entrance-examination to french national engineering schools (Mathématiques Supérieures, Mathématiques Spéciales).
- French:** Mother tongue.
- English:** **Able to read, write, speak** (9 months spent in english speaking countries).  
613 points to the TOEFL exam.
- Spanish:** Fluent (studied during 7 years).

## TRAININGS:

- 1998: (10 months) **Ceramics** laboratory at EPFL.  
Establishment of a production technique by **electrodeposition** compatible with **large scale production** and **improving the quality** of **piezoelectric thin films**.
- 1997: (6 months) Ceramics laboratory at EPFL.  
Quality optimization of **pyroelectric thin films** used as devices in microelectronics.
- 1996: (4 months) Ceramics laboratory at EPFL.  
**Densification** of platinum screen-printed thin layers.
- 1994: (2 months) Zeller Plastik (Chicago, United States).  
**Quality control** in a polymerization laboratory producing plastic caps.

## PERIODICAL SCIENTIFIC WORKS:

- 1996-97: (5 months) CRISMAT, material sciences laboratory in Caen (France).  
Improvement of levitation capacity of **supraconducting** ceramics dedicated to **energy storage**.
- 1995-96: (3 months) Au CRISMAT. Mossbauer spectroscopy.

## PUBLICATIONS AND PARTICIPATIONS TO INTERNATIONAL CONFERENCES:

- 2002: "Influence of the Substrate Coating Temperature on the Vacuum Properties of Ti-Zr-V Non-Evaporable Getter Films", C. Benvenuti, P. Chiggiato, P. Costa Pinto, A. Prodromides, V. Ruzinov, to be published
- 2002: "The Characterisation of Non-Evaporable Getters by Auger Electron Spectroscopy: Analytical Potential and Artifacts", A. E. Prodromides, C. Scheuerlein, M. Taborelli, Applied Surface Science, vol. 191, n° 1-4, pp. 300-312 (2002).
- 2001: Results obtained on the "Influence of substrate material and coating temperature on the vacuum properties of  $Ti_xZr_yV_{1-x-y}$  getter films produced by magnetron sputtering", presented at the IUVESTA 15<sup>th</sup> International Vacuum Congress, November 2001, San Francisco, California.
- 2000: Results obtained on the "Influence of the elemental composition and crystal structure on the vacuum properties of TiZrV non-evaporable getter films" presented at the American Vacuum Society 47<sup>th</sup> International Symposium, Boston, USA.  
The corresponding paper is published in the Journal of Vacuum Science Technology A (Vacuum, Surfaces, and Films), vol. 19, n° 6, pp. 2925-30, Nov. 2001, by C. Benvenuti, P. Chiggiato, A. Mongelluzzo, A. Prodromides, V. Rouzinov, C. Scheuerlein, M. Taborelli, F. Lévy
- 1999: Results obtained on "Lowering the activation temperature of TiZrV non-evaporable getter films" presented at the European Vacuum conference, Lyon, France, 7<sup>th</sup> Decembre 1999.  
The corresponding paper is published in Vacuum, vol. 60, n° 1-2, pp. 35-41, 2001, by A. E. Prodromides, C. Scheuerlein, M. Taborelli.
- 1998: "Cathodic Electrodeposition of mixed oxide/hydroxide precursor for lead-zirconate-titanate thin films", A. E. Prodromides, P. Schmuki, Ferroelectrics, vol. 225, pp. 311-318, 1999, Proceedings of the Fourth European Conference on applications of Polar Dielectrics, ECAPD IV, Montreux, Switzerland, August 24-27 1998.